Chapter 4

S-Band Linear Collider

SBLC Collaboration

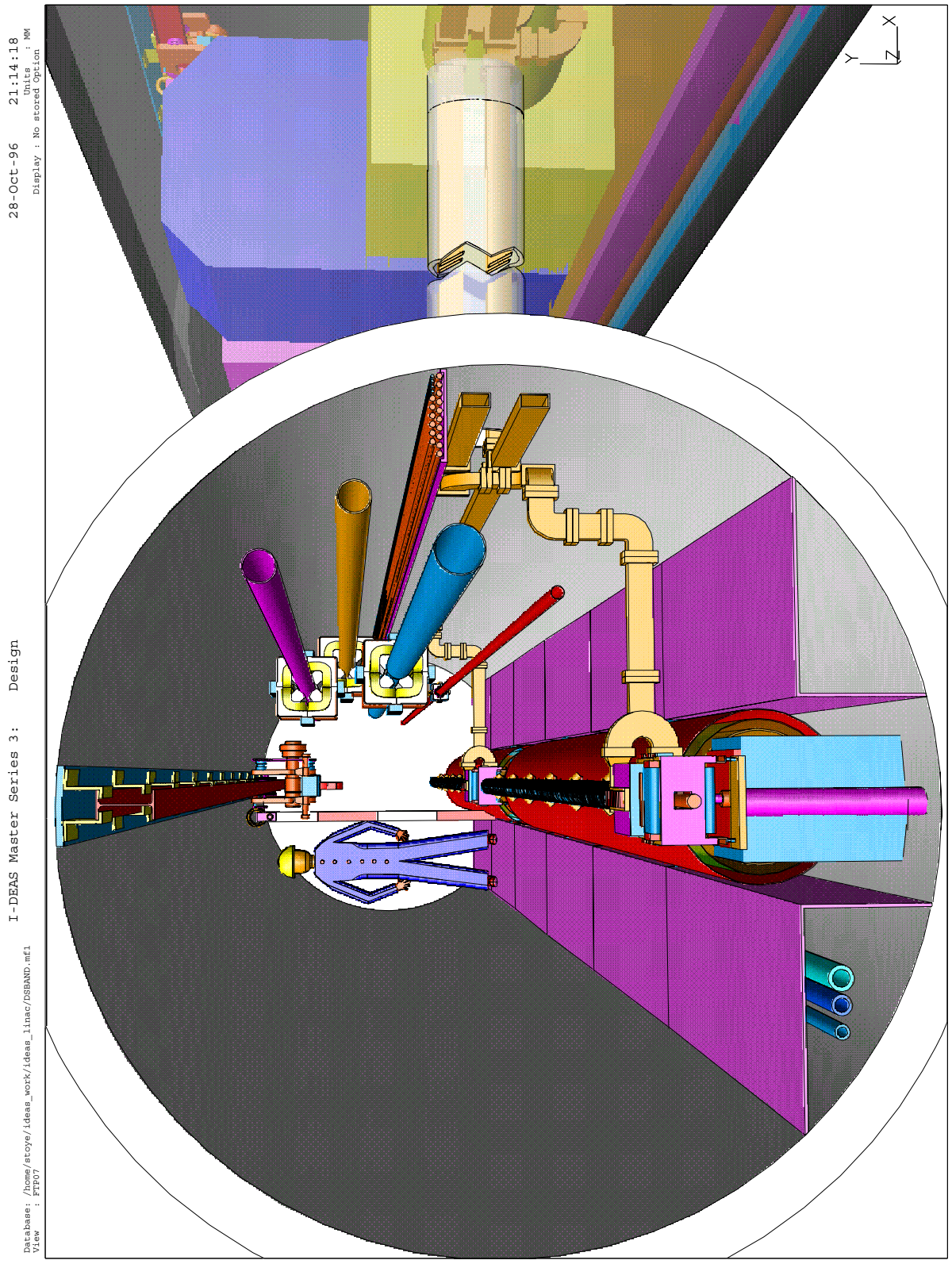
28-Oct-96 21:14:18
Units : MM
Display : No stored Option
I-DEAS Master Series 3: Design
Database: /home/stcoye/ideas_work/ideas_linac/DSBAND.mf1
View : FTP07
Y
X
Z

Author List

DESY (coordinating institute), Notkestr. 85, D-22603 Hamburg: W. Bialowons, M. Bieler, F. Brinker, R. Brinkmann (editor), S. Choroba, M. Dohlus, A. Drozhdin (now at FNAL), J. Eckholt, U. Engelke, K. Flöttmann, R. Glantz, J. Hameister, K. Hanke, H. Hartwig, H. Herold, N. Holtkamp, J.P. Jensen, A. Jöstingmeyer, H. Kaiser, J. Kouptsidis, G. Kreps, H. Kumpfert, T. Limberg, F. Löffler, M. Lomperski, M. Marx, G. Meyer, N. Meyners, C. Montag, M. Nagl, F. Peters, P. Pillat, J. Roßbach, M. Sachwitz, M. Schmitz, H. J. Schreiber, S. Schreiber, D. Schulte (now at CERN), W. Schwarz, M. Seidel (now at SLAC), K. Sinram, M. Sommerfeld, T. Stoye, K. Tesch, G.-A. Voss, N. Walker, R. Wanzenberg, M. Wendt, Su. Wipf, St. Wipf, H. Wümpelmann, F.R. Ullrich;

Budker INP, Protvino Branch, 142284 Protvino, Moscow Region: A. Sery;

CE Saclay, F-91191 Gif-sur-Yvette Cedex: A. Mosnier, O. Napoly, A. Novokhatsky (on sabbatical leave from Budker INP, Novosibirsk);

FH Emden, Constantiaplatz 4, D-26723 Emden D. Einfeld, J. Schaper;

NSRL, Hefei, Anhui, China: K. Jin;

IHEP Protvino, 142284 Protvino, Moscow Region: O. Kourneev, M. Maslov;

INFN Frascati, Via E. Fermi 40, I-00044 Frascati: M. Castellano;

INR Troitsk, 60th Anniversary of October Prospect 7A, 117312 Moskva: T. Khabiboulline, A. Naboka, V. Puntus, G. Romanov, A. Vasyuchenko;

J. Stefan Institute, Jamova 39, SL-1001 Ljubljana M. Plesko;

Nat. Lab. for High Energy Physics, KEK, 1-1 Oho, Tsukuba-shi, Ibaraki-Ken 305: H. Matsumoto;

LAL Orsay, F-91405 Orsay Cedex: J. Gao;

MPEI, Kashirskoe Shosse 31, 115409 Moskva: V. Kalyuzhny S. Ivanov, V. Kaljuzhny, V. Kandrunin, D. Kostin, O. Milovanov, N. Nechaev, A. Parfenov, N. Sobenin, S. Yarigin, A. Zavadov, A. Zavadtsev, B. Zverev;

Sincrotrone Trieste, Padriciano 99, I-34012 Trieste C. Bocchetta, M. Svandrlik;

SLAC, P.O. Box 4349, Stanford, CA 94309: K. Bane, P. Emma;

TH Darmstadt, Inst. f. Hochfrequenztechnik, Schloßgartenstr. 8, D-64289 Darmstadt: U. Becker, M Drevlak (now at MPI f. Plasmaphysik, Greifswald), B. Krietenstein, P. Pinder, O. Podebrad, M. Sommer, M. Timm, U. van Rienen, T. Weiland;

Johann-Wolfgang-Goethe Universität, Inst. f. Angewandte Physik, Robert-Mayer-Str. 2-4, 60054 Frankfurt: H.-W. Glock, P. Hülsmann, H. Klein, M. Kurz, W.F.O. Müller, U. Niermann, C. Peschke;

Yerevan Physics Institute, Alikhanian Brothers St. 2, 375036 Yerevan: V. Tsakanov.

Contents

4.1 Overview

4.1.1 S–Band Concept

The two most important aspects of very high energy linear colliders are their luminosity requirements and their costs. To do meaningful physics in the energy range of 500 GeV cms luminosities above 10^{33} per cm^2 and per sec are necessary, one to two orders of magnitude larger than in existing colliders. On the other hand unit costs of accelerators (costs per GeV) must be considerably smaller than those of existing machines to make these new installations economically feasible.

4.1.1.1 The Rationale for using S-Band Technology

To reach luminosities in the $10^{33}...10^{34}/(cm^2 \cdot sec)$ range, large bunch charges and unprecedentedly small beam cross sections at the collision point are necessary. Also, the bunch collision frequency must be large. These requirements automatically lead to linear collider designs with large pulse currents, many bunches in each pulse and extremely small beam emittances, combined with very small beta functions (i.e. strong focusing) at the interaction point. Typical cross sections at the collision point must be of the order of one hundredmillionth of a square millimeter, five orders of magnitude smaller than typical collision point cross sections in circular colliders. The main problem of large bunch charges and large pulse currents combined with ultra small beam emittances are bunch instabilities in the linear accelerator structures. Such instabilities have been observed almost in all high current linear accelerators since their invention 50 years ago. They are due to electromagnetic wake-fields of the beam current acting through the accelerating structure back on the particle bunches. Transverse single and multibunch instabilities are due to transverse alignment errors between the beam and the accelerating structure and increase with the third power of the accelerating frequency f_{RF} in otherwise scaled accelerating structures. Longitudinal wakefields can create an untolerably large energy spread within the particle bunches, an effect which scales quadratically with the accelerating frequency.

It is evident, that small accelerating frequencies have great advantage. On the other hand there are economical arguments for not going too low in frequency, mostly having to do with the increasing component costs associated with the large stored power for linac pulses at lower frequency. This is the reason, why linear accelerators with warm (i.e. nonsuperconducting) structures seldom are built for frequencies lower than S-band (3 GHz). But avoidance of beam instabilities, preservation of ultra small beam emittances and more relaxed structure and alignment tolerances are strong arguments for choosing S-band technology over designs at higher frequencies.

In S-band structures accelerating fields in excess of 30 MV/m have been used. Recently it has been shown that even with gradients as large as 80 MV/m dark currents from field emission can be kept small, provided the structures were built in clean rooms and with the proper surface treatment [1]. The most economical gradient in a linear accelerator is given by a compromise between length and RF peak power: The lowest costs are reached if the sum of all costs which are proportional to length (structure

costs, tunnel costs, etc.), referred to as linear costs, are about equal to the sum of all costs for creating RF-power (klystrons, modulators, power consumption, etc). For our S-Band design this cost minimum seems to occur at gradients of the order of 20 MV/m. This value is far below the gradient, which in S-band structures can safely be generated. An energy increase at a later stage can therefore be done by simply increasing the peak RF power. Even at twice this gradient safe operation with negligible field emission current and negligible vacuum arcing is possible.

S-Band technology for linear accelerators has been in use for the last 50 years. It is by far the most developed and refined technology and almost the only one in use for linear accelerators. A wealth of experience and knowledge make realistic designs and cost estimates possible. This is another strong reason to favor this technology. Design studies during the last few years have shown that S-band colliders are as efficient as colliders designed for higher frequencies and that luminosities are comparable.

The largest S-band accelerator which has ever been built is the 50 GeV SLAC linac. It has about 20% of the size and energy of each of the two linacs needed in a 500 GeV cms collider. Although built 30 years ago and at that time considerably less sophisticated than the next linear collider will be, it still may be considered to be a prototype of the linear collider to be built, sufficiently close to make unexpected problems much less likely. Colliders to be built with new and different technologies cannot refer to a representative existing prototype. They certainly will have to be built in 2 to 3 stages, each stage having to wait for the previous one to be completed and thoroughly tested. This of course will have a strong effect on costs and time schedules. An important example for this statement is the emittance dilution in this linac, one of the most important aspects in linear colliders: These dilutions have been measured in the SLC and found not to be far off from the tolerable amounts in the SBLC. The final focus test beam FFTB [1] at the SLC produced already vertical beam sizes within a factor of two from the goals of SBLC, considering the larger adiabatic damping to be expected in the SBLC due to the higher energy. These observations represent important confirmation of the technical feasibility of an S-band collider, which so far are lacking for colliders at very different, especially higher, frequencies.

We therefore believe that a linear collider at S-band frequency is a cost efficient and safe choice. Reliable performance predictions and cost estimates can be made.

4.1.1.2 The Basic Collision Cycle

The 2 linear accelerators working at the S-band frequency f (f=3000 MHz, wavelength 10 cm) accelerate trains of electron and positron bunches respectively to energies of 250 GeV (375 GeV in the second stage) and direct them such, that individual elctron bunches will collide with individual positron bunches almost head-on [1]

Before injection and acceleration in the two linacs, the two 600 m long bunch trains, each containing 333 bunches of electrons and positrons respectively, were stored in two damping rings for times of 20 ms, to damp transverse and longitudinal particle oscillations to minimal transverse and longitudinal emittances. Bunch compressors between

[1] A small crossing angle of 6 mrad ensures that particle beams collide only at the interaction point.

the damping rings and the linear accelerators shorten the lengths of the individual bunches to 0.3 mm. At the entrance of the linac, a feedback system will remove jitter and bunch to bunch offsets. The combination of very small transverse emittances and very small beta functions at the interaction point (IP) produce there the extremely small beam dimensions of 335 nm $\times$ 16 nm and lead to average luminosities of $5{\cdot}10^{33}/(\mathrm{cm}^2{\cdot}\mathrm{sec})$. Again a feedback system is installed to stabilise the orbit of the incoming bunch train. These feedback systems, at the entrance of the main linac and at the IP, make more than 80 % of the SBLC bunch train practically immune to mechanical vibrations which otherwise could dilute the emittance or separate the beams in the IP.

After collision, following the interaction point, the electron beam goes through an undulator (see section 4.4.2) in which it produces an intense 30 MeV photon beam. This in turn is directed on a thin target to produce positrons, whith a small transverse emittance. These positrons are then accelerated to an energy of 3 GeV and injected into the positron damping ring. Both high energy beams, after collision and after the electron beam has produced the positrons for the next cycle, are dumped in special beam dumps. The electron bunch train for the next collision cycle is formed by a grid controlled electron gun. Electron bunches are also accelerated to energies of 3 GeV befor they are injected into the electron damping ring. To reach the design luminosity of $5{\cdot}10^{33}/(\mathrm{cm}^2\mathrm{sec})$ the cycle just described is repeated at the rate of 50 Hz.

4.1.1.3 The General Layout

The collider to be built, because of its length ($\approx$33 km), cannot be accomodated on the existing DESY site. But it still will be of great advantage to have one end of its long tunnel at DESY to use existing infrastructure more efficiently. Like most of the HERA-tunnel the SBLC-tunnel will have to be under existing housing, roads and industries. Access from the surface will be limited to the ends of the collider tunnel and near the interaction area, located halfway down the machine. The interaction region with its large experimental hall and additional services buildings will require a larger piece of land, on which also the circular tunnel for the two damping rings, the beam dumps and the 3 GeV preaccelerators for electrons and positrons are located. The far end of the collider tunnel must also be located on an available piece of land to locate the necessary service buildings and the 180°-loop for the injection of the low emittance beam coming down from the central damping rings through the collider tunnel. Except for these 3 points, i.e. the two ends of the linac and the central region, no further accesses are planned. All services like electric power, air, cooling water and all control cabling will enter and leave only at those 3 points. Figures 4.1.2, 4.1.1 and 4.1.3 show schematically the end of the SBLC machine as it is located on the DESY-site, the central region, about 16.5 km away from the DESY-site and the far end of the SBLC- machine, about 33 km away from the DESY-laboratory. The tunnel is kept straight even in the beam delivery section, so it can later be used to install linac structures to allow for an extension to 1.5 or 2 TeV. In Fig. 4.1.1 is schematically shown the:

1 the central experimental hall with one IP installed and the possibility to arrange a beam line for the second IP

2 the 600 m long electron and positron damping rings, arranged on top of each other

3 the injection of 3 GeV electron and positron beams into the damping rings

4 the two beam transfer lines guiding the low emittance beams of electrons and positrons from the damping rings back into the electron and positron accelerator tunnels, were they are taken back to the injection ends of the two accelerators

5 the two 3 GeV preaccelerators

6 the undulator and target for positron production

7 the two high energy beam dumps

8 Also shown are a 200 MeV positron preaccelerator which accelerates the positrons coming from the target

9 a 180 ° achromatic isochronous bend to inject the 200 MeV positrons into the 3 GeV accelerator and, on the other side,

10 the electron gun

There are plans to use the first section of the main electron accelerator also to produce low emittance beams with energies up to 50 GeV suitable for driving free electron lasers (see chapter 5). These lasers will produce coherent photon beams with energies up in the x-ray (Å) range and with unprecedented brilliance. The laboratories, in which these x-ray beams are used for research in a wide range of different disciplines, will also be part of the central region complex.

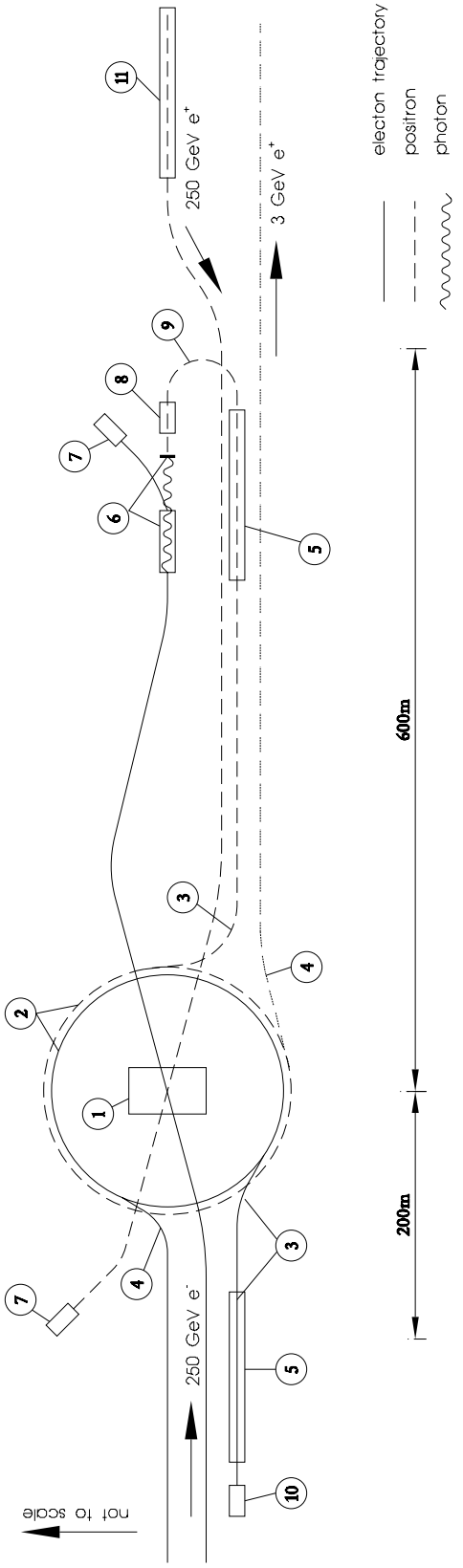

Figure 4.1.1: *Sketch of the SBLC central region. (1): experimental hall, (2): damping rings, (3,4): injection/extraction lines, (5) 3 GeV preaccelerator, (6): positron source, (7): beam dump, (8) 200 MeV positron injector, (9): achromatic isochronous bend, (10): electron gun, (11): main linac.*

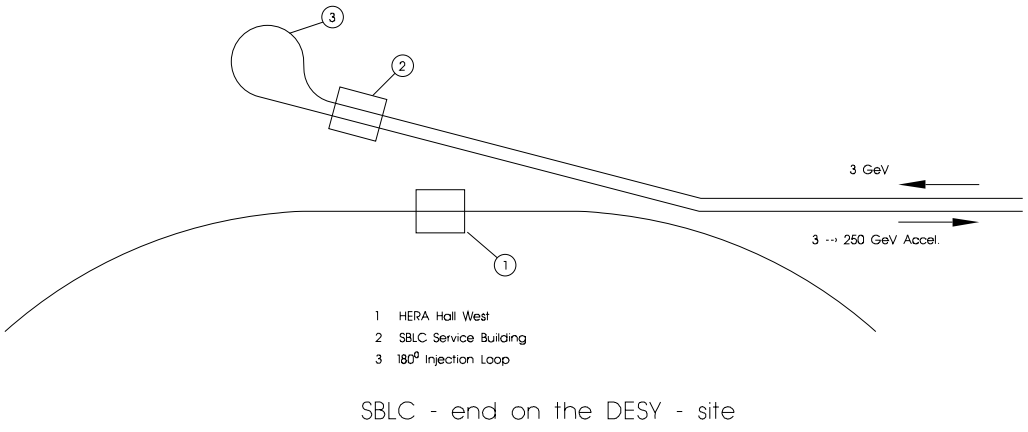

Figure 4.1.2: *The electron linac end at the DESY site.*

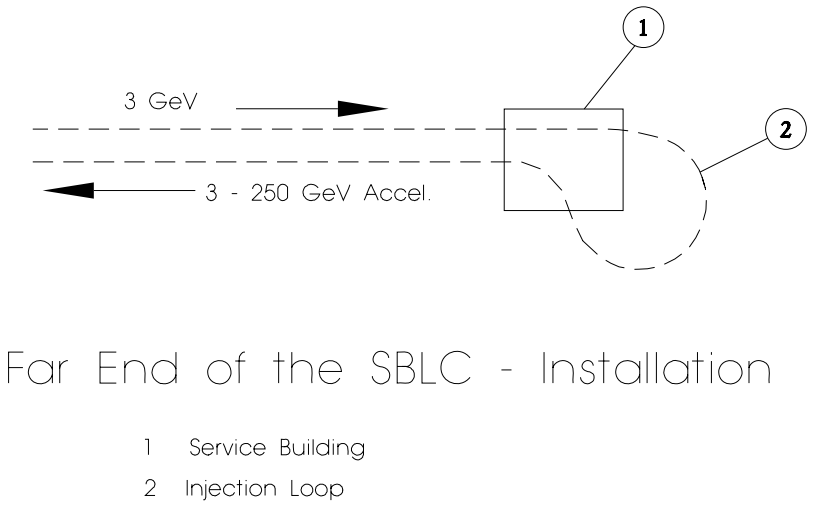

Figure 4.1.3: *The far end of the positron linac.*

Fig. 4.1.2 shows schematically the one end of the SBLC- installation on the DESY site. The tunnel is arranged tangentially to the HERA tunnel. It would be possible to use part of the SBLC as an injector for high energy electrons, up to 25 GeV, in HERA. These electrons can then be stored in HERA and ejected at a slow, continuous rate for Nuclear Physics experiments (see appendix B). Additional linac pulses will be used for the Nuclear Physics and the free elctron laser facilities. Also shown in

Fig. 4.1.2 is the beam loop (3) which turns the low emittance 3 GeV electron beam coming from the central electron damping ring 180° around for injection into the main electron accelerator. This loop contains the feedback system to stabilize the bunch train in front of the linac.

Fig. 4.1.3 shows schematically the far end of the SBLC installation with the loop and the feedback system for the positron injection into the main positron linac. Also shown are service buildings housing tunnel ventilation systems, power supplies, electrical facilities etc. as they also exist in the central service buildings and on the DESY-site.

In order to reach efficiently large integrated luminosities, a machine of such complexity and size will need continuous servicing and maintenance. It is imperative to minimize those parts of the machine, which during normal operation are inaccessible for reasons of radiation safety. But klystrons, their power supplies and all auxilliary equipment, and most of all electronics and controls should be accessible at all times to be serviced and maintained by a relatively small service group. Fig. 4.1.4 shows in cross section two parallel tunnels.

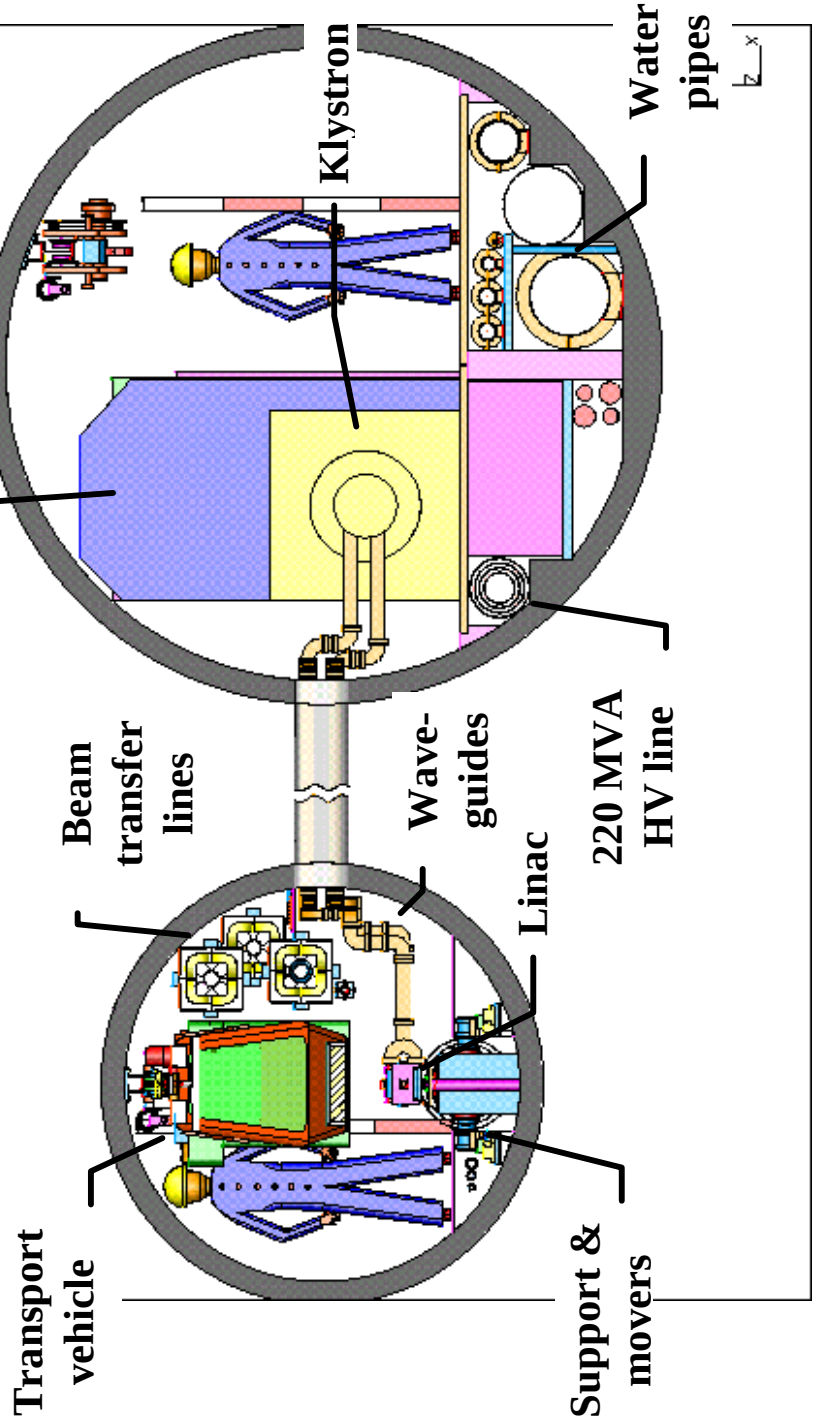

Figure 4.1.4: *Cross section of the SBLC tunnels in the periodic part of the linac. The smaller tunnel, housing the linac, has a diameter of 2.5 m. The larger tunnel, housing the RF-sources, has a diameter of 4 m. The tunnels are separated by 5 m.*

The larger one accomodates the 2500 klystrons with their modulators, power supplies and controls, water supply lines, controls and mixing valves for local supplies, electrical power distribution, transformers and circuit breakers and accelerator control and electronics. The second smaller tunnel houses the accelerator: Accelerating wave guides, focusing quadrupoles, vacuum pumps and beam lines for the 3-GeV low emittance beams, the low emittance beams for the FEL laboratory and possibly beams for the Nuclear Physics installation. At intervalls of 25 meters connecting pipes between the tunnels allow the transfer of RF power lines, water pipes and control circuitry. Connecting tunnels with larger cross section at 1.5 km spacing allow personell access to the accelerator tunnel, when the linacs are not running. This two tunnel arrangement provides for convenient emergency exit routes and simple ventilation systems. It also seems possible to arrange all the components mentioned above in a single tunnel with a somewhat larger cross section. This was the set-up under study in the passed years. It was assumed, that the two tunnel version with its many obvious advanteges would be considerably more expensive and would be technically more difficult. Recent advances in the technology of tunnel construction seem to have resolved many of the earlier difficulties such that the 2- tunnel arrangement now seems to be preferable.

4.1.2 Parameters at 500 GeV

The second key parameter for a linear collider, besides the center-of-mass energy of the colliding beams, is the luminosity L. It is given by

$$L = \frac{n_b N_e^2 f_{rep}}{4\pi\sigma_x^*\sigma_y^*} \times H_D \tag{4.1.1}$$

n_b	number of bunches per pulse
N_e	number of electrons (positrons) per bunch
f_{rep}	pulse repetition frequency
$\sigma_{x,y}^*$	horizontal (vertical) beam size at interaction point
H_D	disruption enhancement factor (typically $H_D \approx 1.5$)

Introducing the average beam power $P_b = E_{cm} n_b N_e f_{rep}$, the luminosity can be written as

$$L = \frac{P_b}{E_{cm}} \times \frac{N_e}{4\pi\sigma_x^*\sigma_y^*} \times H_D \tag{4.1.2}$$

An important constraint on the choice of interaction parameters is due to the effect of beamstrahlung: the particles emit hard synchrotron radiation in the strong space-charge field of the opposing bunch. The average fractional beam energy loss from beamstrahlung is approximately given by [3]:

$$\delta_E \approx 0.86 \frac{r_e^3 N_e^2 \gamma}{\sigma_z(\sigma_x^* + \sigma_y^*)^2} \tag{4.1.3}$$

r_e	classical electron radius
γ	relativistic factor E_{beam}/m_0c^2

Beamstrahlung causes a reduction and a spread of the collision energy and can lead to undesirable experimental background. The energy loss δ_E therefore has to be limited to typically a few percent. By choosing a large aspect ratio $R = \sigma_x^*/\sigma_y^* >> 1$, δ_E becomes independent of the vertical beam size and the luminosity can be increased by making σ_y^* as small as possible. Since $\sigma_y^* = (\epsilon_{y,N}\beta_y^*/\gamma)^{1/2}$, this is achieved by both a small vertical beta function at the IP and a small normalized vertical emittance. The lower limit on β_y^* is given by the bunch length ("hourglass effect"). Setting $\beta_y^* = \sigma_z$, the luminosity can be expressed as:

$$L \approx 5.74/rmm^{-3/2} \cdot 10^{20} \times \frac{P_b}{E_{cm}} \times \left(\frac{\delta_E}{\epsilon_{y,N}}\right)^{1/2} \times H_D \qquad (4.1.4)$$

The choice of a low drive frequency for the linacs results in relatively small transverse

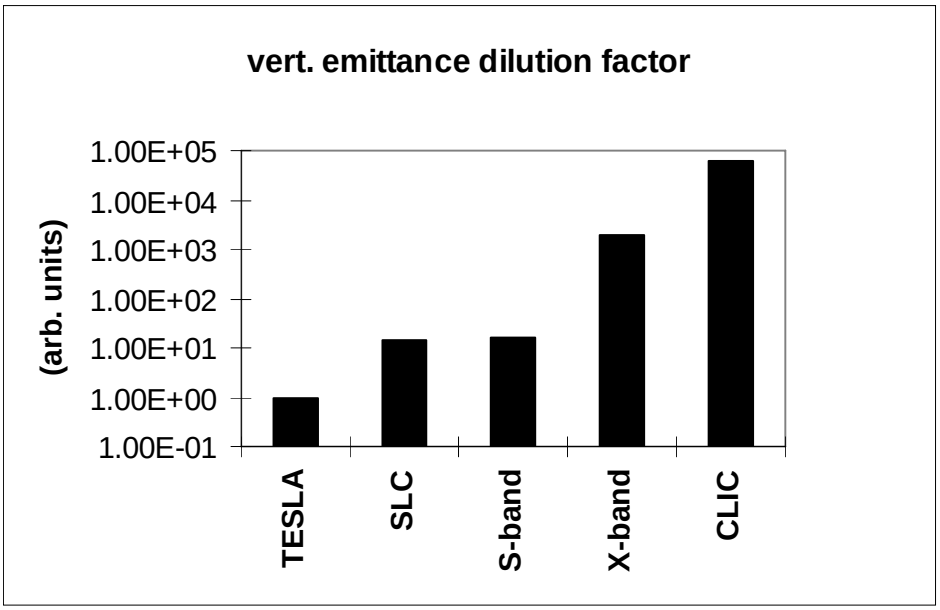

Figure 4.1.5: *Wakefield emittance dilution factor for different 500 GeV linear collider designs. The SLC is included for comparison.*

and longitudinal wakefields in the accelerating structures. Beam dynamics issues are discussed in detail in section 4.3, but it is instructive here to compare the different linear collider design concepts on a basis of simple scaling arguments [4]. One of the most essential contributions to emittance dilution results from short-range transverse wakefields due to random offsets of the accelerating structures w.r.t. the beam orbit. The emittance dilution from this effect can be written as

$$\frac{\Delta\epsilon}{\epsilon} \propto F \cdot \bar{\beta} \cdot \delta y_c^2 \qquad (4.1.5)$$

where $\bar{\beta}$ denotes the average β-function in the linac (the stronger the focussing, the smaller $\bar{\beta}$), δy_c the rms-offset of the structures and F the dilution factor which depends on the beam parameters and very strongly on the linac frequency. In particular, F is proportional to the square of the bunch charge. By choosing a small bunch charge ($N_e = 1.1 \cdot 10^{10}$) the dilution factor in SBLC is comparable to the one calculated for typical SLC operation parameters, even though the vertical emittance in our case is more than an order of magnitude below the SLC value. This is illustrated in fig. 4.1.5, where the considerable variation of F for different collider designs is also shown. It becomes clear that SBLC can afford less stringent requirements for the alignment tolerances and for the beam optics compared to other designs at higher frequency (the superconducting TESLA linac operates at 1.3 GHz and has less tight alignment tolerances).

Accelerating gradient g [MV/m]	17
RF-frequency f_{RF} [GHz]	3
Fill factor (act. length / linac length)	0.95
Total site length L_{tot} [km]	33
# of acc. structures	5032
# of klystrons	2516
Klystron peak power [MW]	150
Repetition rate f_{rep} [Hz]	50
Beam pulse length T_P [μs]	2
RF-pulse length T_{RF} [μs]	2.8
# of bunches p. pulse n_b	333
Bunch spacing Δt_b [ns]	6
Charge p. bunch $N_e[10^{10}]$	1.1
Emittance at IP $\gamma\epsilon_{x,y}[10^{-6}\mathrm{m}]$	5, 0.25
Beta at IP $\beta^*_{x,y}$ [mm]	11, 0.45
Beam size at IP $\sigma^*_{x,y}$ [nm]	335, 16
Bunch length at IP σ_z [mm]	0.3
Beamstrahlung δ_E [%]	2.8
Luminosity $L[10^{33}\mathrm{cm}^{-2}\mathrm{s}^{-1}]$	5
Beam power P_b [MW]	14.5
AC power P_{AC} [MW]	140

Table 4.1.1: *SBLC parameters for E_{cm}=500 GeV.*

With the bunch charge fixed, the pulse current set to 300 mA (corresponding to 20% beam loading) and the pulse length to 2 μs, the number of bunches per pulse (n_b=333) and the bunch spacing (Δt_b=6 ns) are determined. The other beam parameters are chosen under a number of boundary conditions, such as the damping ring emittance, the single-stage bunch compressor, etc. An overview of the SBLC parame-

ters at E_{cm}=500 GeV is given in table 4.1.1.[2]

4.1.3 Stages of Operation and Energy Upgrade Options

Our detailed study presented in this report focusses on the optimized design for 500 GeV cms energy as described above. In this section, we also take a look at possible stages in which the SBLC can be built and operated and at options which open up an economic way to upgrade the energy beyond E_{cm}=500 GeV.

As a boundary condition the site length is kept fixed and the possibility of extending (or shortening) the machine is not further discussed here. Under this condition, the beam energy is completely determined by the available RF-peak power. Changing the number of pulsed RF-power sources is the most straightforward way to change the peak power. Introducing RF-pulse compression is an alternative to raise the peak power with the advantage of low cost, but at the expense of reduced efficiency. Both possibilities (and possible combinations) are discussed in the following.

Under the assumption that the relative amount of beam loading is kept constant by adjusting the beam pulse current proportional to the accelerating gradient, the latter scales simply as $g \propto \hat{P}_{RF}^{1/2}$ where $\hat{P}_{RF}$ denotes the peak power. If we consider the top quark threshold as a reasonable lower limit for E_{cm} ($\approx$ 350 GeV), the simplest way to begin collider operation with a cost-saving 1st stage is to install only half of the klystrons and modulators. According to the condition of having approximately equal linear cost and RF-cost for the reference design, this 1st stage reduces the investment to about 75 % of the 500 GeV machine. The AC-power is half of that at 500 GeV, as is the luminosity. Applying the same scaling in the opposite direction for an upgrade beyond 500 GeV leads to a 700 GeV machine requiring an additional 50 % of investment (twice the number of klystrons, etc.).

In the context of different operational stages normal conducting linear accelerators allow for an additional degree of freedom. At a given energy beam power can be exchanged against available RF peak power, without increasing the AC power requirement, by using RF pulse compression systems. The pulse compressor scheme intrinsically can not provide as high beam power per pulse due to the limited RF pulse length being available for acceleration (compare section 4.2.8). On the other hand one can later on increase the Luminosity by increasing the repetition rate, which of course would increase the AC power requirement. In that sense, for a given RF peak power installed in the linac, higher energies can be achieved at the expense of less beam power by adding comparatively small investment costs, namely SLED cavities.

By adding the SLED concept to the 500 GeV collider, an upgrade path to 750 GeV cms energy is opened. The machine parameters for this low-cost upgrade are summarised in Table 4.1.2. By the time the accelerator is upgraded, several years of opera-

[2]The site length specified does not yet take into account reserve for energy management and diagnostic and beam extraction sections in the linac. We foresee to increase the accelerating gradient over the first km of both linacs by doubling the RF-power per structure in order to create the required reserve. The beneficial effect on the beam dynamics has not yet been included in the study presented here.

tional experience have passed and ways to further decrease the emittance dilution will have been established. We therefore include here the assumption of a moderately (by a factor of 2.5) reduced vertical emittance for operation at higher energy[3]. The beam delivery system (see section 4.7) is layed out such that this first upgrade step can be accomodated without essential modifications.

In a 2nd step, the SLED concept can be combined with doubling the number of klystrons. This leads to E_{cm}=1 TeV with parameters as shown in Table 4.1.2.

Applying the SLED concept for an economic 1st phase of SBLC leads to the machine parameters shown in the first column of Table 4.1.2. The cms energy (380 GeV) is well above the top quark threshold and still a reasonable luminosity is achieved with a relatively small RF-system (650 klystrons) and low power consumption (35 MW). It is interesting to note that already this version of a next generation e^+e^- collider has twice the cms energy of LEP-II, 10 times the luminosity and roughly half the power consumption.

	SBLC-380	**SBLC-500**	SBLC-750	SBLC-1000
g [MV/m]	13	**17**	26	34
T_P [μs]	0.5	**2**	0.5	0.5
n_b	125	**333**	125	125
Δt_b [ns]	4	**6**	4	4
f_{rep} [Hz]	50	**50**	50	50
N_e/bunch [10^{10}]	1.0	**1.1**	1.2	1.69
$\gamma\epsilon_{x,y}$ [10^{-6}m]	5, 0.25	**5, 0.25**	5, 0.1	5, 0.1
$\beta^*_{x,y}$ [mm]	11, 0.45	**11, 0.45**	13, 0.3	25, 0.3
$\sigma^*_{x,y}$ [nm]	384, 18	**335, 16**	303, 6.4	357, 5.5
δ_E [%]	1.6	**2.8**	4.9	8.3
P_{AC} [MW]	35	**140**	140	240
P_{beam} [MW]	3.8	**14.5**	8.6	17.2
L[10^{33}cm^{-2}s^{-1}]	1	**5**	5	10

Table 4.1.2: *Parameters for SBLC with SLED pulse compression at different cms energies in comparison with the 500 GeV reference design.*

For energies up to about 1.3 TeV increasing the klystron pulse length together with the pulse compression technique could be an option. However, going to 2 TeV or beyond requires to increase the length of the machine. By this time optimization between linear and RF costs should be reconsidered.

[3]Note that such an emittance reduction is in principle already possible with the methods and tolerances discussed in section 4.3.

Bibliography

[1] D. Burke for the FFTB Collaboration, *Results from the Final Focus Test Beam*, Proc. of the IVth European Particle Accelerator Conference, London 1994, Vol. I, p.23.

[2] G. A. Loew (ed.), *International Linear Collider Technical Review Committee Report*, SLAC-R-95-471, 1995.

[3] P. Chen and K. Yokoya, *Beam-Beam Phenomena in Linear Colliders*, KEK-report 91-2, 1991.

[4] R. Brinkmann, *Beam Dynamics in Linear Colliders- What Are the Choices ?*, DESY-M-95-10, 1995.

4.2 Linac Technology

4.2.1 The Accelerating Section

The main goal of the accelerating structure is, to transform rf-power to beam power in an efficient manner. On the other hand, given the frequency, only small improvements over a typical S-Band section are possible in terms of shunt impedance, Q-value or resonator geometry. Therefore the design is mainly guided by the necessity to control the longitudinal and transverse wakefields. The production on the other hand has to guarantee ultra-clean structures in order to achieve high gradients with small dark currents and excellent vacuum conditions. Several aspects, which are essential for both items, are still under investigation and aim for minimum linear costs of the production of approximately 5000 sections in a 30 kilometer long collider.

The design of the accelerating section has been developed during the R & D program for the S-Band Linear Collider Test Facility at DESY which started in 1992. Four accelerating structures for the test facility are under production which fulfill the requirements of a linear collider. In addition many technological aspects have been worked out during the production of spare accelerating structures for the injector linac at DESY (LINAC II) where overall fourteen sections have to be replaced because of corrosion in the cooling system. The main parameters of both structures are listed in Table 4.2.1. From the production and operation of these two types of accelerationg sections sufficient experience has been aquired to extrapolate to a large scale series production. During operation of these sections, especially those for the test facility, the aspects which are essential for the linear collider are investigated and will be discussed in more detail in the following part.

section parameter			
		L C	Linac II
section length	m	6	5.2
attenuation	neper	0.55	0.5
group velocity variation	% of c	4.1–1.3	3.3–1.2
filling time	nsec	790	750
shunt imped. variation	MΩ/m	45–61	52–62
number of cells		180	156
tolerances			
straigthness over 6 m	μm rms	≈ 50	$\approx \leq 500$
alignment	μm rms	≤ 50	≤ 1000

Table 4.2.1: *Parameters of the S-Band Linear Collider Section and the Linac II sections, both built at DESY.*

The straightness and alignment tolerances which are quoted later on in this part

mainly result from tracking calculations. These calculations are described in great detail in section 4.3. They are based on the longitudinal and transverse wakefields which have mainly been calculated and partly measured in accelerating structures. While the order of magnitude of the wakefields is essentially determined by the choice of the operating frequency, the effective long range wakefield can be reduced with HOM dampers, internal damping and/or detuning. These strategies are an integral part of the design of the S-Band Linear Collider section and the different aspects concerning the design and fabrication will be presented in detail.

Other isssues are the design and construction of a small size symmetric high power coupler which has been proposed and built for the test facility structures. The collinear load, a design copied from the old LINAC II sections replaces the coupler at the output end and guarantees a good rf match as well as perfect symmetry to avoid transverse kicks in the coupler cell, has been redeveloped and new production techniques have been applied. Finally the design of the Higher Order Mode (HOM) couplers is still ongoing and size and complexity has to be further reduced to make application of modern production and assembly techniques possible.

4.2.1.1 Structure Design

The choice of the accelerating gradient is determined by a balance of linear costs as compared to costs which apply to the rf system. For the S-Band Linear Collider study, with the assumptions which have been made and the cost basis which is available already, this leads to broad optimum around a gradient of 20 MV/m. Given the shunt impedance, mainly determined by the choice of the operating frequency of 3 GHz and the peak power available from one power source, based on today's available technology, one klystron can feed roughly 12 m of accelerating structure.

The reason to choose 6 m long accelerating sections as compared to the well known 3 m long structure from SLAC, is the reduced number of couplers, input windows or valves and a simpler power distribution system. On the other hand, with longer sections and a fixed filling time, the average iris diameter increases which reduces the attainable shunt impedance. This results in a trade-off between loss in average shunt impedance using long rf-sections as well as constructional feasibility versus a larger number of input couplers and a more complex rf power distribution system. Having in mind a future energy upgrade by doubling the number of klystrons, which is the maximum to be expected, underlines this decision because every section may then be connected to one klystron.

Each section is equipped with one high power coupler. The high power coupler is symmetric and has a power splitter on top. The symmetry of the coupler minimizes the amplitude and phase assymmetry. In additon the power transmission per coupling iris is reduced. The output power is not extracted through an output coupler but sufficiently absorbed in an integrated load, which consists of the last eight accelerating cells of the travelling wave structure.

The behaviour of the wakefield in this type of accelerating structure has been investigated in much more detail during the last years R & D for Linear Colliders. The total

long range wakefield is given by the sum of all modes in each passband of the structure. Because the geometry is changed from cell to cell in, for example, a standard constant gradient structure, the electric field pattern and correspondingly the interaction with the beam is quite complex. The frequency spread which is introduced due to these geometric variations, naturally detunes the long range wakefield on a time scale given by the width of the frequency distribution.

This effect of decoherence of the long range wakefield is a part of the design philosophy of the S-Band accelerating structure and is described in greater detail in part 4.2.1.4. Detuning is achieved by variation of the cell to cell frequency of higher order modes to decohere the wakefield on a time scale given by the bunch to bunch spacing of 6 nsec. For example, the first dipole mode single cell frequency changes by approximately 300 MHz from the front to the back end of the structure. In addition ten classes of structures have to be produced which are slightly varied in geometry compared to each other. Here identical modes are shifted in frequency with a total scatter from structure to structure of 36 MHz. This further reduces the beam instability.

Finally each structure is equipped with two HOM pick-ups, which are waveguide type couplers (used in the test facility) or simple coupling loops, which are frequency selective. The pick-up is used to determine to power induced into dipole modes. This information will further on be used to align the structure with respect to the beam axis. Each of the two pick-ups will feedback to a micro mover placed at both ends of the girder. The section is mechanically decoupled from the next quadrupole or the next chamber with bellows which allow transverse displacemnts over the full range of the mover (± 1.5 mm).

4.2.1.2 Structure Fabrication

Given the tolerances and the rf design of the linear collider section, reduction of the fabrication costs for the accelerating sections of a Linear Collider (LC) is one of the figures of merit of the production. Accelerating strucutres for the test facility and for the injector linac at DESY (LINAC II) have been produced using different production techniques. Both sections are quite similar apart from the fact that the straightness tolerances are larger by approximately an order of magnitude for LINAC II. For comparison the parameters are given in table 4.2.1.

Cell Design The six meter long disc loaded LC structure consists of 179 single cups and the coupler cell. Due to the comparatively simple geometry of the disc loaded structure the strategy was to use single cell shapes to be produced easily by conventional machining with reasonable tolerances. The shape of the cavity itself and of the outside walls are a compromise between simplicity and mechanical or rf-requirements.

- The cells should be machined in one piece to form *cups* instead of having a ring and an iris seperately. The cups nest into each other to perform a self alignment during assembly. Especially during vertical brazes, the self-aligning should provide reasonably straight pieces of structures of 0.8-1.5 meter length.

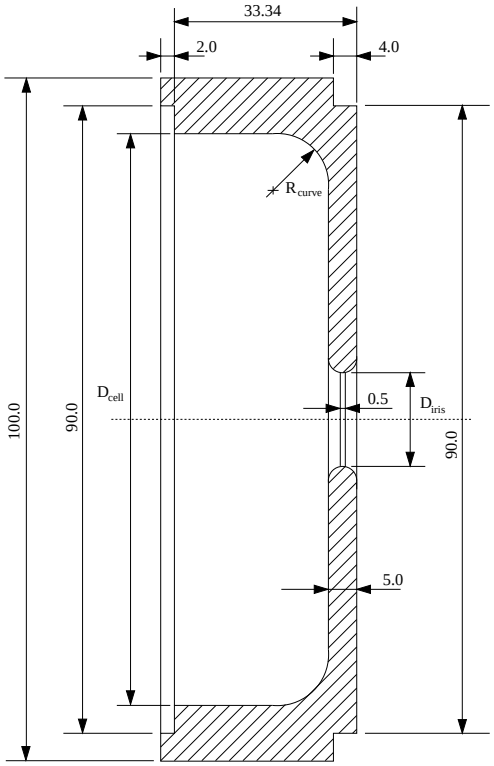

Figure 4.2.1: *Single Cell Geometry.*

- The electric contact between two cups is defined by the copper on copper junction to provide excellent rf properties (high Q values). A knife edge type copper to copper contact prevents any brazing material to penetrate into the cell.

- The tolerance on the outer wall diameter of the cavity has to be similar to the inner cavity wall- and the iris diameter to measure and confirm the straightness with respect to the electrical axis.

Specified tolerances are $\pm 10\,\mu$m for the most sensitive dimensions, namely the cavity diameter and the iris diameter, while tolerances measured so far on average with a statistics of about 2000 cups indicates that less than $\pm 2\,\mu$m can be achieved easily. The specified tolerances have been chosen by the maximum tuning range on one cell while the achieved tolerances are already attractive enough in order not to tune but only to measure the elctrodynamic characteristics of each of the 5000 required sections. The resulting energy loss is less than 1 %, if the section can be operated without any sytematic phase error and is left with the statistical error only. This will be achieved by operating each structure at its optimum temperature, which is expected to vary by less than $\pm 1\,$C° from section to section. The cooling system is designed to handle this feature (see 4.2.4. A significant financial and operational gain is expected because the cup does not need any tuning holes in the outside wall and the production time will be reduced because the time consuming tuning procedure is not required.

Material Handling, Preparation and Assembly The cups itself are machined from forged copper pieces and chemically cleaned afterwards. To improve the outgassing rate and to decrease potential contaminations of the raw copper material, Hot Isostatic Pressure (HIP) procedures have been applied and intensively investigated elsewhere [1]. At a gradient larger than 75 MV/m a dark current of less than 1 mA has been measured. Additional experiments at KEK have proven that dark currents produced by field emission can be reduced by more than an order of magnitude if clean room conditions and high pressure water rinsing is applied. At DESY significant effort has been put into the research of material aspects and the material preperation during production in order to reduce the amount of gas stored in the metal and to increase the breakdown threshold. According to both results different types of pretreated structures have to be tested and the cause of dark current production must be traced using the test facility and the available high power test stands.

Substructrures are preassembled and brazed vertically in pieces of approximately 0.8 m length, which are vacuum checked each. The straightness achieved on these pieces is generally better than 30 μm without additional supports. Longer pieces up to the full structure length will be brazed vertically as well to avoid support strcutures. The stra

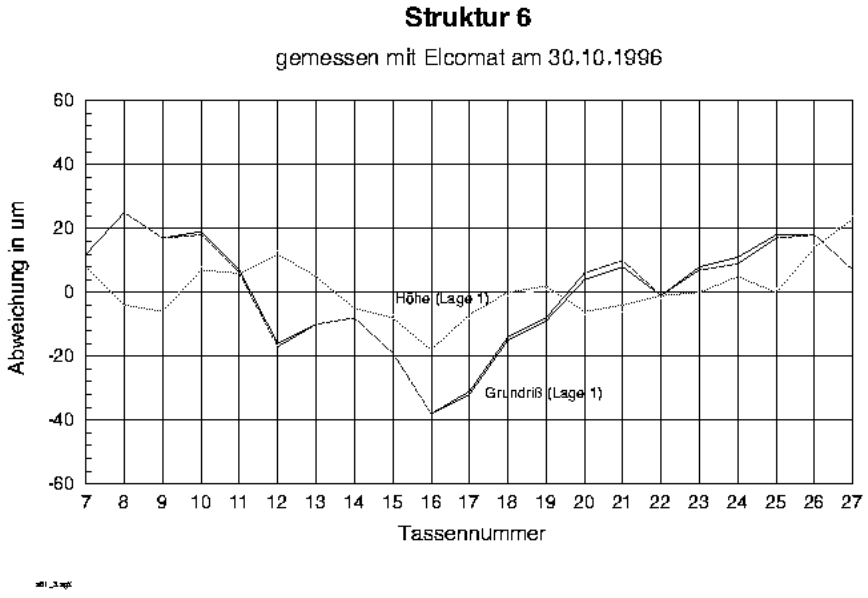

Figure 4.2.2: *Straightness of a 1 meter long piece of accelerating structure brazed vertically without further supports. (Höhe: vertical)*

A new method, namely inductive heating, which is has been investigated recently fullfils almost all requirements for the large series production of more than 5000 sections. Heat-up and cool-down procedures can be applied while the structure is mounted vertically within a small glass or ceramic pipe flooded by hydrogen. Already with the

available hardware at DESY the time required for brazing is approximately half an hour per meter.

Straightening of Accelerating Structures Apart from the electrodynamic characteritics of the accelerating structure, the straightness is a main concern in the linear collider design. The straightness tolerance is mainly given by the multibunch instability threshold which is driven by dipole modes. These modes will be excited even if the average offset of the single cells is zero. In case of tapered structures, constant gradient, gaussian or others, these dipole modes of one passband are loacated at different places in the section. The minimum length for which the straightness is defined is determined by that part of the electric field of each dipole mode which is strongly interacting with the beam, typically 40 cm–60 cm. The desirable straightness tolerance defined from this criterion is: **The section has to be straight over the 6 m length to within 30 μm rms over a length larger than 60 cm.** For longer pieces slightly larger values can be accepted which will later on be removed. This is smaller by a factor of two than actually required for the 500 GeV collider design, but takes into account that future upgrades require the acceleration of smaller emittance beams. A measurement showing a 1 meter long piece brazed vertically is shown in Fig. 4.2.2.

Heating the copper during the braze up to $\approx$900 C° reduces the young's modulus by almost factor of three. Detoriation of the straightness would require more than one support per meter in order to fix the section with the required straightness on the final girder. Straightening the section, if necessary, after the final braze is a more attractive and envisaged solution. A straightening device used for the test structures together with a fast laser measurement system has been constructed and is under test. A sketch is shown in Fig. 4.2.3.

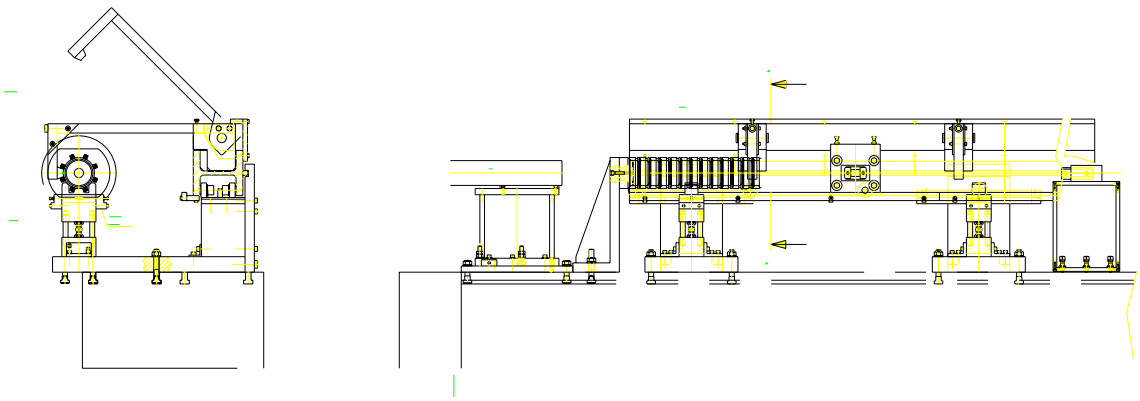

Figure 4.2.3: *Device for straightening of the accelerating sections after the final braze and before installation on the girder.*

Straightness Measurement Techniques In the following text alignment techniques are discussed which are used to control the straightness of a structure. Certainly other techniques can be used and they are described for example in [2].

Straightness Measurement using an Interferometer For straightness measurements in combination with the straightening device a normal laser interferometer is used. In addition to the laser head and the measurement display unit for straightness measurements, a straightness interferometer (compensated wollaston prism) and a mirror (straightness reflector) are also required. The function principle is described in [3]. The mirror is mounted on a fixed support behind the module and the wollaston prism runs along the module. The offset distance of the wollaston prism in horizontal or vertical direction with respect to a straight reference line will be measured, in that the reference line will be given by the mirror axis and not by the laser beam.

At DESY the laser interferometer system HP 5528 A is available. There are two straightness interferometers, one for the short range up to 3 m and another for the long range from 1 m to 30 m. In both systems the measurement range is ± 1.5 mm and the resolution is better than 0.1 μm. The accuracy of the short range interferometer is between 3.5% and 1% and of the long range interferometer between 5% and 2.5% of the measured offset. With an interferometer, only one geometrical position can be measured either the vertical or the horizontal position. During the measurement care must be taken not to move the wollaston prism out of the laser beam or to interrupt the laser beam itself.

Straightness Measurement using Autocollimator An autocollimator can measure the changes in direction of a surface mirror with very high accuracy. For straightness measurement using autocollimation a surface mirror is mounted in a sliding carriage running in defined steps along the module. In each position of the sliding carriage the vertical and the horizontal directions of the mirror axis will be measured by the autocollimator (Fig. 4.2.4). This method is used for the final measurement of the straightness on the actual girder.

The changes in direction for each component in respect of the first mirror position multiplied by the distance of the supporting points of the sliding carriage are accumulated. Therefore the straightness curve of the module can be calculated. By the autocollimator technique in one process horizontal and vertical straightness deviations will be measured simultaneously. This is an important advantage compared to the two straightness measuring techniques described previously. Furthermore there is no laser beam to interrupt and it is possible to put the sliding carriage out of the field of vision of the autocollimator completely. The effects of refraction of air have also to be taken into account. Further it can be seen that the supporting points of the sliding carriage are pressed into the module by the weight irregularly. The weight of the carriage and the surface mirror must therefore be as low as possible.

At DESY the autocollimator Elcomat 2000 of the factory Möller–Wedel in Wedel is used. This electronic autocollimator has in the focal plane two CCD–line scan image sensors mounted perpendicular to each other to detect the crosshair reflecting from

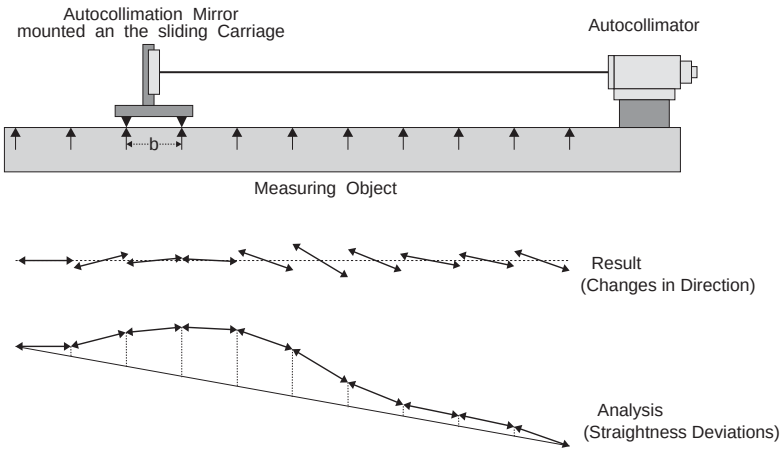

Figure 4.2.4: *Sketch of a straightness measurement using an autocollimator. Changes in direction from point to point, which are given by the angle of the reflected laser beam with respect to the surface of the mirror, are used to determine the transvese offset in both planes.*

the surface mirror automatically. The measuring range is $\pm 1000''$. With increasing distance between autocollimator und surface mirror the measuring range will decrease. For a distance of 3 m the measuring range is now $\pm 500''$ and for a distance of 7.5 m the measuring range is only $\pm 100''$. The accuracy of the Elcomat is between $0.15''$ and $0.50''$.

In [3] the results of several straightness measurements carried out with the described systems are discussed. Fig. 4.2.5 shows the remaining deviations of a 5.2 meter structure after the first straightening the module, where an rms value of 107 and 108 μm in the vertical and horizontal plane has been achieved.

4.2.1.3 Input Coupler and Collinear Load

Description of the Problem The rf power P_{in}, which is provided by a standard rectangular WR284 S-band waveguide, is converted to the traveling accelerating mode in the first cell of the disc loaded structure. The main design issues for the coupler are the symmetry of the accelerating field, the proper amplitude and phase relationship to the rest of the structure, the high power capability (300 MW for the 1 TeV version), perfect matching at the input port and a compact design to save tunnel space. The end of the accelerating section has to be terminated for the accelerating traveling wave to avoid increased electrical peak field strengths, reflections back to the klystron, and to reach the desired traveling wave operation. Therefore the power left over at the end of the structure has either to be extracted by an output coupler to an external load, or to be dissipated in the last few cells which act as an internal load. The internal load - called collinear load - has to fulfill the termination condition and to work simulataneously as accelerating structure.

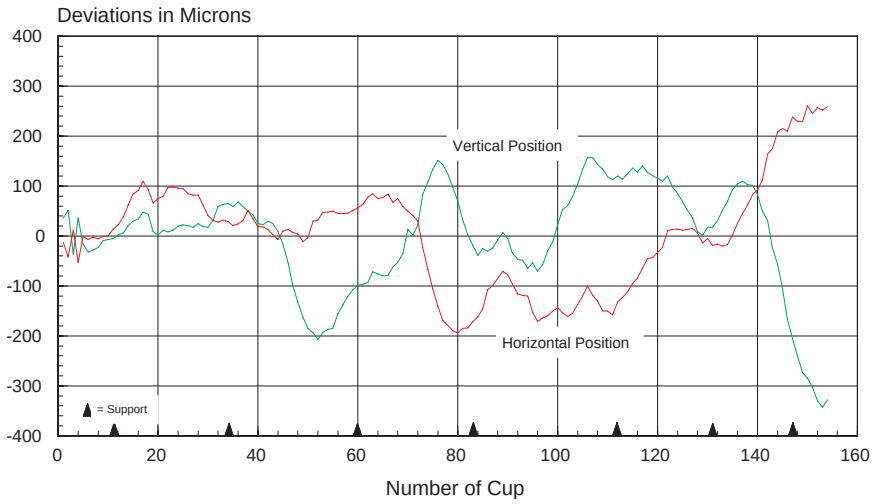

Figure 4.2.5: *Straightness deviations of a 5.2 meter long structure after straightening the module. Seven arrows on the bottom of the graph indicate the suppport points.*

Technical Solutions for the Coupler Arrangements with only one coupling hole at the circumference of the first cell introduce intolerable phase and amplitude asymmetries in the coupler fields with which the beam interacts. The field distortion can be reduced by asymmetric arrangements of the coupler cell with respect to the beam axis or by using compensation elements on the side opposite to the coupling hole [4, 5]. However, the compensation is still imperfect and the transient field in a single coupling hole can be quite large. This can be avoided by input couplers with two coupling holes which are symmetric in the vertical and horizontal plane with respect to the beam axis. In [6] a setup is described where two coupling irises are fed in phase by signals from a power divider. Each iris transmits one half of the total power flow. Very compact designs are possible with side coupled waveguides as it can be seen in Fig. 4.2.6. The symmetry of this configurations is not quite perfect with respect to the horizontal plane, but the field error in the coupler cell is sufficiently reduced.

Side Coupled Input Coupler A high power coupler with two side coupled waveguides has been developed in collaboration with MEPhI in Moscow [7]. The design in Fig. 4.2.6 is composed by two independent units which are connected by vacuum flanges:

- few centimeters for the cut-off pipe, the first two cells of the accelerating structure, the side coupled waveguides terminated on one side by a conducting plane and
- the power splitter, a $\lambda/2$ taper from the cell height of 28.34mm to the height of the standard S band waveguide (34.04mm) and a diaphragm.

The following properties have been measured at the prototype:

- input reflection coefficient below 1.5% ,

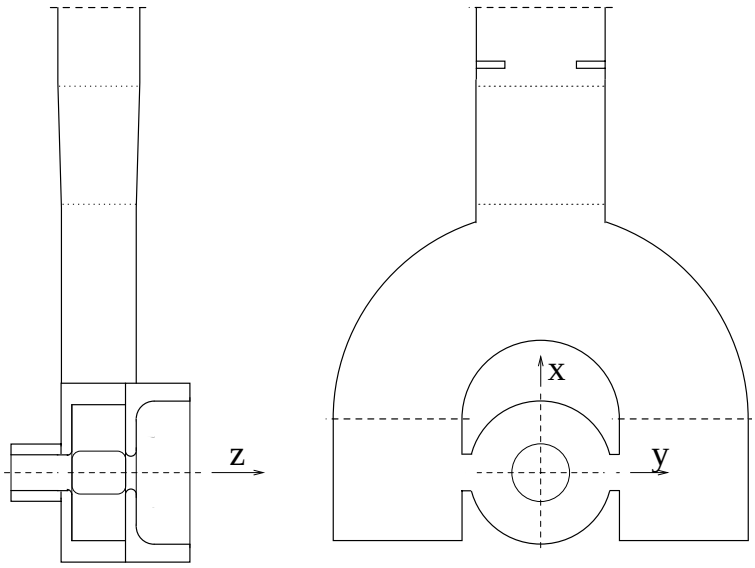

Figure 4.2.6: *Geometry of side coupled symmetric input coupler with power splitter and tapered waveguide.*

- the peak field strength in the coupling hole is 65% of the accelerating field,
- the amplitude- and phase asymmetry are of the order of the measurement accuracy ($(\partial|E_z|/\partial x)/|E_z| = 0.009/\mathrm{mm}$, $\partial arg(E_z)/\partial x = 0.035$ degree/mm)

Hybrid Input- and HOM-Coupler The possibilities of using additional coupling elements at the first cell in order to damp or detect higher order modes have been investigated in theory and with an experimental setup [8]. A sketch of the modified coupler can be seen in Fig. 4.2.7: the conducting terminations at side coupled waveguides have been replaced by two waveguides below cutoff frequency which provide the same reflection coefficient. These waveguides are operated above the cutoff frequency for dipole modes, so that their energy can be absorbed at the terminating loads. Dipole modes with orthogonal polarization couple through two additional holes to a second pair of waveguides. With such a configuration it is possible to decrease the quality factor of dipole modes with both polarizations by a factor 5 while maintaining the match at the fundamental mode frequency. This coupler has been investigated as an alternative approach compared to the HOM dampers which are connected to the cells. This solution has not been chosen due to its complexity and because a large number of modes of the 1st dipole band are trapped apart from the coupler (compare Sect. 4.2.1.4).

The Collinear Load The collinear load, which is proposed instead of an output coupler, consists of the last eight accelerator cells. The surface losses in these cells are artificially increased by an $\approx$0.1 mm thick layer of Kanthal. The quality factor of these cells can be decreased in a controlled fashion by a factor of almost 50. The parameters

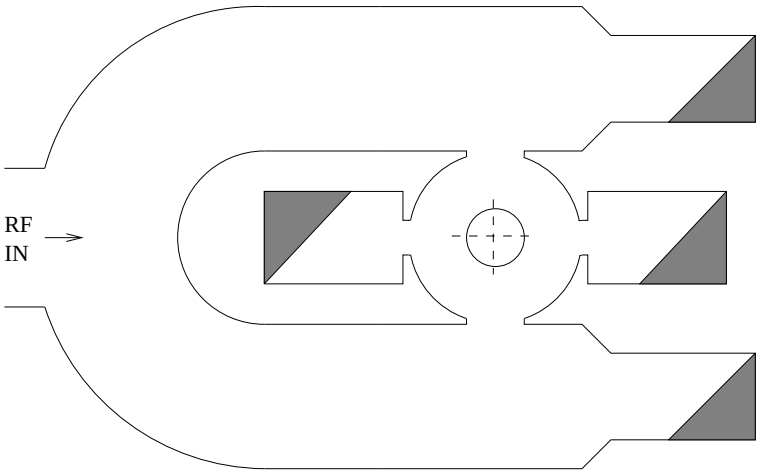

Figure 4.2.7: *Hybrid coupler.*

of each cell (frequency, coupling and quality) are optimised to fulfill the termination condition and to be close to the desired amplitude and phase distribution. An other criterium for the optimization is the power dissipation along the load. Apart from the fact that significant cost savings have been achieved, using a collinear load has a number of advantages as compared to a standard output coupler:

- The collinear load is perfectly symmetric which avoids transverse excitation of the beam and intrinsically does not contribute to any emittance growth.
- All the higher order modes with field in the last few cells are automatically damped via losses in the cavity walls.
- No output coupler together with a load is required which reduces the failure risk significantly.
- The loss in linear length is neglegible because the particles are still accelerated in the collinear load.

4.2.1.4 Higher Order Mode Damping and Detection

Deterioration of the intense particle beams in a multibunch collider scheme is caused by the long range wake fields. Theses deflecting fields build up by parasitic higher order modes (HOMs) in the accelerating structures which have been excited by preceeding bunches. If no special damping is applied the energy of the beam induced fields will be dissipated by wall losses (in the cells or the collinear load), propagate through the beam pipe or through the high power coupler. Because the energy propagation through the beam pipe leads only to an exchange of rf power between adjacent structures this mechanism does not really cause damping unless beam pipe absorbers are present. Due to the existance of modes which are completely trapped inside a section (compare Figure 4.2.8) and due to the low velocity of energy propagation (typically few percent

of the velocity of light) many modes are only damped by wall losses. In this case an upper limit for the decay time τ can be estimated using the asymptotic limit of a pill box resonator:

$$\tau = \frac{r_{cell}}{\pi f_\nu \sigma}$$

with r_{cell}=cell radius, f_ν=mode frequency and σ= skin depth. Therefore even for frequencies much higher than the fundamental mode, decay times in the order of microseconds have to be expected.

The dominant and lowest order contributions to the longitudinal and transverse wake are related to monopole and dipole fields. The longitudinal monopole effects are independent from offsets between the beam and section axis induced for example due to the injection offsets and alignment errors of structures and quadrupoles. Therefore they are predictable and can be compensated easily (see Sect. 4.2.9) or are negligible. In contrast to this, dipole mode effects depend strongly on geometric errors and require special structure designs to prevent multibunch beam break-up and emittance dilution. A key quantity for the analysis of these effects is the normalized transverse dipole wake $w_D(s)$ which is related to the change of the transverse momentum $\Delta\mathbf{P}_t$ of a test charge q_2 caused by the fields of a source bunch q_1 by:

$$\Delta\mathbf{P}_t = w_D(s) \cdot \frac{q_1 q_2}{c}\mathbf{r}_{1t} \ ,$$

$\mathbf{r}_{1t}$ is the transverse offset of the drive charge with respect to the structure axis and s is the distance between q_1 and q_2.

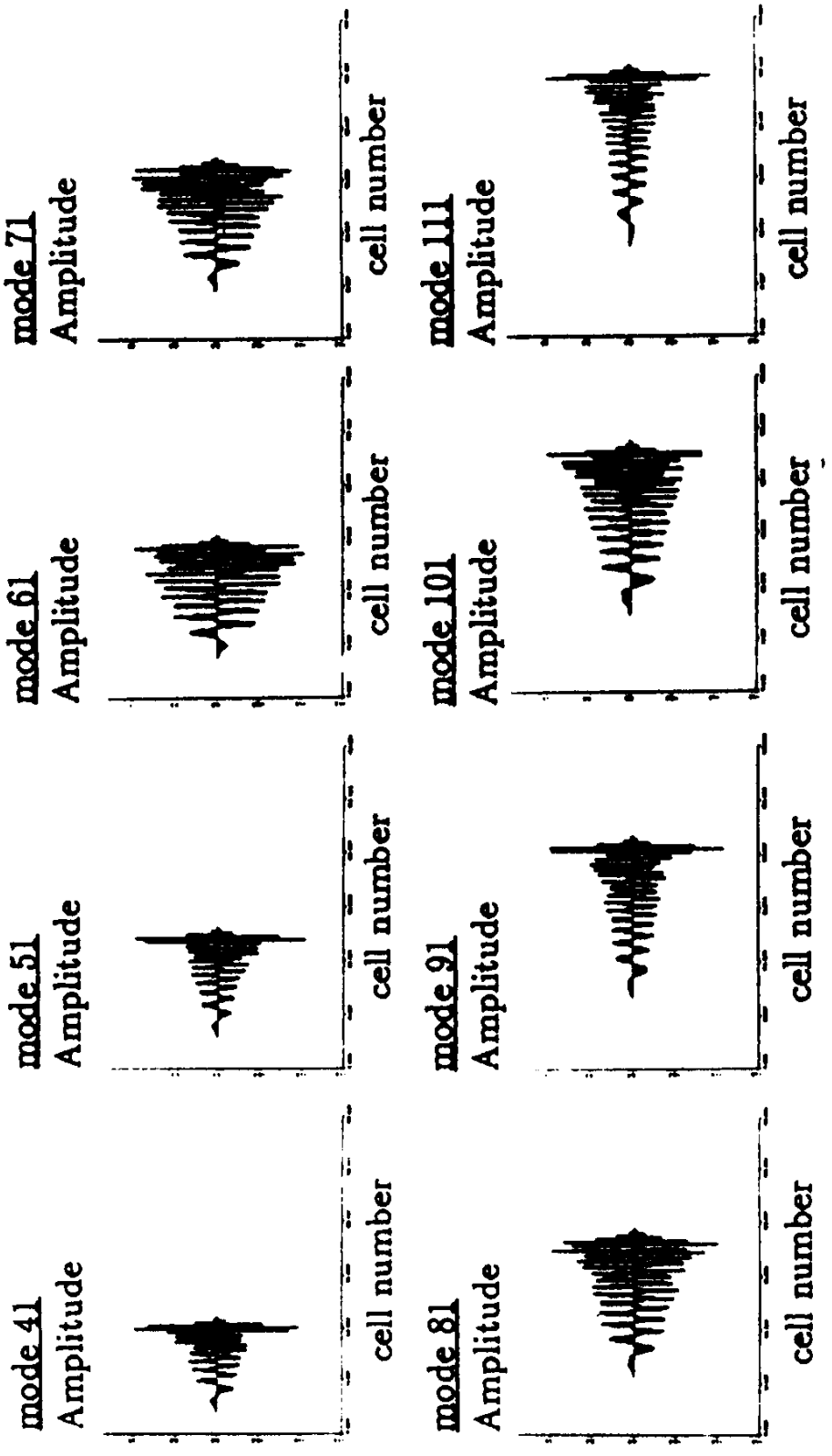

Figure 4.2.8: Normalized voltage amplitudes of some trapped HOMs in the 180-cell quasi-constant gradient structure as function of cell number.

Computation of the Dipole Long Range Wake The normalized transverse dipole wake function $w_D(s)$ can be split into a resonant term $w_r(s)$ and a transient term $w_t(s)$. The resonant part can be expressed by a summation over all eigenmodes ν:

$$w_r(s) = \sum_{\nu} 2k'_{\nu} \frac{c}{2\pi f_{\nu}} \sin\left(\frac{2\pi f_{\nu}}{c} s\right) \quad \text{for } s > 0,$$

where f_ν and k'_ν denote the resonance frequency and the normalized longitidinal loss-parameter (definition see [10]) corresponding to the ν-th cavity mode. Usually this equation is modified by damping terms with the time constants $\tau_\nu = Q_\nu/(\pi f_\nu)$ to take into account small losses e.g. due to the finite wall conductivity.

The application of grid-oriented methods for tapered disc-loaded structures is limited by the realizable number of mesh points and the accuracy of the eigenvalue solver. Semi-analytical methods like the Modal Field Matching Technique do not suffer from this limitation and can be applied for the HOM calculation [10]. To make the problem tractable the 180 cell constant gradient structure of the SBLC Design was approximated by a 180 cell model which is tapered in groups of six cells with rectangular instead of rounded corners [10]. In order to further study the phenomenon of trapped modes a 36-cell structure has been designed [11] and a double-band coupled oscillator model has been developed. The parameters f_ν, k'_ν and Q_ν of the resonant wake and the complete function $w_D(s)$ have been calculated and compared by different methods:

- Calculation of f_ν and k'_ν in the frequency range 4.1 GHz to 4.6 GHz for a piecewise tapered section (in groups of six) using the mode matching technique [10]. The electric field distributions of the modes which have been found in this frequency range correspond to those which are given from the first and part of the second dipole passband, taking the individual cells in periodic approximation. The individual passbands with the dispersion curves for the first, the last cell and some cells in between are shown in fig 4.2.9. The plot displayed in Figure 4.2.10 shows a scatter (due to the piecewise tapered geometry being used) of the loss factors between 2 and 14×10^{15} extended over 2/3 of the first dipole passband. A major part of these modes is trapped *inside* the structure, that is without contact to the end cells which can be seen from the electric field distributions of the modes as well (compare Figure 4.2.8). This loss-parameter distribution has been used for the beem dynamics simulations in [9, 16].

- Calculation of f_ν and k'_ν in the frequency ranges from 4.1 GHz to 4.6 GHz and from 9.3 GHz to 9.4 GHz using the mode matching technique [18]. The modes in the second frequency range correspond to the sixth dipole passband, which significantly contributes to the impedance of the structure.

- Calculation of f_ν, k'_ν and Q_ν in the frequency range of the first and second passband (4.1 GHz to 5.6 GHz) by a double-band coupled oscillator model [20]. This model takes into account weak and strong losses (e.g. wall losses, HOM couplers). The loss-parameter distribution of the disc loaded SBLC-section without

couplers and collinear load is plotted in Fig. 4.2.11 and can be directly compared to fig. 4.2.10.

- Calculation of $w_D(s)$ in the frequency range below 15 GHz in time domain [9].

In addition the computation methods [10, 18, 20] have been verified by a comparison with finite-integration-codes (MAFIA and URMEL-T) and with measurements for a simplified 36 cell structure [11]. An excellent agreement between the mode matching results [18] and MAFIA was found as well as a good accuracy of the coupled oscillator model [20].

According to the time domain calculation [9] the dominant contributions to the transverse wake are found in the frequency range between 4.1 GHz and 4.5 GHz, related to modes of the *first dipole passband*, and between 9 GHz and 10 GHz, related to modes of the *sixth dipole band*. Contributions from other passbands are intrinsically small compared with the two main bands. The behaviour of the dominant dipole bands is sumarized in Table 4.2.2.

	band 1	band 6
initial coherence	no contribution above $0.05\hat{w}$ and at multiples of the bunch distance	contribution between $0.05\hat{w}$ and $0.15\hat{w}$ for the first 8 bunches
decoherence	contribution below $0.05\hat{w}$ at the first 72 bunches	contribution below $0.05\hat{w}$ for the next 33 bunches
maximal recoherence	$\max\{\lvert w_D(s = 135\,\mathrm{m})\rvert\}$ $=0.2\hat{w}$	$\max\{\lvert w_D(s = 80\,\mathrm{m})\rvert\}$ $=0.07\hat{w}$

Table 4.2.2: *Contribution of the 1st and 6th passband to the normalized transversal dipole wake $w_D(s)$ at the position of following bunches $n \cdot s_{\mathrm{bunch}}$ for s_{bunch}=1.8 m (or t_{bunch}=6 nsec) in a perfect conducting structure without dampers. All values are related to the peak value $\hat{w} = \max\{\lvert w_D(s)\rvert\} = 1.64 \cdot 10^{16}$ V/(Cm). For small values of s modes of one band are coherent and may substantially contribute to the wake. As the frequency separation of the modes is approximately constant they recohere again on a longer distance (time) scale.*

Wake Field Suppression Three different cures are foreseen in the design of the accelerating structure to reduce the wake-field kick of the dominant bands below $0.05\hat{w}$, which is the peak of the wake field at t = 0, to fulfill the present requirements given

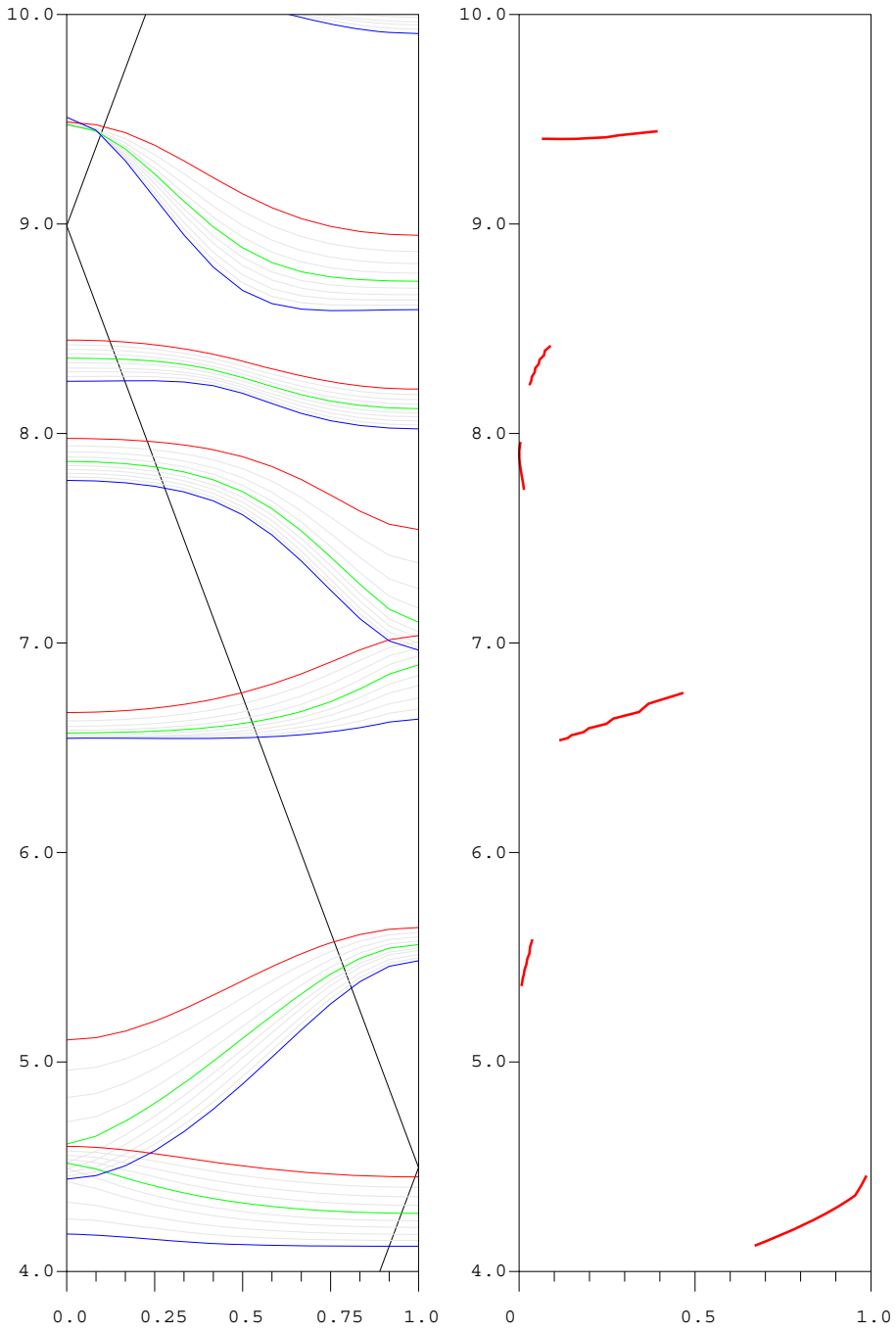

Figure 4.2.9: *Dispersion curves for the accelerating structure assuming periodic boundary conditions for the individual cells are presented in the left plot. The upper and the lower curve in each passband correspond to the first and the last cell in the structure (or vice versa). The plot on the right hand side shows the corresponding loss parameters (normalized to the strongest one) as a function of the frequency of the modes interacting with the beam.*

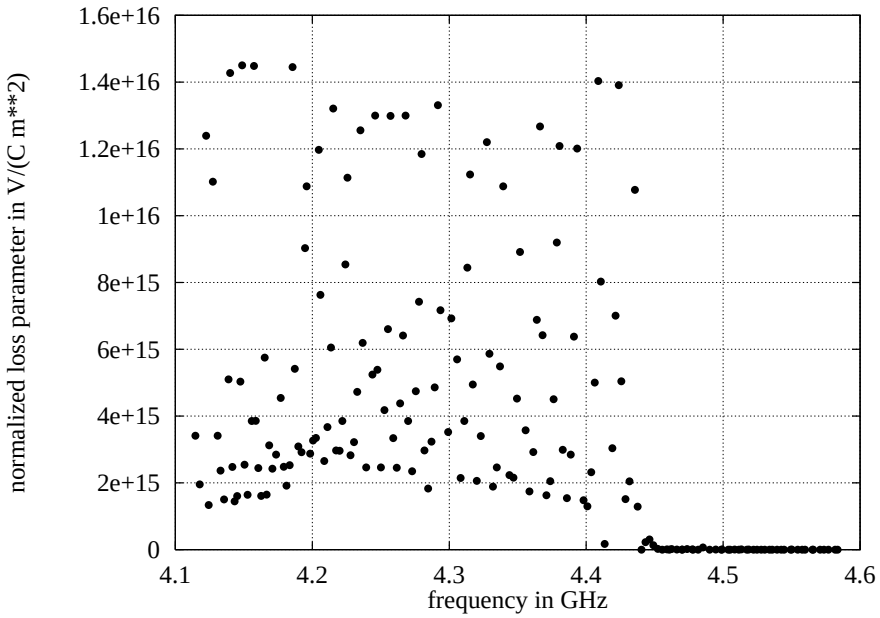

Figure 4.2.10: *Normalized longitudinal loss-parameters of a piecewise tapered 180 cell S-band structure calculated by the mode matching technique [10]. The strong variation of the parameters is caused by the piecewise tapered geometry.*

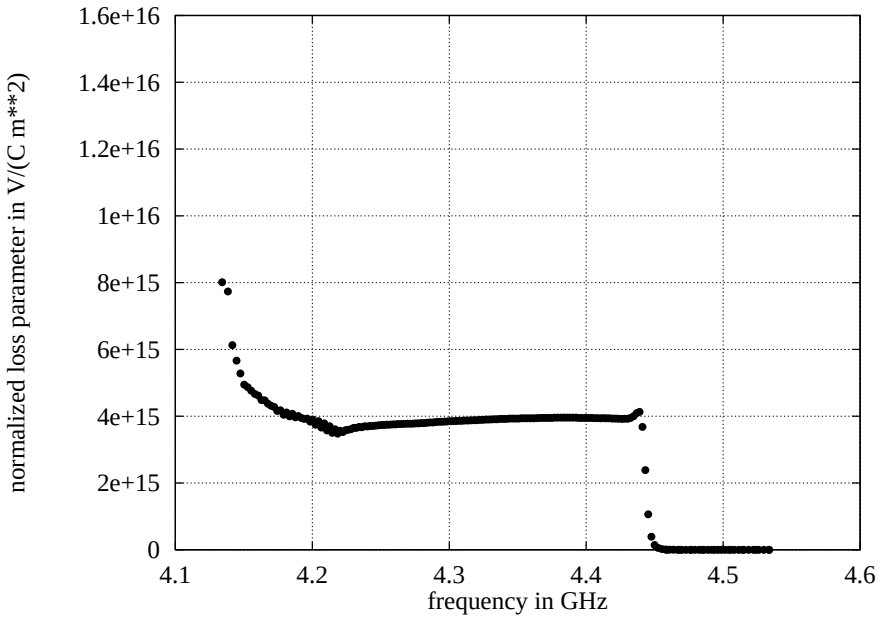

Figure 4.2.11: *Normalized longitudinal loss-parameters of the continuous tapered SBLC-structure calculated by the double-band coupled oscillator model [20]. Most of the modes with high loss-parameter are completely trapped in the disc loaded structure.*

by the current and emittance from the 500 GeV table of parameters. In addition, the potential to accelerate a significantly smaller emittance is part of the design as well.

- The first method is almost given for free, because constant gradient structures are proposed. Due to the taper of the iris which is necessary to produce a constant power loss per unit length, the structure is intrinsically *detuned* for other passbands than the band of the accelerating mode [10]. The DETUNING can be improved be variing further cell dimensions (e.g. the iris thickness) along the section [17].

- Any detuning is limited by re-coherence of these modes given by the inverse of the typical mode spacing in frequency within the passband. In our case the re-coherence length is short compared to the bunch train length. Therefore additional DAMPING of these modes is necessary.

- In order to keep the excitation intrinsically small an ACTIVE ALIGNMENT system is foreseen (compare Sect. 4.2.2) which can move the accelerating structure according to dipole mode signals extracted from higher order mode pick ups. The resolution is limited by the straightness of the structure and the sensitivity of the HOM pickup.

Detuning Cell-to-Cell Detuning In a constant gradient structure the iris diameter is tapered (decreased) from the front to the end cell to provide a constant power loss per unit length and therefore a constant (unloaded) gradient. The SBLC structure is tuned to have a constant phase velocity in the accelerating $2\pi/3$ mode at a given frequency of 3 GHz. For all other passbands the synchronous frequency changes slightly from cell to cell because of the geometry change. Therefore not only one mode per passband with n times the single cell loss factor is excited by an off axis beam, as e.g. in a constant impedance structure, but many modes of each passband contribute to the transverse kick with a loss factor of the same order of magnitude. The destructive interference of these oscillations can be used to suppress the wake-field on at time scale given by the total frequency spread and the typical frequency offset between modes.

For X-band structures it has been shown in [12, 14, 15] that the first part of the long range wake can be reduced by more than two orders of magnitude by pure detuning. Such a suppression factor is required as shown by beam dynamics calculations and can technically be achieved by modifying the group velocity profile and simultaneously tapering the iris thickness. The requirements for wake field suppression, straightness and alignment of a S-band structures are comparatively relaxed even with higher bunch charges because the transverse wake fields scales with the third power of the frequency. This is one of the strong arguments for low operation frequency.

The 'natural detuning' (constant gradient group velocity profile) provides a destructive interference for modes of the *first passband* which reduces their contribution to the wake field by more than a factor of twenty for the next seventy bunches. Beam dynamics simulations in Sect. 4.3 and [9, 16] which are based on the dipole modes

of the first passband calculated in [10] have been done. They indicate that the initial decoherence reduces the wake field of the lowest band sufficiently for the first few bunches.

The time domain calculation [9] and the mode matching analysis [18] predict in good agreement, that in the *sixth passband* only very few modes in a narrow frequency interval will be excited by the beam. For this reason the spectral components between 9.45 GHz and 9.48 GHz do not decohere within a few nanoseconds and dominate the wake function for the first couple of bunches. To suppress this contribution below $0.05\hat{w}$ either strong damping ($Q < 200$) is necessary or the detuning bandwidth has to be increased to 150 MHz. For X-band structures it is been shown in [17, 15] that this can be achieved by tapering the iris thickness.

Section-to-Section Detuning Section to section detuning is a well known and proven technique to increase the multi-bunch beam breakup threshold. It has first been applied to the SLAC linac after installation. Later on this technique has artificially been introduced in many linac designs, where long current pulses are used, e.g. in low energy nuclear physics high duty cycle accelerators [19]. At SLAC three classes of structures have been provided by shifting the resonance of the first and strongest mode from the first passband at 4140 MHz by 2 MHz and 4 MHz by specifically detuning the first few cells of the accelerating structure. While for the SLAC structure the most disturbing modes are located at the front end of the three meter section, with a six meter structure more modes are completely trapped inside. In addition, with the parameters used for the S-Band collider study, the frequency spectrum of the beam exciting the structure is much denser because the bunch to bunch distance is 6 nsec as compared to 0.3 nsec (fundamental of S-Band with every bucket filled used for SLAC operation). For both reasons more modes will be excited as compared to the operation mode of the SLAC linac. In addition ten different classes of sections with a scatter in resonant frequencies for the same modes have been assumed for the beam dynamics calculations (compare Sect. 4.3). The frequency spread of the shift is ± 18 MHz shifting the frequency of each mode in the passband by the same amount. Technically this will be achieved by changing the single cell geometry and/or the group velocity taper of the structure.

Damping Damping of the wake-field is necessary on a time scale determinded by the *re-coherence* of the wake-fiel which itself is affected by detuning imperfections due to *manufacturing tolerances*. Both effects become important on a much longer time scale compared to the bunch to bunch distance. The quality factor of modes in the first passband has to be less than 4000 to prevent intolerable emittance growth caused by the re-coherence after approximately 450 ns. For this calculation a 1 MHz rms frequency error of the dipole mode resonances has been assumed. The re-coherence time of modes in the sixth band is approximately 270 ns, but due to the lower maximum wake-field after re-coherence and the higher frequency the Q has to be reduced to 8000 only.

Although very weak additional damping is required the quality reduction for modes in the first dipole band cannot easily be achieved with a few HOM dampers distributed along a section. This is due to the existence of *trapped modes* which are localized in

certain parts of the tapered structure and do not have any field close to the input or output end. In the SBLC structure approximately 140 modes (in the first dipole band, for each polarization) are completely trapped. Such a trapped mode has a field distribution within 1/3 of the section with a very non-uniform energy distribution. To sufficiently couple to all the trapped modes approximately four to six pairs of higher order mode dampers would be required for each polarization. The disadvantage of this method is not only the large number of specialized cells which complicate the structure assembly, brazing and tuning but also their interference with the detuning. The different geometry of damper cells changes the frequency, amplitude and phase distribution within the structure of the beam driven modes, leads to a less perfect decoherence and consequently asks for even stronger damping. Instead we propose to intrinsically damp every cell and use loosely coupled higher order mode damper cells for HOM detection only, which change the mode patterns only weakly. The goal is to increase the surface resistivity at certain parts of the cell without decreasing the accelerating mode impedance by more than 5%, in order to damp the most harmful HOMs sufficiently [20]. By evaporating a $10\,\mu$m to $20\,\mu$m surface layer on the tip of the iris with a material of low conductivity the required damping of modes in the first and sixth band can be achieved [20, 21]. The materials which have been used are stainless steel or Kanthal and dependent on the thickness, but more on thechoice of the material, this corresponds to one or a few skin depth.

The integrated load at the end of the structure which is normally used to terminate the accelerating mode power, additionally fulfills the purpose of a higher order mode absorber for those modes which extend into the load. This does not work for the majority of modes, which are trapped apart from the load, but the other modes can be damped. For instance the modes of the sixth dipole band with a high shunt impedance extend along the whole structure length. The matching for these modes is not perfect as the local group velocity is approximately three times higher than for the accelerating mode and the the quality is about 40% higher, but the power dissipation is still substantial.

HOM Damping by Intrinsic Losses The damping of dipole modes in the first passband by increasing the surface losses in the coupling holes has been proposed in [20, 21]. In contrast to the electric cell to cell coupling of the accelerating field the lowest dipole modes essentially couple via magnetic fields and the magnetic energy distribution on the surface of the iris tips is very different (see Fig 4.2.12). The surface currents in the coupling iris are much higher for dipole modes as compared to the accelerating field. Therefore dipole modes are more sensitive to high loss material in this area. In order to reduce the quality factor of a dipole mode from 14000 to 3000 the surface resistivity in the iris holes has to be increased by a factor 15 to 20. At the same time the quality factor of the monopole mode is only reduced by about 5% .

To increase the surface losses the cavity is covered partially by a thin metallic layer (see Fig. 4.2.13) with a reduced conductivity or increased permeability. In [20] a test with sputtered layers of stainless steel and Kanthal are described. The electric properties of such a layer can be controlled in a wide range (absorption factors between 10 to 30) by the choice of material and the thickness of the layer. A third degree of

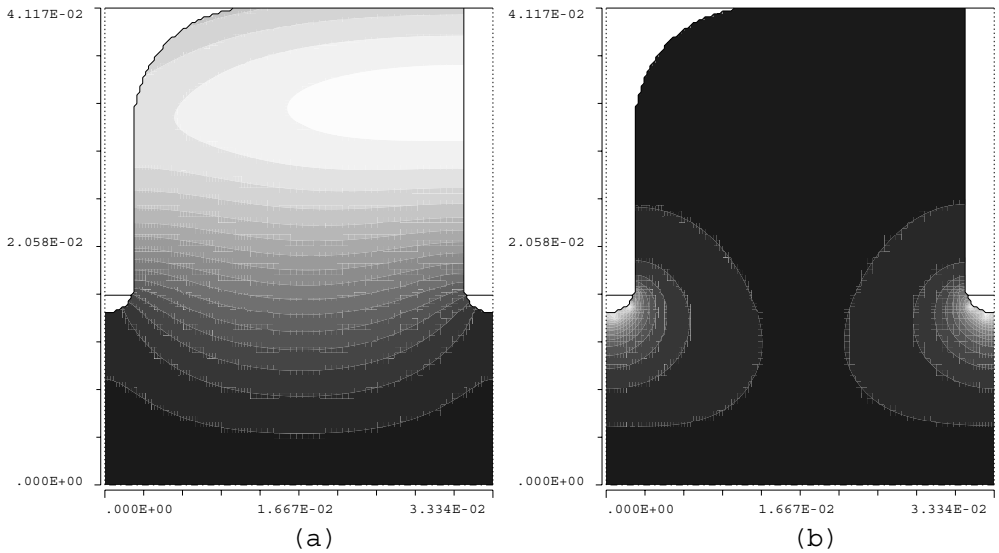

Figure 4.2.12: *Magnetic energy distribution in one cell of the SBLC structure: a) accelerating mode. b) dipole mode (first passband, $\pi/3$ traveling wave mode). The surface losses are proportional to the magnetic energy distribution at the surface. Plotted is the energy density averaged over time and azimuthal position. Low energy corresponds to dark gray.*

freedom is the height d_{coat} (see Fig. 4.2.13) of the covered surface.

The iris coating is exactly at the location with the highest electric field strength. In [21] a two cell test resonator was used for high power test. The maximum available power of 900 kW in this setup generates a $\pi/2$ standing wave field with the same iris field strength as compared to the unloaded accelerating field ($2\pi/3$) of 25 MV/m in the traveling wave structure. For the processing time and the result no difference could be found between cavities with sputtered stainless steel, sputtered Kanthal or galvanic Kanthal layers as compared to plain copper cells and no indication for extraordinary surface breakdown could be observed.

For all modes from the first passband with a high loss factor the quality factor has to be below Q = 4000. If the power dissipation for the acclerating mode should be constant at the same time and the height d_{coat} (see Fig. 4.2.13 of the covered area around the iris tip does not change, the absorption factor P (P = surface resistivity with covering/ surface resistivity without covering) has to be increased approximately linear with the cell number, because the ratio of covered to uncovered area decreases along the section:

cell number	group velocity	Q reduction acc. mode	absorption factor P
1	4.06	5%	10
		10%	21
180	1.35	5%	21
		10%	43

With a constant absorption of the accelerating modes in all 180 cells, the quality

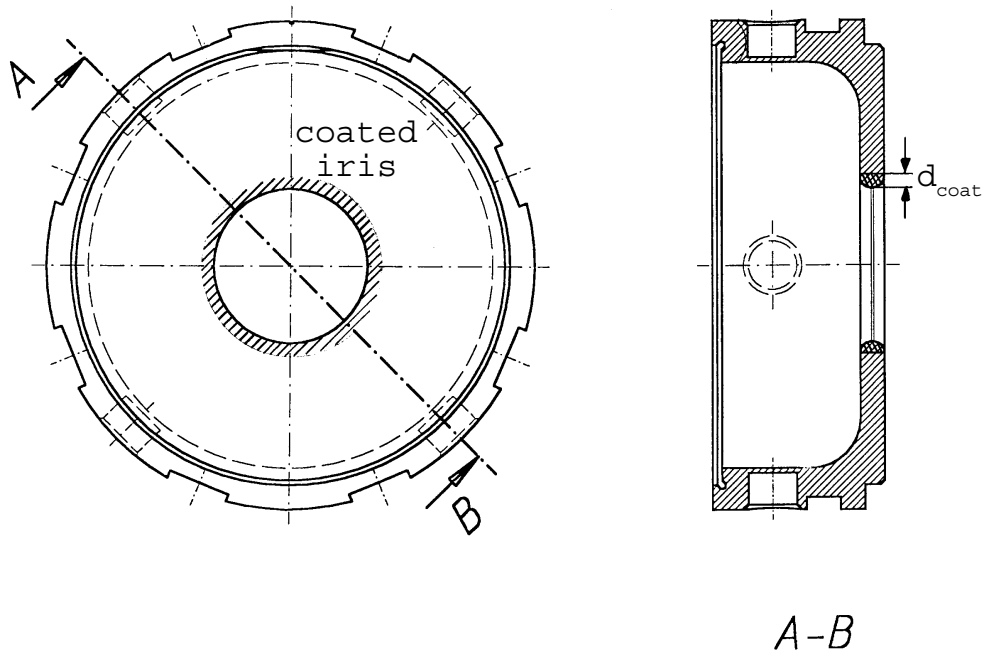

Figure 4.2.13: *Iris tip coating with a thin metallic layer.*

factors of modes in the first dipole band are shown in Fig. 4.2.14. Note that only modes below 4.45 GHz have a high HOM loss parameter as can be seen in Fig. 4.2.10 and Fig. 4.2.11.

For a constant gradient structure the fill time τ_{fill}, the damping parameter τ and the quality factor Q of the accelerating mode are related by

$$\tau_{\text{fill}} = 2 \cdot \tau \cdot Q/\omega.$$

If the fill time is kept constant the reduced quality factor allows to increase the damping parameter τ by changing the group velocity profile along the structure. Due to the higher damping parameter more of the input power P_a is available for the absorption inside of the structure ($P_a - P_b = P_a * (1 - \exp(-2\tau))$ and therefore the additional losses caused by the coating are partially compensated. Increased monopole losses of 5% and 10% as asumed for the Q-distributions in Fig. 4.2.14 reduce the average section shunt impedance only by 2.6% and 5.2% .

Active Structure Alignment The necessary components for the structure alignment are: the HOM pickup, the readout electronics and a feedback loop including the movers to position the section (compare Sect. 4.2.2). The active alignment uses single bunch operation because even small misalignments upstream would cause deflections of following bunches so that the beam axis is not unique and the resolution of the measurement is decreased. This effect would accumulate for structures downstream.

The structure alignment should not be limited by the sensitivity of the beam offset measurement and provide the potential of accelerating and maintaining a factor of two to three smaller emittance beams. Therefore the goal for the resolution is 10 μm

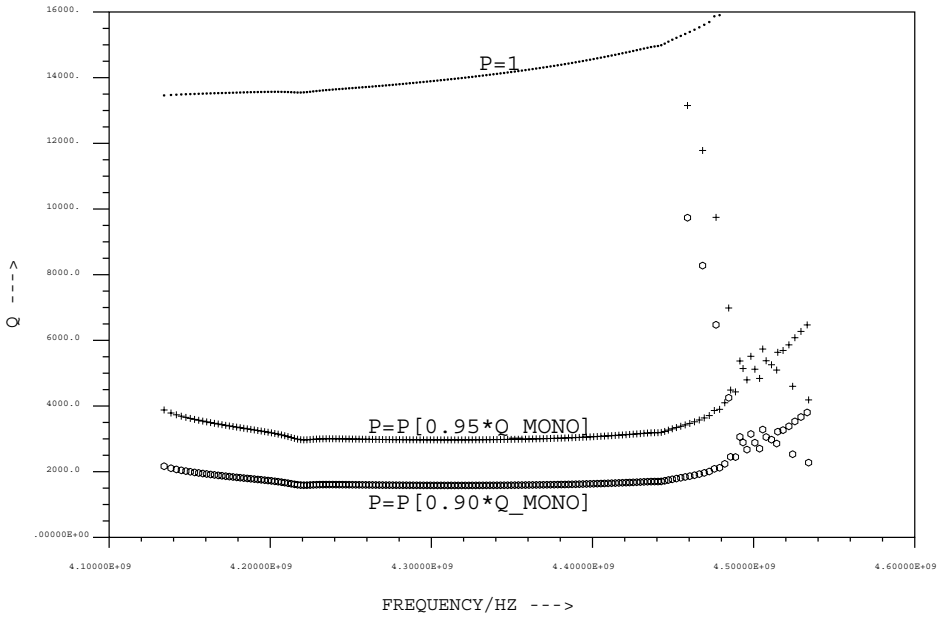

Figure 4.2.14: *Quality factors of the first 180 dipole modes in the tapered SBLC structure without iris coating and with length dependent coating. The surface absorption coefficient P is set for every cell so that the absorption of the accelerating mode is increased in every cell by 5% and 10% (d_{coat}=1.5mm). The quality for modes with high loss-parameter ($f < 4.45$ GHz) is significantly reduced. Some modes above 4.46 GHz have a qualitatively different field pattern and q factor due to a coupling to the second band in some cells.*

whereas only 50 μm is required for the 500 GeV parameters. With the offset of 10 μm a single bunch with design population (1.1×10^{10} particles) deposits approximately 1.3×10^{-12} joule in each of the 140 dipole modes of the first passband. Due to iris coating (leading to a Q of 3000) the energy decays with a time constant of 0.22 μsec which corresponds to a power flow of about 5 μW per mode. Only a fraction of this amount can be extracted by a HOM pickup which is designed for small change of the cell to cell detuning. The signal diagnostics can either lock to a particular mode with a bandwidth determined by its decay time constant (approximately 1.5 MHz) or it can use the full pickup bandwidth which is approximately half the width of the passband of the coupler cell ($\approx$ 0.5*100 MHz). Only a fraction of the modes within the pickup bandwidth provide sufficient coupling so that only 10 to 20 resonances are observable. In contrast to the small signal level of dipole modes, the power flow of the accelerating mode is more than ten orders of magnitude larger. One way to improve this situation is to switch off the klystron power of the section to be aligned, but beam loading still creates significant field levels towards the end of the section. On the other hand, mode or frequency selective equipment can provide sufficient performance.

HOM Coupler For every SBLC section two HOM pickups with four orthogonal

waveguides at one cell are foreseen. Two opposite waveguides are used for one polarization plane. The pre-selection is given by the cutoff frequency of the waveguide. After coupling to a TEM transmission line bandstop filters reject the accelerating mode and hybrids are used to distinguish between symmetry and anti symmetry of monopole and dipole signals.

The HOM coupler shown in Fig. 4.2.15 uses azimuthal wall slots for coupling [22]. The slots and the rectangular waveguides are 37.5 mm in width and thus have a cutoff frequency of 4 GHz. The acceleration mode at 3 GHz, which is well below the cutoff frequency, decays exponentially along the waveguide. The HOMs are above the cutoff frequency. For good rejection of the accelerating mode, the pickup (for the signal) is

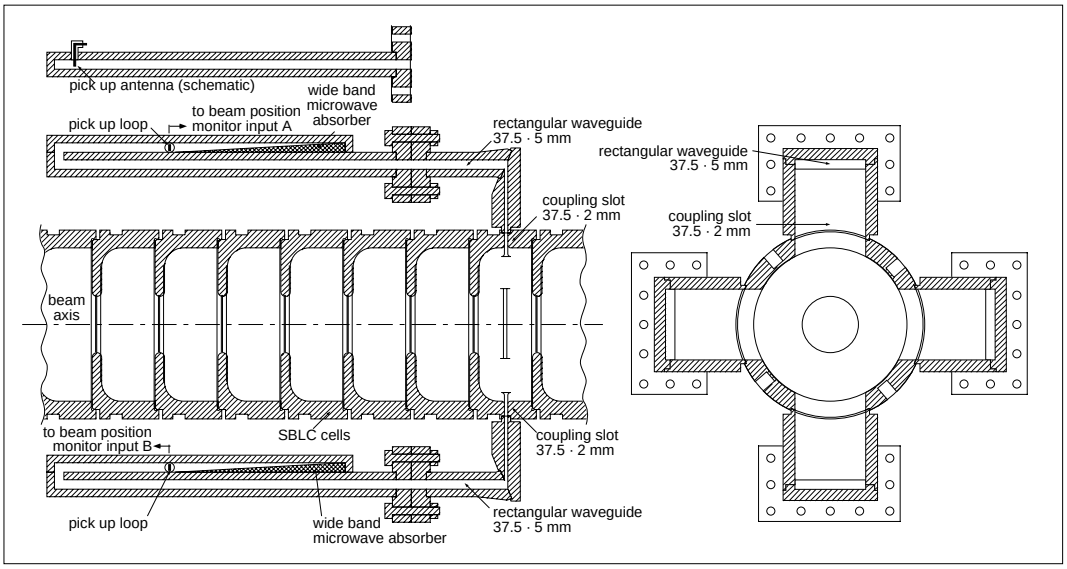

Figure 4.2.15: *Cross sectional view of the accelerator structure with one HOM-coupler*

mounted as far as possible away from the slot. Fig. 4.2.15 shows two alternative designs for the waveguide behind the flange. The upper illustration shows a straight waveguide with a pick up antenna mounted with a vacuum sealed connector. The length is limited by the free space which is left by the structure support. The other option which is also shown in Fig. 4.2.15 is a folded waveguide with wide band microwave absorber material at the end of thus waveguide. The pick up is realized by a wire loop mounted on a vacuum sealed connector at the side of the waveguide. This option has a better rejection for the accelerating mode and avoids disturbing standing waves, which influences the measurement. The disadvantage is a higher price and a more complicated fabrication.

A more compact solution with only one coupler is possible by coupling to modes of the sixth passband which are not trapped. Due to the high frequency of 9.4 GHz the coupling geometry and waveguides need only the half size and the frequency separation to the fundamental mode is wider.

Signal Processing for Active Structure Alignment To detect both sign and mag-

nitude of a transversal beam displacement the signal processing electronic needs signals from a TM-like dipole mode at about 4.3 GHz and a monopole mode at 6.2 GHz [23]. The accelerating monopole mode is not suitable for this purpose, because it does not propagate through the waveguide and has an amplitude which is not proportional to the beam current. The usage of a higher order monopol mode makes it possible to measure the beam position without klystron power. The magnitude information is derived from a dipole mode amplitude whereas the sign follows from phase comparison of a dipole and a monopole HOM during the time of bunch passage. Both signals are taken from the pair of pickups at the waveguide HOM-couplers. Figure 4.2.16 shows a possible scheme to process the signals from the coaxial pick-ups for one direction. The first stage is a 180° ring hybrid. The dipole signals from the HOM couplers have

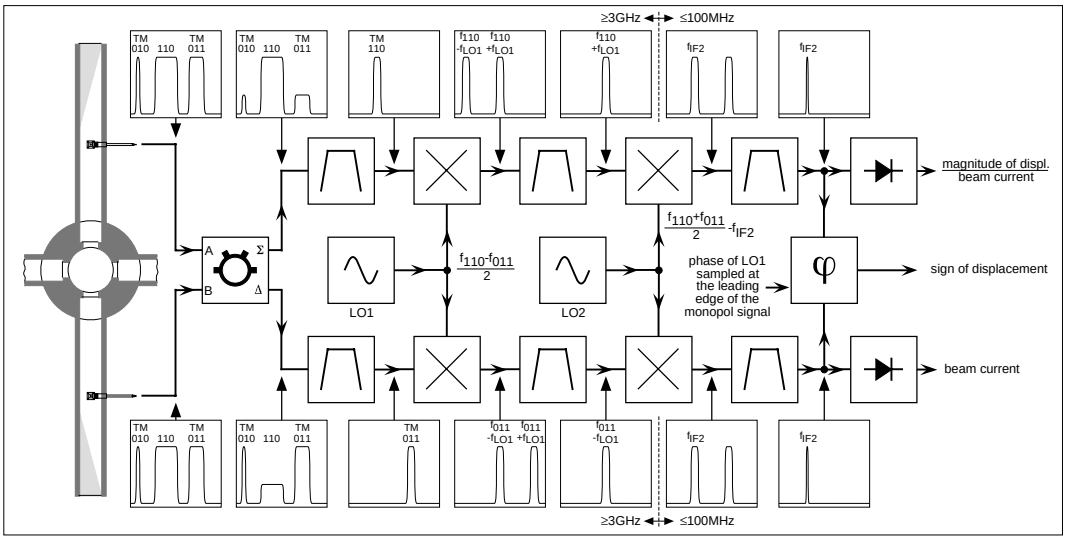

Figure 4.2.16: *Signal processing scheme for beam position monitoring in one direction (developed at IAP Frankfurt [23]) using HOM coupler signals*

same phases at the two pick-ups, which are mounted in opposite direction, thus the signals are transmitted to the Σ-port. The monopole signals have opposite phases and thus they are transmitted to the Δ-port. The hybrid is designed to reject monopole signals from the Σ-port which occur at the frequency of the dipole mode due to the finite Q of the cavities. The ring hybrid has to be mounted near by the couplers to avoid unsymmetrical phase shifting and damping by long transmission lines.

The first pair of filters consists of micro strip-line resonators with a bandwidth of about 50 MHz. It rejects modes of wrong passbands. A filter with a small bandwidth at this position has the disadvantage that it becomes impossible to tune the monitor to a different mode. Further the phase shift due to the temperature drift of the filter becomes too large. The filter block includes also variable amplifiers for the adaption to different operating situations. For fine tuning or pilot bunches one needs higher

amplification than for coarse adjustment and full current bunch trains. The first local oscillator is tuned to one half of the frequency difference of the dipole and the monopole mode. With this frequency the monopole signal is mixed downwards and the dipole signal is mixed upwards to the common frequency:

$$\omega_{IF1} = \frac{\omega_{mono} + \omega_{dipol}}{2}$$

The common frequency is needed for the phase comparison behind the second mixer. The filter behind the mixers selects the correct side band of the mixer signal. The second mixer stage mixes both signals downwards to a frequency of 70 MHz for the final filtering.

So far all components are micro strip-line circuits. This allows to integrate the ring hybrid, the filters and the phase shifters inside the mixers as line structures on a single PTFE printed circuit board. The following lower frequency components are lumped circuits on an unmatched printed circuit board.

Both quartz SAW filters have a narrow bandwidth and separate a single mode of each signal. The following rectifiers and low pass filters extract the amplitude of the signals. The magnitude of displacement and the beam current is determined by these two signals. The phase difference between the two second intermediate frequency signals is measured by the complex mixer between both paths. Due to the scheme of the first mixer pair (up-/down-mixing) the phase difference between the monopole and the dipole signal cannot determined only by measuring the phase difference of the second intermediate frequency (IF2) signals. The signals are given by:

$$u_{IF2mono} \propto u_{mono} \cdot \cos(\omega_{IF2} t + \phi_{LO1} + \phi_{LO2})$$

$$u_{IF2dipole} \propto u_{dipole} \cdot \cos(\omega_{IF2} t + \phi_{dipole/mono} - \phi_{LO1} + \phi_{LO2})$$

The measured phase difference depends on the phase of the first local oscillator at the time of the bunch passage. To get this phase we detect the leading edge of the monopole signal. A diode rectifies the envelope of the signal. This is done at a position with broad bandwidth, so we have a sharp rising edge. From the envelope a clipping line pulse former produces a short pulse to drive a dual sampling bridge sampling the complex signal of the first local oscillator to allow the determination of its phase at the time of the bunch passage.

After the A/D-conversion of all resulting signals a microprocessor does the non real time signal processing and the control and regulation of the local oscillator frequencies and amplifications. A frequency offset of the first local oscillator results in linear ramps instead of a constant signal for the phase. The frequency of this ramps is equal to the offset. A frequency offset of the second local oscillator results in an offset of the second intermediate frequency.

The information about the displacement and the beam current will be transmitted digitally from the microprocessor to the position control system of the structures.

4.2.2 The Support Structure

The approximately 6 m long accelerating structure has seven support points, spaced 933.8 mm apart, resting on a tubular steel girder (called "tube"). The tube is mounted on four remote controlled micro movers which are fastened via course adjustment units to the concrete floor. The cross section and a side view is shown in Fig. 4.2.17. At the first support the rf-structure is fixed to the tube, while at the six other supports it rests on adjustable pairs of rolls. Therefore the structure is aligned transversely but longitudinal motion due to thermal expansion is still possible.

The distance of ≈940 mm between structure supports is a compromise between the minimum number of supports and the natural sag. The tolerance given for straightness is $\leq 50\,\mu$m rms while the calculated sag for the given set-up is $3\,\mu$m only. The supports are adjusted with respect to an ideal line and the structure is fixed by its own weight. Deviations from this axis with a wavelength shorter than the support distance can of course not be corrected this way (compare: Material Preparation and Assembly).

Thermal effects which disturb the straightness of the support tube dominate the transverse displacements once the rf structure is aligned on top. These effects have been investigated in detail with the FEM code ANSYS. The steady state heat distribution and the time dependent behavior for heat-up are of main interest. The relevant parts of the somewhat simplified system which has been used in the model are the rf-structure as a linear heat source at a constant temperature of 75°, which is the foreseen operating temperature, together with the supports connected to the tube and the tube itself. Radiation into the environment (e.g. tunnel air at 20 deg C) and heat flow into the support structure has been taken into account. In the 2 D model the components are considered to be infinitely long. The final geometry consists of an inner support tube made from stainless steel and two outer heat shields made from aluminum. In between Styrofoam layers are used for isolation.

One main influence is given by conduction via metal parts. Heat flows from the rf-structure via the supports through the mechanically stable and thermally resistant INVAR tube downwards to the center. These tubes are fixed like spokes into the main tube with a diameter 457×6.3 mm. The "spoke"-tube equally splits the heat flow to enter the main support symmetrically (Fig. 4.2.17). Heat then flows mainly in the direction of the tube axis. A heat sink is given by the tunnel floor. Only temperature distributions symmetrical with respect to vertical and horizontal mid-planes of the tube result, They will locally set up mechanical stresses in the tube but, because they are symmetrical as well, cannot produce bending deformation.

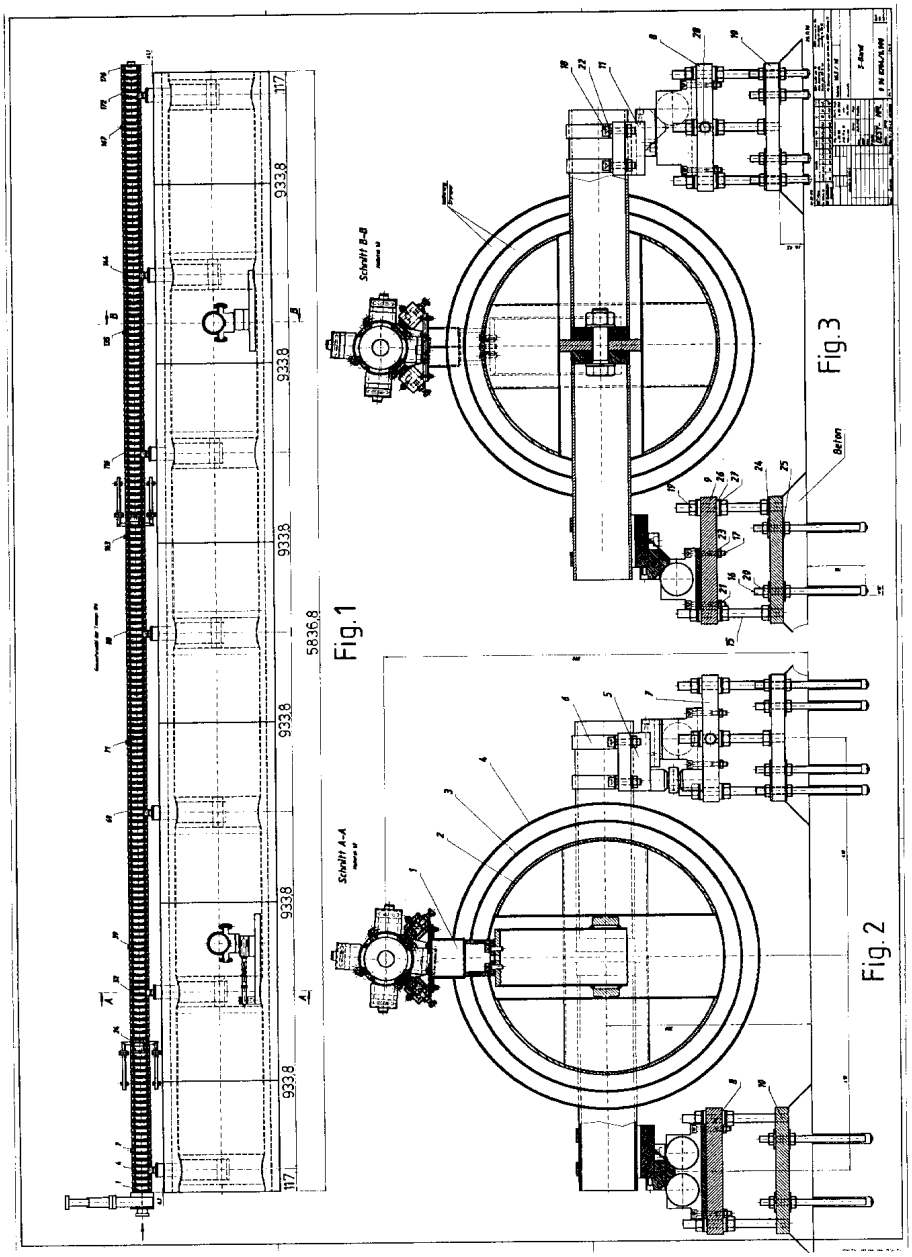

Figure 4.2.17: *The support structure together with the six meter long accelerating structure and two cross sectional views (front end and back end) is shown. Seven supports for the accelerating structure on top of the support tube can be seen. Vertical and horizontal support tubes inside the main six meter long support tube are shown as well. These "spoke"-tubes are at every support point. Close to the front end and at the back end the micro movers as well as the HOM mode pick up stations on the structure are shown.*

The second main distortion is given by heat radiating from the rf-structure and heat conduction via air. The power coupled into the outer Al-shield tube flows through the shield wall to the bottom and continues to the tunnel floor. In Fig. 4.2.18, for steady state conditions, the larger heat conductivity of the shield tube together with the comparatively lower heat conductivity between tube and heat source as well as tube and tunnel floor results in a low temperature difference of 1.32K between the top and the bottom of the outer shield. Only a very small fraction of total heat flow will enter

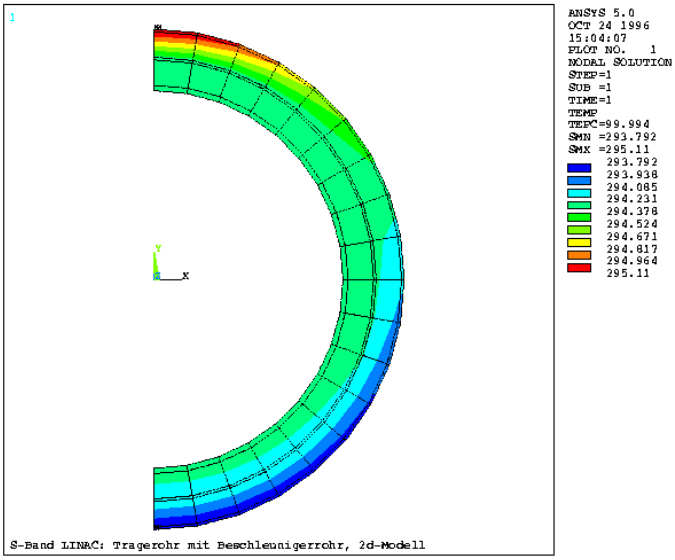

Figure 4.2.18: *The steady state temperature in one half of the support geometry is shown. The heat source is on top.*

through the outer Styrofoam layer to the inner shield. This results in a temperature difference over the shield of $\Delta T = 0.11\,K$ from top to bottom. By the same principle the main tube (made from iron) will have a temperature difference of $\Delta T = 0.013\,K$ from which a sagitta of only $2\,\mu m$ results. This value is much lower compared to the initial goal of $10\,\mu m$ and - after verification in the S-Band Test Facility - simplifications can be considered. in addition time dependent calculations show that due to the Styrofoam isolation the thermal response is very slow. In Fig. 4.2.19 the steady state and the temperature distribution after 72 hours is shown. Still a difference can be seen. Due to the slow thermal response fast temperature changes will be decoupled from the motion of the support.

Vibration, another very important aspect for the design of the support structure,

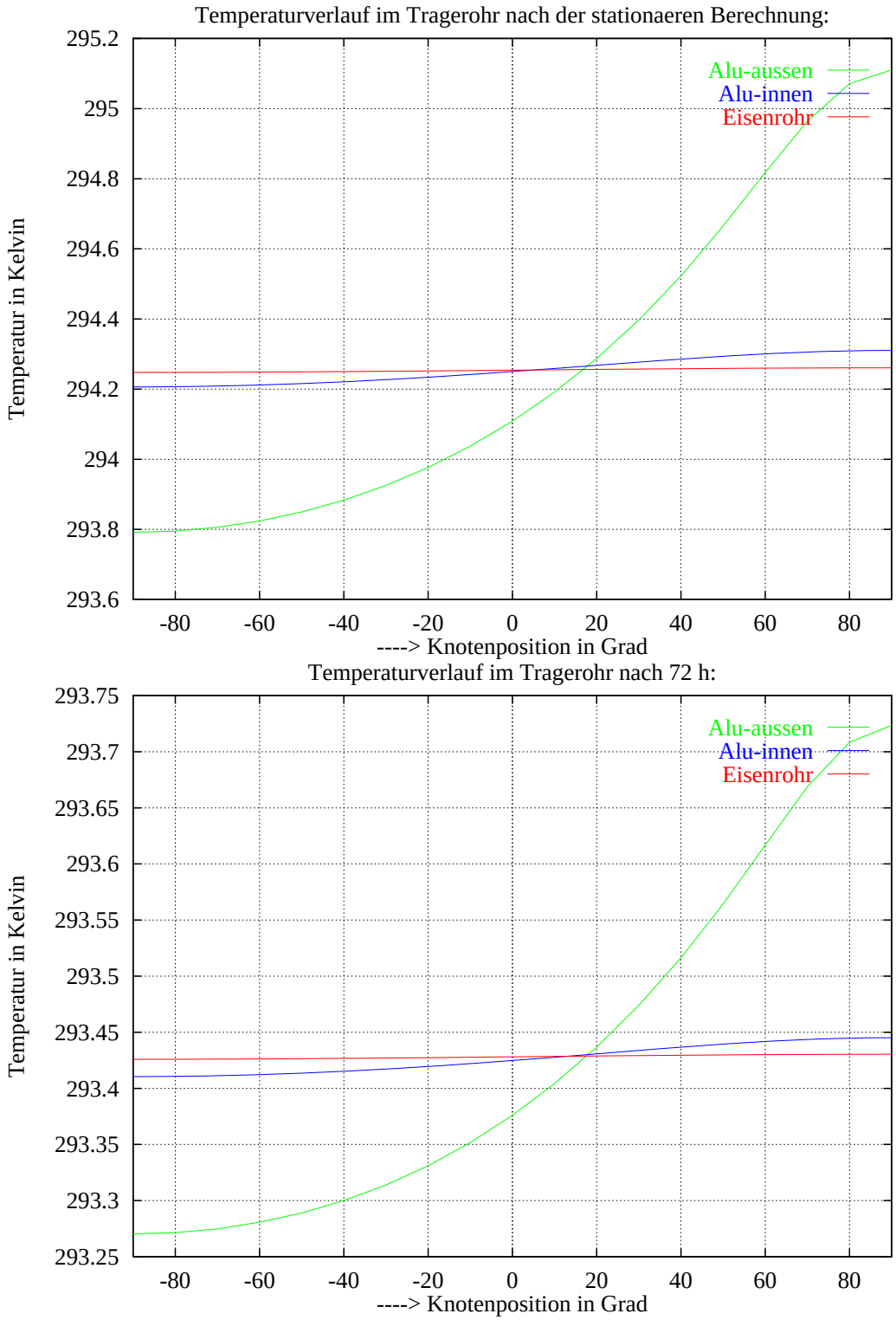

Figure 4.2.19: *The steady state temperature distribution (top) and the temperature distribution after 72 hours (bottom) of the two outer aluminum tubes and the inner iron support tube is shown. A linear heat source on top (75 C°) of the support structure and a 20 C° floor is assumed for the calculation. The temperature is shown versus the angle measured from the bottom (-90°). The calculation demonstrates the demonstrates the thermal inertia of the support structure.*

has been investigated as well. The lowest resonant frequencies for the tube is 35 Hz for any vertical flexure. Resonant modes close to 50 Hz or multiples have been avoided.

4.2.3 Alignment and Movers

The optimum orbit in the linear collider is determined by the magnetic axis of the focusing quadrupoles. Once this orbit has been achieved, the electric center of each accelerating structure has to be aligned with respect to this orbit. This will be achieved by minimizing the higher order mode power coupled by the beam into the dipole modes of the section. Therefore the position of the accelerating structure has to be changed and periodically adjusted during operation. Any transverse motion can be done by a system similar to that used for moving the focusing magnets in the Final Focus Test Beam[24] at SLAC. Cams are driven in phase via step motors to adjust the position to about $\pm 10\mu$m relative to the the beam. Some technical details of the the solution chosen for the S-Band Test Facility are given in Table 4.2.3.

As illustrated in Fig. 4.2.17, each section will be mounted on two micro-mover units, supporting two points at each end. The micro-mover unit at one end will have three drive motors and the one at the other end two, giving altogether five motors for motion with five degrees of freedom. Any long term motion ($\geq \approx 1$ minute) thermal or tectonic up to ± 1.5 mm will be compensated using this technique.

Table 4.2.3: *Micro-mover specifications*

Parameter/Item	Specification
Principle of movement	Cams phase-driven via step motors
Cavity section:	
Weight	1000 kg
Length	6 m
Positioning per section	
Two micro-mover units:	Front end unit á 3 motors
	Back end unit á 2 motors
Cam Radius/offset	40mm/1.6mm
Maximum range:	
Horizontal	± 2.2 mm
Vertical	± 1.6 mm
Overall ratio of transmission system	400:1
Step size of the positioning system	Minimum $< 0.3\mu$m
Tolerances	
achieved positioning precision:	
Horizontal	$\sigma_{rms} < \pm 8\mu$m
Vertical	$\sigma_{rms} < \pm 10\mu$m

4.2.4 Temperature Stabilization

An important issue for the operation of a Linear Collider with heavy beam loading is the temperature stability of the accelerating structure. Simultaneously the flexibility to handle large variations in beam loading and average power dissipation is required. The heat source is the rf dissipated in the walls given by the difference of the total input power and the power extracted by the beam. This power is calculated from the vector sum of the accelerating voltage and the beam induced voltage, taking the shunt impedance and the attenuation per unit length as well as the repetition rate and the rf pulse length into account. The temperature variations along the structure lead to energy variations of the beam, which are given by the phase error per cell integrated along the accelerating section. The single cell phase error is determined by the frequency change due to thermal expansion and the group velocity of the cell. This value is calculated from an average temperature change at each cell with respect to a constant temperature, where the beam is assumed to be in phase with the rf wave.

The structure is geometrically tapered to achieve a constant power loss per unit length for no beam loading. Overall four cooling tubes are soft soldered on the surface of the structure. The water feed and outlet is only at the input end and there is "u-shaped" flow (forward and backward flow with short connectors at the end) over the structure length. In order to calculate the exact temperature distribution, one fourth of the total geometry is modeled. The incoming cold water is going downstream, has a return loop over the last cell and flows upstream to the outlet while constantly heating up and reaching the maximum temperature at the outlet.

For the calculation the following assumptions have been made:

- because of the symmetry only one quarter of the geometry is calculated
- the temperature gradient over the wall with a thickness of 1 cm has been neglected
- the detailed temperature distribution inside the cell has been neglected
- the water inlet and outlet are on the same end as the input coupler with counter flow in the tubes
- brazed onto the first and the last cell are a return loop (last cell) and a feed pipe (first cell)

shown in Fig. 4.2.20 in a 3-D plot assuming a beam current of 300 mA. The temperature is shown as a function of the azimuthal position between 0 and $\approx$ 8 cm and the longitudinal position between the input coupler and the structure end. Fig. 4.2.21 shows the average temperature between the cooling tubes for different beam loading conditions. This is calculated as the arithmetic average over the azimuth between the two cooling tubes at each position along the structure length.

The temperature at the surface rises continuously along the length of the structure in absence of beam current. With increasing beam current the power which is dissipated along the structure decreases, because the beam induced field is small in the first cell and maximum at the end. Therefore the heat flow into the water is lower at the end of

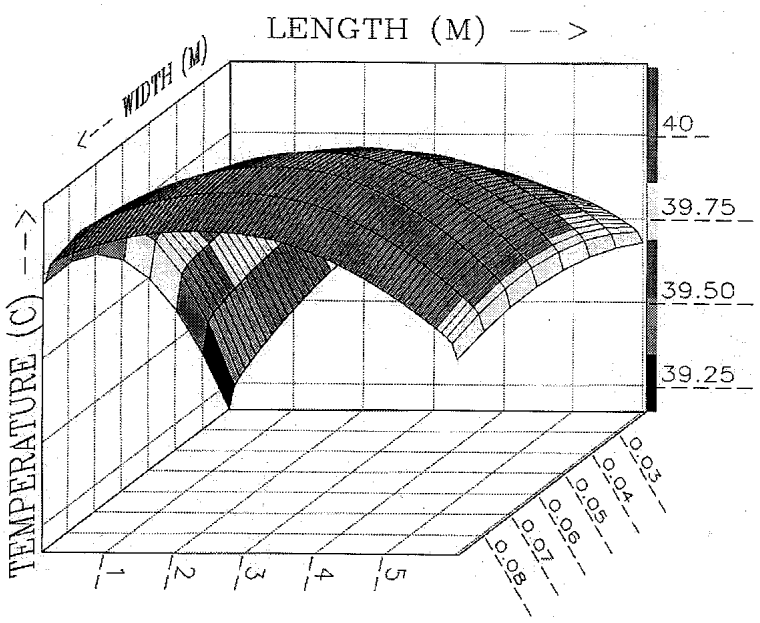

Figure 4.2.20: *Distribution of the surface temperature with a beam current of 300 mA. One quarter of the structure geometry is used for the simulation of the heat transport. Shown is the surface between two cooling tubes over the total structure length of 6 meter. The (cold) water inlet shows the lowest temperature while the temperature rises following the outer boundary of the displayed surface until the water outlet (hot) is reached.*

the structure than at the beginning. Because the heat flow from the structure surface to the water is a function of the temperature difference between them, the surface temperature increases at first and then decreases along the length with increasing currents. This effect is more pronounced with increasing beam current. The strong gradients on both ends are produced by the heat flow into the return tubes.

The integrated phase error turns into a beam energy error along the structure length. A minimum energy error can always be achieved, if the integrated phase error cancels towards the end of the structure. Using the inlet water temperature as a parameter, the phase error is zero if negative phase deviations with respect to the 120° phase shift per cell cancel with positive deviations towards the structure end. Calculation shows that at a specific point the temperature remains constant independent of the dissipated rf power or beam loading conditions. This point is used for temperature regulation and phase error compensation [26]. This location of this point is shown in Fig. 4.2.22, given by the cross-over of the curves .

For the details of the technical realization of the water cooling system see section 4.10. A similar system has been operated very successfully for many years in a high duty cycle electron linac for nuclear physics [27], where sudden power changes of more than a factor of hundred have been handled.

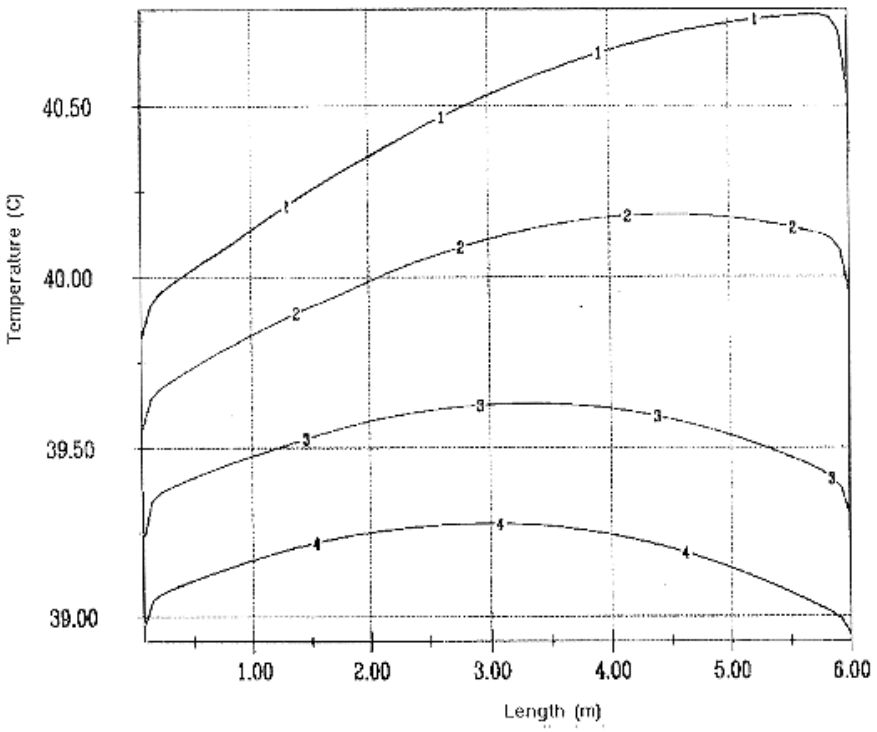

Figure 4.2.21: *Distribution of the surface temperature averaged over the azimuth for different beam loading conditions: curve 1 : no beam; curve 2 : beam current 100 mA; curve 3 : beam current 200 mA; curve 4 : beam current 300 mA. In this case the inlet water temperature was kept constant.*

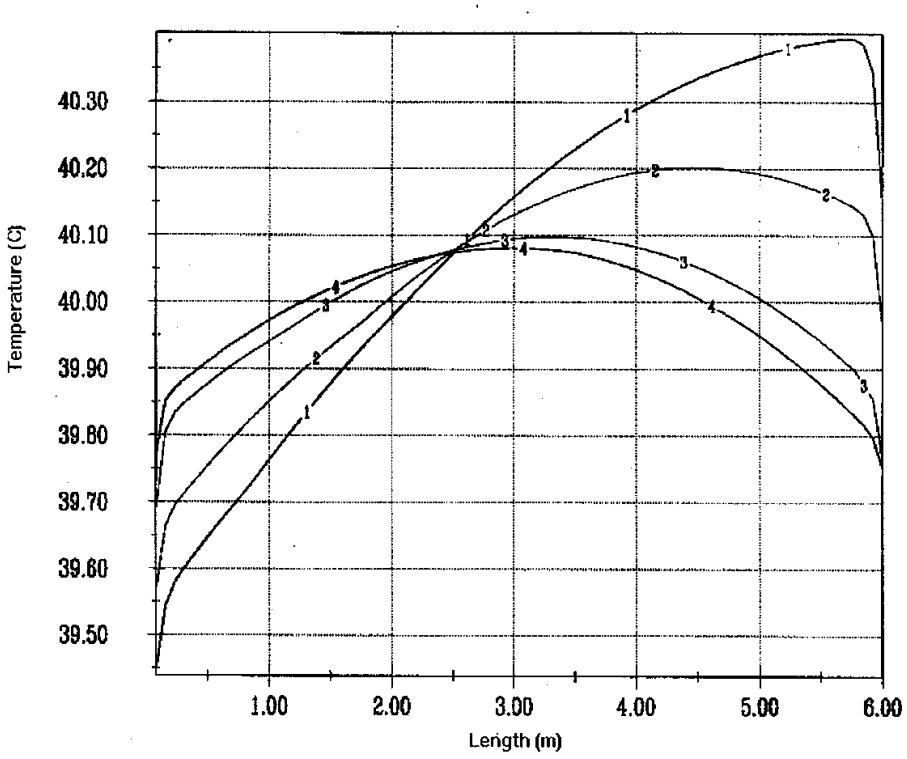

Figure 4.2.22: *Surface temperature with optimized inlet water temperature in order to cancel the sum of the single cell phase error towards the end of the structure: curve 1 : no beam; curve 2 : beam current 100 mA; curve 3 : beam current 200 mA; curve 4 : beam current 300 mA.*

4.2.5 Material Preparation, Assembly and Vacuum System Set-Up

The vacuum system of the main linac is dominated by the accelerating structure with a filling factor of more than 90 %. The achievable vacuum in the beam line is therefore given by the residual outgassing rate of the section under high power conditions. The achievable vacuum pressure in those structures is dominated by H and H_2 and is in the range of $10^{-9} - 5 \times 10^{-10}$ mbar. At the same time the required time for processing is reduced and the breakdown threshold increases.

Each accelerating section is connected to two vacuum pumps which are placed close to the input coupler. Nevertheless, the combined conductance of the beam pipe is determined by the average iris diameter, which is 26 mm. Assuming a residual outgassing rate of $10^{-8} \frac{\text{torr lit}}{\text{m}^2 \text{ sec}}$ which can only be achieved with carefully cleaned and assembled structures, the conductance of the six meter section limits the average pressure to approximately 2×10^{-8} Torr. Two pumps are installed next to the high power input coupler. At the coupler the main source of breakdown can be expected and optimum pumping should be applied. One pump is connected to the rectangular waveguide on top of the coupler and the second pump is directly connected to the coupler cell. Given the average pressure in the beam line and a base pressure at the pump which is ten times smaller, the installed pumping speed should be approximately 40 lit/sec per section.

4.2.6 The Radio-frequency-System

The radio-frequency system provides the rf peak power for the linear accelerator by converting ac-power to rf power. This, of course, has to be done in the most efficient possible manner. Apart fromt the fact that a lot of industrial experience exists for S-Band klystrons, again lower frequencies are favourable because the peak power, which could in principle be extracted from a single source, scales with (f^{-2}) [4]. Independent of frequency, in order to achieve the highest possible efficiency, a low micro- perveance is required. At a fixed peak power, this increases the required beam voltage. The feasible limit today on the high voltage, which we think is around 600 kV, certainly represents one limit for this value. Together with the specified efficiency this almost determines the maximum peak power which can be extracted from one klystron station.

The modulator consists of two main parts. The AC line to DC converter and the energy storage device together with the pulse transformer. The modulator has to convert the AC line power to DC pulsed power for the klystron which is already the first stage where efficiency plays a dominant role. Classical systems with power supplies and charging chokes (to double the voltage) are not efficient enough to be used in the linear collider. New types of power supplies, which are used to directly charge the energy storage device exist but have to be tested at the test facility. The energy storage device, which is a classical Pulse Forming Network (PFN) in our case, has to provide the energy per klystron pulse. Long RF pulses, which reduce the relative portion of the pulse which is lost during rise and fall time, require more storage capacity of the PFN. Economic arguments set an upper boundary, because the investment costs increase with an increasing number of capacitors, which is one of the cost driving items of a modulator. This argument also limits in some sense the frequency choice towards the lower end, because the energy which must be stored per pulse increases ($\approx f^{-7/2}$) poportional to the filling time of the accelerating structure and following the scalling law for the klystron which has been discussed before.

4.2.6.1 The Klystron

One of the strongest reasons for choosing S-Band to be the most favorable frequency for a linear collider design, is the klystron. S-Band klystrons are industrially manufactured at many places in the world and a tremendous experience is available, especially from the continuous operation of more than 240 tubes at the SLAC linac [28]. Both arguments present a strong bases for the R & D required for the power sources of such a large linear accelerator, where the highest peak power possible per station should be used. This way the number of klystrons per linac can be reduced, which contributes to cost saving since the cost per klystron does not increase proportional to the peak power.

The S-Band linear collider requires approximately 2600 klystrons operating at an output power of 150 MW, a pulse duration of 2.8μs and repetition rate of 50 upgradable

[4] f:=frequency; This is simply given by the maximum beam current which can be extracted from the gun area, at a given reasonable limit for the current density, in a otherwise geometrically scaled klystron.

to 100 Hz. The efficiency must reach 55 % to limit the total AC power. The power required for focusing must be minimized, or even better, period permanent magnet (PPM) focusing should be used. Nevertheless it should be pointed out, that the S-Band linear collider could be operated with solenoid focusing at the expense of power which would increase by approximately 18 %. The life time of the klystrons should be of the order of 50.000 hours, which requires a robust design with a minimized number of critical components. Still on average, approximately every 20 hours a klystron will have to be changed during operation and while the accelerator is running.

The following pages present the status of the development of 150 MW S-Band klystrons. Then further necessary developments which will lead to a klystron meeting the specifications of a klystron for an S-Band linear collider will be discussed.

Until 1985 the klystron producing the highest output power at S-Band frequencies was the 5045 klystron at SLAC. It operates at a peak power of 65 MW with a pulse width of 3.5 μs and a repetition rate up to 180 Hz [29]. In 1985 a 150 MW S-Band klystron was developed at SLAC. It produced a power of 150 MW, but at a shorter pulse width of only 1 μs and a repetition rate of 40 Hz at full peak power [30]. Following this development it was anticipated that a 150 MW Klystron with 3 μsec pulse length and 50 Hz repetition rate is a reasonable R & D goal which can be achieved in few years. In 1993 a collaboration between SLAC, DESY, Philips and the Technical University of Darmstadt started to develop this S-Band klystron and the first one was successfully tested in 1994, only $1\frac{1}{2}$ years later. Until 1995 two klystrons have been built and successfully tested [31][32]. Table 4.2.4 presents the design and the achieved parameters of the klystron.

	Design	Tube 1	Tube 2
Power Out	150 MW	153 MW	150 MW
Pulse Duration	3 μs	3 μs	3 μs
Repetition Rate	60 Hz	60 Hz	60 Hz
Average Power	27 kW	27.5 kW	27 kW
Beam Voltage	535 kV	527 kV	508 kV
Beam Current	700 A	680 A	652 A
Perveance	1.79×10^{-6} A/V$^{3/2}$	1.78×10^{-6} A/V$^{3/2}$	1.80×10^{-6} A/V$^{3/2}$
Efficiency	40 %	43 %	45 %
Gain	50 dB min	56 dB	57 dB

Table 4.2.4: *Design and measured parameters of the 150 MW klystrons for the S-Band test facility*

Both klystrons, tube 1 and 2, will be used at the S-Band test facility at DESY. The first tube is already in operation. Figure 4.2.23 shows tube 1. The total height is

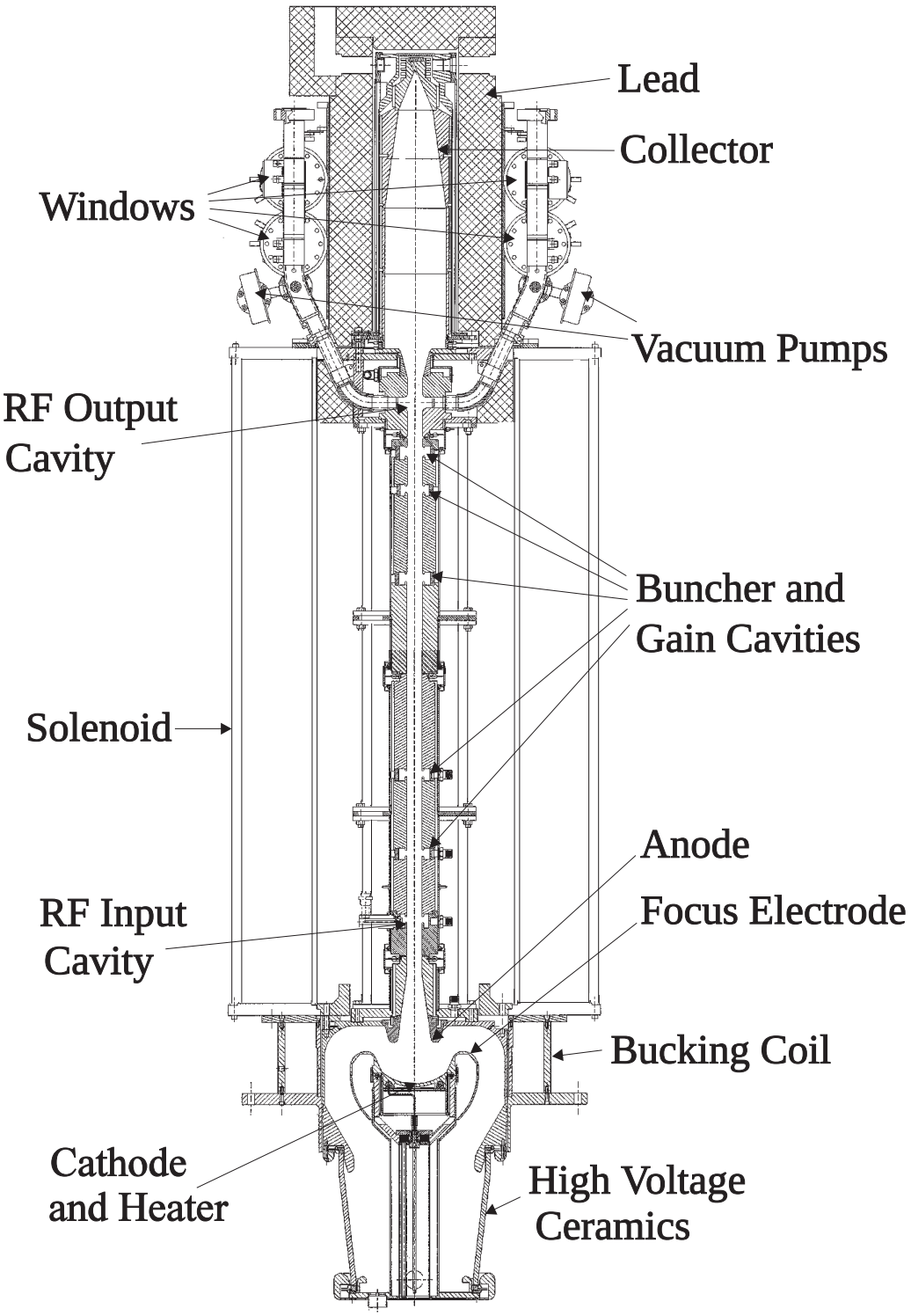

Figure 4.2.23: *150MW S-Band klystron for the S-Band test facility (Klystron 1)*

2.6 m, the diameter of the anode housing is 40 cm and the weight is about 300 kg without lead. The cathode has a diameter of 13.3 cm and a cathode loading of 6.12 A/cm^2. The beam area convergence is 40:1. The maximum electric fields on the focus electrode and anode are 180 kV/cm and 210 kV/cm, respectively. Seven cavities including the input and output cavities are in the 3.2 cm wide drift tube.

The klystron has two output waveguides, which are split and recombined, with two RF windows in each output waveguide. The waveguide assembly on each side is the well proven design of the 5045 klystron. The klystron requires a solenoid with a magnetic field of 1800 G which has a power consumption of 14 kW. The weight of the solenoid is 1800 kg. A bucking coil is required to achieve zero magnetic field on the cathode surface.

Although both tubes are very similar in general, there are three differences between the two tubes. Already at the design stage it was decided to use different output cavities for them. Tube 1 operates with one single cavity whereas tube 2 has two coupled cavities at the output. The expectation was, that the second tube would have a slightly better efficiency compared to the first tube. As presented in Table 4.2.4, this has been achieved. During the test of tube 1 an oscillation at 8.1 GHz was observed depending on the beam voltage and solenoid field settings and in a less sensitive way on the filament power. Therefore it was decided to fabricate tube 2 with a stainless steel drift tube between the cavities 3 and 4, and 4 and 5 instead of using only copper for the drift tube as for klystron 1. This provided additional losses to the disturbing modes. The cathode was changed to a scandate cathode for tube 2, whereas tube 1 uses an osmium coated M-type cathode. The M-type cathode is known to have a distinct roll-off for the beam current versus filament power curve. Scandate cathodes have a softer transition while going from the temperature to the space charge limited regime. This allows to operate tube 2 over a wider range of filament power settings compared to tube 1. These measures have been proven very successful. No oscillations were observed during the tests with tube 2.

Figure 4.2.24 shows the output power versus drive power for different beam voltages for klystron 1. At about 400 W of drive power the output starts to saturate. Similar data exist for tube 2.

Although the development of the first two 150 MW klystrons for the S-Band collider was very successful, further R&D is required. The first two tubes have been constructed in a conservative way by using as much of proven sub-assemblies as possible. In order to increase the efficiency and to built a robust, simpler and cost effective klystron a number of changes are required.

The klystrons for the test facility are mounted vertically, but for a klystron to be used in a linear collider tunnel a horizontal mounting position is required to save tunnel space. For that reason the klystron must be stiffened and especially the klystron gun and the cathode assembly must be supported.

Each of the four windows in the two output waveguides represents a possible source for klystron failure. Instead of using two windows per output waveguide by splitting and recombining one could use one window without splitting the waveguide. This reduces the number of windows to two in total and might reduce the number of window

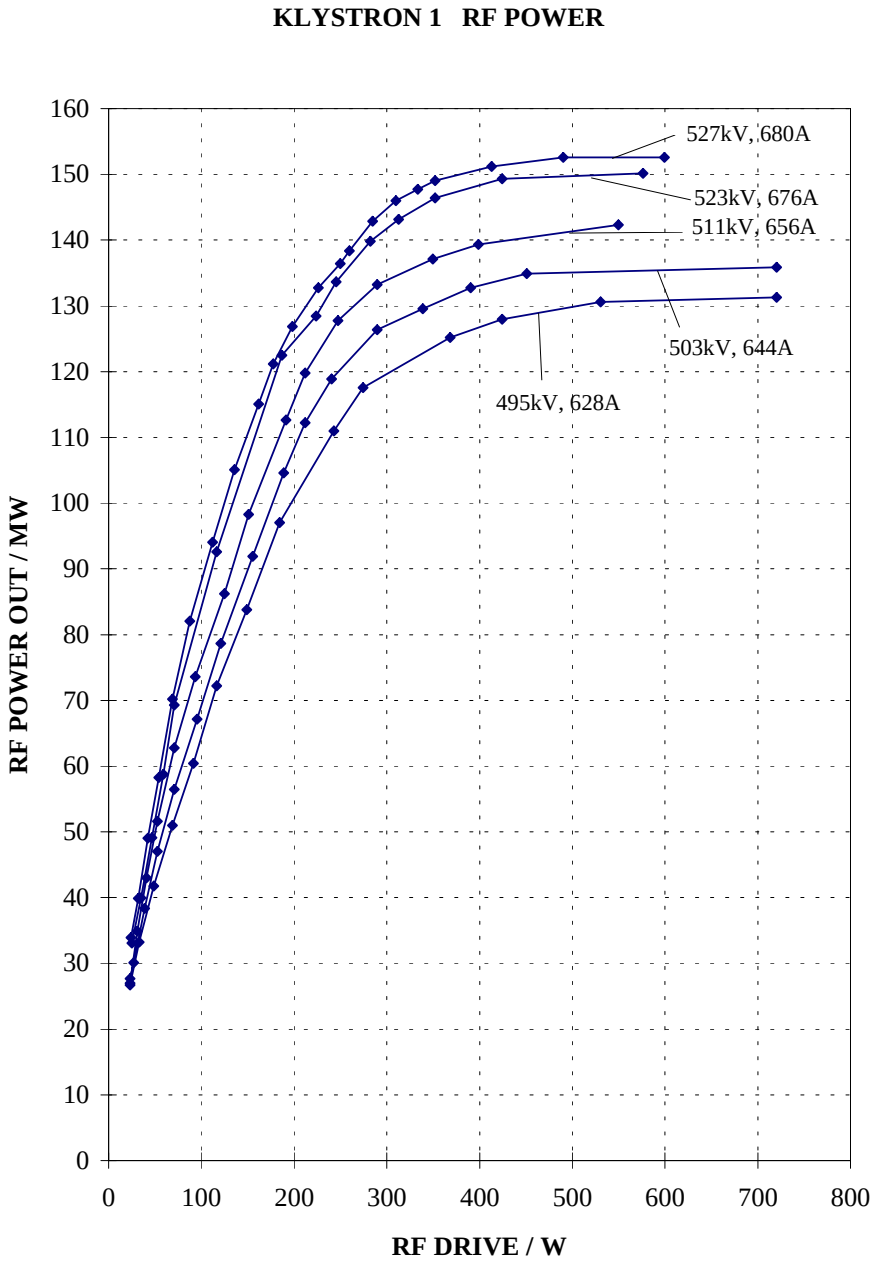

Figure 4.2.24: *RF power versus drive power for test facility klystron 1*

failures although the power per window is increased. In this case the window in one waveguide has to transmit 75 MW instead of 37.5 MW. Further research on window materials must be performed to achieve this goal. Besides these considerations, the output waveguide assembly represents an expensive part of the klystron, which makes the entire production process costly. Another possibility to reduce the costs for a klystron is the gun assembly. A gun for instance without a big tapered ceramics would make the fabrication of a klystron easier and cheaper, too.

The maximum efficiency achieved with the klystrons for the test facility was 45 % which is almost sufficient for the linear collider. It is a well known fact that if the perveance of a klystron decreases the efficiency increases (for instance see [34]). This means that the beam voltage needs to be increased and the beam current must be decreased. On the other hand one has to take into account that the the beam voltage must be still controllable and can not exceed technologically feasible limits. The proposed solution is a klystron operating at a micro-perveance of $1.0\times10^{-6}\,\mathrm{A/V^{3/2}}$. An efficiency of 55 % could be achieved and the beam voltage is kept at 595 kV, which is only about 10% above the voltage of the test facility klystrons. Decreasing the micro-perveance from 1.8 to $1.0\times10^{-6}\,\mathrm{A/V^{3/2}}$ in addition supports the construction of a klystron using periodic permanent magnet focusing (PPM). Because the beam current decreases, the effect of the space charge forces in the beam is reduced and the beam confinement is easier. Table 4.2.5 presents the design parameters of a 150 MW S-Band klystron with micro-perveance $1.0\times10^{-6}\,\mathrm{A/V^{3/2}}$.

Peak Power Out	150 MW
Pulse Duration	2.8 μs
Repetition Rate	50 Hz
Average Power	21 kW
Beam Voltage	595 kV
Beam Current	459 A
Perveance	$1.0\times10^{-6}\,\mathrm{A/V^{3/2}}$
Efficiency	55 %
Gain	55 dB
Focusing	Periodic Permanent Magnet (PPM)

Table 4.2.5: *Parameters for a PPM focused S-Band klystron*

At SLAC a PPM focused X-Band (11.424 GHz) klystron with an output power of more than 50 MW and with an efficiency up to 60 % [35] has already been developed. Because of the larger drift tube, the conditions for beam focusing are more relaxed for an S-Band klystron and the development of an S-Band PPM focused klystron should be straight forward. S-Band klystrons operating at an output power of 150 MW are available and their performance has been demonstrated successfully. Some changes, most of them only moderate, are required to achieve the goals demanded for a linear

collider klystron.

In parallel to the R&D program discussed before, Thomson [5] has developed a 150 MW klystron as well and the results have recently been presented [33]. This, as a matter of fact, proves the industrial available capabilities, specifically at S-Band. This klystron requires a higher beam voltage (up to 590 kV) as compared to the test facility klystrons, but less current. The micro-perveance is $1.35\times10^{-6}\,\mathrm{A/V^{3/2}}$. About 2 kW of drive power are necessary to saturate the klystron. Up to now this tube has been tested at 1 μs pulse duration and a repetition rate of about 1 Hz.

Other companies with well known capabilities in this field have as well offered, as a first step, to rebuild the 150 MW tube which resulted from the common R&D program at SLAC. This represents, to our opinion, a strong basis of future R&D for the development of a PPM focused S-Band tube.
Industry type production lines have been investigated for this klystron [36] and show cost reductions which reach the final per item cost goal taking into account the anticipated production number per year, both for first installation and for the continuous exchange and upgrade in the linear collider as well. In this study a dedicated klystron facility is proposed with a plant being designed to finally produce approximately 1000 klystrons per year with an increasing yield starting from 40 % and over the first four years going up to 100 %.

Apart from the production of the klystron, the mean time to repair (MTTR) is a major issue for the operation of a linear collider. As already mentioned, even with the anticipated lifetime of 50,000 hours every 20 hours a klystron has to be changed, while the accelerator is operating. Assuming 5,000 hours of operation 250 klystrons per year have to be transported into the tunnel, and brought back to the klystron factory for repair. Clearly the capability for klystron replacement must be higher than the rate for klystron failure. A semi-automatic exchange and start up procedure in the collider tunnel is conceivable. It should allow a klystron replacement and start up with a minimum of activies, which must be performed by specially skilled personal. These considerations must be already taken into account for the klystron design and its mechanical layout. Collaborations with automatization specialists and klystron manufactures should be settled. A first investigation of the replacement process has already been performed [37].

4.2.6.2 Line Type Modulator

Line type modulators represent the type of modulator which is most used for the production of high power, high voltage pulses. Almost all pulse klystrons at linear accelerators in the world make use of line type modulators, for instance all 240 klystrons at the SLC at SLAC are supplied by line type modulators [38]. Line type modulators therefore represent a well established and proven technique and therefore are one possible choice for the generation of pulse power at the S-Band linear collider. The following pages represent the status of the development of line type modulators for the 150MW S-Band klystrons. After presenting the status, parameters of a line type modulator

[5] Trademark of the French company THOMSON CSF

meeting the demands of an S-Band linear colldider will be given and a possible setup will be shown.

The present status of line type modulators for the 150 MW klystrons is given by the modulators for the S-Band test facility [39]. The facility requires two line type modulators for the generation of high voltage pulses for two 150 MW klystrons. The requirements for these modulators are determined by the klystron parameters (see klystron chapter), i. e. by the cathode voltage and current, the pulse duration and repetition rate. The numbers for the line type modulators are listed in Table 4.2.6, the circuit is shown in Fig. 4.2.25.

Pulse Voltage	535 kV
Pulse Current	700 A
Flat Top Pulse Duration	3μs
Repetition Rate	50 Hz
Equivalent Square Wave Duration	4.8 μs
Rise Time 10 - 90%	700 ns
PFN	four lines parallel, each line ten sections
PFN impedance	1.34 Ω
Total Capacitance	1.8 μF
Capacitor Capacitance C_i	45 nF
Coil Inductance L_i	1.3 μH
Charging Voltage	50 kV max.
Peak Current (primary side)	16 kA
Pulse Transformer Ratio	1 : 23

Table 4.2.6: *Parameters of the present line type modulator for the S-Band test facility.*

The PFN is charged by resonant charging up to twice the power supply voltage. The total PFN capacitance of 1.8 μF together with the charging choke inductance of 16 H gives a charging time of 17ms. The HV power supply is rated to a maximum voltage of 26.5 kV and an average current of 5A. Because the HV power supply is SCR controlled, which leads to a pulse to pulse voltage stability better than 1%, it is not necessary to use a de-Qing system. The PFN consists of four lines in parallel with ten PFN sections per line. The nominal PFN impedance calculated by $Z=1/4(L_i/C_i)^{1/2}$ is 1.35 Ω. Two lines of the PFN are connected to one thyratron. This reduces the maximum pulse current per thyratron to less than 10 kA. The two thyratrons can be triggered independently by two thyratron drivers. The PFN energy is transferred by a 1:23 step up transformer into the klystron. The klystron impedance at the nominal secondary pulse voltage of 535 kV and 700 A is 764 Ω, which represents an impedance of 1.44Ω to the PFN, i.e. there is a slight positive mismatch. The rise time of the high voltage pulse of 700 ns is mainly determined by the pulse transformer with the

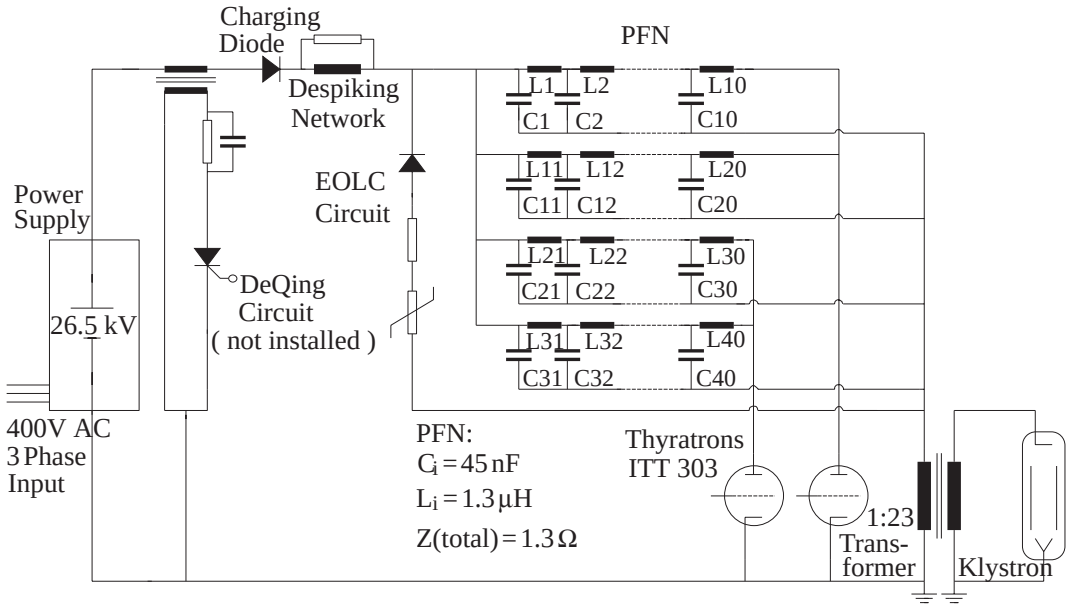

Figure 4.2.25: *Schematic drawing of the circuit of the present line type modulator at the S-Band test facility.*

transformer ratio of 1:23 and the finite number of 10 sections per PFN line. An end of line clipper circuit (EOLC) made by resistors, varistors and a diode absorbs the energy stored in the PFN in case of klystron arcing. Typical waveforms are shown in Fig. 4.2.26.

The modulator consists of five separate units in total, the PFN unit with the pulse transformer tank, the charging unit, the HV power supply, a control unit and the power supplies for the klystron solenoid.

The PFN unit is 2.6 m high and requires a ground space of 1.5m times 1.4 m. The PFN with its capacitors and coils, the EOLC, the thyratrons and their drivers are installed in this unit. The PFN capacitors are mounted horizontally with one side connected to the aluminum mounting rack. The coils are connected to the other side. The inductances of the coils can be adjusted by c hanging the tap on the coils and changing the position of a slug inside the coil. This allows to tune the shape, especially the flat top of the HV voltage pulse.

The pulse transformer tank is directly connected to the PFN unit. The oil filled tank has a diameter of 1.2 m and a height of 1.6 m. Besides a filament transformer, a blocking coil and some diagnostics like a capacitive voltage divider and current monitors, the pulse transformer is the biggest component in the tank. The connection between the transformer and the PFN unit is made with a transmission line like feed through. It consists of three parallel copper bands, one band is connected to the PFN capacitor mounting rack, the other two are connected to the thyratrons. The klystron with the solenoid sits on top of the tank with the cathode and gun ceramics in the tank oil.

The charging choke and diode and the despiking network are installed in the charg-

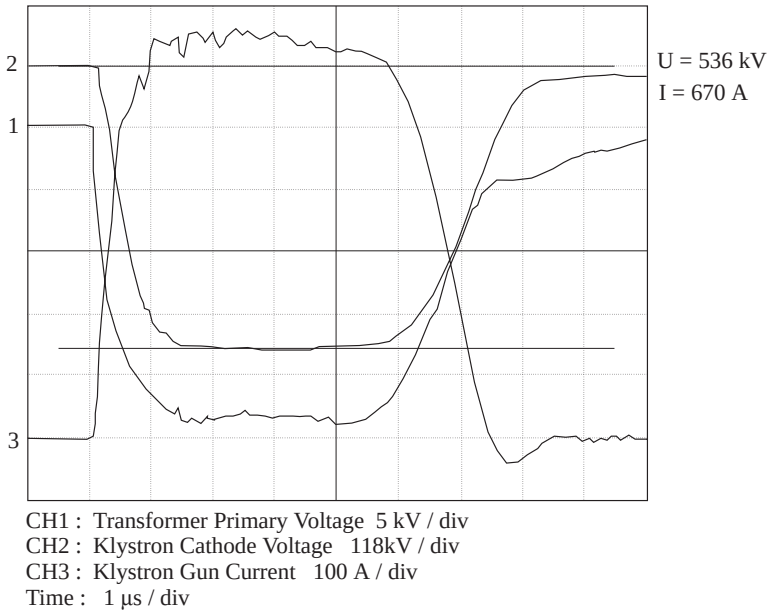

Figure 4.2.26: *Typical waveforms of the line type modulator at the S-Band test faciltiy (without efforts to tune the PFN)*

ing unit. It has a height of 2.45 m and is 1.45 m times 1.35 m wide.

The HV power supply is a commercial power supply. It is 2.25 m high and 1.4 m times 1.85 m wide. It can be operated locally or remotely via a GPIB interface.

All controls are installed in four nineteen inch racks. It is possible to control the modulator locally and remotely by these racks. About two racks are occupied by scopes and printers, which were required during commissioning. The interlocks are accomplished by a programmable logic controller, which also serves for data logging of analog signals like cooling flow rates, temperatures and vacuum pressures. The vacuum power supplies for the klystron, heater power supplies for klystron and thyratrons, bucking coil power supply and trigger generators are also installed in the control rack. The solenoid power supplies require the space of three nineteen inch racks.

The total efficiency of the modulator at the test facility reaches 58%. It is defined by the power transferred to the klystron during the $3\,\mu$sec flat top of the HV pulse, devided by the wall plug power. The efficiency contributions of the HV power supply and the resonant charging system are each nearly 94%. This means that most of the wall plug power, which can not be used for RF generation, is lost during the energy transfer from the PFN to the klystron. Only the flat top of the HV pulse can be used for RF generation. Besides a small fraction of ohmic losses during the HV pulse, it is mainly the energy during the rise and fall time of the HV pulse, which is lost.

Power required for the auxiliaries like the filaments, drivers, core bias or solenoid power supplies has not been taken into account for the numbers above. A comparison of the total power required per modulator and the power for the auxillaries for the

test facility modulator and the modulator foreseen for the Linear Collider is given in table 4.2.8

Adding these numbers together a wall plug power of 87 kW is required for one line type modulator at full repetition rate and output power, plus about 20 kW for the solenoid and auxiliaries, which is clearly not acceptable for a large scale installation. The goal for the modulator efficiency from wall plug to klystron without auxiliaries is 70%.

In order to enhance the efficiency of the present modulator and to meet the demands of a future PPM focused klystron, further development of the existing line type modultors is required. Therefore it is necessary to have a closer look at the reasons for the losses in the present modulator.

The dominant loss in the present modulator is due to the limited power transfer from the PFN to the klystron. As explained above, this is mainly due to the power lost during the rise and fall times of the HV pulse. Two effects determine the rise and fall times of a modulator, the number of sections per PFN line and the characteristics of the pulse transformer. As a rule of thumb the rise time T_r of a PFN consisting of N sections is given by T_r=T/N, where T is the equivalent square wave duration. For the modulators at the test facility for instance where T is 4.8 μs and N is 10, one calculates 480 ns. Another important effect on the rise time is caused by the characteristics of the pulse transformer. Two parameters of a transformer limit the rise time. The first is the leakage inductance of the transformer. The coupling between the primary and secondary side of a pulse transformer can never be ideal due to the necessary insulation between the primary and the secondary high voltage side. A part of the magnetic field produced by the primary side does not pass through the secondary winding of the transformer, which leads to a leakage inductance in series with the load. The second parameter is the capacitance between the primary and secondary winding. This capacitance, the stray capacitance of the klystron cathode and the transformer to ground in addition must be charged during the HV pulse.The higher these capacitances are the longer is the rise time. Experience shows that decreasing the step up ratio of a transformer decreases the leakage inductance and the capacitance between primary and secondary winding, which leads to faster rise and fall times.

A trade off must be made between these considerations and the fact that decreasing the step up ratio of the pulse transformer leads to an increase of voltage on the primary side, i.e. an increase of charging voltage of the PFN. The availability of HV power supplies, low inductance capacitors and thyratrons must be taken into account. Assuming that 75 kV is a technically feasible limit for the voltage on the the PFN and that a future klystron operates at 595 kV, a step up ratio of 1:16 for the transformer ia applicable. By using 1:17 instead, a charging voltage of 70 kV is required. This leaves some safety margin if more voltage would be required. The parameters for a future modulator are shown in Table 4.2.7. A shorter flat top pulse duration of only 2.8 μs is required by the klystron. Figure 4.2.27 shows the schematic of the circuit.

The PFN has two lines in parallel. Each line consists of 20 sections. The contribution of the PFN rise time to the total rise time calculated by the rule of thumb formula given above is less than 200ns. The decrease in step up ratio also lowers the pulse cur-

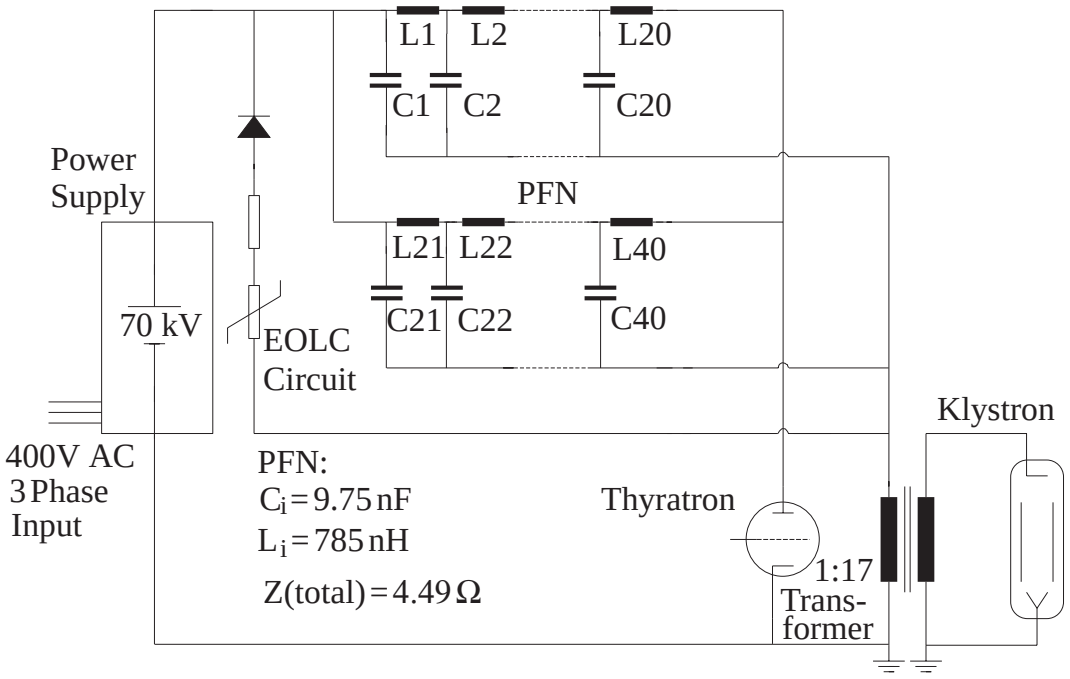

Figure 4.2.27: *Schematic drawing of the circuit of a future line type modulator*

rent on the primary side to 7.8 kA. Thyratrons capable of more than 70 kV and 10 kA are already available from industry. This allows to reduce the number of thyratrons per modulator from two to one, thus reducing the investment and the operations costs .

With the numbers in Table 4.2.7 one obtains an efficiency of 80% for the power transfer from the PFN to the klystron. Taking into account ohmic losses by introducing a factor of 0.97 one gets an efficiency of 77% from the PFN to the klystron. Power is also lost during the resonant charging process of the PFN. This is mainly due to ohmic losses in the huge charging choke, which has a resistance of about 100 Ω, and other components in the charging path. Installing a DeQing system would further decrease the efficiency.

Fortunately inverter power supplies are available today, which allow a direct charging of a PFN to the desired voltage with a good regulation (for instance from Maxwell, San Diego, USA). Resonant charging and DeQing is no longer necessary. The supplies available at the moment are limited to 50 kV, but this is mainly because of the limited demands for higher voltage up to now. An extensions of this technique to higher voltage should be possible with only small effort. By using these supplies, almost no losses would appear between power supply and PFN during the charging process. The intrinsic efficiency of these supplies from wall plug to power supply output is 92%. Therefore it can be assumed that an efficiency of 92% from wall plug to the PFN can be reached.

Inverter power supplies require a protection against voltage reversal, which is usually achieved by installing a protecting diode at the output of the supply. Since an

Pulse Voltage	595 kV
Pulse Current	459 A
Flat Top Pulse Duration	2.8 μs
Repetition Rate	50 Hz
Equivalent Square Wave Duration	3.5 μs
Average Output Power	47.8 kW
Rise Time 10 - 90%	500 ns
PFN	two lines parallel, each line twenty sections
PFN impedance	4.49 Ω
Total Capacitance	390 nF
Capacitor Capacitance C_i	9.75 nF
Coil Inductance L_i	780 nH
Charging Voltage	70 kV
Peak Current (primary side)	7.8 kA
Pulse Transformer Ratio	1 : 17

Table 4.2.7: *Parameters of a future line type modulator*

EOLC diode must be installed at the PFN on the HV power supply side for klystron protection reasons anyway, a careful design of this circuit will protect the power supply, too, and no additional components would be required. Inverter power supplies can be built in a modular way. Many modules in parallel represent one supply. By installing one spare module per supply one can run the power supply even in the case that one module fails. The input voltage of the supplies usually is 400 V, three phase, 50 Hz, but it is conceivable to allow an input voltage up to 1000 V, which would further reduce the transfer losses in the tunnel.

Multiplying the number for the power supply efficiency of 92% with the number for the pulse efficiency of 77% one gets a total modulator efficiency of 71% from wall plug to the klystron. Assuming the klystron efficiency of 55%, the power demand from wall plug per modulator is 54 kW.

As for the modulators at the test facility the power for the auxiliaries is not included in this number. The power required by the auxiliaries is given in Table 4.2.8. The power for a solenoid is not included, because it is assumed that a klystron for a linear collider would be PPM focused.

The modulator would basically consist of three main components, the PFN unit with the pulse transformer tank, the HV power supply and a local control unit.

The size of the PFN unit would be approximately the same as for the modulators for the test facility. The mounting of the different components in the cabinet could be done in almost the same way as for the modulator at test facilty. The PFN unit at the test facility was built with a safety margin for the distances of the high voltage components, which allows to increase the voltage. The same holds for the pulse transformer tank. In any case, both components must be transportable in the tunnel via the installed transport system.

	SBTF	**LC**
rf pulse length	3.0 μsec	2.8 μsec
Klystron efficiency	45 %	55 %
electric efficiency AC to HV flat top	58 %	77 %
power required for HV production	86 kW	54 kW
Klystron filament	1.3 kW	1.3 kW
Thyratron filament and reservoir	1 kW	0.5 kW
Core bias power supply	0.3 kW	0.3 kW
Solenoid	15 kW	–
Other	2 kW	2 kW
Total	19.6 kW	4.1 kW

Table 4.2.8: *Power demands for the high voltage supply of the klystron as well as the auxiliaries of the line type modulator at the S-Band test facility and the modulator foreseen for the Linear Collider. The number listed under SBTF (S-Band Test Facility) have been achieved up to date.*

The power supply fits in one nineteen inch rack of 2.5 m height. It is also conceivable that one uses two of the racks with reduced height if more space is required. Existing supplies operating at the same power level confirm these assumptions.

The control unit has to take the auxiliary supplies and the programmable logic controller for the interlock. Two nineteen inch racks are required for the installation.

A possible setup of a future line type modulator is shown in Fig. 4.2.28.

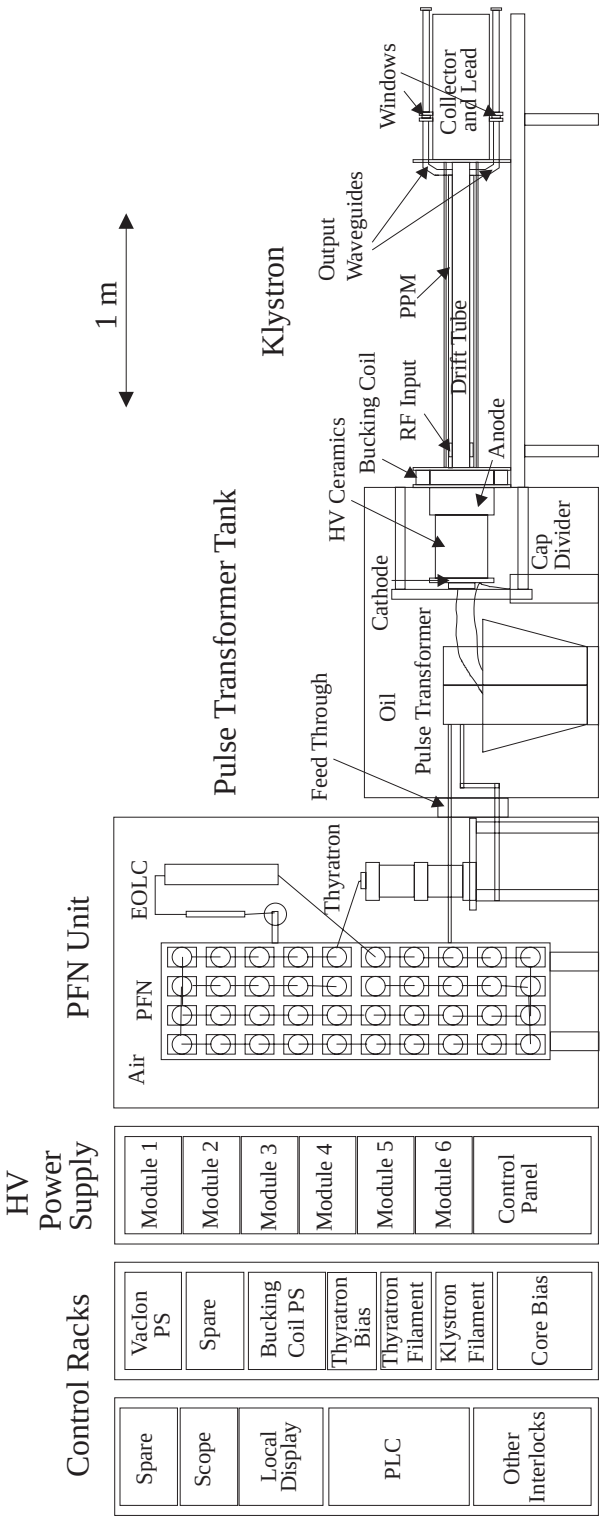

Figure 4.2.28: *Possible setup of a future line type modulator*

4.2.7 Rf Drive System

Description of the Problem In a linear collider, the drive line is the power feed line which is used to excite the high power klystrons, along the linac tunnel. In the proposed 500 GeV center of mass S-Band linear collider, 2500 klystrons will require approximately 400 W drive power each. These klystrons are distributed along the 30 km long accelerator. Therefore approximately every 12 m the drive line has to deliver this amount of power with the appropriate phase and amplitude control within one pulse and with the required pulse to pulse stability.

So far different ideas have been discussed to solve this problem. For example, a low power glass fiber could be used to drive a solid state preamplifer in front of every klystron, or a special drive klystron could power groups of klystrons. While the first version turns out to be a rather cost intensive one, it has certainly the greatest flexibility, because the low power rf can be manipulated in front of every klystron. The second version is certainly cheaper but also requires a widely distributed rf control network. Both systems involve a dedicated distribution system for the low power rf and consist of a large number of components which tend to fail or have to be replaced according to the lifetime.

Therefore a technical solution will be discussed which is based on the idea of using a single high power drive line for many klystrons. This drive line would be powered by the same type of klystron used to feed the accelerating structures (150 MW peak power) and is a passive system which should not require any maintenance. Such a drive line system has a number of drawbacks but also many advantages.

The main problem of a very long drive line is dispersion and energy propagation velocity. The rf pulse which fills the accelerating structure and accelerates the beam is only 2.8 μs ($\approx$ 900 m) long. To excite every klystron in time, the drive pulse has to travel with the speed of the beam pulse, here the velocity of light, along the linac. At the same time the pulse shape (amplitude and phase) is not allowed to change (mainly due to dispersion and mode conversion), especially if phase or amplitude modulation is used within each single rf pulse.

Ridge waveguide as a drive line A drive line concept based on a ridge waveguide [40], see Fig. 4.2.29, has been developed which allows a large number of the high power klystrons to be fed with a single drive line. This type of waveguide fulfills requirements which are necessary for a drive line, namely, low losses, low signal distortion due to dispersion and good suppression of higher order modes. With this concept it should be possible to cover at least a length of 3 km with a single drive line if one of the high power klystrons is used to generate the drive signal.

Dispersion In a waveguide which does not support a TEM mode, signal distortion occurs due to the non-linear frequency dependence of the propagation constant β. Different portions of the signal travel with different velocities so that the output signal becomes dispersed. Nevertheless, for narrow band signals β may be approximated by a linear function throughout the frequency band of interest. In this case the transmitted

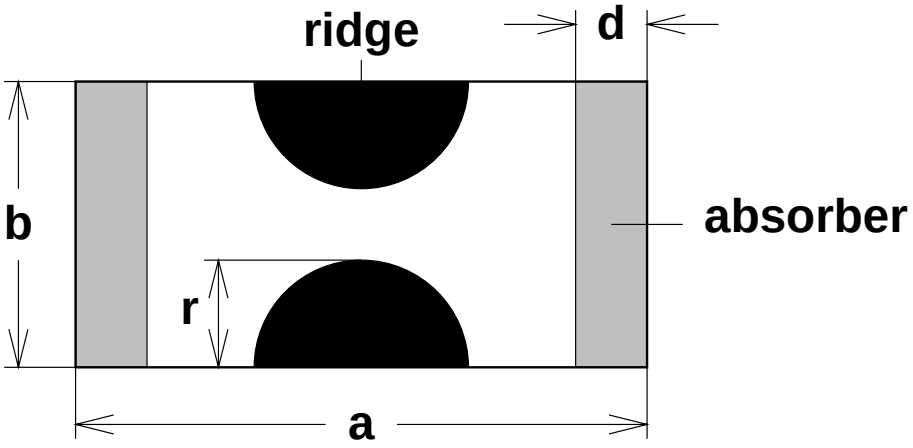

Figure 4.2.29: Cross section of a ridge waveguide with circular ridges and absorbers at the side walls.

signal is identical to the input signal, apart from the amplitude and a time delay. Let us assume a bandwidth of 1 MHz and a group velocity of $v_{gr} = 98\% \cdot c_0$. With these parameters and a length of the drive line of 3 km, one obtains a transmission time error of about 0.15 ns which is small compared to the rf pulse length. From this point of view an even larger dispersion (lower group velocity) would be permissible.

Nevertheless one has to keep in mind that, if the group velocity is smaller than the velocity of light, delay lines with well-defined length have to be inserted between the drive line and each individual klystron feed, in order to keep the drive pulse synchronous to the particles. In our case, the length of the first delay line is 60 m whereas the last klystron feed is directly connected to the drive line. In between, the length of the delay lines has to be linearly decreased. For practical reasons one would realize the delay lines as coaxial cables which unfortunately suffer from a high damping, typically 0.4 dB/m. Hence the first delay line leads to an additional damping of 24 dB which is not serious because the full klystron power of 150 MW is available at the beginning of the drive line.

Suppression of higher order modes In order to keep the signal delay and dispersion small it cannot be avoided to use a highly overmoded waveguide. Two serious effects arise from the excitation of higher order modes. Obviously some of the power in the fundamental mode is lost if it is converted into other modes with higher damping. The second more serious effect gives rise to signal distortion if the fundamental mode is converted into higher order modes and some of the power of these modes is converted back into the fundamental mode at a position farther along the waveguide. In order to avoid signal distortion by conversion and re-conversion the undesired modes have to be suppressed (attenuated) to avoid re-conversion.

Nevertheless such an overmoded waveguide may be used if one can control the higher order modes. In a ridge waveguide, the electro-magnetic field of the fundamental mode is concentrated in the vicinity of the ridges whereas higher order modes extend

Mode	Case 1	Case 2	Case 3	Case 4
α_f in dB/km	7.11	3.29	8.04	9.66
α_{h1} in dB/km	6.71	$3.93{\cdot}10^3$	$1.94{\cdot}10^1$	$4.15{\cdot}10^1$
α_{h2} in dB/km	6.85	$3.95{\cdot}10^3$	$1.96{\cdot}10^1$	$4.18{\cdot}10^1$
α_{h3} in dB/km	6.14	$3.51{\cdot}10^1$	$1.29{\cdot}10^1$	$2.50{\cdot}10^1$
α_{h4} in dB/km	9.93	$8.28{\cdot}10^1$	$2.52{\cdot}10^1$	$5.20{\cdot}10^1$
α_{h5} in dB/km	$1.18{\cdot}10^1$	$1.91{\cdot}10^3$	$2.81{\cdot}10^1$	$5.67{\cdot}10^1$
α_{h6} in dB/km	$1.12{\cdot}10^1$	$1.94{\cdot}10^3$	$2.80{\cdot}10^1$	$5.74{\cdot}10^1$
α_{h7} in dB/km	$3.00{\cdot}10^1$	$4.12{\cdot}10^3$	$8.15{\cdot}10^1$	$1.71{\cdot}10^2$
α_{h8} in dB/km	$3.09{\cdot}10^1$	$4.20{\cdot}10^3$	$8.42{\cdot}10^1$	$1.77{\cdot}10^2$
α_{h9} in dB/km	$2.53{\cdot}10^1$	$7.01{\cdot}10^2$	$6.07{\cdot}10^1$	$1.23{\cdot}10^2$

Table 4.2.9: Attenuation constants α_f and $\alpha_{h1} \ldots \alpha_{h9}$ for the fundamental mode and the propagating higher order modes, respectively, of a ridge waveguide.
Case 1: Empty drive line made of copper (Conductivity= $5.8 \cdot 10^7$ S/m).
Case 2: Additional damping due to absorbers at the side walls.
Case 3: Steel shielding (Conductivity = $0.5 \cdot 10^7$S/m).
Case 4: Kanthal shielding (Conductivity = $0.1 \cdot 10^7$S/m).

throughout the cross section of the waveguide. Hence these modes can be suppressed by suitable absorbers located at the side walls. A similar effect can also be achieved by lossy side walls made of steel or Kanthal.

Numerical results A ridge waveguide with shielding dimensions of ($a = 200$ mm) $\times$ ($b = 100$ mm) and a ridge radius of $r = 33$ mm is assumed. Due to the high field strength in a drive line it is not recommended to use rectangular ridges which may lead to discharge at the sharp edges. Instead of this, circular ridges seem to be most suitable. Figs. 4.2.30–4.2.33 show the transverse field distributions of the four propagating modes with the lowest cutoff frequencies which have been computed with the MAFIA program package [4]. Keeping in mind that the density of the field lines is proportional to the field strength, Fig. 4.2.30 demonstrates that the fundamental mode is well concentrated at the ridges. The group velocity of this mode amounts to $98.4\% \cdot c_0$ which means that for a 3 km long drive line a coaxial delay line of 48 m, see Fig. 4.2.34, has to be used at the first klystron feed (corresponding to an insertion loss of 19.2 dB).

In Table 4.2.9 the attenuation of the fundamental and the propagating higher order modes is presented for various cases. Case 1 means that we consider an empty drive line completely made of copper. The attenuation of the dominant mode amounts to 7.11 dB/km which corresponds to a damping of 21.3 dB for a 3 km long drive line. Note that in the empty ridge waveguide the attenuation of the some higher order modes is approximately the same or even less than that of the fundamental mode. The situation changes completely if we insert a lossy material at the side walls of the shielding. Two

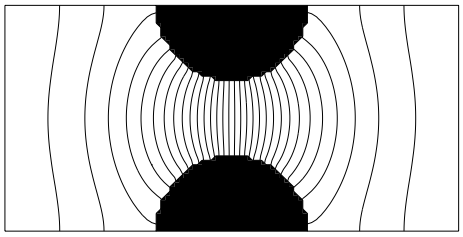

Figure 4.2.30: First TE mode.

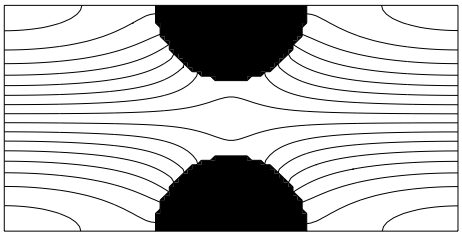

Figure 4.2.31: Second TE mode.

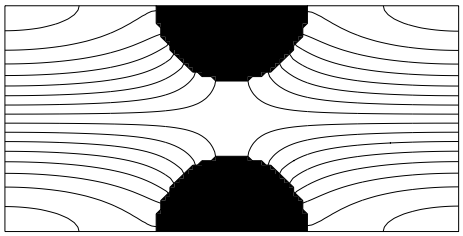

Figure 4.2.32: Third TE mode.

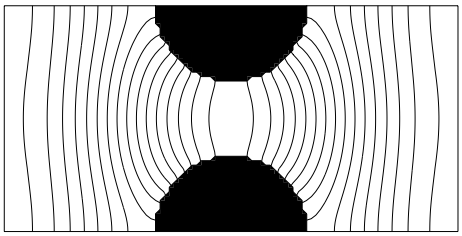

Figure 4.2.33: Fourth TE mode.

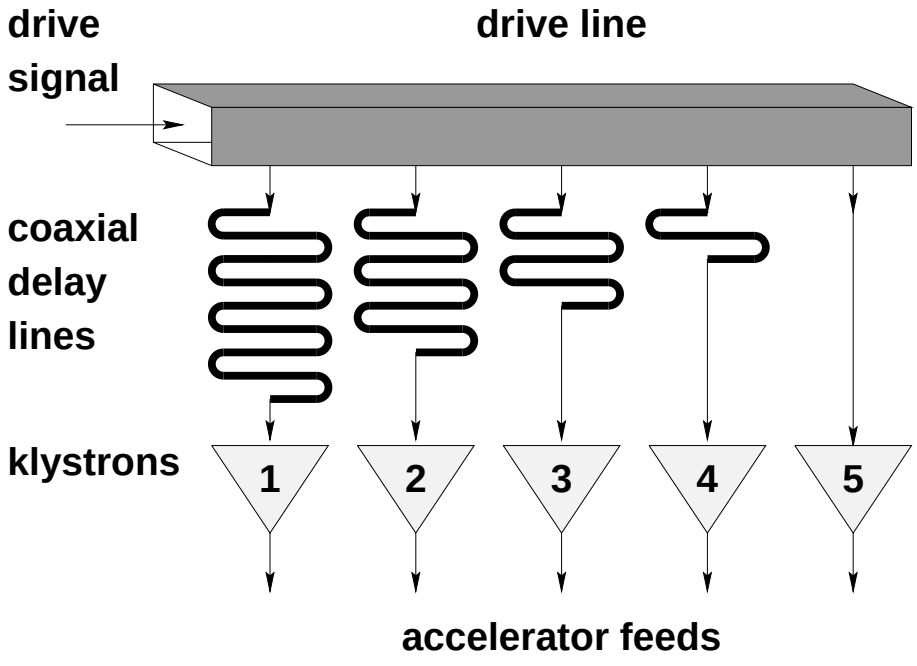

Figure 4.2.34: Schematic drawing of a drive line system with five feeds in which the group velocity of the drive line is less than the velocity of light.

absorbers with a thickness of $d = 4\,\mathrm{mm}$ and a loss tangent of 0.2 are assumed (case 2). Table 4.2.9 gives the additional damping due to the absorbers. The attenuation of the fundamental mode is increased by only 3.29 dB/km whereas the absorbers give rise to a damping of the higher order modes of at least 35.1 dB/km (third higher order mode) which seems to be strong enough in order to guarantee mode stability.

Since it may be difficult to find absorbers which simultaneously satisfy the high power and the vacuum requirements, it has also been investigated whether a sufficient suppression of higher order modes can be achieved by a lossy shielding, i.e., a shielding made of steel or Kanthal. Results for a ridge waveguide with a steel shielding are also given in Table 4.2.9 (case 3). The ridge is still assumed to be made of copper. The numbers presented in Table 4.2.9 demonstrate that the steel shielding has only a minor influence on the damping of the fundamental mode whereas the attenuation of the higher order modes is significantly increased. Nevertheless the mode selectivity is not nearly as good as with the absorbers. In order to get a sufficient damping of the higher order modes the conductivity of the shielding has to be further decreased. With a conductivity of $0.1 \cdot 10^7 \mathrm{S/m}$ an acceptable suppression of the higher order modes can be obtained (case 4).

In any case, the overall damping of a 3 km long drive line amounts to approximately 30 dB. In order to keep the mode conversion small at the klystron feeds, the coupling at each individual feed should not exceed $-20\,\mathrm{dB}$ leading to an total attenuation of about 50 dB which is tolerable.

4.2.8 SLED Pulse Compressor Option

In our reference design two six meter long accelerating structures are directly powered by one klystron. With this set-up a loaded gradient of 17 MV/m is achieved at a design beam pulse length of $2\,\mu\mathrm{s}$. In this section, we discuss the option of using a pulse compression system (SLED) which enhances the rf-peak power at the structures at the expense of shortening the pulse length. The operation of such a system has been calculated elsewhere in detail and proven by measurements at many accelerator laboratories around the world [41]–[45]. In the particular case considered here, one klystron still feeds two six meter long structures. Nevertheless a higher loaded gradient is achieved and thus an energy upgrade of the collider is realised without the need to increase the number of pulsed rf-sources.

The SLED concept uses two additional storage cavities with a high quality factor which are charged over the first part of the klystron pulse. Then the klystron phase is switched by 180deg and the field energy is extracted from the cavity. Fig. 4.2.35 shows the principle behavior of the SLED system with the respective field, cavity charging and accelerating voltage as a function of time. In Fig. 4.2.35, an rf pulse width of $3\,\mu\mathrm{s}$ is assumed. After $2.2\,\mu\mathrm{s}$ of operation, the phase switch of the klystron takes place. Taking into account beam loading compensation (see next section), the beam pulse can use approximately $0.5\mu\mathrm{s}$ of the remaining $0.8\,\mu\mathrm{s}$ rf-pulse, delivering a beam energy width of approximately 10 percent by compensating the rising part of the accelerating voltage with the negative slope of the beam loading. The higher rf-peak power allows

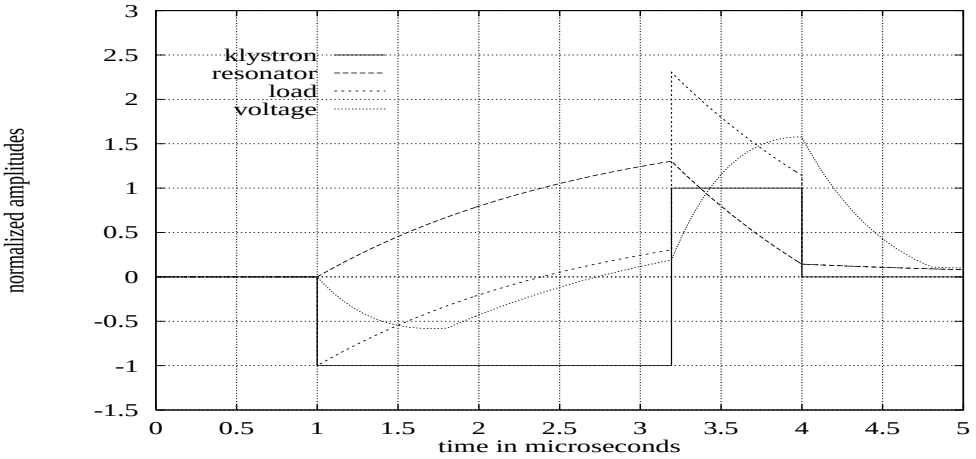

Figure 4.2.35: *Principle operation of the SLED cavity system. All curves show the field amplitudes normalized to the klystron field amplitude which itself is normalized to one. "Load" here means the rf field going to the accelerating structure and "voltage" the integrated acclerating voltage as a function of time.*

SLED cavity parameters		
resonant frequency	GHz	2.998
unloaded Q		180 000
coupling coefficient		13
beam parameters		
number of e^- per bunch		$1.2{\cdot}10^{10}$
bunch to bunch distance	nsec	4
number of bunches		125
performance		
minimum average loaded gradient	MV/m	27.5

Table 4.2.10: *Parameters used for the simulation and gradient achieved with the SLED cavity system.*

to increase the beam pulse current, keeping the fractional beamloading approximately constant. In the simulation we assume a train of 125 bunches with a bunch to bunch distance of 4 ns and a charge of $1.2 \cdot 10^{10}$.

The performance of the proposed SLED cavity system is described in Table 4.2.10 assuming standard parameters for the section and the klystron. The original pulse compressor used at SLAC [41] is based on cavities with $Q_0 = 115000$. In this proposal, cavities with $Q_0 = 180000$ are suggested. In [43], the performance of a cylindrical TE_{038}-cavity with the required properties has already been realized. It turned out that

the main problem in the design of such a cavity is, to find an operating mode which is far enough separated from other modes in order to guarantee stable operation.

As shown in Table 4.2.10, a minimum loaded gradient of 27.5 MV/m can be achieved with the proposed SLED system, about a factor of 1.6 higher than for the design without SLED. It should also be taken into account, though, that the overall power transfer efficiency is lower by about a factor of 0.6 compared to the reference design.

4.2.9 Beam Loading Compensation

Description of the Problem For normal conducting linear colliders (compare [46]) the transient beam loading in the accelerating structures is typically of the order of 20-30 %. This results in a multi-bunch energy spread if no cure is foreseen. On the other hand, in a linear collider the transient energy spread has to be controlled down to a few tenths of a percent.

In this section two methods which are suitable for a sufficient compensation of the multi-bunch energy spread are presented, namely, amplitude and phase modulation of the klystron pulse. Both methods can be used with and without SLED system. Since either concept suffers from specific disadvantages, e.g., two drive lines are required for the phase modulation approach, it has not yet been decided which method is to be used. A final decision will be taken based upon measurements on the test facility.

Energy Spread Compensation with the SLED System Let us consider a set-up with SLED system first. In such a scheme the end of the bunch train typically fits the end of the rf pulse. In general, for a given pulse train length which has to be significantly shorter than the decay time of the SLED cavity, there is always a specific current per pulse in order to achieve the same energy at the beginning and the end of the current pulse while in the middle the energy is higher by several percent. For the parameters used here the energy spread remains to be of the order of 10 % for a beam current of $\approx$ 500 mA. Solutions to further reduce the energy spread have been discussed and published already [47, 48]. A typical result is presented in Fig. 4.2.36 using amplitude modulation, where the klystron amplitude is reduced by $\approx$ 30 % and linearly step by step ramped back to the maximum value towards the end of the pulse. In this case, the resulting energy spread is less than 0.2 %.

In a set-up where no SLED cavity is used and the beam pulse is comparable or longer than the filling time of the section, the amplitude ramp would start at the beginning of the rf pulse. A linear amplitude ramp almost perfectly compensates the beam loading of a constant current pulse in a constant gradient section with constant shunt impedance per unit length. This can be seen in Fig. 4.2.38. The rf amplitude (normalized to the maximum amplitude; solid line) and the rf phase (normalized to π; dashed line) are given in the upper graph, while the lower shows the unloaded and loaded accelerating gradient with a beam pulse switched on after one filling time. In the calculation presented in Fig. 4.2.38, the amplitude starts at 23 % of the maximum value. The resulting total energy spread over the bunch train lenght is better than 0.1 % and limited by errors due to the amplitude modulation and klystron power jitter

within the pulse. For the case presented in fig. 4.2.36 the resulting energy spread is shown in fig. 4.2.37.

In general, continuous amplitude modulation has the disadvantage of operating the klystron not saturated. This enhances the amplitude and phase jitter which has a negative impact on the performance during the ramp. For a detailed study assumptions on the flatness of the amplitude have to be made and measurements using the test facility are required.

Energy Spread Compensation with two Anti-Phased Klystrons A second method for compensating the transient beam loading will be investigated here. Going off crest in two succeeding klystron stations towards a phase angle (klystron n: $+\phi$ and klystron n+1: $-\phi$) will compensate the beam loading at every station and compensates the single bunch energy spread over two stations. Following this strategy, the single bunch energy spread is increased at station n but already compensated at station n+1. The residual effect on the beam emittance from chromatic dilution is estimated to be negligible.

Although it is not foreseen here, even the single bunch energy spread can be compensated using this scheme, as has been described in detail in [49].

Technically the method can be applied by introducing a phase ramp. While the phase of the electric field stored in the section is still at an average phase angle the phase ramp starts travelling through the section over the filling time, comparable to the filling of the section with beam induced field. In Fig. 4.2.39, the rf amplitude (normalized to the maximum amplitude) and the rf phase (normalized to π) are given in the upper graph, while the lower shows the unloaded and loaded accelerating gradient with a beam pulse switched on after one filling time. Here the klystron amplitude is always at the maximum and the klystron operates saturated. Again the resulting energy spread (for bunch nr. 1 and for a bunch after reaching stady state conditions) is shown in figure

Technical Impacts For both methods proposed to compensate the transient beam loading, it is obvious that control for the drive power or the drive phase of the klystrons is required. From the results presented here it is obvious as well, that the drive signal is either the same for all klystrons (compare method 1 used with SLED cavities) or two classes of klystrons (with $\pm\phi_{off}$) with equal drive signals are existing. Therefore one common drive line for one linac (or two drive lines for one linac) could in principle be used and the control problem with the operation and drive for more than thousand klystrons per linac could be reduced by orders of magnitude.

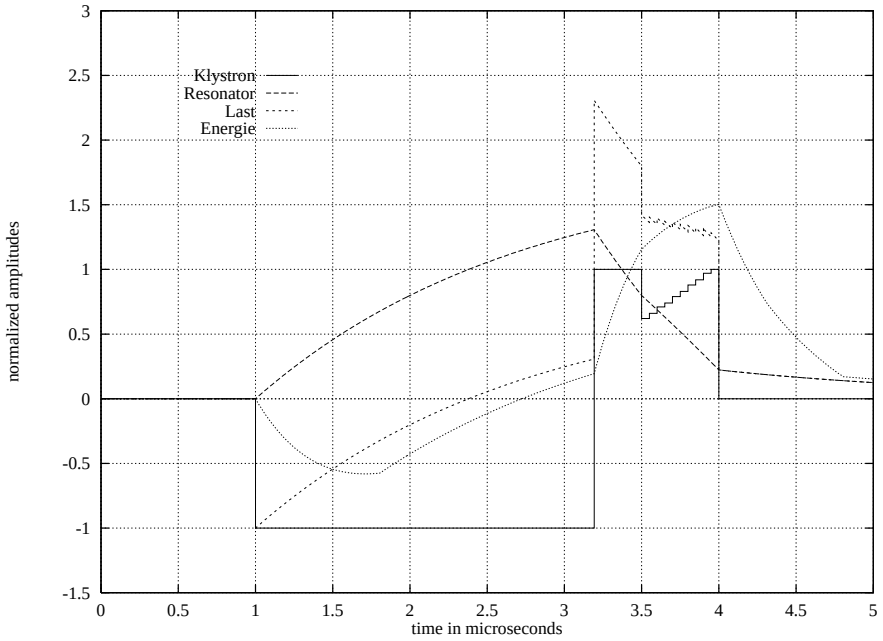

Figure 4.2.36: *Amplitude modulation for optimum compensation of the transient beam loading. The amplitude is reduced after injection and linearly step by step ramped back to the maximum value.*

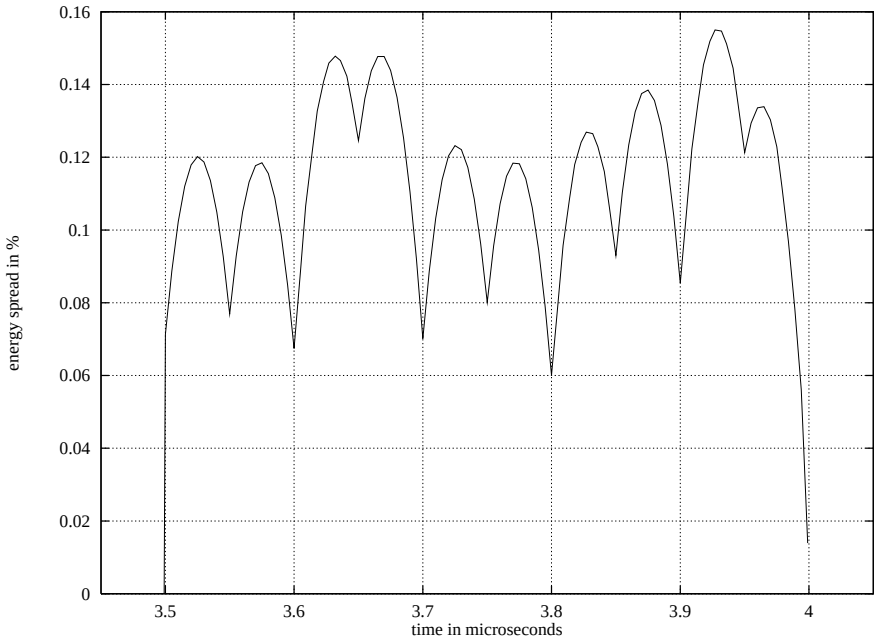

Figure 4.2.37: *The energy spread along the bunch train is shown for the amplitude modulation presented in fig. 4.2.36.*

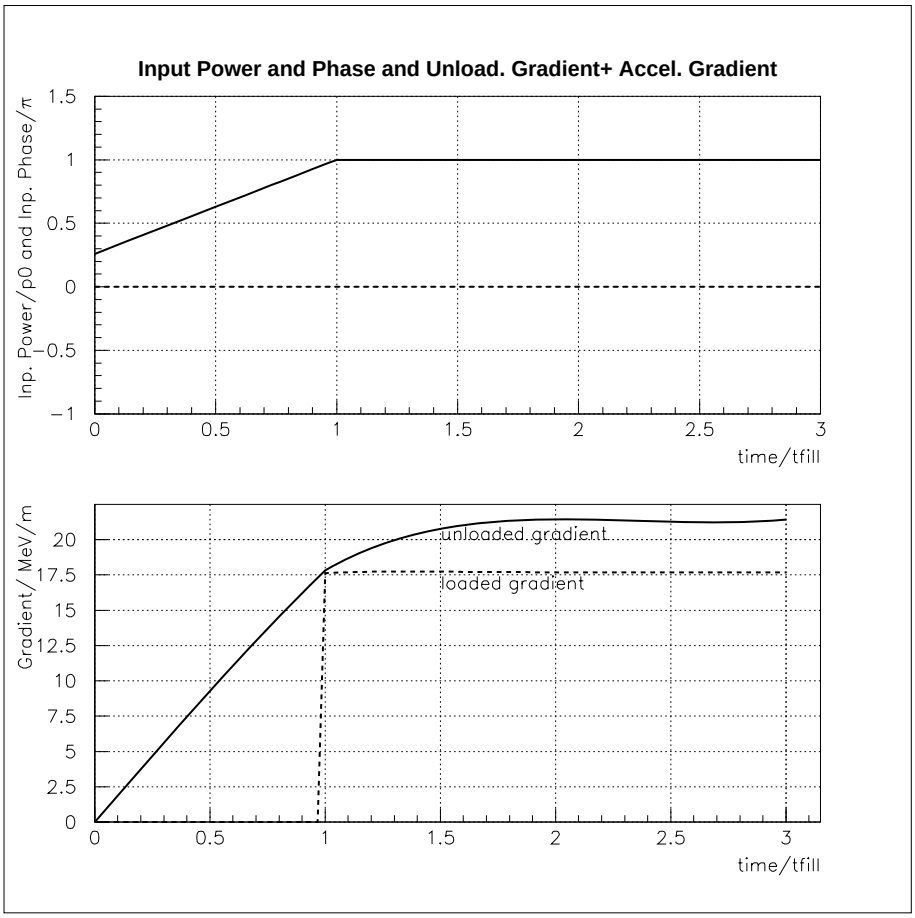

Figure 4.2.38: *Unloaded and loaded gradient with a beam pulse long compared to one filling time and rf amplitude modulation to compensate the beam loading.*

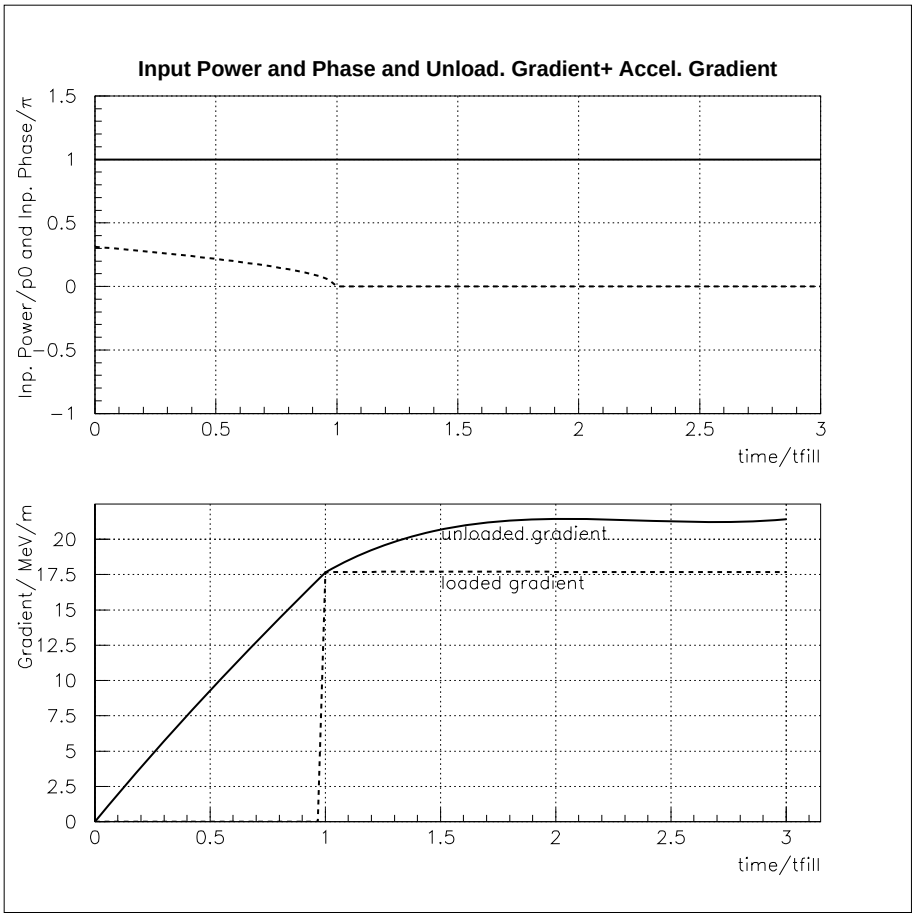

Figure 4.2.39: *Resulting energy spread after phase ramp in front of the accelerating section.*

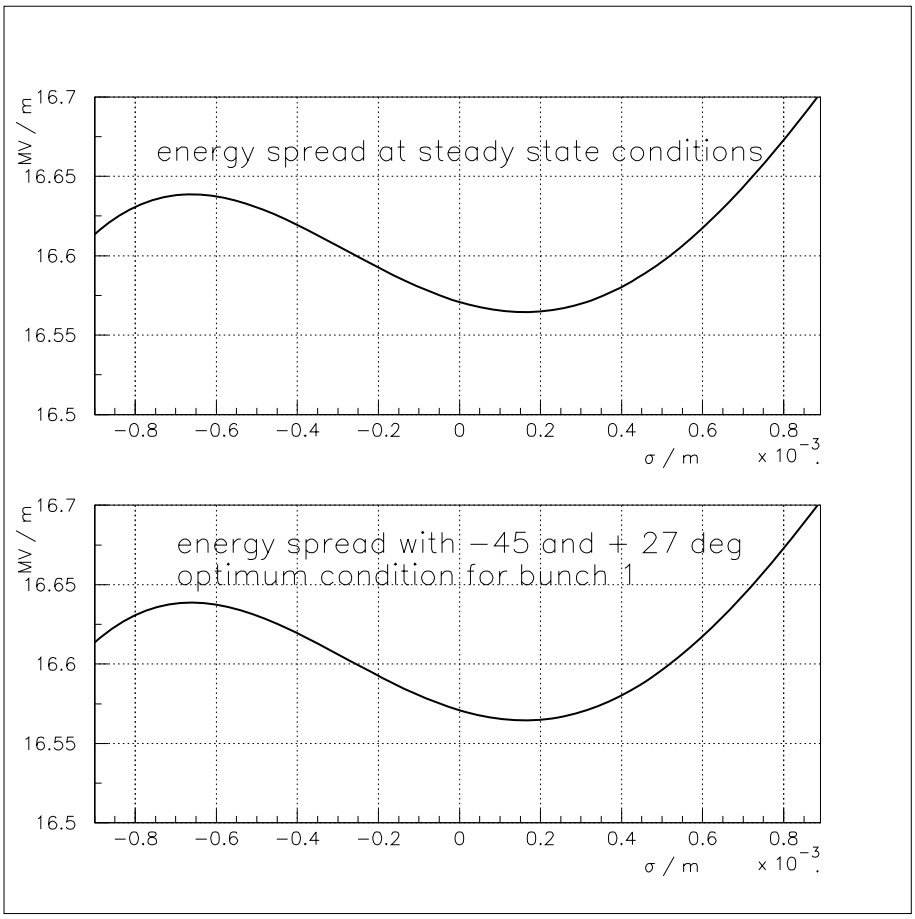

Figure 4.2.40: *The final energy spread for bunch # 1 (start of the rf pulse) and some final bunch after steady state is reached is shown. As can be seen, the single bunch energy width is not disturbed.*

4.2.10 The Quadrupole and Corrector Magnets in the Linac

The linear accelerator will have a FODO structure with 90° phase advance per cell starting from the 3 GeV damping ring towards the end of the linac. While the phase advance per cell is kept constant the FODO cell length changes roughly with the square root of the energy. Overall eight steps are used with a quadrupole magnet between each section in the beginning and having eight accelerating structures in between close to the end of the accelerator. Given a maximum pole tip field of 0.8 T, the length of a quadrupole is given by the high energy end of each of the eight sectors. For optimal beam steering and beam based alignment capabilities, each quadrupole vacuum chamber is equipped with a x/y - strip line beam position monitor, and a **x** as well as a **y** corrector. The correctors are designed with a maximum pole field of 0.1 T which makes air cooling feasible.

The free aperture in the quadrupoles and the correctors is determined by the vacuum chamber diameter. This diameter is constant starting from the cut-off tubes of the accelerating section throughout the quadrupole chamber. This diameter was chosen according to the smallest iris in the section, which allows modes above the cut off frequency of the cut off tube to leave the accelerating structure. These modes travel through the beam pipe and can partly be absorbed at this position or travel into the next strcuture, where the wave will not be in phase with beam any more. The final diameter of the beam pipe is chosen to be 24 mm.

4.2.10.1 The quadrupoles

The quadrupole is a standard magnet with a maximum pole tip field of 0.8 T and an aperture of 24 mm. The necessity to keep the phase advance per FODO cell constant leads to a variation in maximum pole tip fields of not more than a factor of two. Each sector contains one quadrupole type with a given length. The list of quadrupoles and parameters are presented in Table 4.2.11. For the collider and also in the S-Band test facility, quadrupoles are foreseen which have the windings not fixed to the pole but to a separate aluminum support. This support is used to decouple the vibration from water cooling from the pole itself. The concept is described in more detail in 4.8.4.

The total amount of quadrupoles according to Table 4.2.11 is roughly 600 per linac. Every quadrupole will have its own power supply. And the total additional length required for the quadrupoles, the quadrupole chamber and the correctors (one x and one y corrector at every quad) is 600 m over a length of approximately 15 km. Therefore the packing factor is 96% in each of the two linacs. The power consumption per linac will be 1.5 MW for the quadrupoles.

4.2.10.2 The Corrector Magnets

Beside each quadrupole one x and one y corrector magnet is foreseen. The orbit deviation which should be achievable are assumed to be ±5 mm, which is almost the complete aperture of the quadrupoles. The maximum design field is 0.1 T and with approximately 400 windings, the corrector does not need any additional cooling. The

section parameter				
Sector nr	max. Energy	drift space	L_magn	nr. of quads tot
	GeV	m	m	
1	12	0.5	0.14	90
2	27	0.5	0.21	75
3	48	0.8	0.28	70
4	75	1.0	0.34	68
5	108	1.0	0.41	66
6	147	1.5	0.47	65
7	192	1.5	0.53	65
8	250	1.7	0.62	73

Table 4.2.11: *Parameters for the Linac quadrupoles in different sectors of the linear accelerator.*

length of the correctors is different in each sector as well and starts from 0.06 m going up to 0.48 m at the end. Because two correctors per quad are foreseen, 2/3 of the required additional length is determined by the corrector magnets. Optimization could slightly reduce this factor at the expense of more electrical power or less kick strength, especially towards the end of the linac, if the x/y corrector winding are on one yoke. So far two separate correctors are foreseen. So far a simple C-type dipole corrector is assumed. In total 1200 corrector magnets are required per linac.

An additional possibility which has not been investigated in detail, is to mount the quadrupole magnets on micro-movers. These micro movers are comparable to those for the FFTB [50]. This way space otherwise necessary for correction coils can be saved. A cost comparison between the two possibilities is needed before a conclusion can be drawn.

Bibliography

[1] H. Matsumoto et al, *Applications of Hot Isostatic Pressing (HIP) for High Gradient Accelerator Structure*, Proc. 1991 Part. Acc. Conf. 1008-1010, San Francisco (CA), 1991. and H. Matsumoto et al, *Dark Currents*, Proc. of the 1996 Linac Conference, CERN, Geneva 1996, to be published.

[2] W. Schwarz, *Vermessungsverfahren im Maschinen– und Anlagenbau.* Vermessungswesen bei Konrad Wittwer, Band 28, Konrad Wittwer Verlag, Stuttgart 1995.

[3] W. Schwarz, *Straightness Measurements for Accelerator Structures*, In: Proceedings of International Workshop on Accelerator Alignment, Nov. 14–17, 1995 at KEK, Tsukuba, Japan.

[4] R.B.Neal, editor: *The Stanford Two-Mile Accelerator*, Stanford University, W.A. Benjamin, Inc., New York, 1968.

[5] S.Ivanov, M.Dohlus: *Investigation of Field Asymmetries in the Asymmetric Input Coupler of the e+e- Injector Linac at DESY*, Internal Report, DESY M-95-01, January 1995.

[6] H.Deruyter, H.Hoag, K.Ko, C.Ng: *Symmetrical Double Input Coupler Developement*, SLAC-PUB-5887, August 1992.

[7] V.E.Kaljuzhny, N.Sobenin, M.Dohlus, N.Holtkamp et al., *Design and Performance of a Symmetric High Power Coupler for a 6 Meter S-Band Linear Collider Accelerating Structure*, Internal Report, DESY M-94-11, Oktober 1994.

[8] V.E.Kaljuzhny, N.Sobenin, M.Dohlus, N.Holtkamp et. al: *Investigation of a Hybrid Coupler for a 6 Meter S-band Linear Collider Accelerating Structure*, Internal Report, DESY M 96-05, April 1996.

[9] M. Dohlus: *Long range Dipole Wake in a 180 Cell Traveling Wave Section*, Internal Report, to be published.

[10] Ulla v. Rienen: *Higher Order Mode Analysis of Tapered Disc-Loaded Waveguides Using the Mode Matching Technique*, Particle Accelerators, 1993, Vol 41, pp. 173-201.

[11] THE S BAND 36 CELL EXPERIMENT. B. Krietenstein et al, *The S-Band 36 Cell Experiment* DESY-M-95-08T, Jun 1995. 3pp. Presented at 16th IEEE Particle Accelerator Conference (PAC 95) and International Conference on High Energy Accelerators (IUPAP), Dallas, Texas, May 1995.

[12] K.Bane, R.Gluckstern: *The Transverse Wakefield of a Detuned X-Band Accelerator Structure*, SLAC-PUB-5783, March 1992.

[13] M.Yamamoto: *Analysis of Detuned Structure by Open Mode Expansion*, LC95, Tsukuba, Japan, March 1995.

[14] C.Adolphsen et. al.: *Measurement of Wakefield Suppression in a Detuned X-Band Accelerator Structure*, Proceedings of the 17th International Linear Accelerator Conference, Tsukuba, Japan, August 21-26, 1994.

[15] K.Thompson et. al.: *Design and Simulation of Accelerating Structures for Future Linear Colliders*, Particle Accelerators, Vol 47, pp 65-109, 1994.

[16] R. Brinkmann, M. Drevlak and R.Wanzenberg, *Improved Beam Stability with New Parameter Set for the S-Band Linear Collider*, LINAC96, Geneva, August 1996.

[17] N. Kroll (UC, San Diego), K. Thompson, K. Bane (SLAC), R. Gluckstern (Maryland U.), K. Ko, R. Miller, R. Ruth (SLAC), *Higher Order Mode Damping for a Detuned Structure*, SLAC-PUB-6624, Aug 1994. 4pp. Contributed to 17th International Linear Accelerator Conference (LINAC 94), Tsukuba, Japan, 21-26 Aug. 1994.

[18] A.Jöstingmeier, M.Dohlus, C.Rieckmann, *Application of the Generalized Scattering Matrix Method and Time Domain Computation of the Transverse Long Range Wake in Linear Accelerator Structures*, to be published.

[19] J. Haimson, *High Duty Factor Electron Linear Accelerators*, Linear Accelerators, P. Lapostolle, A. Septier, North holland Publishing Company, Amsterdam, 1970.

[20] M.Dohlus, *Higher Order Mode Damping by Artificially Increased Surface losses* , Martin Dohlus, DESY Report, to be published.

[21] M. Dohlus, H. Hartwig, N. Holtkamp (DESY), K. Jin (Hefei, NSRL), A. Jostingmeier (DESY), V. Kalyuzhny (Moscow Phys. Eng. Inst.), A. Naboka, A. Vasyuchenko (Moscow, INR), S. Yarigin (Moscow Phys. Eng. Inst.), *High Power Test of the Iris Coating in the S-Band Linear Collider*, DESY-M-96-19, Sept. 1996.

[22] M. Dohlus, M. Marx, N. Holtkamp, P. Hülsmann, W.F.O. Müller, M. Kurz, H.-W. Glock, H. Klein: *S-Band HOM-Damper Calculations and Experiments*, Particle Accelerator Conference and International Conf. on High-Energy Accelerators, Dallas (Texas), May 1995.

[23] C. Peschke, Peter Hülsmann, W.F.O. Müller, H. Klein: *Beam Position Monitoring for SBLC Using HOM-Coupler Signals*; proceedings of the 5th European Particle Accelerator Conference (EPAC 96), Sitges (Spain), 1996

[24] V. Balakin, et al., Phys. Rev. Lett. **74**(1995)2479.
G. Bowden, et al., SLAC-PUB-6132 (1995).

[25] U. Ristau, *Optimierung und Automation der Positioniereinrichtung Micromover*, Diploma Thesis, Fachhochschule Ostfriesland FHO, Emden (1996).

[26] J. Hamsom, *High duty factor electron linac*, edit. P. Lapostolle, A.Septier, *Linear Accelerators Accelerating Structures Technology* , North Holland Publishing Company, Amsterdam 1980.

[27] J.G. Noomen, N. Geuzebroek, C. Schiebaan, *A Modular Cooling System for the MEA High Duty Factor Electron Linac*, IEEE Transactions on Nuclear Science, Vol. NS-28, No. 3, June 1981.

[28] R.F. Koontz, T.G. Lee, C. Pearson, A.E. Vlieks (SLAC), *Recent Performance, Lifetime, and Failure Modes of the 5045 Klystron Population at SLAC*, SLAC-PUB-5890, Aug 1992. 3pp, Presented at LINAC 92, Ottawa, Canada, 24-28 Aug 1992.

[29] T.G. Lee, J. V. Lebacqs, G.T. Konrad, *A Fifty Megawatt Klystron for the Stanford Linear Collider*, SLAC-Pub-3214, September 1983.

[30] T.G. Lee, G.T. Konrad, Y. Okazaki, M. Watanabe, H. Yonezawa,*The Design and Performance of a 150 MW Klystron at S-Band*, SLAC-PUB-3619, April 1985.

[31] D. Sprehn, R.M. Phillips, G. Caryotakis, *Performance of a 150-MW S-Band Klystron*, AIP Conference Proceedings 337, Pulsed RF Sources for Linear Colliders, Montauk, NY 1994, p. 43.

[32] D. Sprehn, *Final Report on the Development of a 150-MW S-Band Klystron*, to be published in Proceedings of Pulsed RF Sources for Linear Colliders, Shonan Village Center, Hayama, Kamagawa, Japan, April 8 -12, 1996.

[33] G.J. Faillon, *Short Presentation on High Peak Power TH 2153 Klystrons*, to be published in Proceedings of Pulsed RF Sources for Linear Colliders, Shonan Village Center, Hayama, Kamagawa, Japan, April 8 -12, 1996.

[34] R.B. Palmer, *Linear Collider RF: Introduction and Summary*, AIP Conference Proceedings 337, Pulsed RF Sources for Linear Colliders, Montauk, NY 1994, p. 1.

[35] P.B. Wilson,*Advanced RF Power Sources for Linacs* , to be published in Proceedings of the XVIII International Linac Conference, Linac96, Geneva, Switzerland, 26 -30 August, 1996.

[36] W. Matziol, PHILIPS Semiconductors RHW, Hamburg, *Series Production of High Power Klystrons*, talk given at the 'S-Band Linear Collider Meeting', December 7th to 8th, 1995, not published.

[37] H. Thom, IPEA, Berlin, *Automatic Klystron Exchange in the Linear Collider Tunnel* , study performed in collaboration with DESY, October, 1996, to be published.

[38] A.R. Donaldson, J.C. Cron, R.R. Hanselman, *The Second Generation SLAC Modulator*, SLAC-Pub-3993, June 1986.

[39] S. Choroba, M. Bieler, J. Hameister, Y. Chi,*A 375MW Modulator for a 150MW Klystron at the S-Band Linear Collider Test Facility at DESY*, to be published in Proceedings of the XVIII International Linac Conference, Linac96, Geneva, Switzerland, 26 -30 August, 1996.

[40] A. S. Omar and K. Schünemann, *Analysis of waveguides with metal inserts*, IEEE Trans. Theory Microwave Tech., vol. MTT-37, pp. 1924–1932, 1989.

[41] P.B. Wilson, *SLED: A Method for Doubling SLAC's Energy*, Technical Note SLAC-TN-73-15, 1973.

[42] Z.D. Farkas, *Binary Peak Power Multiplier and its Application to Linear Accelerator Design*, IEEE Trans. Microwave Theory Tech. , volume MTT-34, 1986.

[43] A. Fiebig, R. Hohbach, P. Marchand and J.O. Pearce, *Design Considerations, Construction and Performance of a SLED Type Radio Frequency Pulse Compressor using very high Q Cylindrical Cavities*, CERN-PS/87-45, presented at 1987 Particle Accelerator Conf., Wash., D.C., 1987.

[44] A. Fiebig and C. Schieblich, *A Radio Frequency Pulse Compressor for Square Output Pulses*, Proc. of EPAC, Rome, 1988.

[45] T.L. Lavine, Z.D. Farkas, A. Menegat, R.H. Miller, C. Nantista, G. Spalek and P.B. Wilson, *High-Power Radio-Frequency Binary Pulse-Compression Experiment at SLAC*, Proc. of IEEE Particle Accelerator Conference, San Francisco, 1991.

[46] G. A. Loew (ed.), *International Linear Collider Technical Review Committee Report*, SLAC-R-95-471, 1995.

[47] Z.D. Farkas, *SLEDED SLAC Beam Loading Compensation.*, SLAC–AAS–Note–86, Dec 1994.

[48] Z.D. Farkas, N. Holtkamp, private communication, Jan. 1994.

[49] N. Holtkamp and A. Jöstingmeier, *Multibunch Energy Compensation in Travelling Wave Linear Accelerators*, DESY-06-043, 1996.

[50] G. Bowden et al, *Precision Magnet Movers for the Final Focus Test Beam*, Nucl. Instr. and Meth., A368:579–592, 1996.

4.3 Beam Dynamics

4.3.1 Introduction

The main linac has to provide a beam not only of very high energy but also of very high quality (i.e. high intensity, low emittance, small energy spread). The requirements on the quality of the beam are defined by the demands of the high energy physics experiments at the interaction point. This section will study essentially the emittance preservation of a multi bunch train on its way through the main linac. The generation of a low emittance beam is described in section 4.5, while the collimation of the beam and the final focus system can be found in section 4.7.

The transverse quality of the beam can be degraded by misalignments and vibrations of the main linac components, i.e. accelerating structures and focusing magnets. The misalignment and the resolution of the beam position monitors (BPM) are also very important since this determines the possibilities to control the beam quality by various correction methods. The chromatic effects of the focusing system and the transverse wake effects in the accelerating structures are the physical mechanism of the emittance growth. These effects are studied to determine the alignment and vibration tolerances of the main linac components.

The bunch length is practically frozen in the main linac since the bunch is injected at an energy of 3.15 GeV and is rapidly accelerated to even higher energies. The longitudinal quality of the beam is defined by the energy spread in the bunch. The acceptance of the final focus systems sets a loose upper limit of ± 1.2 % on the tolerable energy spread. A lower energy spread is desirable to minimize chromatic effects and their implications on the transverse quality of the beam, or can arise from high energy physics demands for an extremely narrow energy distribution.

The acceleration of a relatively long bunch train can cause various problems with respect to the stability of the bunch train. A current pulse with 333 bunches and a population of $1.1 \cdot 10^{10}$ Electrons per bunch can excite strong resonant transverse electro-magnetic fields, which can cause cumulative beam break-up, a severe instability first observed at SLAC [1]. Therefore it is an absolute necessity to damp and detune this higher order parasitic modes in the accelerating structure, as described in section 4.2.1. The required amount of damping (Q-values of the modes) are investigated from a beam dynamics view point by computer simulations.

The use of a multi-bunch scheme introduces another complication due to strong transient beam loading which amounts to roughly 20 % energy deviation (peak-to-peak) over the first part of the bunch train if no correction method is applied. The inter-bunch energy spread can be reduced by the control of the amplitude or phase of the rf-pulse to a level of 10^{-3}, see section 4.2.9.

4.3.2 Beam Optics

The beam is focused by quadrupole magnets which are arranged in a FODO lattice. This lattice is characterized by the phase advance per cell and the beta function which

is scaled with the energy along the main linac. Since the normalized emittance of $\gamma\,\epsilon_y = 0.25 \cdot 10^{-6}$ m in the vertical plane, envisaged for the SBLC, is a factor 20-30 smaller than in existing linacs, i.e. the SLC at SLAC [2], the preservation of the emittance is even in the absence of wakefields in the accelerator structures a critical issue. For the SBLC a constant phase advance of $\mu = 90°$ and a scaling of the beta function with the square root of the energy has been adopted:

$$\mu = 90°, \qquad \beta \sim \sqrt{E}.$$

As explained below, a correlated energy spread in the bunch provides a reduction of emittance growth from coherent betatron oscillations by cancelling chromatic with wakefield effects (so-called BNS-damping). With the above choice for the scaling of the beta function, this energy spread is constant along the linac. Generally, the choice of the lattice parameters takes into account a balancing of transverse wakefield and chromatic effects.

	cells	structures		β/m	ΔE/GeV	E /GeV
1	48	$\times 2 =$	96	13.3	9.8	13.1
2	36	$\times 4 =$	144	26.6	15.0	28.1
3	36	$\times 6 =$	216	40.0	22.4	50.5
4	32	$\times 8 =$	256	53.3	26.6	77.1
5	32	$\times 10 =$	320	66.6	33.2	110.3
6	32	$\times 12 =$	384	80.0	39.9	150.2
7	32	$\times 14 =$	448	93.3	46.5	196.7
8	32	$\times 16 =$	512	106.6	53.2	250.0
Σ	280		2376			

Table 4.3.1: *FODO lattice for the SBLC main linac. The linac is divided into eight sections. The beta function is scaled approximately with the square root of the energy.*

Actually, the main linac is divided into 8 section with a constant beta function FODO lattice in each section. The first section is built from FODO cells with one 6 m long accelerator section between the quadrupole magnets, while the eights section has eight 6 m long accelerator sections between the quads. Table 4.3.1 summaries the lattice of the main linac. The number of FODO cells and accelerator sections is given without any overhead for energy management. The energy gains (ΔE) and energies (E) are calculated assuming a loaded gradient of 17.3 MeV/m and an injection energy of 3.15 GeV. The beta function $\bar{\beta}$ is the mean of the beta function in the focusing and defocusing quadrupoles assuming a filling factor of 90 %, i.e. a cell length of about 13.3 m in the first section of the linac. The required qaudrupole strengths, apertures and lengths are discussed in section 4.2.10.

The emittance growth of the bunch train is studied by a tracking code, called L [3], with uses the environment of the program MAFIA [4]. For these simulations a thin

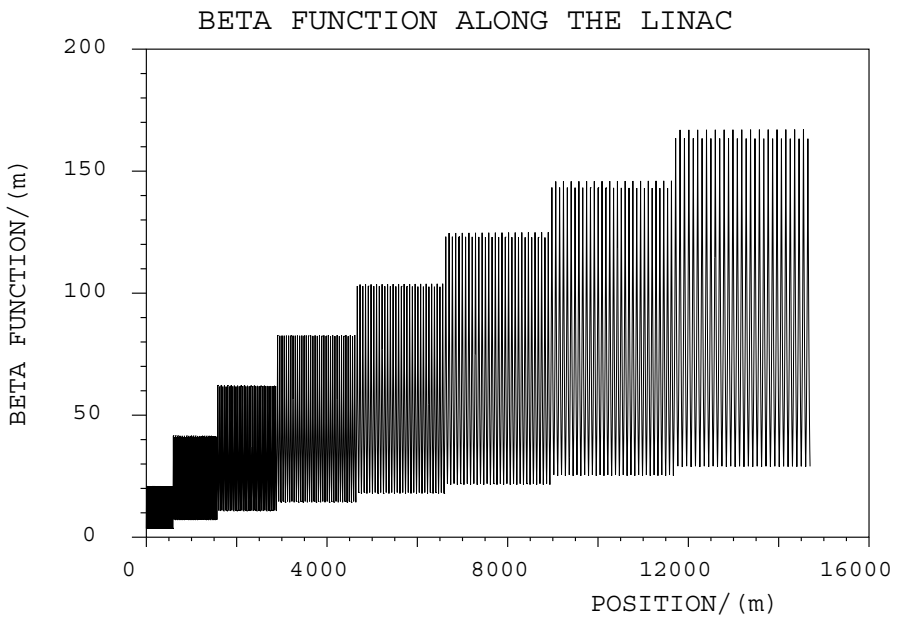

Figure 4.3.1: *Beta function along the SBLC main linac.*

lens FODO lattice is used with ideal telescopic system between the eight sections to match the beta function. Fig. 4.3.1 shows the beta function along the SBLC main linac. One can clearly identify the eight sections of the main linac and the scaling of the beta function with energy.

4.3.3 Wake Fields and Beam Loading

The accelerating structures of the main linac are (normal conducting) traveling wave structures operated in the $2\pi/3$ - mode at a frequency of 2.998 GHz. Each 6 m long section is a 180 cell structure made from "cups" (see Fig. 4.3.2). The cell and iris diameters decrease along the structure in the direction of the beam to achieve a constant accelerating gradient. The power dissipation is constant along the structure. An important characteristic parameter of a constant gradient structure is the attenuation constant τ, which is defined from the ratio of output and input power of the structure and determines dP/dz, the rf power dissipated per unit length:

$$\frac{P_{out}}{P_{in}} = \exp(-2\,\tau), \qquad \frac{dP}{dz} = -P_{in}\,\frac{1-\exp(-2\,\tau)}{l_{sec}}$$

($l_{sec} = 6$ m is the length of an accelerating structure). The attenuation τ, the frequency and the Q-value of accelerating mode directly determine the group velocity of the wave and therefore the iris diameter. The choice of the attenuation $\tau = 0.55$ is a trade off between unwanted effects due to transient beam loading and wakefields and on the other side the required rf-power.

Wakefields are electromagnetic fields due to the interaction of the bunch with the environment, i.e. the accelerating structures. One can distinguish between **short range**

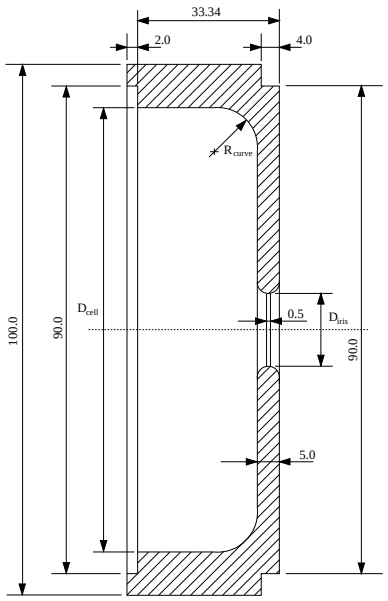

Figure 4.3.2: *One "cup" of a 6 m long accelerating structure. The structure is made from 180 cups (and one end plate) with slightly different cell and iris diameters (D_{cell}, D_{iris}).*

wakefields, which have implications for a single bunch and **long range wakefields**, which could drive instabilities affecting the whole bunch train.

The short range wakefields are numerically calculated by the computer code MAFIA [4] for a 15 cell accelerating structure, which represents the properties of the real 6 m long structure sufficiently [5]. Fig. 4.3.3 shows the longitudinal (short range monopole) wake potential as a function of the position in the bunch. The bunch charge distribution is shown in arbitrary units.

The longitudinal wake fields directly contribute to the energy distribution in one bunch (see Fig. 4.3.4). The change of the energy distribution after one accelerating structure is:

$$\Delta E(s) = G\, l_{sec}\, \cos(\varphi_0 + 2\pi\, f_0\, s/c) \; + N\, e\, W_{||}(s)$$

(G is the accelerating gradient, l_{sec} the length of the accelerating structure, φ_0, f_0 the rf phase and rf frequency). The wake potential multiplied by the bunch charge $N\, e$ is added to the contribution from the accelerating mode which depends on the rf-phase along the bunch.

Transverse (dipole) wakefields are excited if the beam traverses an accelerating structure off axis. The fields excited by the head of the bunch will kick the tail of the bunch even more off axis. The whole bunch may develop a banana shape tail. This can strongly degenerate the emittance of the beam. Fig. 4.3.5 shows the transverse dipole wake potential as calculated with MAFIA [4, 5]. The head of the bunch is on the left side of the figure.

Long range wakefields are a severe concern with respect to instabilities. Dipole modes are trapped in the accelerating structure over several cells. The frequency of the 180 dipole modes of the lowest passband is in the range from 4.1 GHz to 4.6 GHz.

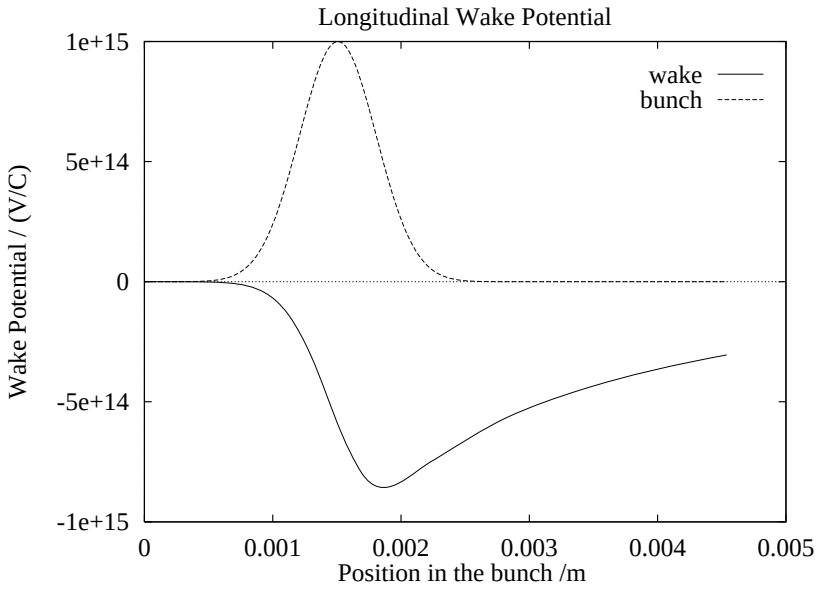

Figure 4.3.3: *Longitudinal mono-pole wake-potential for a 6 m accelerating structure. The Gaussian bunch ($\sigma = 300\mu m$) is shown in arbitrary units. The wake potential is scaled from a MAFIA calculation performed for a 15 cell structure [5].*

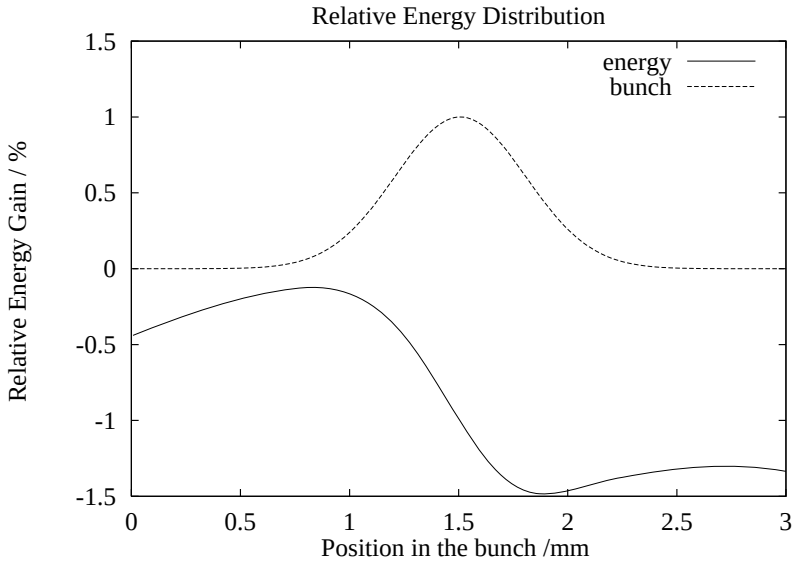

Figure 4.3.4: *Energy spread in the bunch caused by the longitudinal wake field. The bunch center is at $z = 1.5\,mm$. The peak-to-peak and rms energy spread amount to 1.8 % and 0.35 %, respectively.*

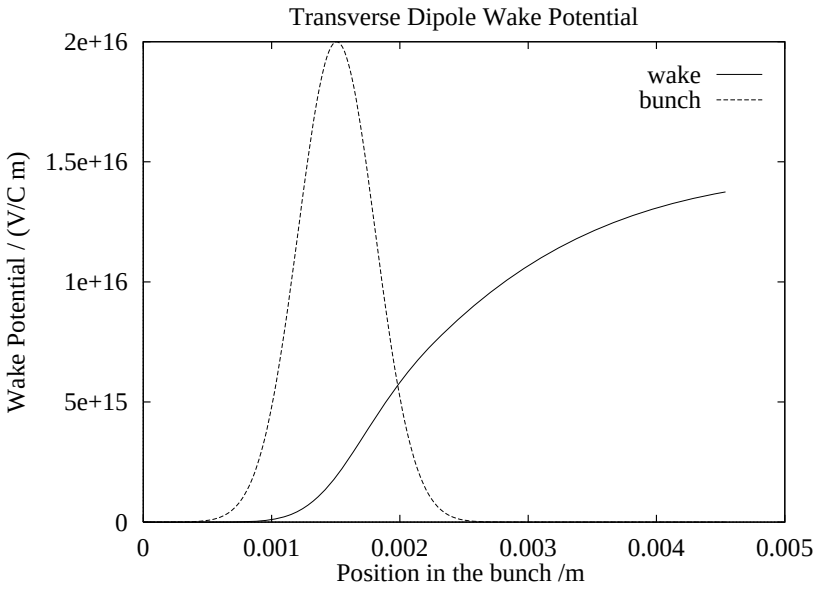

Figure 4.3.5: *Transverse dipole wake-potential for a 6 m accelerating section. The Gaussian bunch ($\sigma = 300\mu m$) is shown in arbitrary units. The wake potential is scaled from a MAFIA calculation performed for a 15 cell structure [5].*

Each mode is characterized by the frequency, the Q-value and the longitudinal loss parameter $k_{||}^{(1)}$. The transverse dipole wake potential can be calculated according to the Panofsky-Wenzel-Theorem [6]:

$$W_{\perp}^{(1)}(s) = \sum_{\text{modes}} 2\,\frac{k_{||}^{(1)}(a)}{a^2}\,\frac{c}{2\pi f}\sin(2\pi f\ s/c)\,\exp(-\,(2\pi f/2Q)\,s/c)$$

The loss parameter is computed for a reference offset a of the beam. The kick Δy_n on the bunch n due to the fields generated by bunch m depends linearly on the offset y_m of the bunch m from the axis of the accelerating structure: $\Delta y_n \sim W_{\perp}^{(1)}(s_{n,m})\ y_m$ ($s_{n,m}$ is the distance between bunch n and m).

Using a mode matching technique the modes of the lowest dipole passband have been calculated [7] for a simplified geometry with subsections of six homogeneous cells. The envelope of the long range dipole wake potential is shown in Fig. 4.3.6. These modes are used for the tracking calculations. If no damping method is used then all modes will have Q-values of at least 10000. Instabilities can be reduced if the modes are damped. In the following section it is discussed in detail how the emittance of the multi-bunch train depends on the Q-values of the dipole modes.

More recent calculations [8] indicate that the long range wake due to the *lowest* passband is overestimated with this set of modes while contributions from higher passbands are missing. There are several modes in the 6th passband (frequency about 9.3 GHz) with large loss parameters. Fig. 4.3.7 shows the envelope of the long range dipole wake potential of the first and sixth passbands for a smoothly tapered 6 m long accelerating structure. A detailed discussion of the subject can be found in section 4.2.1.

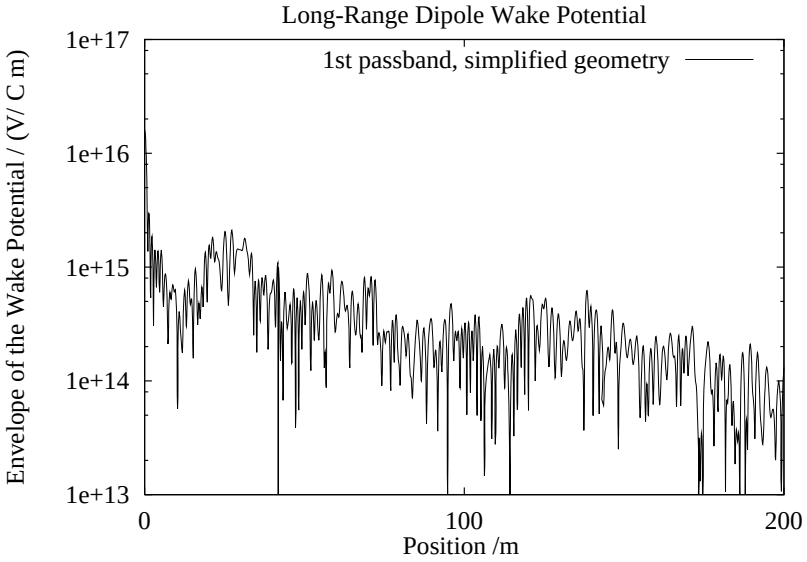

Figure 4.3.6: *Envelope of the long range dipole wake potential of a 6 m accelerating section, using 180 modes from the first passband calculated by [7]. it is assumed that all modes are damped to Q-values of 3000.*

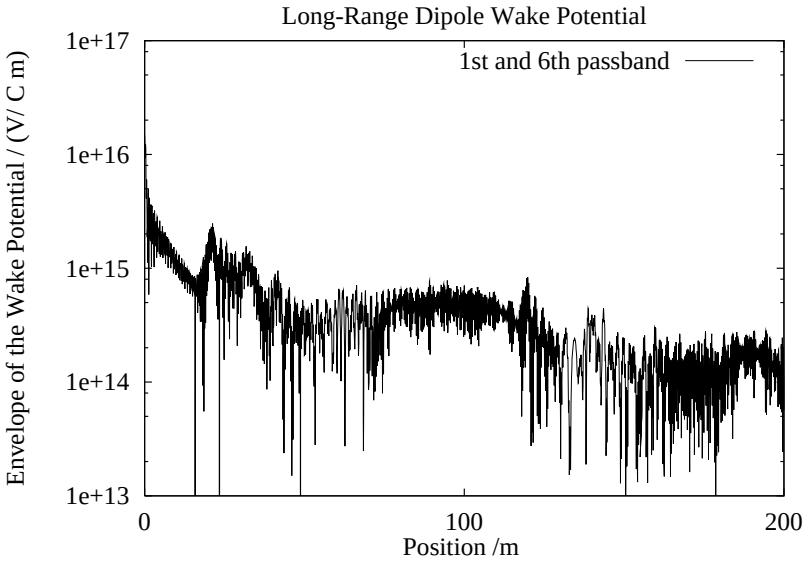

Figure 4.3.7: *Envelope of the long range dipole wake potential of a 6 m accelerating section, using all modes from the first and sixth passbands calculated by [8]. It is assumed that the modes of the first passband are damped to Q-values of 3000, while the modes of the sixth passband are damped to Q-values of 8000.*

Another long range effect is the bunch-to-bunch energy difference due to **transient beam loading**. One filling time ($t_{fill} = 0.789\mu$s) is needed to build up the accelerating field in the structure. Then the bunch train is injected. After a second filling time a steady state is reached. If no compensation method is used this leads to a bunch to bunch energy difference of about 20 % over the first third of the bunch train. It is assumed in the following that this energy spread is corrected quasi-locally by the methods described in section 4.2.9.

4.3.4 Emittance Preservation

The primary sources of emittance growth are wake field effects and dispersive errors caused by small misalignments and vibrations of the main accelerator components. To avoid a significant degradation of the beam quality, i.e. essentially to preserve the transverse emittance, the following cures are considered:

- Beam based quadrupole/BPM alignment,
- Beam based accelerating structure alignment,
- Damping of higher order modes (HOM),
- Active stabilization of quadrupoles.

It is assumed that the starting point of any beam based alignment technique is a good survey of all accelerator components. All presented results of the study are based on a *prealignment precision* of 100 μm of accelerating structures and quadrupole magnets. This precision has to be obtained with respect to a "straight line" over a distant of about 500 m, (i.e. one betatron wave length at the end of the linac). The beam position monitors (BPMs) have also to be aligned with respect to the magnetic axis of the quadrupoles with a precision of 100 μm. Even more important is a high resolution of the BPMs to measure difference orbits with a precision of 5 μm.

A common orbit correction technique is a so called "one-to-one" correction using the readings of nearby BPMs to determine the settings of the corrector magnets. Since the position of the BPMs with respect to the quadrupoles is only known with a precision of 100 μm this correction method is not sufficient to preserve the very low vertical emittance of the bunches. More sophisticated beam based alignment techniques have been developed at SLAC [12]. A steering technique called "DF" (Dispersion Free) can be used if the emittance dilutions are primary caused by dispersive effects in the quadrupole magnets. The strength of the quadrupole magnets is varied to determine the dispersion from difference orbits. An improved so-called "WF" (Wake-Free) version of these methods [12] uses even more difference orbits. The strengths of the focusing and defocusing quadrupole magnets are differently varied in order to avoid any enhancement of wake field effects.

The alignment of the accelerating structures can be improved by active movers at each structure which adjust the structure with respect to HOM coupler signals. Two pairs of HOMs couplers mounted at each 6 m long accelerating structure are sufficient to determine the offset and tilt of the structure with respect to the bunch train. It is assumed that with this method an alignment of the accelerating structures of 50 μm (rms) can be achieved.

The dependence of the emittance growth on the various alignment tolerances and parameters of the HOMs is investigated by computer simulations [9, 10]. The (projected) emittance of the bunch train is computed from the moments of the particle distributions in phase space. Each bunch is divided into several slices with a centroid (y_n, y'_n) and an individual phase space distribution with moments $\sigma_{yy}^{(n)}$, etc. The vertical emittance of the bunch train is given by:

$$\epsilon_y = \sqrt{\sigma_{yy}\,\sigma_{y'y'} - \sigma_{yy'}^2}$$

The second order moments $\sigma_{yy}, \sigma_{y'y'}, \sigma_{yy'}$ of the positions (y) and slopes (y') are calculated according to

$$\sigma_{yy} = \frac{1}{\sum_n q_n} \sum_n q_n \left((y_n - < y >)^2 + \sigma_{yy}^{(n)} \right),$$

and analog for σ_{yy} and $\sigma_{yy'}$. The sum includes all bunches and all slices with charge q_n. The emittance is calculated with respect to mean value $< y >$ of the slice centroids in the bunch train.

4.3.4.1 Multi Bunch Effects

First, the multi-bunch effects are studied separately, i.e. essentially the cumulative multi-bunch beam break-up instability. The beam quality of the bunch train is characterized by the relative centroid emittance, i.e. the moment σ_{yy} is calculated only from the centroids $(y_n,\ y'_n)$ of each bunch. The vertical single bunch emittance $\epsilon_y = 0.25 \cdot 10^{-6}\,\mathrm{m}/\gamma$ ($\epsilon_y = 5.1 \cdot 10^{-13}$ m at 250 GeV) is used as a reference.

It is assumed that the transient beam loading is compensated by the above mentioned local methods (control of the rf-amplitude). These results are compared with simulation where the beam loading is switched off during the tracking of the bunch train. Fig. 4.3.8 shows the results for different Q-values of the dipole modes [10]. The Q-values of the *undamped* HOM's are larger than 10000. An rms accelerating structure misalignment of 100 μm has been assumed. The quadrupoles are perfectly aligned for this computer simulation. Each data point corresponds to one random seed of the simulation. If the beam loading is taken into account but assumed to be locally compensated to $\Delta E/E \approx 6 \cdot 10^{-4}$ then the relative emittance growth is (8.8 ± 8.0) % for a Q-value of 2000 and (352 ± 160) % for a Q-value of 10000 for all the dipole modes.

Therefore, the dipole modes have to be damped to Q-vales between 2000 and 4000. This can be achieved by coating of the iris of each cell of the accelerating structure with lossy material. Additionally, HOM couplers are used which serve also as beam position monitors and provide the signal for the accelerator structure movers.

Furthermore, it is beneficial to use slightly, with respect to HOMs, detuned accelerating structures to disturb any coherence from one accelerating structure to the next one. The results show in Fig. 4.3.8 are obtained for 10 classes of accelerating structures with a total detuning range of 36 MHz. This detuning of the dipole modes can be done by a variation of the radius R_{curve} of the cups (see Fig. 4.3.2).

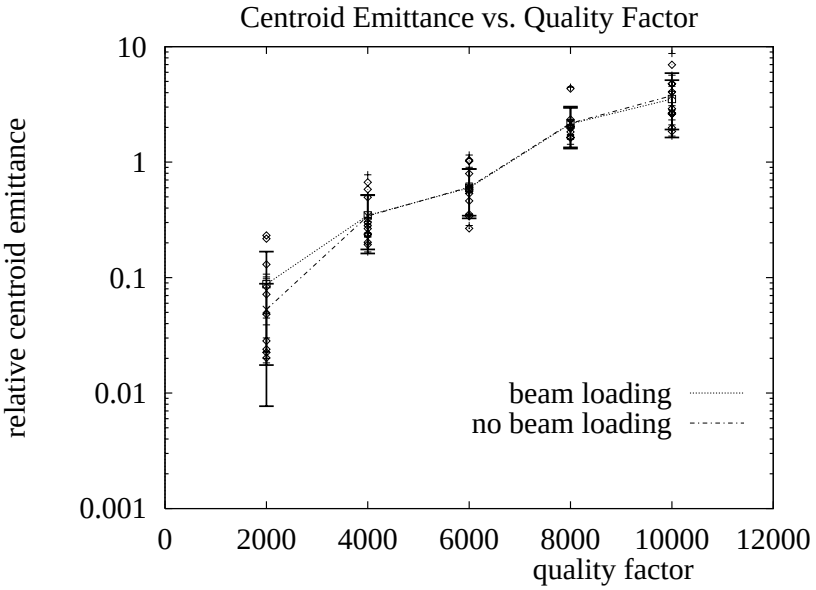

Figure 4.3.8: *Multi-bunch centroid emittance growth due to misaligned accelerating structures as a function of the Q-value of the dipole modes. An rms accelerating structure misalignment of 100 μm has been assumed. The vertical single bunch emittance is used as a reference.*

4.3.4.2 Single and Multi Bunch Effects

Once that the cumulative multi bunch beam break-up is controlled by appropriate damping of the dipole modes the single bunch dynamics determines the alignment tolerances of the main accelerator components. Since multi bunch effects still contribute to emittance growth due to a residual bunch-to-bunch energy difference and the long range wakefield effects of the HOMs, single and multi bunch effects are studied together. The emittance of the whole bunch train is again measured in units of the initial vertical single bunch emittance. Fig. 4.3.9 shows the results obtained by computer simulations [10]. The following correction techniques have been used:

- Local compensation of the bunch-to-bunch energy difference,
- Beam based WF steering,
- Accelerating structure adjustment by means of movers.

The orbit correction with the WF algorithm is applied during a single bunch operation mode with a reduced bunch population of $2.0 \cdot 10^9$. This corrects the dispersion effects due to the quadrupole misalignment (100μm rms after the survey) and defines the required BPM resolution of 5μm. The short range transverse wakefield effects are reduced by a beam based realignment of the accelerating structures with movers with an rms accuracy of 50μm. Transverse short range wakefields effects are reduced by a method called **BNS damping** according to the inventors of the method [11]. The effect of transverse wakefields can be partly canceled by chromatic effects due to a correlated energy spread in the bunch. For the SBLC parameters this energy spread is

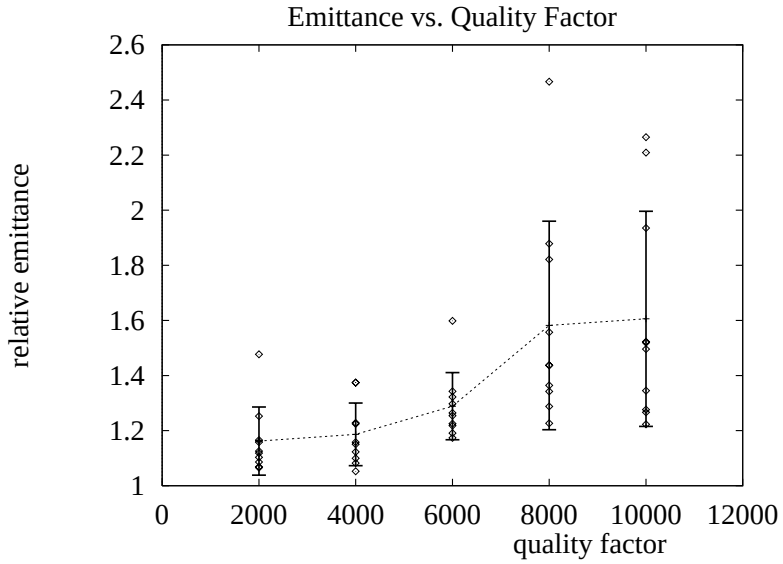

Figure 4.3.9: *Emittance growth due to misaligned accelerating structures and quadrupole magnets as a function of the Q-value of the dipole modes. Single and multi bunch effects are included. Beam based orbit corrections techniques and an adjustments of the accelerating structures by means of movers has been applied. Each data point corresponds to a random seed.*

just produced by the longitudinal short range wakefields, i.e. the optimal BNS rf-phase is just on the crest of the wave [10]. It is not necessary to add an additional energy spread to the bunch. Under these conditions the emittance growth is

$$\frac{\Delta\epsilon_y}{\epsilon_y} \leq 20\,\% \pm 10\,\% \qquad \text{for} \quad Q \leq 4000\,,$$

as shown in Fig. 4.3.9.

The influence of single bunch charge fluctuation and longitudinal jitter on the emittance preservation has been studied in [10, 9]. Provided that the total charge of the bunch train is constant a rms charge fluctuation from bunch to bunch up to 10 % has no significant impact on the emittance growth. Longitudinal jitter of the bunches is not important as long the jitter amplitude is smaller than the rms bunch length of $\sigma_z = 300\,\mu$m. If the charge fluctuation and longitudinal jitter amplitudes stay in this limits then the influence on the energy spread is also not relevant.

4.3.5 Orbit Stability

The beam quality is sufficiently preserved for luminosity operation if beam based alignment techniques are successfully applied. The WF algorithm is based on at least three orbit measurements: one with the nominal strength of all quadrupoles and two with a reduced strength of the focusing and defocusing quadrupoles respectively. Usually it is assumed that the misalignment of the quadrupoles is unknown but constant during the application of the algorithm. But this approximation is only valid for short time

scales and small distances since slow diffusive ground motion processes will change the displacement of the accelerator components with time. This sets an upper limit on the time available for performing the WF-steering procedure.

The orbit drift induced induced by the quadrupole motion also has an effect on the emittance dilution. Therefore orbit correction in the linac has to be applied periodically after certain time intervals.

Additionally, fast (i.e. pulse-to-pulse) quadrupole vibrations due to ground motion or environmental noise will reduce the luminosity because of transverse separation of the beams at the IP if their amplitudes are too large. A mechanical feedback system has been developed [13] which can stabilize the quadrupoles to an accuracy of 20 nm (see section 4.8.4). In addition, a fast orbit feedback at the IP can be used within a bunchtrain (see section 4.8.3). As is discussed in section 4.8.4, the expected vibration amplitudes are not a serious problem, but the above mentioned feedback systems can become more important if a luminosity upgrade with smaller vertical emittance is considered.

4.3.5.1 Effect of Diffusive Ground Motion

Diffusive ground motion processes will vary the displacement of two points in the accelerator with time. The so called "ATL-rule" seems to apply to a wide range of ground motion processes. This rule states that the relative displacement Δy of two points separated by the distant L is expected to be

$$< \Delta y^2 >= A \cdot T \cdot L$$

after a time T (see also the subsection on ground motion in section 4.7). The coefficient A depends on the site and ranges from 10^{-8} μm^2/m s in quiet places to 10^{-4} μm^2/m s in very noisy places. This study assumes a coefficient $A = 10^{-5}$ μm^2/m s, which is a safe choice compared with the value of $A = 4 \pm 2 \cdot 10^{-6}$ μm^2/m s measured for the HERA accelerator at DESY [14].

The question how fast the orbit measurements for the WF steering have to be performed to avoid degradation due to ground motion was first studied in [10]. The simulation assumes perfectly aligned accelerating structures and an rms misalignment of the quadrupoles and BPMs of 100 μm. The time interval between the simulated orbit measurements is varied and a ground motion process is applied to the accelerator components according to the ATL-rule. Fig. 4.3.10 shows the centroid emittance of the slices of a single bunch obtained after WF steering as a function of the time interval between simulated orbit measurements. The results found under the assumption for the ground motion is that the time interval between subsequent measurement of orbits should not exceed two minutes, which should not present a problem.

After addressing the problem how fast a beam based alignment has to be performed the question arises how often it is necessary to repeat the procedure. We first investigate how the emittance dilution develops as a result of orbit drift caused by uncorrelated random motion of the quadrupoles. The result is shown in Fig. 4.3.11 for a random misalignment of 1 μm (note that the emittance dilution scales with the square of the

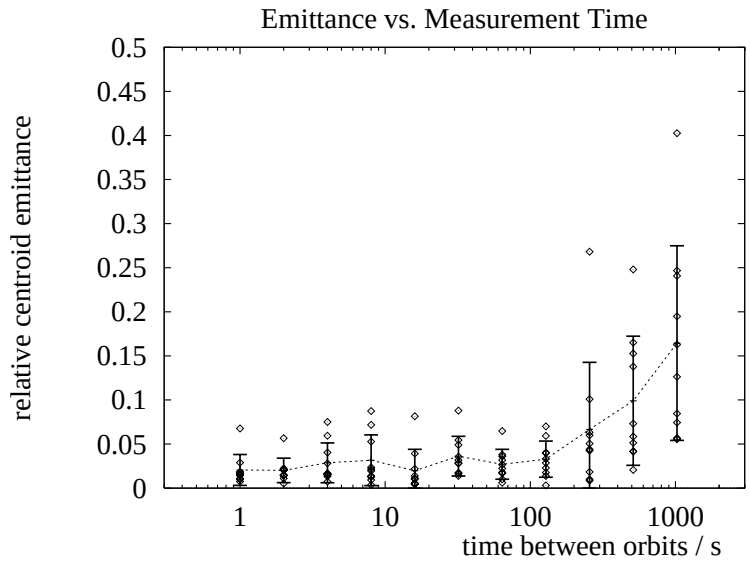

Figure 4.3.10: *Relative single-bunch centroid emittances after WF steering versus the time interval between simulated orbit measurements. In the beginning the quadrupoles and BPMs were randomly misaligned with an rms value of* 100 μm *(each data point corresponds to one random seed). Between simulated orbit measurements a ground motion process was applied according to the ATL-rule.*

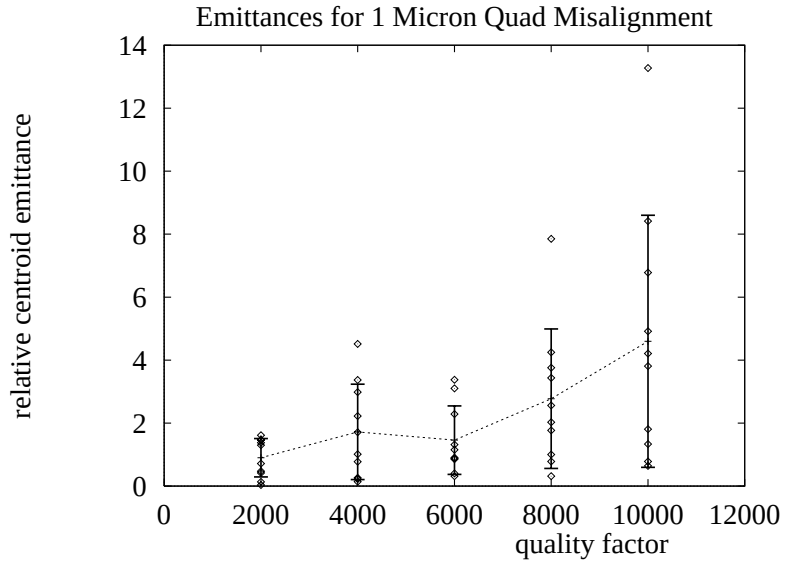

Figure 4.3.11: *Centroid emittance growth due to random quadrupole motion with* 1 μm *rms offset for different Q-values of the HOMs. No orbit correction method has been applied. Each data point corresponds to one random seed. The vertical single bunch emittance is used as the reference.*

rms quadrupole misalignment). With Q-values below 4000, we conclude that orbit correction has to be applied after the quads have moved by 250 nm (rms) in order to limit the emittance dilution to less than 6 %. In terms of the ATL-model for diffusive ground motion, this translates into a time of 25 minutes after which the beam must be re-steered to the "golden" orbit which was found previously with the WF-procedure [10]. A new "golden" orbit with a WF beam based technique has to be established every 11 days. Otherwise, accumulated errors, which are not corrected by a simple one-to-one correction, will lead to an emittance growth of more than 6 %.

4.3.6 Possible Improvements

The methods described in the preceding sections are sufficient to safely achieve the required design emittance at the end of the linac. Additional methods, briefly summarised in the following, can be applied to further reduce emittance growth and to open up the possibility of luminosity upgrade with smaller vertical emittance.

- Empirical orbit steering with either non-dispersive bumps (to reduce wakefield effects) or dispersion bumps (to reduce chromatic dilution) are common practice at the SLC and can be used here as well. Transverse beamsize diagnostic stations will be installed at different points along the accelerator to facilitate empirical optimization for sub-sections of the linac.

- The effect of long-range wakefields from misaligned accelerating structures can be compensated to a large extend by fast kickers which are capable to act on individual bunches. At the end of the linac, each bunch has a slightly different orbit due to the deflection by the HOMs. This pattern (more precisely: the part of it which is reproducable over many pulses) of multi-bunch orbit deviations can be measured and fast (less than 6 ns pulse width) kickers can be used to remove it.

- The alignment of BPMs to the magnetic axis of the quadrupoles can be drastically improved with a beam based technique (by measuring difference orbits after changing the strength of each quadrupole individually). If the alignment thus obtained is sufficiently stable over long periods of time, the repeated application of the WF-method may become unnecessary.

4.3.7 Summary: Tolerances and Emittance Dilution

The beam dynamics of a multi bunch train in the main linac has been studied. To preserve the emittance of the bunch train it is necessary to ensure that several tolerances are kept into partly tight limits. All data given here correspond to a (vertical) emittance dilution of $20\% \pm 10\%$ for the whole bunch train. The implications on the following issues are discussed:

- alignment tolerances,
- instrumentation (BPMs),

- accelerator structures.

The quadrupole magnets and accelerator section have to be prealigned to a precision of 100 μm (rms) by a good survey. The reference of the survey is a "straight line" over a distant of a betatron wavelength (i.e. about 500 m). The BPMs are mounted in the quadrupole magnets with the same rms precision of 100 μm. The position of all accelerator section can be changed by movers between the girder and the section. Finally, the accelerator section has to be aligned with respect to the beam with a precision of 50 μm (rms). A good instrumentation is necessary to achieve this goal.

There are two types of beam position monitors, the stripline BPMs in each quadrupole magnet and the HOM-couplers at each accelerator section. The signals of the HOM-couplers are used to set the motors of the movers while the stripline BPMs are used to set the corrector strength of the dipole correctors according to a beam based orbit correction method. The system HOM-coupler/mover has to achieve the above mentioned alignment precision of 50 μm (rms) for the accelerator structures. The BPMs have to measure difference orbits with a high resolution of 5 μm (rms), which includes electronic drifts, etc. . The control system has to ensure that it is at least possible to set all quadrupole magnets and measure the orbits in about 100 s to avoid degradation of the WF steering algorithm due to ground motion. The amplitude of fast quadrupole vibrations determines the orbit stability at the interaction point, but is not expected to have an effect on emittance dilution in the linac.

The long range wake field effects due to dipole modes in the accelerator section can cause cumulative beam break-up of the bunch train. Therefore it is important to damp and detune these HOMs. Ten types of accelerator structures are foreseen which are different with respect to the dipole mode. The total detuning range is 36 MHz for the dipole modes. Coated irises and the HOM-couplers are used to damp all HOMs to Q-values between 2000 and 4000. The straightness of the 6 m long accelerator section has been at least as good as the mover/HOM-coupler alignment system, i.e. 50 μm.

Bibliography

[1] O.H. Altmueller et al., *Beam Break-Up Experiments at SLAC*, Proceedings of the 1966 Linear Acc. Conf., Los Alamos, 1966

[2] P. Emma, *The Stanford Linear Collider* , 16th IEEE Particle Acc. Conf. (PAC95), Dallas 1995

[3] M. Drevlak, M. Timm, T. Weiland, *Simulation of Linac Operation Using the Tracking Code L*, 18th Int. Linac Conf., Geneva 1996

[4] T. Weiland, *On the numerical solution of Maxwell's Equations and Applications in the Field of Accelerator Physics*, Part. Acc. 15 (1984), 245-292

[5] M. Drevlak, *Wake Potentials of Short Bunches in the SBLC Accelerating Structure*, Internal Report, DESY M-95-13, Dec. 1995

[6] W.K.H. Panofsky, W.A. Wenzel, *Some Considerations Concerning the Transverse Deflection of Charged Particles in Radio - Frequency Fields*, Rev. Sci. Instrum. 27 (1956), 947

[7] U. van Rienen, *Higher Order Mode Analysis of Tapered Disc-Loaded Waveguides Using the Mode Matching Technique*, Part. Acc. 41 (1993), 173-201

[8] M. Dohlus, private communication

[9] M. Drevlak, *On the Preservation of Single- and Multi-Bunch Emittance in Linear Accelerators*, Thesis, DESY 95-225, Nov. 1995

[10] M. Drevlak, *New Results on the Beam Dynamics in the SBLC* Internal Report, DESY M-96-01, Jan. 1996

[11] V. Balakin, A. Novokhatsky and V. Smirnov, Proc. 12th Int. Conf. on High Energy Accelerators, Fermilab 1983.

[12] T. Raubenheimer, *The Generation and Acceleration of Low Emittance Flat Beams for Future Linear Colliders*, Thesis, SLAC-387, Nov. 1991

[13] C. Montag, J. Rossbach, *A Mechanical Feedback System for Linear Colliders to Compensate Fast Magnet Motion* Particle Accelerator Conference PAC95, Dallas, May 1995

[14] R. Brinkmann, J. Rossbach, *Observation of closed orbit drift at HERA covering 8 decades of frequency*, Nucl. Instr. and Mech. A 350 (1994) 8-12

4.4 Injection System

4.4.1 Electron Source

4.4.1.1 Polarized Gun

At present, all operating polarized electron sources are using DC-guns generating long pulses in the ns range, usually followed by a bunching system (see e.g. [1]). A GaAs cathode is illuminated by suitable laser pulses to extract pulses of polarized electrons.

An injection system, which meets the requirements for SBLC is being built at the S-Band Test Facility. It uses a pulsed DC-gun operating at 90 kV. The following discussion is based on a gun with similar performances.

Space charge and cathode charge limit Space charge limits the extractable current of a DC-gun. The limit can be estimated using Child-Langmuir's law. The 90 kV gun has a perveance of $0.23\,\mu A/V^{3/2}$, limiting the current to 6 A.

A more severe limitation specific to GaAs-type cathodes is the so called cathode charge limit [2]. This limitation is typical for semiconductor cathodes with a negative electron affinity (NEA) surface, where a high electron extraction probability is achieved by the application of alkalis and oxides to the surface of the GaAs crystal. The NEA surface (together with the p-dopant, which bends the energy bands downwards at the surface) lowers the vacuum level below the conduction band minimum in the bulk, resulting in high extraction rates. The limit can be understood as a competition between the rate of near-thermal electrons arriving from the conduction band at the surface and the discharge rate of electrons from the surface [3].

The cathode charge limit can be estimated using SLC data [4]: the SLC gun produces about 10 nC in a 2 ns long pulse from a cathode of an area of $1.5\,cm^2$ close to the cathode charge limit. A 100 nm medium-doped ($5{\cdot}10^{18}/cm^3$) strained-lattice GaAs cathode layer is used. The acceleration voltage is 1.8 MV/m. Thus, the charge density is limited to $7\,nC/cm^2$.

Since the current density scales linearly with the acceleration voltage E [5], the charge density on the cathode will be limited to $8\,nC/cm^2$ for a field at the cathode of 2 MV/m. With a cathode area of $2\,cm^2$, the extractable charge is about 16 nC well above the SBLC requirements.

The charge limit is experimentally verified for bunch lengths in the order of ns. Conservatively, one may assume that the charge density limit turns into a current density limit already for bunches as short as 0.3 ns [6]. With this assumption, the current will be limited to $3.7\,A/cm^2$ for the SBLC gun. To extract bunches of 2 nC from the $2\,cm^2$ cathode, the bunch length must exceed 300 ps.

Shorter bunch lengths are preferred, since it would simplify the bunching system. This can be achieved by increasing the acceleration voltage or by using a larger cathode. On the other hand, to avoid damaging the cathode by ion bombardment, the dark current should be kept as low as possible. Besides a careful processing of the gun this requires low fields at the electrodes. The SLC gun operates at 120 kV with a dark current of less than 50 nA. The highest field on the electrodes is 7 MV/m [1].

Multi bunch operation For multi bunch operation, an additional effect of the cathode charge limit gets important: the temporary flattening of the bands in the band bending region due to trapped electrons in the surface states, preventing further electrons from being extracted. Experiments at the SLC have shown, that the recovery time of the cathode is in the order of 10 to 100 ns depending on the cathode thickness [1]. Using a highly doped, thin cathode ($2{\cdot}10^{19}/\mathrm{cm}^3$, 100 nm), a reduction of the charge of the second bunch is expected to be only 10 % for bunch to bunch separation of 6 ns. For the following bunches, a steady state at a reduced charge will build up.

Polarization, quantum efficiency and lifetime A polarized electron beam is produced by applying circular polarized laser light on a strained lattice GaAs cathode. SLC data show a polarization maximum of more than 80 % at a laser wavelength of 845±10 nm [7]. Unfortunately, the quantum efficiency drops sharply for highest polarization to 0.1 ...0.3 %. In addition, the quantum efficiency depends strongly on the operating conditions of the gun. High dark current of more than 50 nA and poor vacuum conditions reduces the quantum efficiency significantly. The vacuum must be maintained below $1{\cdot}10^{-11}$ mbar. In addition, activation of the cathode by cesiation is regularly required. To obtain a reasonable up time of the source, a loading system which enables loading and removal of the cathode without breaking the gun vacuum is essential. Conditioning of the gun, regular cesiation and other cathode manipulations will be done with the cathode removed. A transport chamber will allow to insert a cathode prepared in a separate preparation chamber.

SLC is operating their gun with the same cathode for more than a year with a quantum efficiency between 0.1 and 0.3 % at highest polarization. The regular cesiation required to maintain this efficiency is done in situ without breaking the vacuum [7].

Laser Most polarized electron sources use lasers based on Ti:Sapphire, which are commercially available, especially for cw and pulsed applications with low repetition rates of a few tens of Hz. These lasers are tunable in a wide range around 800 nm and exceed easily the power or pulse energy requirements for most sources.

The laser may consist of Ti:Sapphire oscillator producing a long pulse of 2 μs with an energy of 1 mJ. It is pumped by a Nd:YAG laser system running at 50 Hz. The long pulse is sliced into 333 short pulses with a distance of 6 ns between the pulses and a length of 1 ns or shorter if required using resonant Pockels cells. It is also possible, to generate the pulse train directly in a pulse train oscillator running at 167 MHz. The pulse train will be amplified by a Ti:Sapphire power amplifier to 50 μJ per pulse. On the cathode, about 10 μJ are required to produce an electron bunch of 3 nC. An extensive feedback system is used to stabilize the pulse energy and phase.

4.4.1.2 Injector Linac

This section explains the conventional electron injector and pre-linac. The injector linac is composed of two main parts. It starts with the injector consisting of the electron source and a bunching system followed by the linac part responsible for accelerating

		SBTF			SBLC
ν_t, train repetition frequency	$[Hz]$	50			
I_t, average current in train	$[mA]$	300			
T_t, length of train	$[\mu s]$	2			
bunchlength at injector exit		$\leq 16^{\circ}_{3GHz}$			
energy at injector exit		$E_{kin} \geq 3\,MeV$			
T_{bb}, bunch to bunch separation	$[ns]$	24	16	8	6
n_t, bunches per train		83	125	250	333
q_b, charge per bunch	$[nC]$	7.2	4.8	2.4	1.8
ν_{SHB1}, frequency of 1. SHB	$[MHz]$	125			166
length of gunpulse	$[ns]$	$\approx 2.0 - 2.5$			$\approx 1.5 - 2.0$
gun peak current	$[A]$	≈ 6			≈ 2

Table 4.4.1: *Comparison between required injector parameters for SBTF and SBLC operation.*

the beam up to the damping ring energy of $3\,GeV$. Determined by the longitudinal and transverse acceptance of the damping ring, upper limits for the energy spread and the normalized emittance at the end of the injector linac are $\Delta E/E \leq 1\,\%$ and $\epsilon_n^{rms} \leq 1 \cdot 10^2\,\pi\,mm\,mrad$, respectively. The time structure and bunch population are given by the collider parameters. Based on a $\nu_t = 50\,Hz$ repetition rate $T_t = 2\,\mu s$ long bunchtrains with an average current of $I_t = 300\,mA$ are required. Being separated by $\Delta t_b = 6\,ns$ each of the 333 single bunches in one train carries a charge of $q_b = 1.8\,nC$ equivalent to a bunch population of $N_b = 1.125 \cdot 10^{10} e^-$. The accelerating part of the injector linac will consist of an S-band linac adopting the same technique as proposed for the SBLC main linac. For $3\,GeV$ roughly 31 regular $6\,m$ long accelerating structures ($\beta = 1$, $2\pi/3 -$ mode, $17MV/m$) intersected by focussing quadrupoles are needed, i.e. an overall accelerator length of about $200\,m$. One $150\,MW\,/\,3\,\mu s$ S-band klystron supplies two $6\,m$ structures. Applying the same scheme of beamloading compensation as in the main linac the energy spread at the end of the linac is dominated by the bunchlength at its entrance. To obtain $\Delta E/E \leq 1\,\%$ the injector has to deliver bunches of a length less than $16^{\circ}_{3GHz} = 14.8\,ps$ in time corresponding to a length of $4.4\,mm$ if the beam is relativistic. In that case the injector is fully responsible for the bunching and the first accelerating section takes over a bunch which longitudinal dynamics is already frozen. The clear-cut between bunching and acceleration guarantees an independant operation of the injector and accelerating sections. For this reason the beam should leave the injector with a kinetic energy of $E_{kin} \geq 3\,MeV \Leftrightarrow \beta \geq 0.9$. Since the damping ring acceptance is large the emittance constraint on the injector part is relaxed and does not represent a severe problem.

Except for the bunch spacing Δt_b the design of the injector for the S-Band Test Facility (SBTF) is based on the same parameters. For the purpose of wakefield related studies the bunch spacing Δt_b can be varied between $8\,ns$, $16\,ns$ or $24\,ns$ in the SBTF. Keeping the average current within the bunchtrain at $I_t = 300\,mA$ results in

a maximum bunchcharge of $7.2\,nC$ in the last case. Table 4.4.1 compares the injector requirements for the SBTF and the SBLC. Having found a reasonable concept for the SBTF injector there is no doubt that an injector for the SBLC can be realized in the same manner, since the operation conditions are more relaxed in terms of bunchcharge. Thus the following paragraphs are going to present the performance of the SBTF injector as derived from EGUN or PARMELA calculations as well as has been measured at the existing part of it. Requiring multibunch operation in combination with high bunchcharge a conventional scheme as sketched in Fig. 4.4.1 based on a thermionic gun with a gridded cathode followed by a bunching system using two subharmonic (SHB1 and SHB2) and two fundamental bunchers (TWB1 and TWB2) was decided for. The impact of the deviating SBLC requirements on the presented layout for the SBTF injector will be discussed at the relevant design steps.

Electron Source Production of $2\,\mu s$ long bunchtrains with $300\,mA$ average current is required. The current the gun has to deliver is determined by the length of the gunpulse and its charge. For clean capture at SHB1 the gunpulse should have a length in the order of a quarter of its period time. In order to relax the requirements on the gun the frequency of the subharmonic buncher SHB1 has to be as low as possible, but nevertheless has to match with the time structure of the bunchtrain. That is why SHB1 runs at $125\,MHz$ in SBTF respectively needs to be $166\,MHz$ at SBLC, which implies a gunpulse length of about $FWHM \approx 2\,ns$ respectively $FWHM \approx 1.5\,ns$. For SBTF operation the maximum charge including a 60 % safety margin has to be $12\,nC = 7.5 \cdot 10^{10} e^-$ resulting in a gun current of $6\,A$. For SBLC parameters the situation is more relaxed. The required guncharge is only $3\,nC$, i.e. less by a factor of 4 and its current reduces by a factor of 3 down to $2\,A$ due to the shorter pulse length.

The gunvoltage of $90\,kV$(dc) has been chosen as low as possible in order to simplify the process of bunching and keeping the SHB amplitudes at moderate levels. On the other hand as shown by PARMELA calculations this value is high enough to tolerate spacecharge effects (bunchlengthening and energy modulation) in the $75\,cm$ long drift up to SHB1. Based on the EIMAC Y796 cathode grid assembly, which emits from a circular cathode area of $2\,cm^2$ (equivalent to $8\,mm$ in radius) a gun geometry was modelled by means of EGUN simulation. The result is shown in Fig. 4.4.2. With a $34\,mm$ anode cathode gap this gun has a calculated perveance of $0.22\,\mu A/V^{1.5}$. At $90\,kV$ this is equivalent to $6\,A$ space charge limited current, which was experimentally proven when driving it with single pulses of a few μs in length.

Extraction of bunchtrains consisting of short pulses is achieved by means of a special pulser that is housed inside the $240\,mm$ long gun ceramic close to the gun cathode. In combination with a high bandwidth optical transmission and amplifier system the pulser input is supplied with $2\,ns$ wide pulses of $60\,V$ peak and the desired time structure. The gunpulser amplifies these pulses by means of a three stage triode circuit interconnected by ferrite loaded coaxial transformers in which the third triode with its anode directly connected to the guncathode operates in a current source mode. Measured at $31.6\,cm$ behind the gun at wall current monitor CM1 Fig. 4.4.3 shows

the beampulses having a FWHM-length of typically $2.2\,ns$, a subnanosecond risetime and a peak current of up to $4.5\,A$, which is less than the gun capability since it is limited by the current output of the last triode stage. Due to a saturation effect of the interstage transformer cores we observe a drop down from $10\,nC$ in the first pulse to a 70 % equilibrium level within the first 3 pulses of a $2\,\mu s$ bunchtrain with 250 pulses in $8\,ns$ mode. Although reduced down to $7\,nC$ this bunchcharge is by a factor of 2.9 well beyond the required $2.4\,nC$ for $8\,ns$ operation. Except for the first 3 pulses the intensity stability is better than 4 % over the whole bunchtrain.

This scheme of bunchtrain production has been sucessfully commissioned and fulfills all the requirements in terms of time structure, bunchcharge as well as stability in intensity and timing [9]. Since the intensity requirements are more relaxed for SBLC this scheme might even work at $6\,ns$ operation but has not been tested yet. If not applicable a resonant driving circuit for the gun can be used alternatively.

Bunching System Starting with the EGUN calculated transverse beam parameters at the gun exit a $90\,kV$ / $12\,nC$ pulse with a length of $FWHM = 2.5\,ns$ ($FW = 3.0\,ns$) was used as an input to PARMELA calculations in order to optimize the process of bunching and lead to a layout as shown in Fig. 4.4.1 [8].

Starting with $z = 0$ at the gun anode a $125\,MHz$ cavity (SHB1) with a $30\,mm$ wide gap is located at $z = 75\,cm$. Running at an amplitude of about $34\,kV$ more than 80 % of the initial charge can be found in 120° of $500\,MHz$ at a distance of $116\,cm$ downstream of SHB1. Therefore a second cavity SHB2 with a gap of $40\,mm$ running at $500\,MHz$ is centered at $z = 191\,cm$. The optimum longitudinal focal point appears already $24\,cm$ behind the SHB2 gapcenter at $z = 215\,cm$. At this position PARMELA predicts a bunchlength of $FWHM \approx 0.19\,ns$ equivalent to about 200° of S-band. Measurements at that position show a bunchlength of $300\,ps$ with a transmission of 85 % when starting with a typical gunpulse ($2.2\,ns$ / $4.5\,A$) of $10\,nC$ [10]. Unfortunately this measurement was bandwidth limited by the wallcurrent monitor and thus represents an upper limit for the true bunchlength. Without further measures the mentioned transmission and bunching results are only valid for the first pulses in the bunchtrain, since the following ones are heavily affected by amplitude and phase changes in the cavities due to beamloading. Made from stainless steel both cavities have a $Q_0 \approx 2700$ and a R/Q about $82\,\Omega$ respectively $101\,\Omega$. They are powered by a $10\,kW$ / $20\,\mu s$ pulsed RF transmitter each. Neglecting its decay the beam induced voltage ($U = \omega \cdot R/Q \cdot q$) after half of the $2\,\mu s$ bunchtrain with $300\,mA$ has passed the cavities is $19\,kV$ in SHB1 and $95\,kV$ in SHB2. By means of a feedforward system acting on the amplitude and phase control circuits of both transmitters it is possible to obtain similar amplitude and phase conditions for every bunch of the train when entering the cavity.

Being still too long for the linac the bunches continue the process of longitudinal compression when entering a 4-cell S-band travelling wave structure (TWB1) having its first cellcenter at $z = 215\,cm$. TWB1 operates in $2\pi/3$-mode, has a phase velocity of $\beta = 0.6$ and is expected to run with a gradient of $7\,MV/m$. TWB1 is followed by a 16-cell, $\beta = 0.95$, $8\pi/9$-mode S-band travelling wave buncher (TWB2) running at

$12\,MV/m$ and being separated from TWB1 by only $9\,cm$ when measuring the distance between the last cellcenter of TWB1 and the first cellcenter of TWB2. The $8\pi/9$-mode was chosen to reduce the group velocity in order to relax the power requirement on the feeding klystron. Looking roughly $70\,cm$ downstream of TWB2 simulations predict a bunchlength of less than $10\,ps$, which has not been experimentally proven yet since the hardware is not commissioned up to this point. Simultaneously both TWB's accelerate the beam up to about $4\,MeV$. Therefore a short relativistic bunch enters the first regular accelerating section at $z = 360\,cm$.

When used as an injector for the injector linac at SBLC the same bunching system can be applied except that SHB1 has to be replaced by a $166\,MHz$ cavity and the distance between SHB1 and SHB2 may be optimized. Beamloading effects are identical because the average current in the bunchtrain remains the same.

Transverse Dynamics Up to SHB2 the free aperture of the beampipe has a diameter of $34\,mm$. While getting shorter, the beampulses are transversely focussed by means of a longitudinal magnetic field B_z created by distributed solenoids AF4 to AF27. At the guncathode B_z is set to zero with the help of bucking coil AF1. With two matching solenoids AF2 and AF3 the beamsize is adjusted to fill about 70 % of the beampipe, because a large ratio reduces spacecharge effects, and is tried to be kept constant up to SHB2. With a level around $100\,Gauss$ around SHB1 B_z slowly increases more or less according to the law of a Brillouin fieldstrength. Just before entering TWB1 the beam is focussed down to half its transverse size by means of a steep rise of B_z, which finally ends at a level of $1800\,Gauss$ and staying constant there until it decays to zero at the middle of the first accelerating section where the last solenoid ends. The longitudinal dependence of B_z and the maximum horizontal beamsize are shown in Figs. 4.4.4 and 4.4.5.

The normalized horizontal and vertical rms-emittance ϵ_n^{rms} as a function of the position z along the injector is plotted in Fig. 4.4.6. Starting with $1.8\,\pi\,mm\,mrad$ at the gun exit as calculated with EGUN the normalized rms-emittance $60\,cm$ further downstream was measured to be about $3\,\pi\,mm\,mrad$ for a $7\,nC$gunpulse ($2\,ns$ / $3.5\,A$) by means of the pepperpot technique [10]. Nevertheless this value is heavily deteriorated when entering TWB1 and stays almost constant at around $100\,\pi\,mm\,mrad$ after that. Off axis particles suffer from transverse forces in the electromagnetic field of TWB1. As they vary in time with the S-band frequency each longitudinal segment of the bunch is affected in a different way, which leads to a so called RF-induced emittance growth. With 200° of S-band the bunch is quite long when entering TWB1. Therefore this effect is most severe in the first few cells of it. When the bunch is short all particles are more or less affected in the same manner and the emittance stays constant. This effect can be reduced by decreasing the transverse or longitudinal beamsize or both. Since compression transversely or longitudinally is easier with a reduced bunchcharge the emittance growth will profit from the SBLC parameters.

Conclusion A feasible concept for the injector linac complex of the SBLC was presented. The SBTF scheme of bunchtrain production and bunch compression, which has been partially commissioned, can be copied for a SBLC injector, when replacing the first subharmonic buncher by a $166\,MHz$ system. Since no switching between different interbunch spacings and a much smaller bunchcharge is required, the SBLC parameters will be easier to achieve compared with the SBTF layout. Acceleration up to the damping ring energy will be done adopting the same technique as proposed for the SBLC main linac.

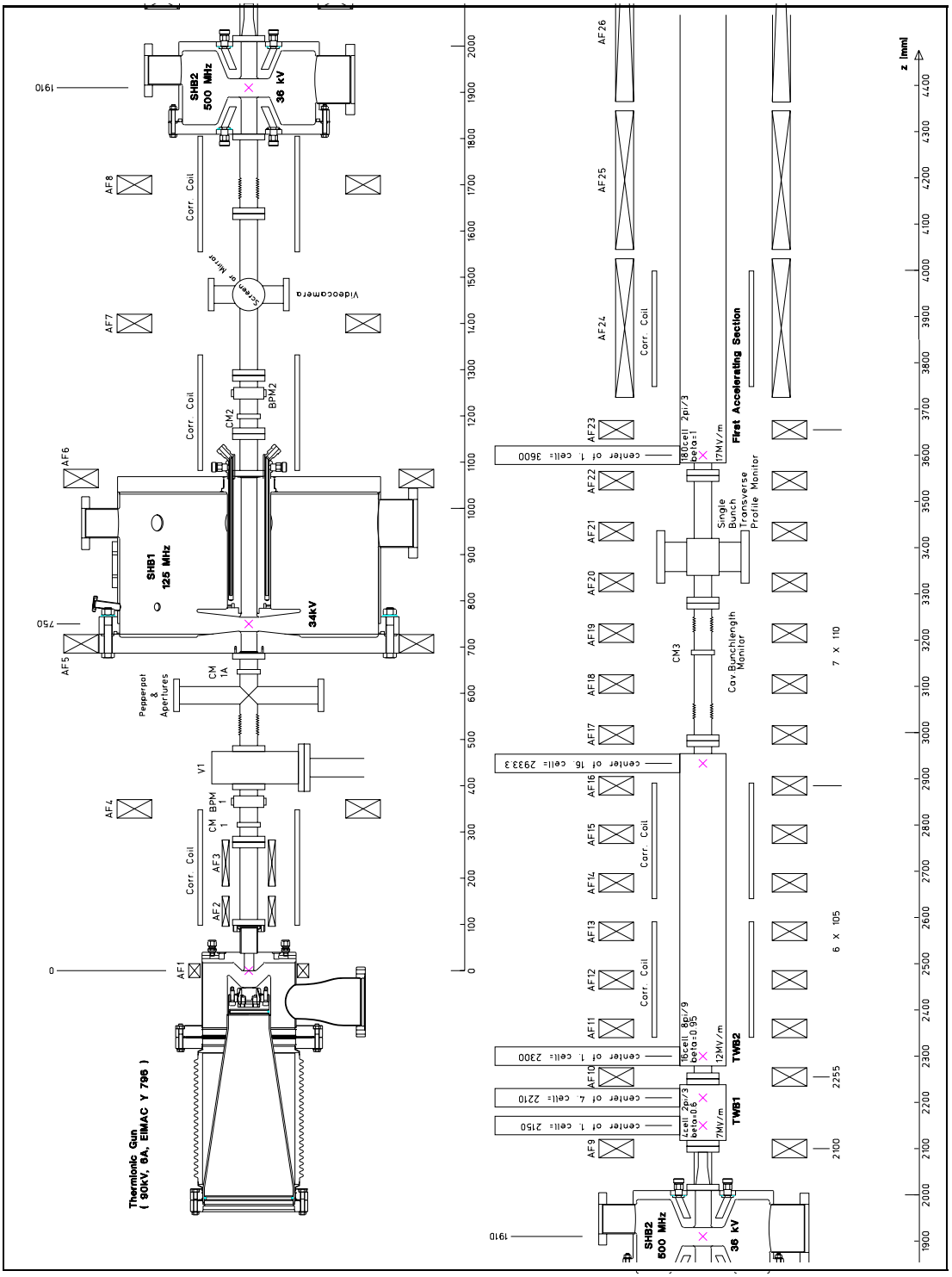

Figure 4.4.1: *Layout of the injector for the SBTF.*

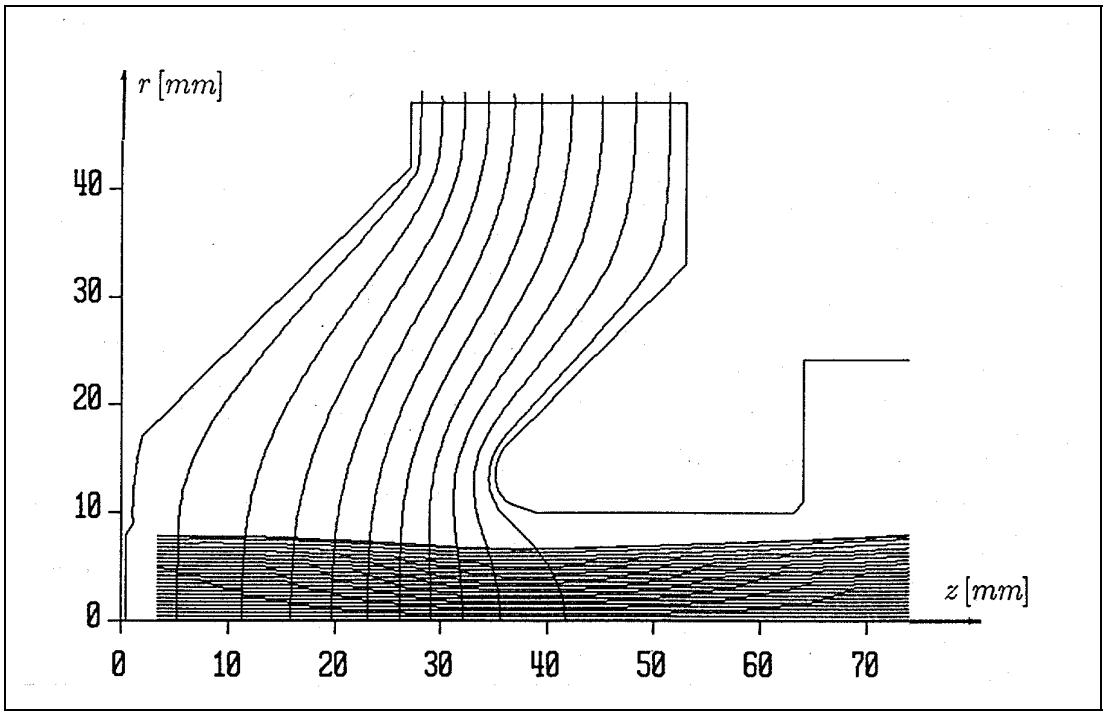

Figure 4.4.2: *Gun geometry with equipotential lines and space charge limited electron rays calculated at* $90\,kV$.

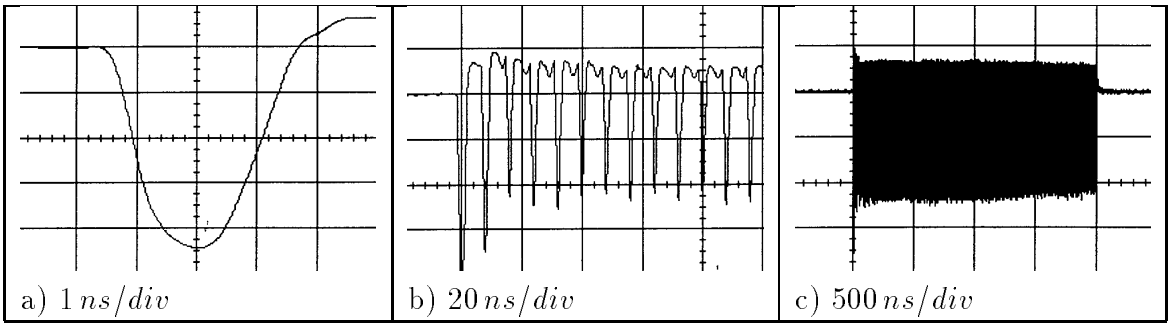

Figure 4.4.3: *Measured gunpulses at CM1. The first pulse of the bunchtrain a), the initial part b) and the whole bunchtrain c) of 250 bunches with* $8\,ns$ *spacing.*

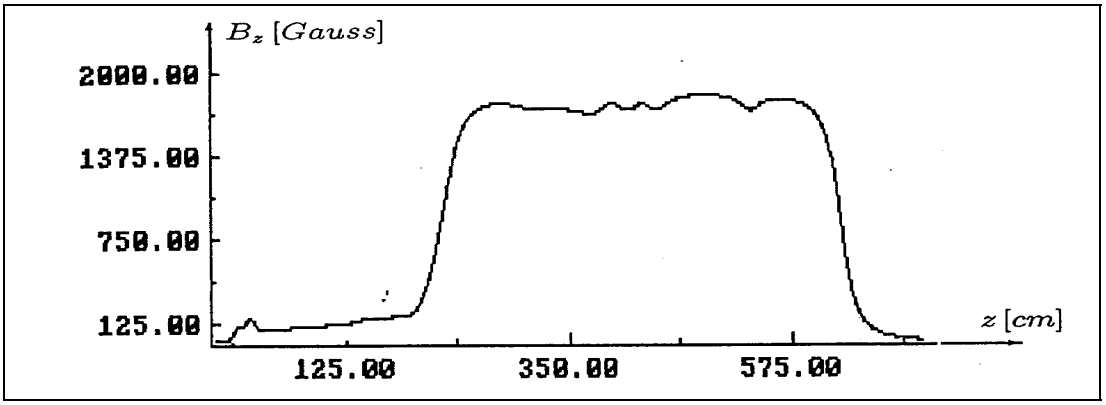

Figure 4.4.4: *Solenoidal fieldstrength B_z along the injector.*

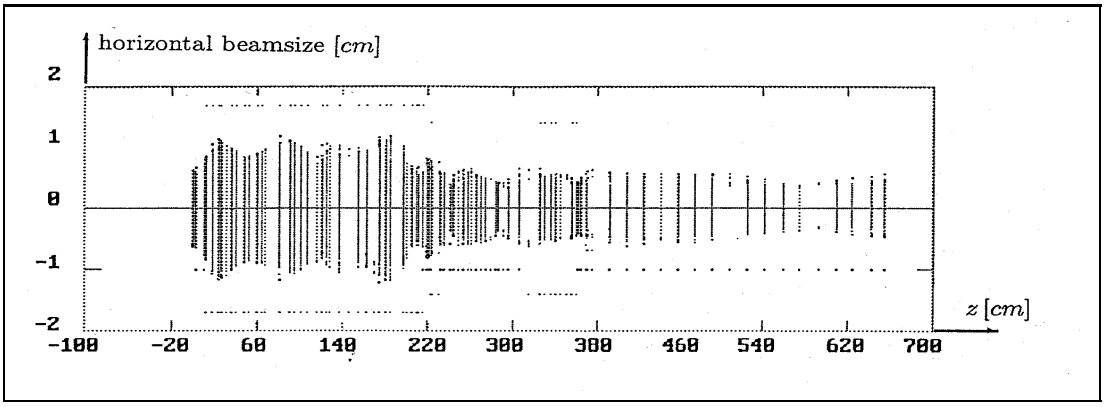

Figure 4.4.5: *Maximum horizontal beamsize and given aperture along the injector.*

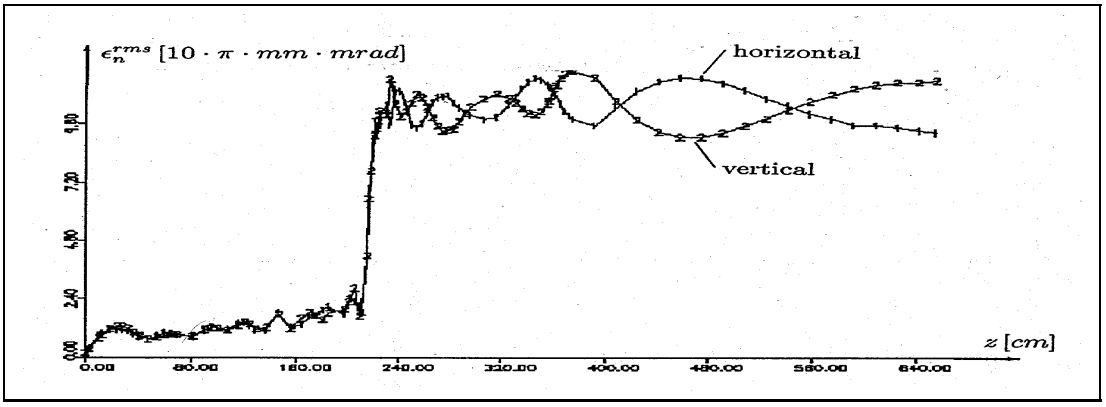

Figure 4.4.6: *Normalized horizontal and vertical rms-emittance along the injector.*

4.4.2 Positron Source

4.4.2.1 Introduction

A fundamental intensity limit for positron sources is given by the thermal stress which is built up in the conversion target due to the energy deposition of the primary beam. In case of the SBLC a complete bunch train contributes to the thermal stress in the target. Between successive linac pulses the target can be rotated so that the heat load is distributed over the target and contributes only to the average heat load. In Table 4.4.2 the design parameters of SBLC are compared with parameters reached at the SLC positron source which is the positron source with the highest intensity operating so far.

The SLC source is operating close to the stress limit of the target. An extension of this kind of source by 2 orders of magnitude in intensity seems to be impossible with a reasonable effort of technological development. Therefore a new concept based on the conversion of high energy wiggler radiation in a thin target has been developed [11, 12]. The scheme allows also to produce polarized positrons but the technological demands for a polarized source are higher than for an unpolarized source. The present design is for an unpolarized source but allows for a later upgrade to produce polarized positrons.

parameter	SLC	SBLC
# of positrons p. pulse	$3...5 \cdot 10^{10}$	$3.66 \cdot 10^{12}$
# of bunches p. pulse	1	333
pulse duration	3 ps	2 μs
bunch spacing	8.3 ms	6 ns
repetition frequency	120 Hz	50 Hz

Table 4.4.2: *Comparison between SBLC and SLC parameters.*

4.4.2.2 General Layout

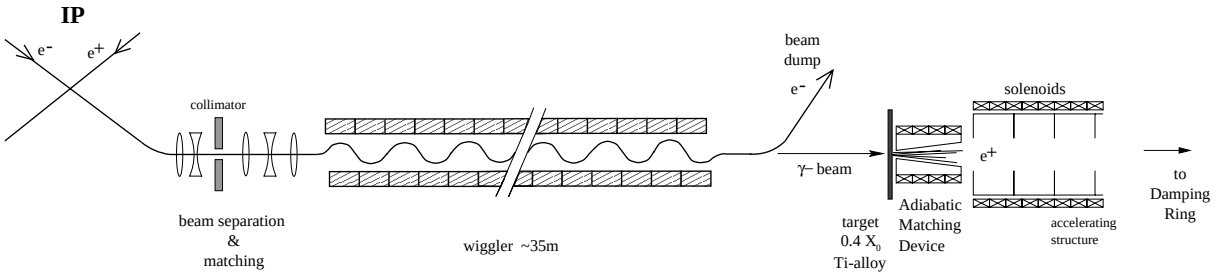

Figure 4.4.7: *Sketch of the positron source layout.*

A schematic layout of the source is shown in fig. 4.4.7. The source is designed to produce twice as much positrons as required. The 250 GeV electron beam is used after collision as primary beam for the positron production. Due to the strong beam-beam forces during the interaction process the emittance of the beam is increased and the energy distribution has developed a long tail of low energy particles. The outgoing electron beam is separated from the incoming positron beam and then collimated in order to remove the low-energy tail. More than 80% of the particles pass through the optics (see section 4.4.2.3). The final beam emittance is $\epsilon_x < 1 \cdot 10^{-8}$ m and $\epsilon_y < 1 \cdot 10^{-9}$ m, sufficiently small to match the beam to the successive wiggler section. The wiggler is a conventional wiggler of 35 m length. Here photons are generated with a broad energy distribution extending up to above 70 MeV. A dipole section of ≈30 m length separates the electron beam from the photon beam and guides it to the beam dump. The photons are used to produce electron-positron pairs in the thin conversion target. A minimum spot size of the photon beam on the target of σ_{min}=0.5mm can be realized. The heating of the target is dominated by the ionization losses of electrons and positrons given by $E_{dep} \approx 2\,\mathrm{MeV\ cm^2/g}$ per charged particle. Thus the temperature rise of the target ΔT can be estimated as:

$$\Delta T[K] = \frac{2Ne \cdot 2 \cdot 10^6}{c \cdot A \cdot \eta} \tag{4.4.1}$$

where c denotes the heat capacity in $\mathrm{Jg^{-1}K^{-1}}$, A the source area in $\mathrm{cm^2}$ and η the efficiency of positron capture after the target.

In order to get N positrons, $2N/\eta$ particles (electrons and positrons) have to emerge from the target. The heat load of the target is determined by three more or less free parameters:
- the heat capacity of the target material c,
- the efficiency of the capture optics η,
- the source area A.

An increased source area counteracts a high capture efficiency, because the phase-space density of the emerging positrons is reduced, thus a small source area is favorable. Since in the present design the photons are generated in a wiggler, rather than by bremsstrahlung in the target, a high positron yield is reached with a thin target of only 0.4 radiation length (X_0) thickness. Compared to a conventional source the thermal stress of the target can be significantly reduced by two effects:
- one is able to use a material with low nuclear charge Z which in general have a high heat capacity.
- the divergence of the positron beam is small due to the reduced scattering in the target and hence the capture efficiency is increased. A conventional target requires many radiation lengths for the full development of the electromagnetic cascade. Positrons which are produced in the first steps of the cascade will not emerge from the target due to the ionization losses inside the material. The ionization loss per radiation length depends on the material and is lower for high Z materials. Hence a high Z material has to be used in a conventional source in order to reach a high positron yield. In thin targets, however, the conversion efficiency is in first order independent of the

material, hence it is possible to use a low Z material which has a higher heat capacity (Dulong-Petit-rule). In the present design a Titanium alloy is foreseen as conversion target which allows to increase the particle density in the target by about an order of magnitude as compared to a high-Z Tungsten-Rhenium alloy.

The second advantage of a thin target is the reduced multiple scattering which determines the transverse beam emittance of the positrons. The rms scattering angle scales with the square root of the path length of the particle in units of X_0. The rms scattering angle scales non-linearly with the target thickness since in a conventional source most of the positrons are produced close to the target exit. Nevertheless, the transverse momenta of the positrons produced in a thin target are considerably smaller than the transverse momenta of positrons from a conventional source. Therefore the capture efficiency is increased by a factor 4-5 in the present design as compared to a conventional source.

The capture optics behind the target is of a conventional design. Since the positrons have a broad distribution of transverse and longitudinal momenta they have to be accelerated in a acceleration section embedded in a solenoid field. The acceptance of a solenoid channel is characterized by a large spot size and small angles while the positrons emerging from the target have a small spot size and large angles. To match the positrons to the acceptance of the solenoid, an Adiabatic Matching Device (AMD) is used. It consists of a tapered solenoid field which starts with a high initial field and tapers down adiabatically to the constant end field.

After acceleration to an energy of 150-200 MeV the positrons are separated from the electrons and the photons in a magnetic chicane. The electron and the photon beams are dumped and the positron beam is accelerated to its final energy and transferred to the damping ring.

The safety margin of a factor of two in the positron production rate is valid for 250 GeV electron beam energy. For operation at lower energy this margin is reduced. Without modifications, the source can be used down to about 160 GeV. Operation at lower energy with full design positron beam intensity requires to increase the length of the wiggler.

In the following the components of the positron source will be discussed in more detail.

4.4.2.3 Spent Beam Capture System

Due to the very strong beam-beam force the particles which do not pass through the center of the opposing bunch are strongly deflected. This disruption effect causes a broadening of the angular distribution after the interaction. The beam size remains nearly constant or even decreases due to the focusing pinch effect.

For all investigations a data set of roughly 12,000 particles was created with a beam-beam simulation code using the parameters at the interaction point. Fig.4.4.8 shows the phase space distributions both in the horizontal and vertical plane. The differences in the distribution are caused by the flatness of the beam.

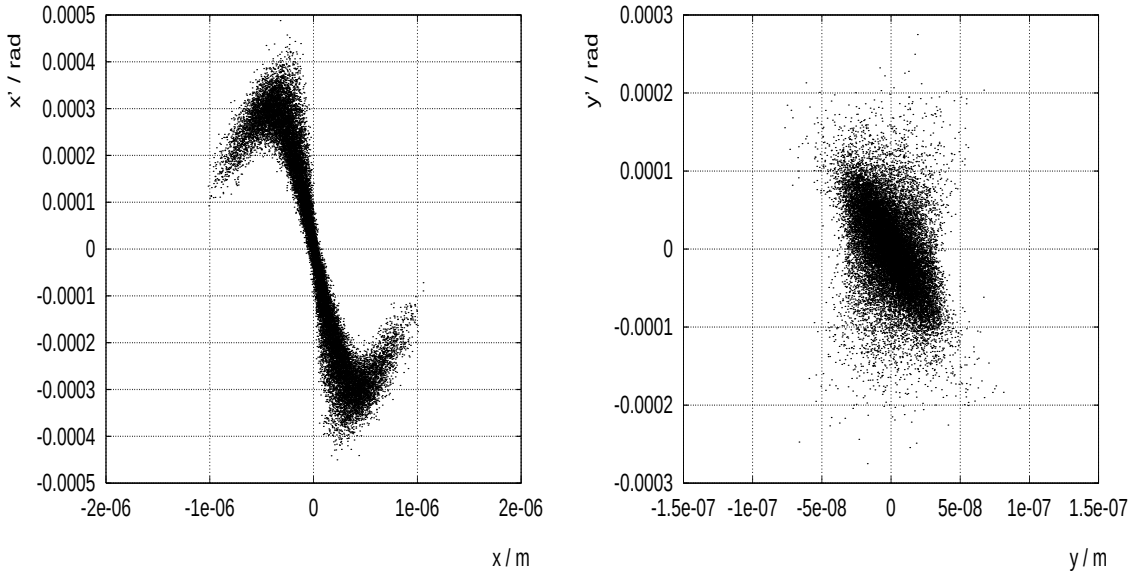

Figure 4.4.8: *Horizontal and vertical phase space distribution after the interaction.*

The deflected particles emit high-energy synchrotron radiation (beamstrahlung). This statistical process causes a broad energy spread of the disrupted beam and a mean energy loss of 3% of the initial energy. A non negligible part of the beam has lost more than 10% energy. Fig.4.4.9 shows the energy distribution after the interaction.

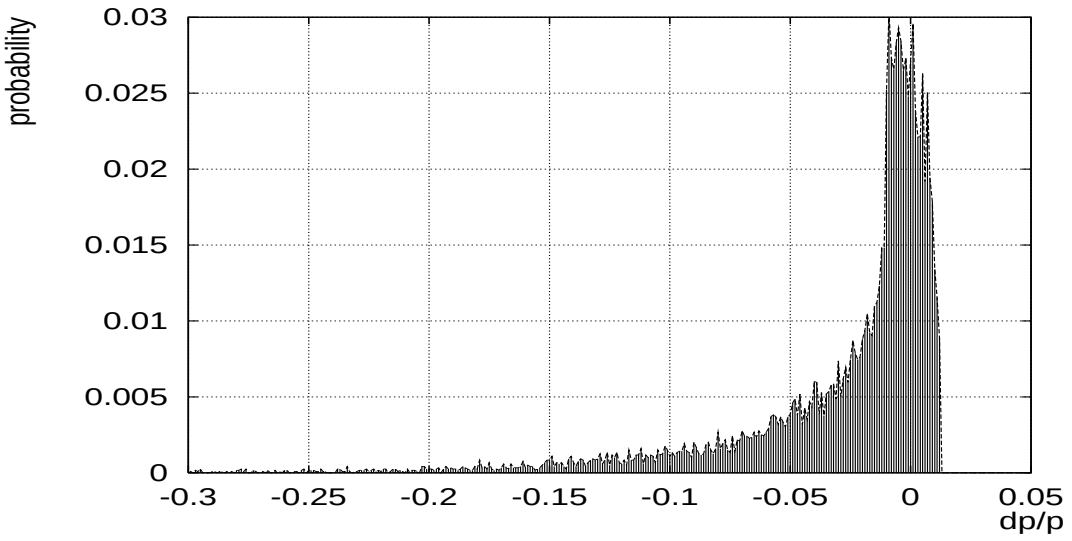

Figure 4.4.9: *Energy spectrum of the disrupted beam*

The disrupted electron beam leaving the IR is separated from the incoming positron beam by a using a crossing angle of 6 mrad. Therefore the disrupted beam after the IR

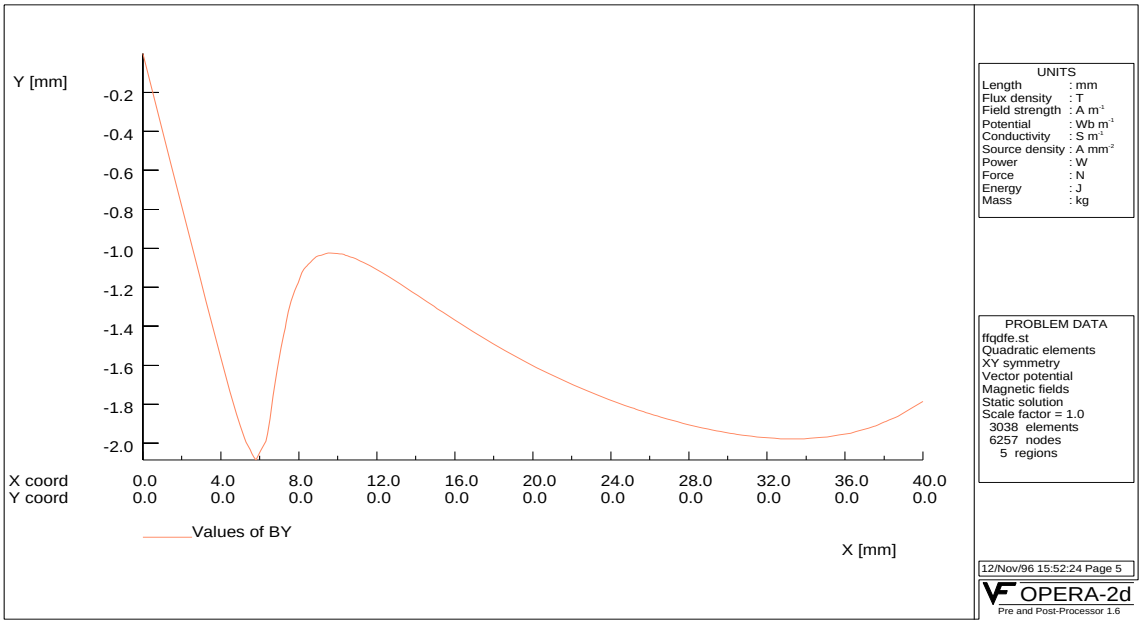

Figure 4.4.10: *Vertical magnetic field as a function of distance from axis. The spent electron beam enters the quadrupole with a horizontal offset of 13 mm.*

enters the final doublet (FD) for the incoming positron beam 13 mm displaced from the magnet axis. The field of the final quadrupole with a geometry as shown in Fig.4.7.16 in section 4.7 has been analyzed numerically. Fig.4.4.10 shows the vertical magnetic field as a function of distance to the symmetry axis of the quadrupole. The shape shows that there are higher order multipole components which are changing along the path through the FD due to the increasing distance from the axis. The emittance growth caused by the non-linearity of the field and by the synchrotron radiation has been determined by particle tracking simulations. It is found that the horizontal emittance is about two orders of magnitude larger than that of the incoming beam.

For the investigation of the beam capture optics the matched optical functions after the FD are determined for sub-ensembles of the spent beam obtained by applying an energy cut removing part of the beam which has lost more than a certain fraction of energy.

At the end of the FD the separation from the incoming positron beam is 4.2cm with a total angle of 8.05mrad (2.05mrad due to the deflecting effect of the FD field). This allows to place a doublet of half-quadrupoles 10 m downstream from the FD. A bending magnet and a second quadrupole doublet are used to match the optical functions to the beginning of the chromatic correction section.

Chromatic Correction System

After initial separation of the spent beam as described above a magnet lattice basically very similar to the horizontal CCS for the incoming beam follows. The boundary

conditions for the design of this beam-optical system are:

- The geometry of the beamline should be such that it fits together with the FFS into the same tunnel.
- The bending magnets have to be sufficiently weak to avoid strong emittance growth from synchrotron radiation.
- The momentum bandwidth has to be large to accomodate a large fraction of the broad momentum distribution of the spent beam.

Starting from a basic layout which fulfills the first two conditions an optimization of the bandwidth is performed by adding sextupoles at strategic positions in the lattice. An ensemble of trajectories representative of the spent beam properties is tracked through the system and optimum sextupole strengths which lead to a minimum beam emittance at the end of the lattice are determined. The procedure is similar to the one applied in ref. [13]. The amount of spent beam accepted by the system is directly related to the maximum tolerable emittance in the wiggler. As shown in fig. 4.4.12, the horizontal emittance starts growing rapidly if more than 85...90% of the beam is passed through the beamline, indicating that the low-energy tail falls outside the bandwidth of the optics. In this range the vertical emittance does not exceed the value of $\varepsilon_y = 10^{-9}$ m which is five times lower than required for the unpolarized source. So due to the limitations on the horizontal emittance, even with an optimized achromatic system it is not possible to transport the whole beam from the IR on through the capture optics and afterwards through the wiggler. Thus the low energy tail which contains a considerable fraction of the beam power has to be collimated.

After the end of the CCS's the optics is continued with a drift space of 20 m and a quadrupole triplet. The beam is focused such that the radiation emitted in a 35m long wiggler hits the target in a focal point 30 m behind the wiggler i.e. 70 m behind the last quadrupole doublet.

Fig. 4.4.13 shows the geometry of the whole capture system with the wiggler and the drift space to the target with regard to the beam delivery system of the oncoming positron beam. The separation between the two beamlines is sufficiently small to fit into a tunnel of 4 m diameter.

The optimization of the optics and the need to collimate the major part of the low energy particles in regions without optical elements (see Table 4.4.3) results in a capture efficiency of 87.5% of the disrupted electron beam.

Fig. 4.4.14 and fig.4.4.15 shows the maximum beam envelopes of the disrupted beam along the capture optics with the position of the collimators. The 35 m long wiggler is positioned between 450 m and 485 m downstream from the IP. In this region the maximum vertical beam size does not exceed values of 2 mm.

Inside the wiggler in the horizontal plane some particle amplitudes are growing although the whole beam is focused on the target. The reason is the remaining chromaticity which causes a defocused low energy subset of the captured beam.

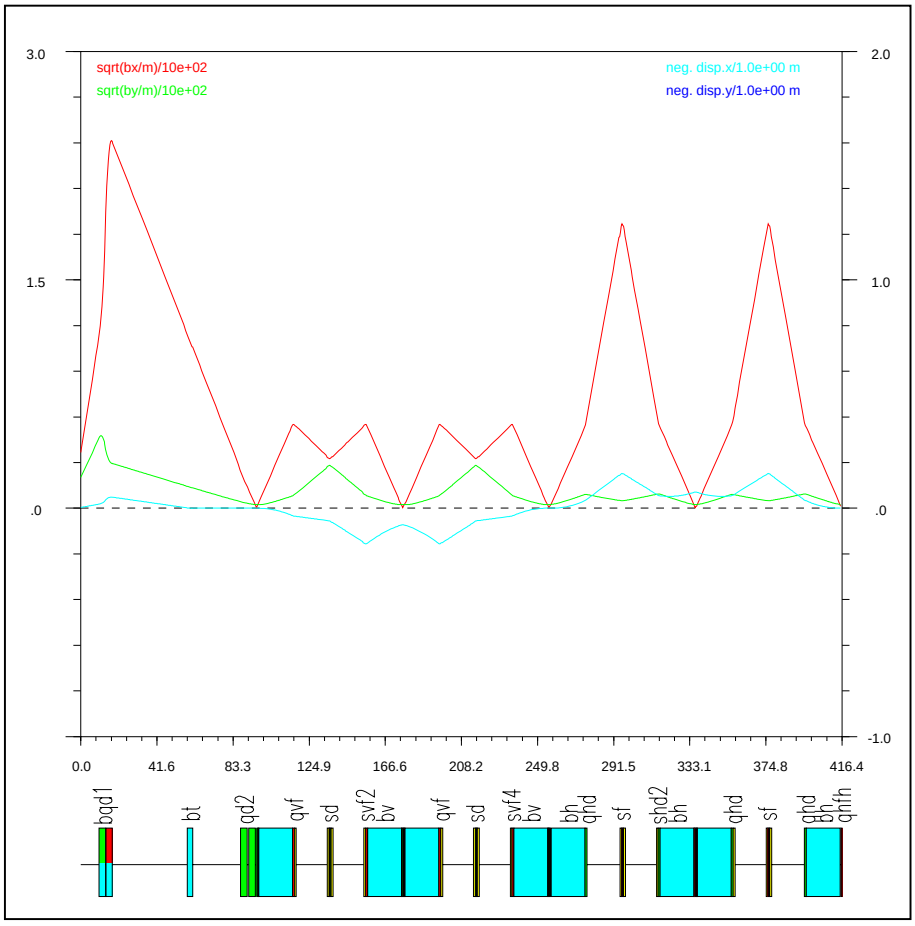

Figure 4.4.11: *Optics of the spent beam capture system from the end of the FFQ's to the end of the CCS.*

Stability of the positron source

The efficiency of the capture optics for the disrupted electron beam depends on the parameters of the interacting bunches. The optics and the collimation system described above are developed for interacting bunches with design parameters. In reality, the capture efficiency for the disrupted beam may not be constant but depends on the energy spread due to beamstrahlung. As explained above, the beamstrahlung is a function of the bunch charge and other interaction parameters.

If we consider a perturbation of the interaction, for example a displacement of the orbit, the spent electron beam would not be disrupted like in a head-on interaction. Hence the number of captured electrons passing the collimation system can be higher. The positron bunches in the next pulse have a higher charge which in turn causes a higher electron beam energy spread after the IP. The fixed energy acceptance of the capture optics then leads to a lower intensity electron beam for the photon production. In the second pulse after the perturbation the positron bunch has a lower charge and so the system can oscillate. For a stable operation of the linac, this oscillation must be

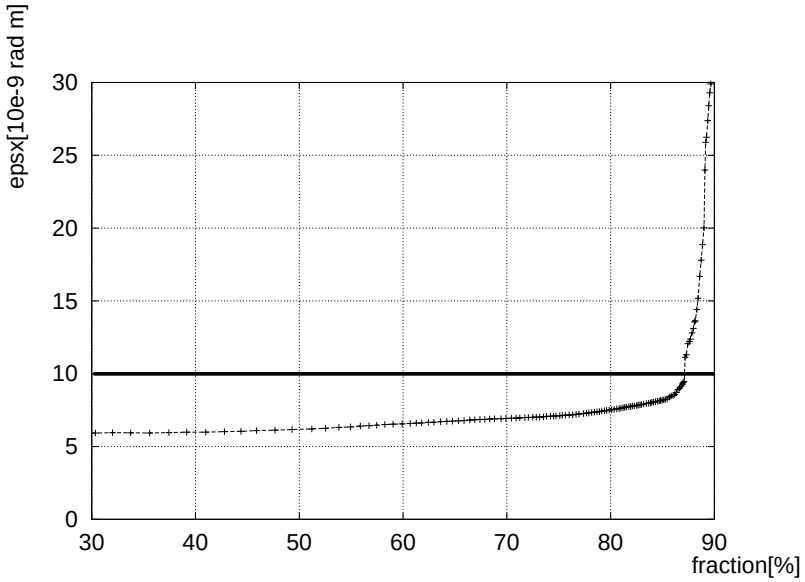

Figure 4.4.12: *Horizontal emittance at the end of the CCS vs. percentage of the initial beam obtained by an energy dependent cut. The thick line shows the horizontal emittance limit for the unpolarized source.*

Collimator	Distance from IR doublet [m]	Collimated power [KW]	Remarks
COL0	0.00-10.00	67.57	between the IR doublet and the 1st half-quad
COL1	38.23-58.23	70.08	between the 2nd half-quad and the first dipole
COL2	61.23-87.40	305.02	behind the first dipole and the following quad
COL3	137.90-154.90	214.56	driftspace inside the CCS
COL4	197.90-214.90	27.99	driftspace inside the CCS
COL5	217.90-234.90	128.50	drfitspace inside the CCS
COL6	377.90-394.90	75.37	driftspace inside the CCS
COL7	416.40-436.40	41.63	driftspace after the CCS
COL8	445.40-450.40	8.17	5m before the wiggler

Table 4.4.3: *Collimator positions and collimated beam power.*

damped.

The investigation of stability is started considereing the maximum possible perturbation, i.e. the case that the bunches do not interact at all. The electrons pass the collimation system completely and the positron bunches for the next pulse have a 14% higher charge than designed. The next interaction is simulated with this asymmetric bunch charges. The outgoing disrupted electron beam was tracked through the capture optics to obtain the efficiency for the following pulse. This yields a new (reduced)

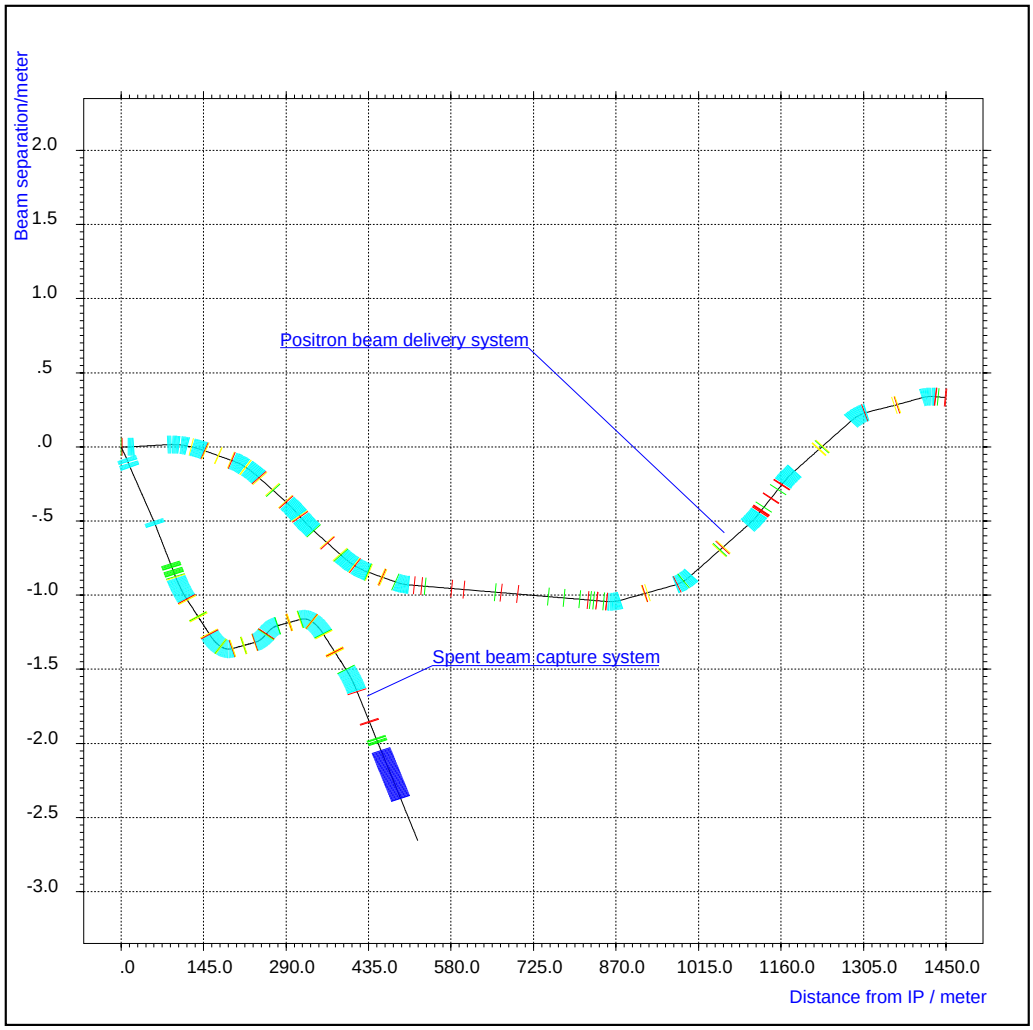

Figure 4.4.13: *Beam line for the disrupted beam with the 35 m long wiggler (lower branch) and the incoming positron beam (upper branch). At the end of the capture optics the separation is 1.7 m.*

positron intensity for the next interaction, etc. Fig. 4.4.16 shows the resulting behavior of the bunch charge as a function of interactions after the perturbation. The oscillation decreases and so the positron source can be operated stably from this point of view.

Efficiency Gain due to Parameter Change at the IP

The efficiency of the capture system is limited by higher order geometric and chromo-geometric aberrations. With a relatively moderate adjustment of the interaction parameters, both the horizontal beam emittance and the energy spread can be reduced, thus decreasing the population of the tails in the spent beam which have to be collimated. This is demonstrated in Fig. 4.4.17 where the spent beam capture efficiency is

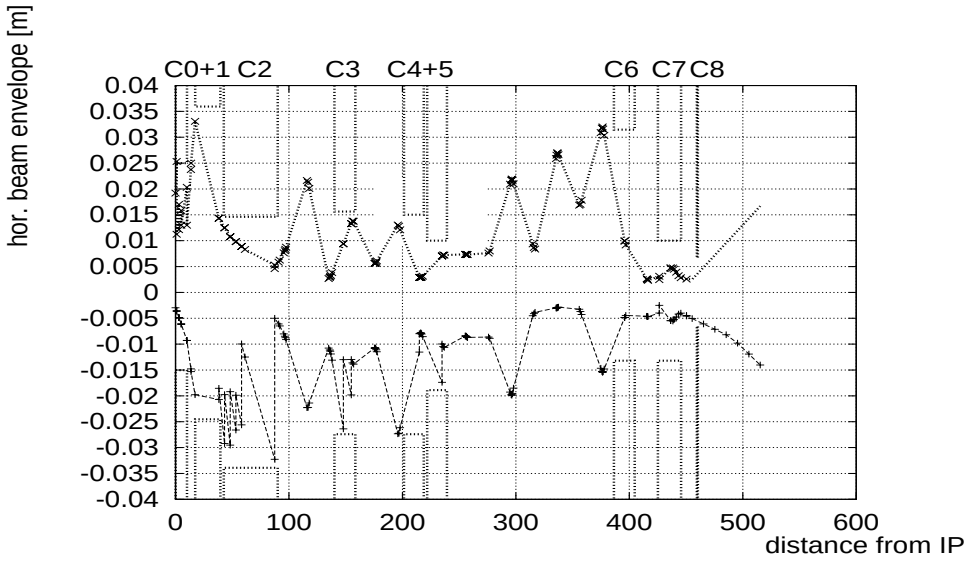

Figure 4.4.14: *Horizontal envelope for an ensemble containing 87.5% of the spent beam.*

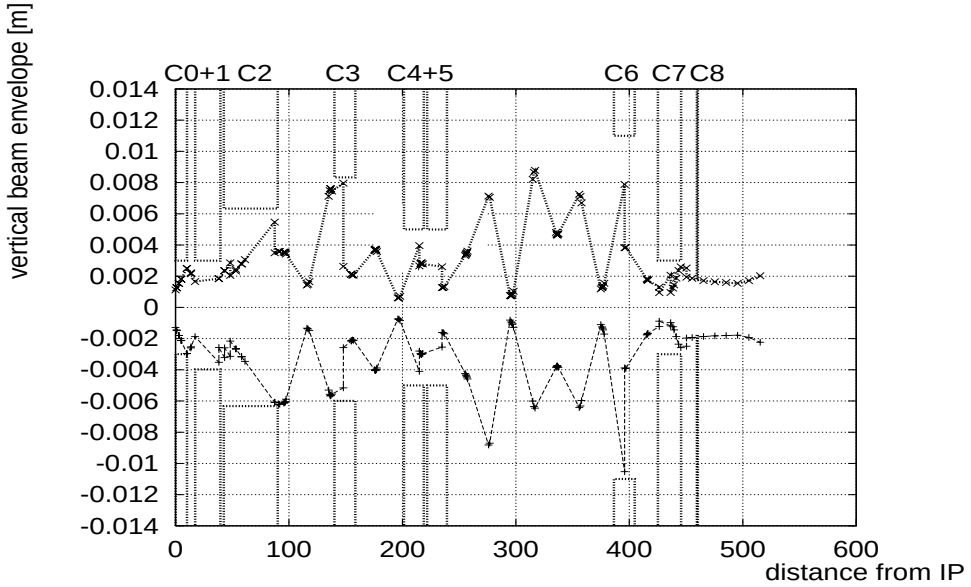

Figure 4.4.15: *Vertical envelope for an ensemble containing 87.5% of the spent beam.*

shown as a function of the horizontal beta of the positron beam at the IP. An increase of $\beta_x^*(e^+)$ by a factor of two already reduces the amount of collimated spent beam from 12.5% to 4%. At the same time, the luminosity is reduced by only about 20%, which can be compensated by a slight reduction of the vertical beam emittance. With such a parameter modification, an efficient operation of a polarized positron source would be greatly facilitated.

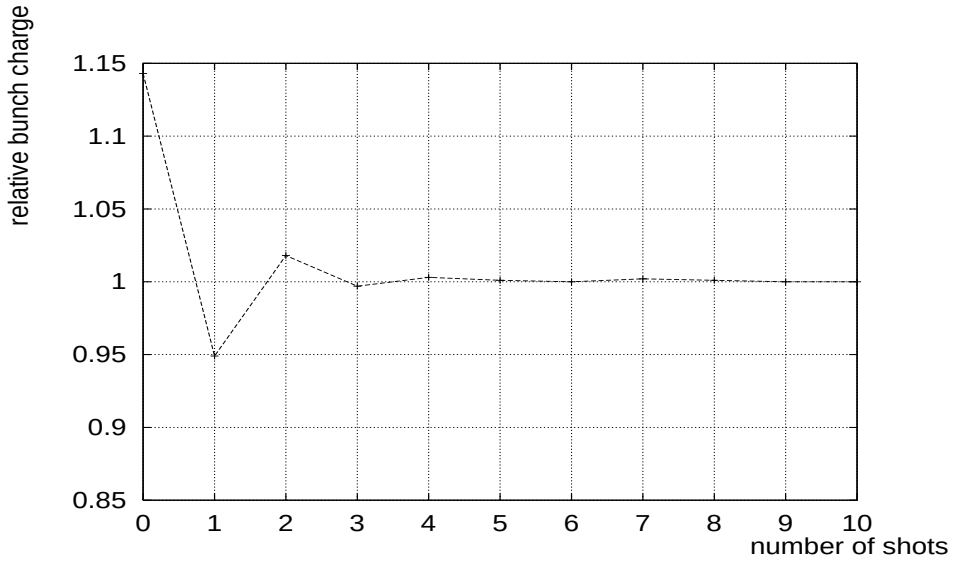

Figure 4.4.16: *Oscillations of the positron bunch intensity after one missing interaction. The bunch charge reaches the design value after 4 pulses.*

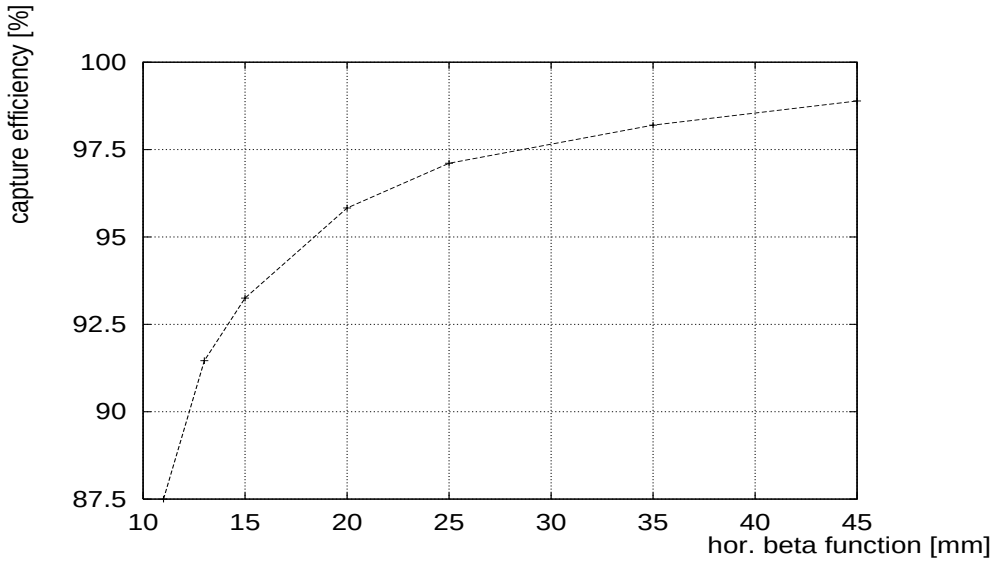

Figure 4.4.17: *Capture efficiency as a function of the horizontal β-function of the positron beam at the IP. Starting from the design value of 11 mm the capture efficiency reaches 98.9 % of the disrupted beam for $\beta_x^*(e^+) = 45$ mm.*

4.4.2.4 Wiggler

A planar wiggler consists of a row of short dipole magnets with constant field strength but alternating field direction. For a large period length λ_w the photon number spectrum can be approximated by the well known photon number spectrum of dipole magnet. Fig. 4.4.18 shows the photon number spectrum of a 1m long dipole with a magnetic field of B=1.7 T.

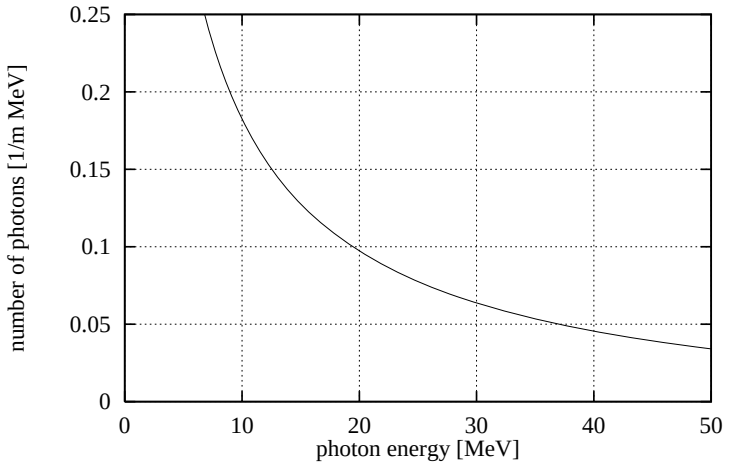

Figure 4.4.18: *Photon number spectrum of a planar wiggler with B=1.7 T at a beam energy of 250 GeV.*

In order to reach a small spot size of the radiation on the target the electron beam is focused through the wiggler onto the target. The contribution of the natural opening of the wiggler radiation to the spot size can be approximated by:

$$\sigma_{SR} \approx \frac{eB\lambda_w}{2\pi p_e} \cdot (L/2 + D) \tag{4.4.2}$$

Here p_e denotes the electron momentum, L the wiggler length and D the driftspace between the wiggler and the target.

For $L \approx$35 m and $D \approx$30 m the period length λ_w should not exceed 3.2 cm in order to reach a spot size contribution of 0.5 mm. Since the electron beam emittance is quite small a gap height of only 5mm is sufficient to transport the beam through the wiggler. Today wigglers and undulators based on permanent magnet technology are widely used in both synchrotron radiation sources and free electron lasers. Period length and magnetic fields similar to the values discussed above are not unusual for these devices. In contrast to the sinusoidal field distribution of a synchrotron radiation device a more rectangular distribution would be favorable for the positron source in order to keep the length of the wiggler shorter. Various inexpensive proposals of wigglers with a rectangular field distribution and similar period length are discussed in ref. [14].

4.4.2.5 Target

A high energy photon passing through a material can create an electron positron pair in the field of a nucleus (pair production). These charged particles again lose energy on their way through the material via collisions with electrons (ionization) and radiation processes in the field of a nucleus (bremsstrahlung). The ionization losses account for the majority of heat deposition in the material, while photons produced via bremsstrahlung may once more produce electron positron pairs. This sequence continues, i.e. the number of electrons, positrons and photons increases exponentially, while the mean energy of the particles decreases. The development of the shower decays when the particle energy drops below $\approx$10 MeV because the energy loss due to ionization exceeds the production of photons at low energies. Bremsstrahlung and pair production are essentially inverse processes, hence they can be characterized by a common parameter called the radiation length X_0. The radiation length of a material is approximated by:

$$X_0^{-1} = \frac{4\alpha r_e^2 N_A \rho}{A} \cdot Z(Z+1) ln(183 Z^{1/3}) \qquad (4.4.3)$$

where A is the atomic weight, Z the nuclear charge, ρ the density of the material and N_A Avogadro's number.

Since for important electromagnetic processes (bremsstrahlung, pair production, multiple scattering) some or all of the dependence upon the medium is contained in the radiation length, it is convenient to measure the target thickness in terms of the radiation length. Besides bremsstrahlung and pair production the shower development is influenced by many other processes like Compton scattering, Møller scattering, Bhabha scattering, photo effect etc. A complete treatment of the development of an electromagnetic cascade is possible only with a numerical simulation code. The following calculations have been performed with the code EGS4 [15]. The EGS code is a general purpose package for the Monte-Carlo simulation of electromagnetic showers. Since its formal introduction in 1978 it has been extended and improved and a lot of comparisons with experiments have verified the performance.

Fig. 4.4.19 shows the positron yield per electron as function of the target thickness for different materials. The incoming photon beam has been generated in a 1m long wiggler of 1.7 T magnetic field. For a target thickness above $0.5\,X_0$ the yield increases slowly before it starts to decrease again. Since the multiple scattering increases the beam emittance with increasing target thickness, the optimum overall efficiency, i.e. including the capture efficiency, is found at about $0.4\,X_0$. At this thickness the yield for a low Z material like Titanium is only about 16 % lower than for Tungsten.

In Fig. 4.4.20 the temperature distribution in a Titanium target induced by a single train of wiggler photons from a 35 m long wiggler of 1.7 T is shown. As a safety margin the number of positrons produced in this simulation exceeds the nominal value behind the capture optics by a factor of two.

The maximum temperature rise of 760 °C is slightly higher than the maximum temperature reached in a Tungsten-Rhenium target close to the stress limit given in ref. [16]. The density of charged particles is about 5 times higher in the Titanium

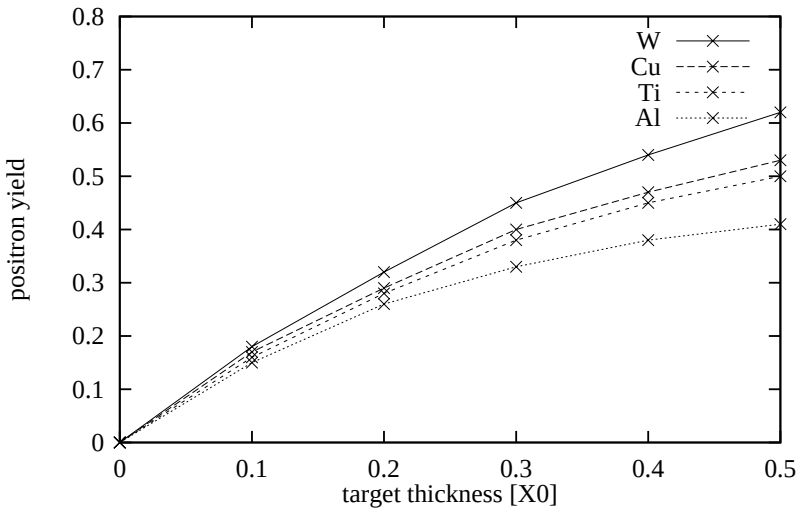

Figure 4.4.19: *Positron yield vs. target thickness for different materials. The photons are generated by a 250 GeV electron beam in a 1 m long wiggler of 1.7 T magnetic field.*

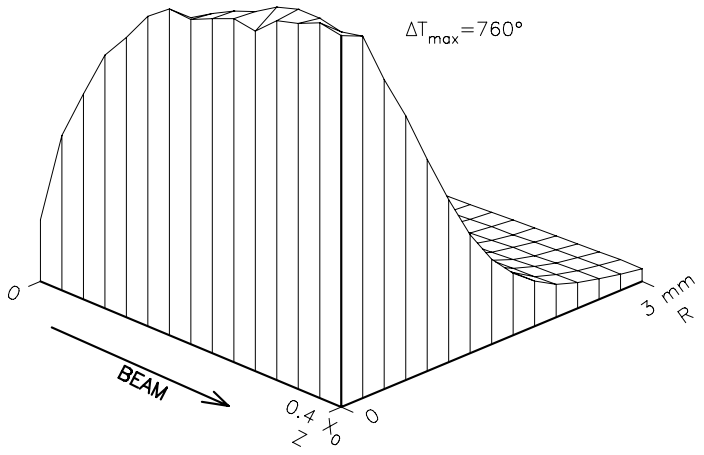

Figure 4.4.20: *Radial and longitudinal temperature distribution in the Titanium target. The spotsize of the incoming beam is $\sigma_{x,y}$=0.7 mm.*

target but due to the 5 times higher heat capacity the temperature does not increase dramatically.

Besides the temperature rise the mechanical constants of the target material have to be taken into account. Experimental data for the maximum heat load of a low Z positron conversion target are not available even though the material is used in high power collimators. In order to scale the results obtained for high Z targets to

material	c [J/kg]	α $10^{-6}K^{-1}$	E $10^{11}N/m^2$	$P_{0.2}$ $10^7N/m^2$	ΔT_{crit} K^{-1}	x_0 cm	ρ g cm^{-3}
W-26Re	0.13	5.0	4.00	91.0	455	0.35	19.3
Ti	0.52	8.4	1.16	55.0	564	3.56	4.54
Ti-5Al-2.5Sn	0.52	9.3	1.17	86.3	793	3.5	4.46
Ti-13V-11Cr-3Al	0.62	8.8	0.98	96.1	1114	3.5	4.82

Table 4.4.4: *Material constant of Tungsten-Rhenium and various Titanium alloys.*

the case of low Z targets the material constants can be combined with respect to their proportionality to the mechanical stress $P_t \approx \Delta T \alpha E$ induced by heating (α: expansion coefficient, E: elastic modulus).

The induced stress has to remain below the 0.2% yield strength $P_{0.2}$ which is the stress where the deformation of a material ceases to be elastic, $P_t < P_{0.2}$.

Table 4.4.4 lists material constants for the Tungsten-Rhenium alloy used in the SLC positron source and various Titanium alloys. The geometrical dimensions of the SLC target (thickness: 2.1 cm) and a Titanium target (thickness: 1.4 cm) as well as the dimensions of the electron and photon beam spot size on the target are comparable. Therefore the temperature distribution in the targets is similar and the ratio $P_{0.2}/\alpha E = \Delta T_{crit}$ can be used to compare the maximum temperature rise that the target can withstand. It is seen from Table 4.4.4 that the maximum temperature in a Titanium target can be up to twice as large as in a Tungsten target.

The average heat load of the target amounts to 6 kW, therefore water cooling of the target is necessary. In order to avoid a rotating feed through for the cooling water a winch mechanism can be utilized as at the SLC source [17].

4.4.2.6 Capture Optics

The particles which emerge from the target have to be accelerated in a cavity embedded in a solenoid field for focusing. Here the final emittance and the efficiency of the positron source are defined. Since, compared to the thick target of the conventional source the multiple-scattering is reduced in a thin target, the transverse momenta of the positrons emerging from the target are smaller. Fig. 4.4.21 compares transverse momenta of a SLC-like source with those of a thin target source driven by photons from a wiggler.

The smaller transverse momenta lead to a higher capture efficiency of the positrons behind the target. In order to match the emittance of the positron beam, characterized by a small spot size and a large divergence, to the acceptance of the solenoid which is determined by a large spot size and a small divergence a matching section is introduced between the converter target and the first accelerating cavity. The matching section consists of a so-called Adiabatic Matching Device (AMD), a tapered solenoid starting with a high initial field and tapered adiabatically down to the constant end field. The acceptance of the system is matched to the acceptance of the damping ring so that no particle losses occur later in the damping ring. Besides the acceptance of the damping

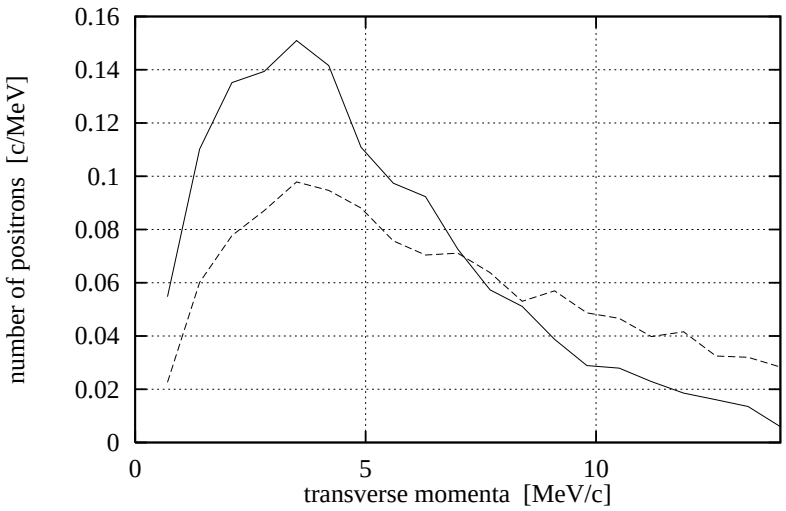

Figure 4.4.21: *Comparison of transverse momentum distribution for a SLC-like source ($6X_0$, W, dotted line) and a thin target as proposed here ($0.4X_0$, Ti, solid line).*

ring that limits the useful acceptance of the matching device two mechanisms lead to an emittance growth of the positron beam in the matching device and hence to additional particle losses:
- emittance growth due to non adiabatic fields.
- bunch lengthening due to path length and velocity differences.
R. Helm has found a solution for the particle motion in an adiabatically varying solenoid field [18] from which he derived the optimum on-axis field distribution for the matching device along the longitudinal coordinate z as:

$$B(z) = \frac{B_i}{1 + g \cdot z} \tag{4.4.4}$$

where B_i is the initial solenoid field and g the taper parameter.

The condition for an adiabatic field variation is then given as $(gp_e)/(eB_i) \ll 1$. In order to fulfill this condition for particles with higher energy the taper parameter g has to be small. However, this means that the matching section becomes long and that the bunch lengthening becomes stronger. An optimum is reached with g=30 m^{-1} in the present design. Figure 4.4.22 shows the energy distribution of the positrons as they emerge from the target and the fraction of captured particles for the optimized optics. Figure 7 shows the longitudinal distribution of the positrons behind the AMD. While the core of the distribution represents the incoming electron beam (σ_s= 0.3mm or $\approx 1°$ RF phase) a long tail has been developed due to bunch lengthening effects. The positrons in the tail will be lost in the damping ring since the curvature of the RF leads to a large energy deviation of these particles. In the simulation an energy acceptance of $\pm 1\%$ corresponding to an RF phase of $\pm 7.5°$ is assumed.

A capture efficiency of 17 % is reached with an initial field of $B_i = 7$ T. Fields of up to 8 T have already been realized [19]. For the preacceleration a standard S-band structure

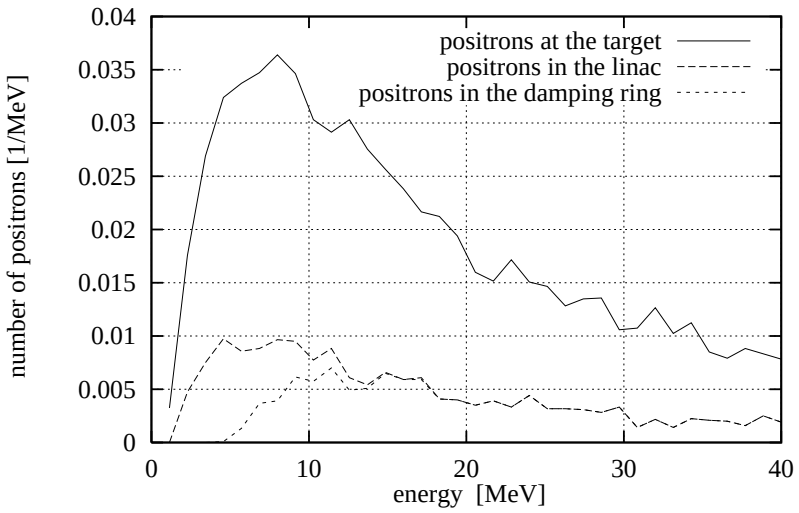

Figure 4.4.22: *Energy distribution of the positrons after the target (solid line) and the fraction of captured positrons (dashed lines).*

embedded in a solenoid field of 0.7 T can be used. With a gradient of 20 MV/m the bunch lengthening in the first acceleration section is sufficiently suppressed. Table 4.4.5 collects important parameters of the positron source.

4.4.2.7 Low Intensity Auxiliary Source

For the commissioning of the positron damping ring, the main positron linac etc., a source that works independent of the main electron linac would be desirable. Most of this work can be done or even has to be done at low intensities. Therefore a conventional low intensity source will be integrated into the high intensity source. An electron beam of only 500 MeV is sufficient to produce a few per cent of the design positron current using the thin Titanium target and the capture optics of the high intensity source. In this case the heat load of the target is high but does not reach the limits that have been previously discussed. The electron source for the low intensity positron source can also be used to provide electrons for the main linac for electron-electron and gamma-gamma collisions, respectively.

4.4.2.8 Potential Upgrade to a Polarized Positron Source

The proposed positron source allows also to produce polarized positrons as it was originally proposed by V. E. Balakin and A. A. Mickhailichenko [12, 11]. The technological demands are, however, much stronger in this case. Therefore the polarized source is regarded as a potential upgrade option.

In order to produce circularly polarized photons a short period helical undulator of about 100 m length has to be used instead of the planar wiggler. Since only the on-axis photons are completely circularly polarized off-axis photons have to be scraped

Wiggler	
peak field	1.7 T
period length	31 mm
gap height	5 mm
γ-spot size on target	0.7 mm
# of photons p. electron	368
mean photon energy	22 MeV
photon beam power	230 kW
Target	
material	Ti-alloy
thickness	1.42 cm ($0.4X_0$)
pulse temperature rise	760 K
av. power deposition	6 kW
Adiabatic Matching Device	
initial field	7 T
taper parameter	30 m^{-1}
end field	0.7 T
capture cavity iris radius	11 mm
General	
capture efficiency	17 %
# of positrons p. electron	2
norm. e^+-beam emittance	0.007 m
total energy width	$\pm$30 MeV
required D.R. acceptance	0.04 m

Table 4.4.5: *Overview of the positron source main parameters.*

off. This requires that the spot size of the photon beam on the target is dominated by the natural opening of the radiation rather than by the emittance contribution of the electron beam. Therefore the distance between the undulator and the target has to be increased to 150 m and the electron beam emittance has to be decreased to $\epsilon_x = 5 \cdot 10^{-10}$ m and $\epsilon_y = 10^{-10}$ m. The emittance requirement can easily be fulfilled for the vertical plane but is difficult to achieve in the horizontal plane. Improvements of the interaction region layout are necessary to avoid the strong emittance growth resulting from the offset of the outgoing beam in the final quadrupole.

The parameters of the helical undulator are demanding and have not been reached so far. With a period length of 1 cm an on-axis field of 1.3 T has to be reached. These parameters can be realized only with superconducting technology at a gap radius of only 2 mm. A detailed technological design of an undulator with the required parameters has not been worked out yet.

The polarization of the circularly polarized photons is transferred to the electron-

positron pairs during pair production. For the calculation of the processes in the target the EGS4 code has been extended. The code includes polarization effects for pair production, Bremsstrahlung and Compton scattering and yield a maximum longitudinal polarization of a polarized positron source of 50-60%.

Bibliography

[1] R. Alley et al., *The Stanford Linear Accelerator Polarized Electron Source*, Nucl. Instrum. And Meth. A365 (1995) 1.

[2] M. Woods et al., J. Appl. Phys. 73 (1993) 8531.

[3] A. Herrera-Gómez and W.E. Spicer, Proc. SPIE 2022 (1993) 51.

[4] D. Schultz et al., *The Polarized Electron Source of the Stanford Linear Accelerator Center*, SLAC-PUB-6606, August 1994; presented at 17th International Linear Accelerator Conference (LINAC 94), Tsukuba, Japan, 21-26 Aug 1994.

[5] H. Tang et al., *Experimental Studies of the Charge Limit Phenomenon in NEA GaAs Photocathodes*, SLAC-PUB-6515, June 1994; presented at 4th European Particle Accelerator Conference (EPAC 94), London, England, 27 Jun - 1 Jul 1994.

[6] K. Aulenbacher et al., *RF Guns and the Production of Polarized Electrons*, CLIC Note 303 and NLC-Note 20, May 1996.

[7] J.E. Clendenin, *Polarized Electron Sources*, SLAC-PUB-95-6842, May 1995; Talk given at 16th IEEE Particle Accelerator Conference (PAC 95) and International Conference on High Energy Accelerators, Dallas, Texas, 1-5 May 1995.

[8] M. Schmitz, D. Yeremian, *The Injector for the S-Band Test Facility at DESY*, Proceedings of the 1994 International Linac Conference p.71-73, Tsukuba, Japan.

[9] M. Schmitz et al., *First Tests at the Injector for the S-Band Test Facility at DESY*, Proceedings of the 1995 Particle Accelerator Conference p.929-931, Dallas, Texas, USA.

[10] M. Schmitz, *Performance of the First Part of the Injector for the S-Band Test Facility at DESY*, Proceedings of the 1996 International Linac Conference, Geneva, Switzerland.

[11] V. E. Balakin and A. A. Mikhailichenko, *The Conversion System for Obtaining High Polarized Electrons and Positrons*, Preprint INP 79-85, 1979.

[12] K. Flöttmann, *Investigations Toward the Development of Polarized and Unpolarized High Intensity Positron Sources for Linear Colliders*, DESY-93-161, 1993.

[13] R. Brinkmann, *Optimization of a Final Focus System for Large Momentum Bandwidth*, DESY-M-90-14, 1990.

[14] R. Brinkmann, J. Pflger, V. Shiltsev, N. Vinokuro, P. Vobly, *Wiggler Options for TESLA Damping Ring*, DESY-TESLA-95-24, 1995.

[15] W. Nelson, H. Hirayama and D. Rogers, *The EGS4 Code System* SLAC-265, 1985.

[16] S. Ecklund, *Positron Target Materials Tests*, SLAC Collider Note-128, 1981.

[17] E. M. Reuter and J. A. Hodgson, *3D Nummerical Thermal Stress Analysis of the High Power Target for the SLC Positron Source*, SLAC-PUB-5370, 1991.

[18] R. H. Helm, *Adiabatic Approximation for Dynamics of a Particle in the Field of a Tapered Solenoid*, SLAC-4, 1962.

[19] H. Ida, *Present R&D Status of Positron Sources for JLC-1 and ATF*, presented at Sixth International Workshop on Linear Colliders, Tsukuba 1995.

4.5 Damping Ring

4.5.1 Introduction

In a first design of a damping ring for the SBLC [1] the FODO, Inverse-Bending-Cells and the Chasman-Green lattices were investigated. The Chasman-Green lattice has been chosen, because its dynamic aperture was two to three times higher than for the other structures. For a storage ring built of 72 identical cells the acceptance is 42 mm mrad, not taking into account magnet errors.

In order to meet the strict requirements on the damping time, damping wigglers have to be introduced in the storage ring. Conventionally, the ring is replaced by a racetrack structure: two arcs with bends and two long straight sections that accommodate the damping wigglers, injection, extraction and the RF-system. In such a scheme the dynamic aperture is drastically reduced. In the design of [1] the length of the straight section was around 80 m and the acceptance dropped from 42 to 6.5 mm mrad.

The damping rings for the ATF-damping-test-facility [2] and the NLC-project [3] are also racetrack in shape. But there the arcs are based on the TME (Theoretical Minimum Emittance) [4] lattice, which results in a smaller emittance. The application of a TME-lattice to a storage ring has been done first for Super-ACO [5] and recently proposed for a low-emittance synchrotron light source [6, 7, 8].

In a recent design [9] for a 300 m damping ring for the SBLC project we found that the reduction of the dynamic aperture is less drastic when the damping wigglers are distributed around the ring. The requirements concerning the emittance and the damping time could be fulfilled with a TBA-lattice [10] whose straight sections are occupied by damping wigglers.

Furthermore, the radiation power of a wiggler with a length of 5 m (E = 3 GeV, I = 0.3 A) is in the same order as that of the ESRF-Wigglers. Hence the handling of such a power can be done.

In this section we present a re-design of the damping ring which profits from the larger dynamic aperture of a lattice with distributed wigglers. The proposed design is based upon the ESRF-synchrotron-light source [11].

4.5.2 Damping Ring Requirements

The requirements for the damping ring are given by the parameters of the SBLC (Section 4.1) and the specification of the injection system (Section 4.4). The time structure of the SBLC, relevant for the damping ring design, is presented in figure 4.5.1.

The emittance of the beam from the pre-accelerator is 10^{-4} m for electrons and 10^{-3} to 10^{-2} m for positrons. According to the parameters, the damping ring has to reduce the emittance within a time of 20 ms down to $4 \cdot 10^{-6}$ m horizontally and $2 \cdot 10^{-7}$ m vertically. Here, an emittance dilution budget of 25 % from the damping ring to the IP is taken into account. Having a pulse length of 2μs, the circumference of the damping ring has to be more than 600 m.

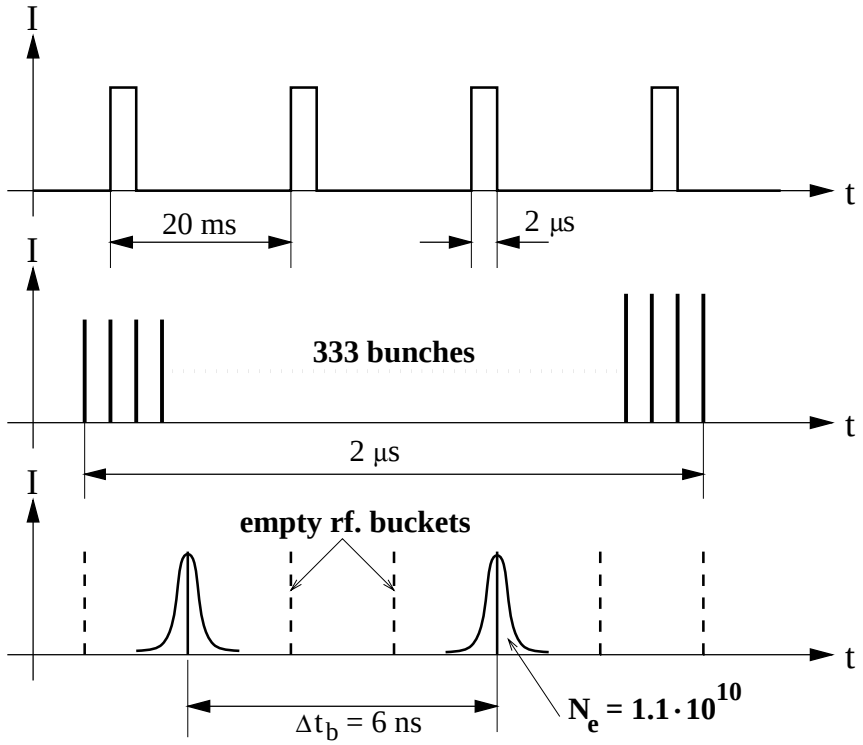

Figure 4.5.1: *Time structure of the SBLC (f_{rep} = 50 Hz, $t_{puls} = 2\,\mu s$, Δt_{puls} = 6 ns, f_{RF} = 500 MHz for the ring RF-system).*

The damping of the emittance within a storage ring is:

$$\varepsilon_f = \varepsilon_{inj} \cdot e^{-2N_\tau} + \varepsilon_{equ} \cdot (1 - e^{-2N_\tau}) \tag{4.5.1}$$

where ε_{inj} is the emittance of the injected beam and ε_{equ} is the equilibrium emittance of the damping ring. N_τ is the number of damping times the beam has been stored, i.e. $N_\tau = t/\tau_D$, where τ_D is the damping time.

From eq. (4.5.1) follows the necessary equilibrium emittance ε_{equ} at a given accumulation time t:

$$\varepsilon_{equ} = \frac{\varepsilon_f - \varepsilon_{inj} \cdot e^{-2 \cdot t/\tau_D}}{1 - e^{-2 \cdot t/\tau_D}} \tag{4.5.2}$$

The required vertical damping times for the different injection emittances are given in table 4.5.2. The requirements for the horizontal plane are more relaxed: $N_{\tau_x} = 1.5$ and $\tau_x = 13.1$ ms.

The equilibrium emittance ε_{equ} in the vertical direction as a function of the damping time τ_D with is presented in figure 4.5.2 for the the injection emittances $1 \cdot 10^{-2}$ m and $5 \cdot 10^{-3}$ m respectively. The vertical equilibrium emittance is determined by the alignment tolerances and the correction procedures (see below). At 3rd generation light sources coupling factors of less than 1 % are normal. With an emittance in the x- direction of $4 \cdot 10^{-6}$ m and a coupling factor of 2 %, the vertical emittance will be

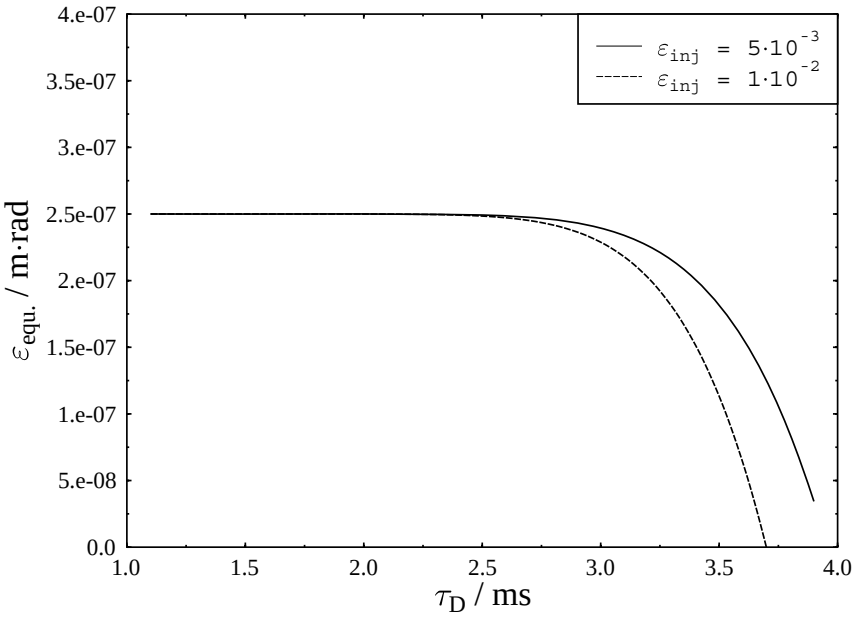

Figure 4.5.2: *The equilibrium emittance in the vertical direction as a function of the damping time* τ_D. $\varepsilon_f = 2 \cdot 10^{-7}\ m \cdot rad$, $t = 20\,ms$ *and* $\varepsilon_{inj} = 1 \cdot 10^{-2}$ *and* $5 \cdot 10^{-3}\ m$ *respectively. The final emittance* $\varepsilon_f = 2 \cdot 10^{-7}\ m$.

$1 \cdot 10^{-7}$ m. In order to meet the requirements for the SBLC-DR, the damping time must be smaller than 3.5 ms.

ε_{inj} $m \cdot rad$	N_{τ_y}	τ_y ms	Remarks
$1 \cdot 10^{-2}$	5.60	3.50	Positrons
$1 \cdot 10^{-3}$	4.45	4.40	Positrons
$1 \cdot 10^{-4}$	3.17	6.00	Electrons

Table 4.5.1: *Required vertical damping time* τ_y *for the SBLC damping ring for a storage time of 20 ms and a final emittance* $\varepsilon_{y,n}$ *of* $2 \cdot 10^{-7}\ m$.

We thus adopt the following requirements for the damping ring:

$$\varepsilon_{x,n} \leq 4 \cdot 10^{-6} m\ ,\ \varepsilon_{y,n} \leq 10^{-7} m \qquad and \qquad \tau_y \leq 3.5 ms. \tag{4.5.3}$$

The energy of the damping ring should be in the range between 2.5 and 3.5 GeV. At an energy of 3 GeV the normalized emittance of $4 \cdot 10^{-6}$ m translates into an absolute

horizontal emittance of $6.7 \cdot 10^{-10}$ m which is in the domain of a fourth generation light source [12], about an order of magnitude below existing third generation light sources [13].

The damping time of a storage ring without any insertion devices is given by:

$$\tau_i = \frac{[C/m] \cdot [\rho/m]}{13.2 \cdot J_i \cdot [E/GeV]^3} ms \tag{4.5.4}$$

with C the circumference, ρ the curvature of the bending magnets, J_i the partition number for the corresponding mode and E the energy of the beam. With the circumference and energy fixed to 600 m and 3 GeV, respectively, and the highest reasonable magnetic flux of 1.5 T, the lowest possible vertical damping time becomes 12 ms. A further reduction can be done only with damping wigglers which, on the other hand, influence also the emittance [14, 15]. By a proper design of the wigglers, however, the equilibrium emittance may be lower, too.

4.5.3 Lattice of the Damping Ring

In principle the requirements set on the damping ring can be met with a racetrack design, as already proposed for the other linear collider projects. However, another variable to consider is the dynamic aperture which has to accommodate the required beam current. Based on our investigations for a fourth generation synchrotron light source [16] we propose to adopt a design with a distributed wiggler arrangement similar to a light source, with the places for insertion devices occupied solely by damping wigglers.

The design of - existing or proposed - light sources are based on different lattice structures: FODO, DBA, TBA and TME [13]. Their emittances scale by the following law:

$$\varepsilon = C_q \cdot \gamma^2 \cdot \frac{1}{J_x} \cdot K \cdot \frac{1}{12\sqrt{15}} \cdot \varphi^3 \tag{4.5.5}$$

with the constant $C_q = 3.84 \cdot 10^{-13}$, and the variables: γ the Lorentz factor, φ the deflection angle of the bending magnet, J_x the horizontal partition number, and K the quality factor of the lattice. The quality factor as it is defined through eq. (4.5.5) is implicitly a measure for how compact a machine can reach a given emittance. The K-values for different optics are summarised in table 3. The DBA lattice has the lowest K value achieved in practice.

Because damping wigglers have to be introduced, one should also consider how much space for insertion devices are available with different optics. The DBA has the most space, which has been shown in an investigation by Wrulich [17].

According to both arguments above, we have chosen a DBA lattice based on the ESRF design [11] as the best candidate for the damping ring lattice. The lattice functions within a unit cell of our SBLC damping ring design are given in Fig. 4.5.3a and in Table 4.5.3 the parameters of the ring are compared to those of the ESRF. The machine functions within a unit cell including the damping wiggler are presented in

Optic	K/theoretic	K/real	Machines
FODO	58	2000	PETRA
DBA	3	6.3	ESRF
		4.6	ELETTRA
TBA	2.33	13	BESSY I
		11	ALS
TME	1	-	-

Table 4.5.2: *The quality factor K for different optics.*

Fig. 4.5.3b. As a result of the focusing of the wigglers in the vertical direction the shape of the vertical betatron functions looks differently by installing a wiggler in the straight section. The betatron functions in Fig. 4.5.3 have been matched to the same working points $Q_x = 30.18$, $Q_y = 10.24$, respectively, with and without wigglers.

	ESRF	SBLC-DR
Energy (GeV)	6	3
Beam current (mA)	200	300
Magnet bending radius (m)	24.9555	13.5427
Bending field (T)	0.802	0.7389
Deflection angle per magnet	5.625	5.000
Circumference (m)	844.4	660
Number of super periods	16	36
Horizontal working point Q_x	36.2	30.18
vertical working point Q_y	11.2	10.24
Momentum compaction factor	$3.1 \cdot 10^{-4}$	$1.64 \cdot 10^{-4}$
Synchrotron damping time (ms)	3.7	12.4
Horizontal damping time (ms)	7.4	24.8
Vertical damping time (ms)	7.4	24.8
Horizontal emittance (nm rad)	6.20	3.2
Vertical emittance (nm rad)	0.62	0.32
Horizontal chromaticity	-113.9	-48.8
Vertical chromaticity	-34.50	-31.5
Energy spread (σ_E/E)	$1.03 \cdot 10^{-3}$	$0.7 \cdot 10^{-3}$

Table 4.5.3: *Comparison of the main parameters of the SBLC damping ring with the ESRF design.*

As given by eq. (4.5.4) the damping time is determined by the circumference, the radius of curvature and the energy. To reach a small damping time at a fixed circumference, the radius should be as small as possible. The radius of curvature also influences the emittance and the momentum compaction factor α: ε is proportional to

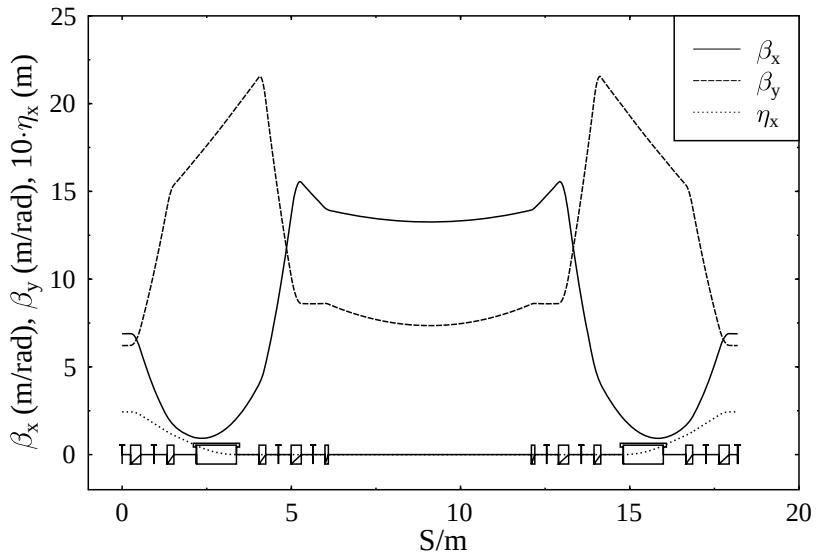

(a) (b)

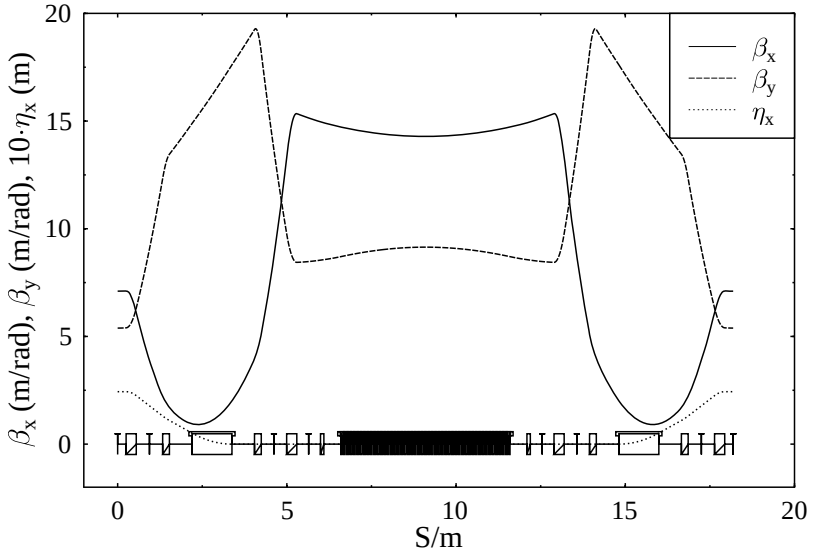

Figure 4.5.3: *The lattice functions within a unit cell of the proposed SBLC damping ring. The deflection angle per magnet is 5 degrees and the periodicity is 36. (a) the bare DBA-cell and (b) half of the DBA-structure with a damping wiggler in the straight section.*

$1/\rho$ (eq. (4.5.5)) and α is proportional to ρ. The momentum compaction factor of a DBA lattice is given by:

$$\alpha[DBA] = \frac{\rho \cdot N_M}{C}\{2 \cdot \pi \cdot \frac{\varphi}{360} - \sin\varphi\} \tag{4.5.6}$$

with N_M is the number of bending magnets of the ring and φ the deflection angle of each bending magnet in degrees. Due to the larger bending radius of the ESRF, its α is approximately 2 times higher than the SBLC-damping ring. All other factors of the two designs are more or less in the same range.

The dynamic aperture of the bare ring (without damping wigglers) is given in Fig. 4.5.4. The corresponding acceptances are 128 mm mrad horizontally and 100 mm mrad vertically. Although the dispersion function of the SBLC-damping ring is smaller than for the ESRF-ring which leads to higher sextupole strengths, the dynamic aperture is larger. The calculations for the dynamic aperture have been performed with the codes MAD [19], RACETRACK [20] and BETA [21]. The results of all three codes are in good agreement (better than $\pm 10\%$).

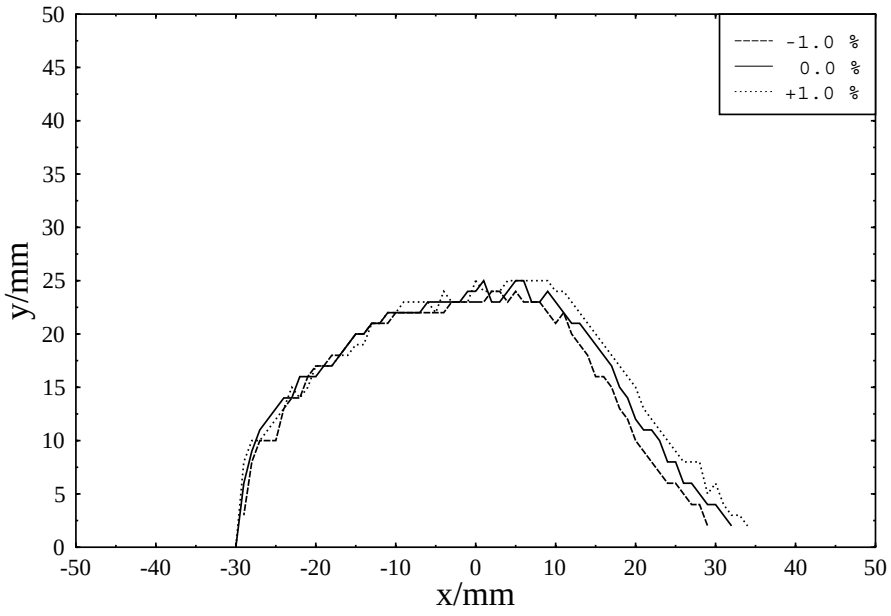

Figure 4.5.4: *The dynamic aperture of the bare SBLC damping ring including harmonic sextupoles. These values have been calculated with the code MAD.*

The shifts of the tune with energy and betatron amplitude are presented in Fig. 4.5.5 and Fig. 4.5.6, respectively.

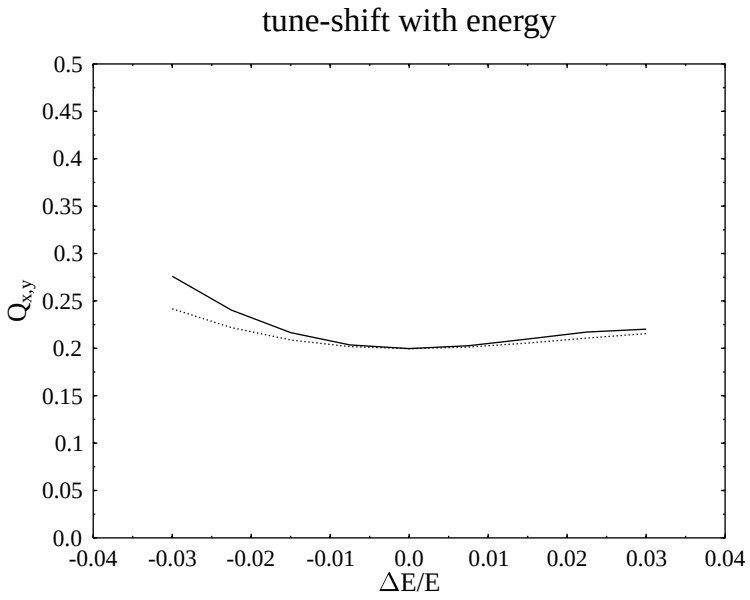

Figure 4.5.5: *Tune shift with energy of the bare damping ring according to figure 4.5.3, above. Without any errors.*

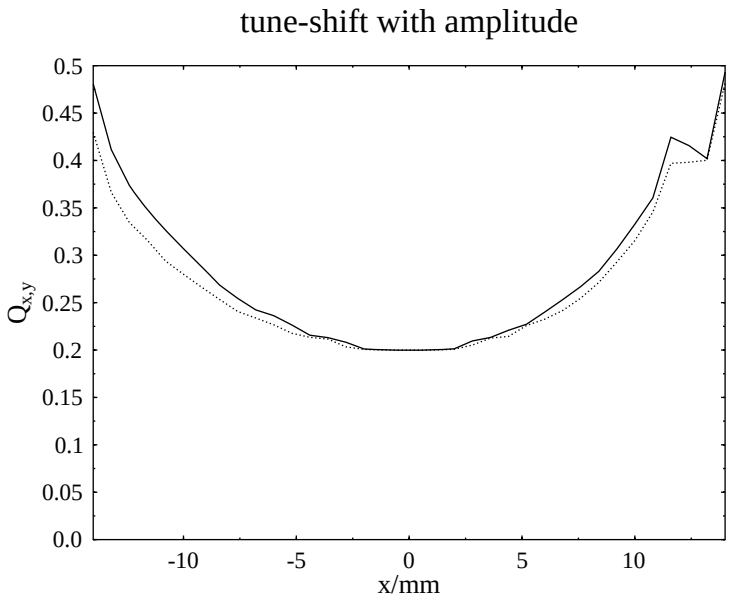

Figure 4.5.6: *Tune shift with amplitude of the bare damping ring as determined by the optics of figure 4.5.3a. No errors have been taken into account.*

The calculations of the tune shift with the energy deviations have been done in the range of $\pm 3\,\%$. From Fig. 4.5.5 one can conclude that the energy acceptance of the bare lattice is larger than $\pm 4\,\%$ which is more than sufficient.

With increasing amplitudes of the betatron oscillations the tunes are moving in the directions of the half order resonances, which determines the dynamic aperture too. With the amplitudes of figure 4.5.6 the working point crosses only the resonance line $Q_x + 4 \cdot Q_y = 2 \cdot 36$ which is a harmless one.

The maximum amplitudes in figure 4.5.6 are smaller than in figure 4.5.4 for the dynamic aperture. The reason is because for the calculation of the tune shift a combined effec from the x and y direction exists. Taking this into account the results shown in Figs. 4.5.4 and 4.5.6 are compatible.

4.5.4 Introduction of Wigglers

The wigglers have an effect on the damping time, the energy spread and the emittance. The relations [14, 15] are given in Table 4.5.4.

4.5.4.1 Effect on the Emittance

The SBLC damping ring has 36 straight sections. Six are needed for injection, extraction and the RF system. The length of a straight section - from quadrupole to quadrupole - is 6 m. Therefore, the length of one wiggler could be around 5 m, resulting in an overall length of 150 m of installed wigglers. The maximum magnetic field of a wiggler is 2 T leading to a minimum radius of curvature of 5 m. The period length of the wigglers has been set to 0.2 m. With these values, the emittance is according to Table 4.5.4:

$$\begin{aligned} \varepsilon_{x,wi} &= \varepsilon_{x,0} \cdot 0.202 = 6.5 \cdot 10^{-10} mrad \\ \varepsilon_{x,n} &= \gamma \cdot \varepsilon_{x,wi} = 3.8 \cdot 10^{-6} mrad \end{aligned} \tag{4.5.7}$$

The contribution of the term I_5^{ID}/I_5^0 is roughly 34 %. Hence a reduction of the emittance can be achieved by altering the period length of the wiggler, the β- value in the middle of the straight section or the magnetic flux in the wiggler, as is demonstrated in the following examples:

By changing the period length to 0.175 m, the emittance is reduced to $3.5 \cdot 10^{-6}$mrad.

In our special case the emittance scales with the β- value in the middle of the straight section as:

$$\varepsilon \beta^{-0.335} = const \tag{4.5.8}$$

which means that by reducing β from 14.0 m to 7.0 m the normalised emittance becomes $3.0 \cdot 10^{-6}$ m.

The emittance as a function of the radius of curvature in the wigglers is shown in Fig. 4.5.7. This curve runs through a minimum at a curvature of $\rho_{wi} = 5$ m, which was chosen for the wiggler.

Table 4.5.4: *Effects of the wigglers on the damping time, emittance and energy spread*

$$\tau_{wi} = \tau_0 \cdot \frac{1}{1+(L_{ID}\cdot\rho_0/4\pi\rho_{wi}^2)}$$

$$\varepsilon_{x,wi} = \varepsilon_{x,0} \cdot \frac{1+[I_5^{ID}/I_5^0]}{1+[(I_2^{ID}-I_4^{ID})/(I_2^0-I_4^0)]}$$

$$\sigma_{E,wi}^2 = \sigma_{E,0}^2 \cdot \frac{1+[I_3^{ID}/I_3^0]}{1+[(2I_2^{ID}-I_4^{ID})/(2I_2^0-I_4^0)]}$$

$I_1^0 \cdots I_5^0$ are the well known synchrotron integrals,
$I_1^{ID} \cdots I_5^{ID}$ are the contributions of these integrals by the wigglers.
These integrals are given by [16],[17]

$$I_2^{ID} = L_{wi}/(2\rho_{wi}^2)$$

$$I_3^{ID} = 4 \cdot L_{wi}/(3 \cdot \pi\rho_{wi}^2)$$

$$I_4^{ID} = -(3 \cdot L_{wi} \cdot \lambda_{wi}^2/(32 \cdot \pi^2\rho_{wi}^4)$$

$$I_5^{ID} = I_5^{ID}(\langle\gamma\rangle) + I_5^{ID}(\langle\alpha\rangle) + I_5^{ID}(\langle\beta\rangle)$$

$$I_5^{ID}(\langle\gamma\rangle) = \frac{\lambda_{wi}^4\cdot L_{ID}}{40\pi^2\rho_{wi}^5}(\frac{3}{5\pi} + \frac{3}{16}) \cdot \langle\gamma\rangle$$

$$I_5^{ID}(\langle\alpha\rangle) = -\frac{9\cdot\lambda_{wi}^3\cdot L_{ID}}{40\pi^4\rho_{wi}^5} \cdot \langle\alpha\rangle$$

$$I_5^{ID}(\langle\beta\rangle) = \frac{\lambda_{wi}^2\cdot L_{ID}}{15\pi^3\rho_{wi}^5} \cdot \langle\beta\rangle$$

In a straight section of length l_0 and with the initial values
β_0, α_0 and γ_0 one gets the values:

$$\beta(s) = \beta_0 + \frac{s^2}{\beta_0},\ \alpha(s) = -\frac{s}{\beta_0},\ \gamma(s) = \frac{1}{\beta_0}$$

$$\langle\beta(s)\rangle = \beta_0 + \frac{1}{9} \cdot \frac{l_0^3}{\beta_0}$$
$$\langle\alpha(s)\rangle = -\frac{1}{2} \cdot \frac{l_0^2}{\beta_0}$$
$$\langle\gamma(s)\rangle = \frac{1}{\beta_0}$$

From the evaluation of the different contribution it follows that
$I_5^{ID}(\langle\gamma\rangle)$ and $I_5^{ID}(\langle\alpha\rangle) \ll I_5^{ID}(\langle\beta\rangle)$. Hence $I_5^{ID}(\langle\alpha\rangle)$ and $I_5^{ID}(\langle\gamma\rangle)$ can be neglected.

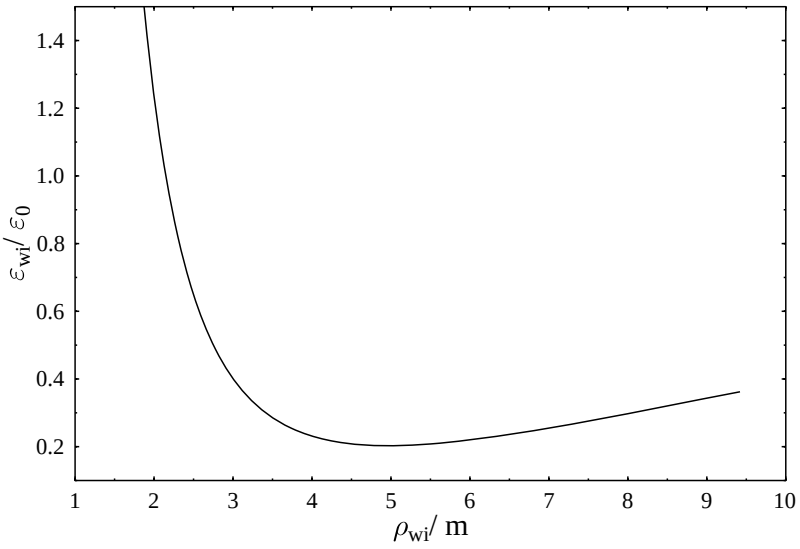

Figure 4.5.7: *Dependency of the emittance on the radius of curvature in the wiggler.*

In summary, by changing the period length from 0.2 to 0.175 m and reducing the β-value in the centre of the straight section from 14.0 m to 7 m a factor of 1.34 in the emittance can be gained.

4.5.4.2 Effect on the Damping Time

The damping time τ_i as function of the Energy E_0, the revolution time T_0, the partition function J_i and the radiation loss U per turn is as:

$$\tau_i = 2 \cdot \frac{E_0 \cdot T_0}{J_i \cdot U} \tag{4.5.9}$$

U on the other hand is determined by the radius ρ_0 of the bendings, the overall length L_{ID} of the wigglers and the curvature ρ_{wi} in the wigglers:

$$U = C_q \cdot \frac{E^4}{\rho_0}\{1 + \frac{L_{ID} \cdot \rho_0}{4\pi\rho_{wi}^2}\} \tag{4.5.10}$$

Combining these equations the damping time results in:

$$\tau_{wi} = 49.75ms \cdot \frac{[\rho_0/m]}{J_i \cdot [E_0/GeV]^3\{1 + \frac{\rho_0}{\rho_w} \cdot \frac{L_{ID}}{4\pi\rho_w}\}} \tag{4.5.11}$$

which is visualised in Fig. 4.5.8 .

According to Fig. 4.5.8 the damping time can be decrease by reducing any or both of the radii of curvature. In our special case the damping time including wigglers scales with the radius of the bendings as well as the wigglers like

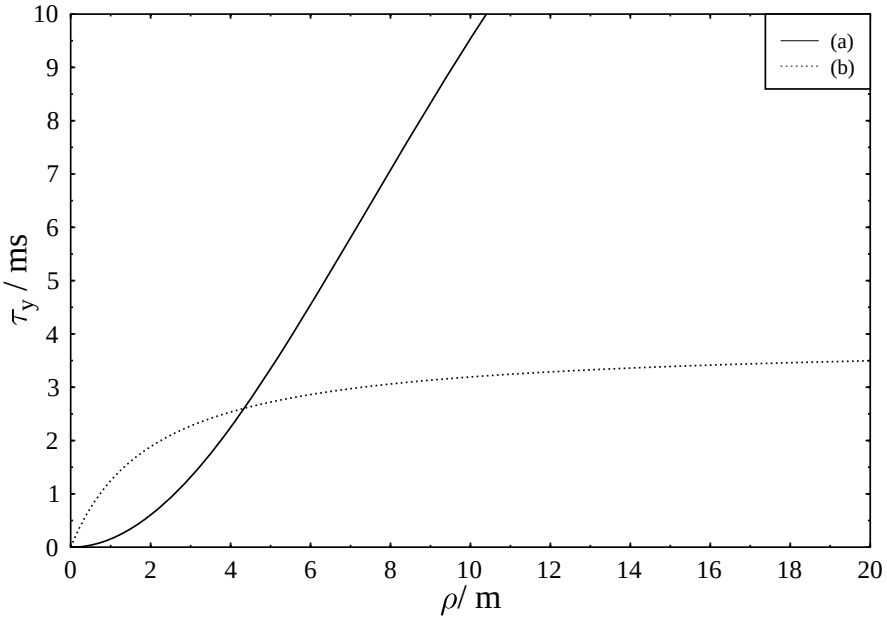

Figure 4.5.8: *The damping time as function of ρ_0 with $\rho_{wi} = 5m$ (b) and as a function of ρ_{wi} with $\rho_0 = 13.54$ (a).*

$$\tau_y \cdot \rho_{Bend}^{-0.14} = const \qquad \text{and} \qquad \tau_y \cdot \rho_{wi}^{-1.65} = const \tag{4.5.12}$$

According to eq. (4.5.12) the most effective way for changing the damping time is the variation of ρ_{wi}.

By keeping the radius of the bending magnet as well as the magnetic flux in the wigglers constant and alternating the energy of the electrons the damping time shows in comparison with eq. (4.5.4) only a small variation with the energy:

$$\tau_y \cdot E^{1.25} = const \tag{4.5.13}$$

The most effective way to change the damping time, without significantly changing the emittance, is to vary the radius of curvature of the wiggler and the beam energy.

For the SBLC damping ring the chosen parameters ($B_w = 2$ T, $\rho_w = 5.0$ m, $\lambda_w = 0.2$ m, E = 3 GeV, $\rho_0 = 13.54$ m) result in a damping time $\tau_y = 3.34$ ms which fulfills the requirements.

In summary it may be stressed that the proposed SBLC-DR design with emittance ε_x of $3.8 \cdot 10^{-6}$ ms and damping time τ_y of 3.34 ms meets the requirements ($\varepsilon_x \leq 4 \cdot 10^{-6}$ m·rad and $\tau_y \leq 3.4$ ms).

4.5.4.3 Effect on the Energy Spread

The installation of the damping wigglers has an effect on the energy spread too (see table 4.5.4). Because I_2^{ID} and I_3^{ID} are larger than I_2^0 and I_3^0 the energy spread increases. With the values: $I_2^0 = 0.464$, $I_3^0 = 0.0343$, $I_2^{ID} = 3$ and $I_3^{ID} = 2.546$ the energy spread increases by a factor of 3.18 to $\frac{\sigma_E}{E} = 2.2 \cdot 10^{-3}$.

4.5.5 RF System

The layout of the RF system is determined by the radiation loss per turn:

$$\begin{aligned} U &= c_\gamma \cdot \frac{E^4}{\rho_0}\{1 + \frac{L_{ID} \cdot \rho_0}{4\pi\rho_{wi}^2}\} \\ &= U_{Bend} + U_{Wiggler} \\ &= 529.4\,KeV + 3422\,KeV = 3.95\,MeV \end{aligned} \tag{4.5.14}$$

The energy acceptance $[\frac{\Delta E}{E}]_{RF}$ of the RF system should be about ten times the energy spread, i.e. around 2 %. It is given by

$$\frac{\Delta E}{E}_{RF} = \sqrt{k^\star} \cdot \sqrt{F(q)} \tag{4.5.15}$$

with

$$k^\star = \frac{U}{\pi \cdot \alpha \cdot h \cdot E_0} \tag{4.5.16}$$

and

$$F(q) = 2\{\sqrt{q^2 - 1} - \cos^{-1}(1/q)\} \tag{4.5.17}$$

With an over-voltage factor of $q = 1.10$ to 2.0 the energy acceptance is from 1.15 % to 5.70 %, which is just in the proper range. For the layout of the RF-system one has to bear in mind, that the over voltage factor q influences the bunch length, too. A high q value leads to a small bunch length, hence also from this point of view the over-voltage factor can be used for choosing the right bunch length.

The klystron has to deliver the following power:

$$P_{Klyst} = P_{CAV} + P_{Beam} + P_{Refl} + P_{HOM} \tag{4.5.18}$$

$$\tag{4.5.19}$$

$$\approx 1.2(P_{CAV} + P_{Beam} + P_{Refl}) \tag{4.5.20}$$

With $P_{\mathrm{refl}} = 0$ the coupling factor becomes

$$\beta_{opt} = \frac{P_{Beam}}{P_{CAV}} + 1 \tag{4.5.21}$$

and with $P_{\mathrm{in}} = P_{\mathrm{Beam}} + P_{\mathrm{CAV}}$ it follows

$$P_{CAV} = \frac{P_{in}}{\beta} \; and \; P_{Beam} = \frac{\beta - 1}{\beta} \cdot P_{in} \tag{4.5.22}$$

By taking an over voltage factor of 2.0 the necessary overall installation of the cavity voltage is 7.9 MV with a beam power P_{Beam} of 1.2 MW.

The number of cavities is determined by the power which can be fed through the input coupler. For the ELETTRA normal conducting cavity [18] as well as the HERA superconducting one [23] it is around 110 kW. Hence overall 10 to 12 cavities have to be installed. The CESR - superconducting cavity [30],[31] is designed for an input power up to 250 kW. Already achieved have been 150 kW. This means that 5 to 8 cavities have to be installed. The specification of the CESR - cavity are: G = 6 MV/m, V_{RF} = 1.8 MV, $Q_0 = 1 \cdot 10^9$, (R/Q = 89 Ω/cell, $Q_L = 2 \cdot 10^5$ and l_{eff} = 0.3 m). Taking 5 cavities with a gradient of 1.8 MV/cell the overall RF voltage leads to q = 2.6, with an RF energy acceptance of 7.2 %.

By taking an over-voltage factor of q = 2.60 and the phase ϕ_s = 22.62 degrees, the synchrotron tune results in

$$\begin{aligned} \nu_s &= \frac{\Omega_s}{\omega_0} = \sqrt{\frac{\alpha \cdot \; h \cdot \cos\phi_s}{2\pi} \cdot \frac{eV_{RF}}{E_0}} \\ \nu_s &= \sqrt{7.96 \cdot 10^{-5}} = 8.92 \cdot 10^{-3} \\ \Omega_s &= \nu_s \cdot \omega_0 = \nu_s \cdot \frac{2 \cdot \pi}{h \cdot T_{RF}} = 2.55 \cdot 10^4 \\ f_s &= 9.724 \; KHz \end{aligned} \tag{4.5.23}$$

The bunch length is then, with $\frac{\sigma_E}{E} = 2.2 \cdot 10^{-3}$

$$\sigma_z = \frac{\alpha \cdot c}{\Omega_s}(\sigma_s/E) = 4.25 \; mm \tag{4.5.24}$$

4.5.6 Instabilities

4.5.6.1 Single Bunch Instabilities

The microwave instability, sometimes referred to as turbulent bunch lengthening, causes an increase in both the momentum spread and the bunch length of a bunched beam. The threshold (peak) current I_p is given by [23]

$$I_p^{th} = \frac{2 \cdot \pi \cdot \alpha \cdot (E/e)}{[Z_L/n]} \cdot (\sigma_E/E)^2 \tag{4.5.25}$$

$[Z_L/n]$ is the broad band impedance of the storage ring. With

$$I_p^{th} = \frac{N_E \cdot e \cdot c}{\sqrt{2\pi} \cdot \sigma_z} \tag{4.5.26}$$

and the average current I_{aver} of one bunch

$$I_{aver} = \frac{N_E \cdot e \cdot c}{2\pi \cdot R} \tag{4.5.27}$$

we get:

$$I_{aver} = \frac{\sqrt{2\pi} \cdot \alpha \cdot (E/e)}{Z_L/n} \cdot \frac{\sigma_z}{R} \cdot (\sigma_E/E)^2 \tag{4.5.28}$$

With $I_{aver} = 0.8$ mA, $\alpha = 1.64 \cdot 10^{-4}$, $\sigma_z = 4 \cdot 10^{-3}$ m, $(\sigma_E/E) = 2.2 \cdot 10^{-3}$ and R = 104 m one gets for the broad band impedance a maximum value of $[Z_L/n] = 0.3\,\Omega$. The broad band impedance is given by the vacuum chamber and the cavities:

$$[Z_L/n] = [Z_L/n]_{chamb.} + N_{CAV} \cdot [Z_L/n]_{CAV} \tag{4.5.29}$$

At the synchrotron light source ELETTRA a broad band impedance of $[Z_L/n] = 0.75$ has been measured [24],[25],[26]. It is assumed by some estimations that the contribution of the four cavities is $0.6\,\Omega$, hence the vacuum chamber has an impedance of $0.15\,\Omega$. We assume a similar value here, too. From the measured loss factor of the CESR superconducting cavity a broad band impedance of 0.03-0.05 Ω could be determined [30],[31]. With 8 cavities the contribution of the RF-system to the broad band impedance is 0.24-0.4 Ω. From this we can estimate the impedance as:

$$[Z_L/n] = (0.4 - 0.7)\ \Omega \tag{4.5.30}$$

which is about a factor of two larger than desirable. However, by taking into account the Spear scaling rule:

$$[Z_L/n]_{eff} = [Z_L/n]_0 \cdot (\frac{\sigma_l}{b})^{1.68} = 0.70 \cdot (\frac{4.5}{20})^{1.68} = 0.06\ \Omega \tag{4.5.31}$$

the effective impedance appears to be below the allowed value. So bunch lengthening seems to be avoidable, but not with a large safety margin and further studies of this issue are required.

4.5.6.2 Multibunch Instabilities

With 333 stored bunches and a total current of 300 mA, multibunch instabilities are of concern. In this case the frequency of a Fourier component of the beam current is in resonance with a higher order mode of the cavities. The resonance conditions for the longitudinal direction is:

$$f_{cbn} = (p \cdot h + N_{cbn} + Q_s) \cdot f_0 \tag{4.5.32}$$

f_0 = revolution frequency, N_{cbn} = coupled bunch number, h = number of bunches, Q_s = synchrotron tune and p is an integer. The distance between coupled bunch mode frequencies is equal the revolution frequency f_0, which has for the DR a value of 454.5 kHz.

The higher order mode frequency f_{HOM} is a function of the dimensions of each cavity (for each cavity the f_{HOM}'s can be slightly different) and furthermore (for conventional cavities) the frequency depends upon the cavity temperature [27],[28],[29].

The growth rate for the longitudinal coupling bunch instability is

$$\frac{1}{\tau_{||}} = \frac{\alpha \cdot I_b \cdot f_0}{2 \cdot f_s \cdot (E/e)} \cdot f_{cbn} \cdot R_{S,||} \tag{4.5.33}$$

I_b is the total current within the ring and $R_{S,||}$ is the shunt impedance of the corresponding HOM. Stability is guaranteed if

$$\frac{1}{\tau_{||}} < \frac{1}{\tau_\varepsilon} \tag{4.5.34}$$

where $1/\tau_\varepsilon$ is the damping rate of the synchrotron oscillations. Taking a shunt impedance of $R_{S,||} = 200\ k\Omega$ (which is typical for a normal conducting cavity) results in a maximum current of 136 mA.

The shunt impedances of the HOM's within a CESR- superconducting cavity are in the range of 0.1 - 0.7 kΩ, leading to an instability threshold of I $\geq$ 380 mA. Hence the coupled bunch instabilities are of no importance when using superconducting cavities.

As in the longitudinal direction there are coupled bunch instabilities in the transverse direction, too. For a transverse impedance of $R_\perp = 11\ M\Omega/m$ (which is typical for a normal conducting cavity) the maximum stored beam within the DR is 4.0 mA. The transverse impedances of the CESR-SC-cavity are smaller than 0.025 MΩ/m leading to a threshold current of 1760 mA. In this case, however, other contributions to the impedance (in particular the resistive wall impedance) may become dominant. Whether or not a feedback system is required, must be determined by more detailed investigations. In any case it should be noted that the issue of multibunch instabilities is significantly relaxed compared to the B-factory rings presently under construction at SLAC and KEK.

4.5.7 Complete Ring Layout

The length of the straight section is 6 m which allows to install four cavities. For the installation of the necessary number of cavities of the RF system a total of four straight sections are needed. Accounting for one straight section each for injection and extraction, every sixth straight section must be without a damping wiggler. Thus the damping ring can be composed of six identical super-periods consisting of six unit cells, five with wigglers in the straight sections and at each side the matching sections (Fig. 4.5.9). The lattice functions within a super period are presented in Fig. 4.5.10.

To get for the full matching section (see figure 4.5.11) the same phase advance as inside the unit cell one has to introduce in the straight sections 3 quadrupoles. The one in the middle must be, according to the behaviour of the wiggler, a defocusing one. The same phase advance has to be kept in order to avoid reductions in the dynamic aperture.

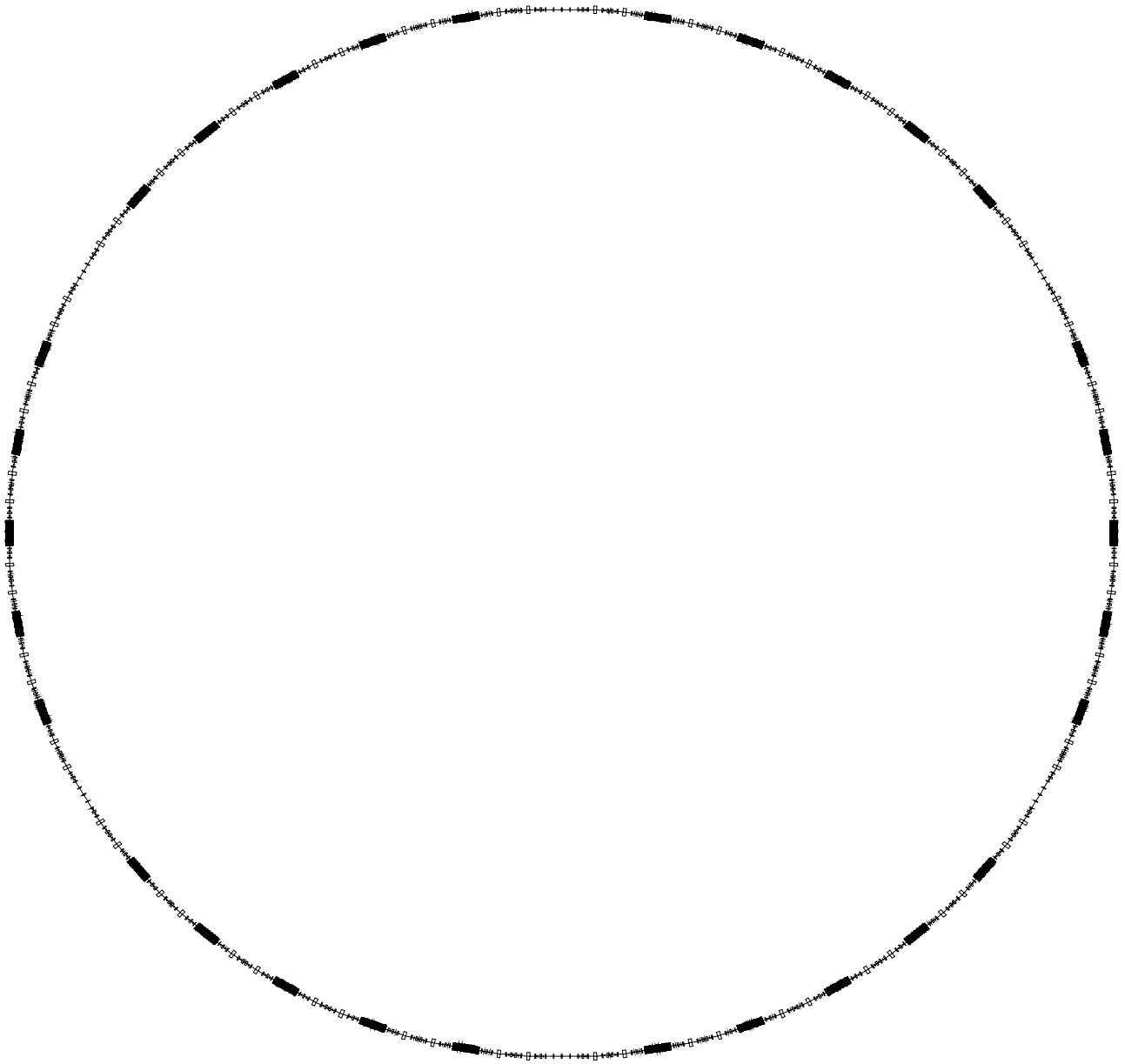

Figure 4.5.9: *Layout of the SBLC damping ring. The periodicity is six.*

The dynamic aperture, the tune shift with energy and the tune shift with particle amplitude of the damping ring with wigglers are presented in Figs. 4.5.12,4.5.13 and 4.5.14, respectively. The calculations have been done without any errors and misalignments.

According to these results the acceptances are $A_x = 145$ mm mrad and $A_y =$

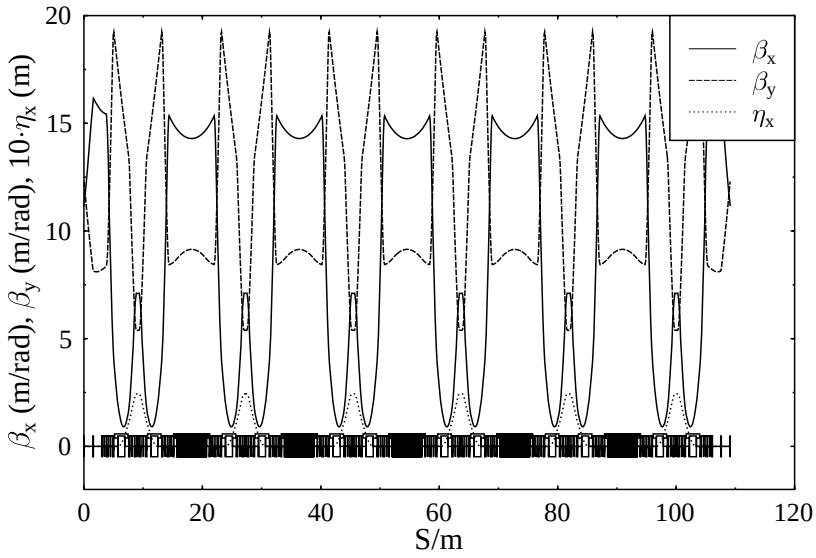

Figure 4.5.10: *Lattice functions within one super period of the SBLC damping ring. Each super period consists of the unit cells with wigglers and two matching sections at each side.*

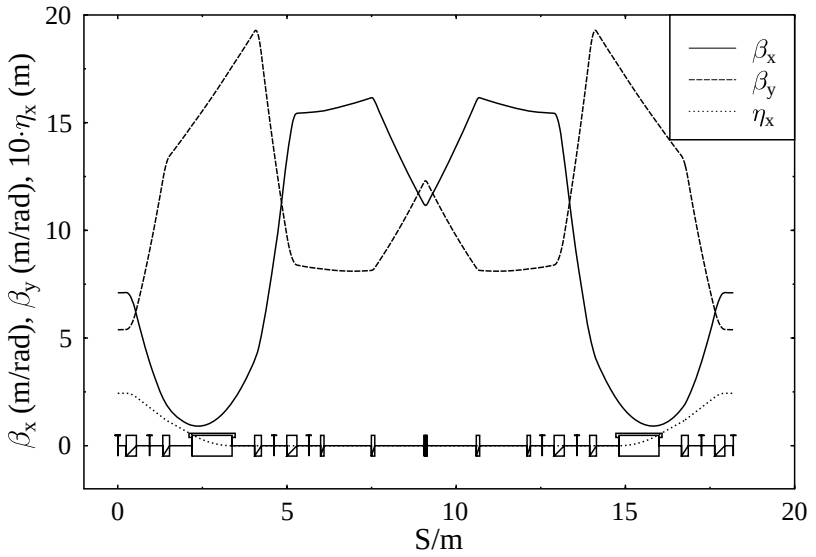

Figure 4.5.11: *Lattice functions within the matching sections of the super period of the SBLC damping ring.*

242 mm mrad, which is sufficient. The energy acceptance is larger than 3 %. The calculations of the tune shift with amplitude (see Fig. 4.5.14) are performed with a coupling of 75 % between the y- and the x- direction. Hence the maximum amplitudes according to Fig. 4.5.14 are in agreement with the dynamic aperture presented in Fig. 4.5.12.

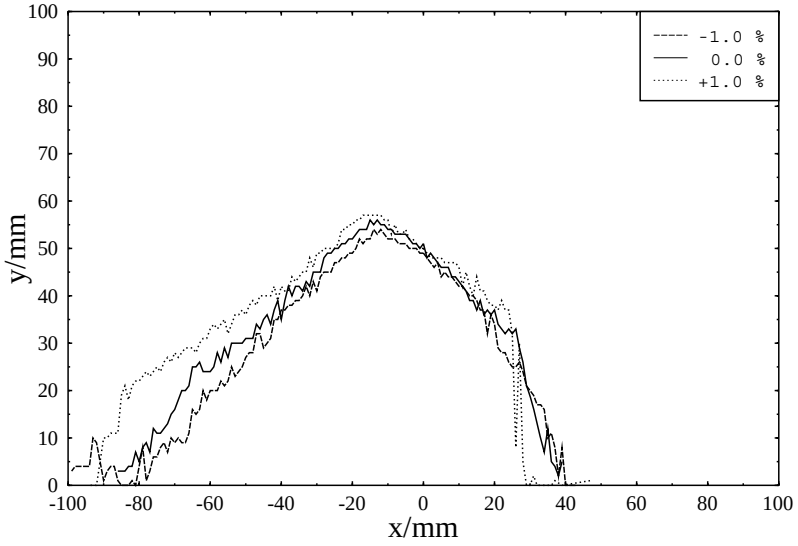

Figure 4.5.12: *Dynamic aperture of the SBLC damping ring.*

The reduction of the dynamic aperture in the presence of magnet misalignments is demonstrated in Figs. 4.5.15 and 4.5.16. The graph corresponds to normally distributed alignment errors of $\Delta_x = \Delta_y = 75\mu$m where the Gaussian distribution was truncated at 2σ.

Figure 4.5.15 includes the misalignment of bendings, quadrupoles and sextupoles, Fig. 4.5.16 shows the effect of sextupoles misalignments only. In both cases a correction of the closed orbit has not been performed.

The dynamic aperture including closed-orbit deviations due to magnetic misalignment and field errors ($\Delta B/B = 5 \cdot 10^{-3}$, $\Delta G/G = 1 \cdot 10^{-3}$) is presented in Fig. 4.5.17. Drawing an inside semi circle of the dynamic aperture the stable region would be $\Delta x \leq 35\,mm$ and $\Delta y \leq 40\,mm$ resulting in the acceptances $E_x = 108$ mm mrad and $E_y = 128$ mm mrad. For the injected positron beam with $\varepsilon_{inj}/\gamma = 1.7\text{mm} \cdot mrad$ it follows a ratio $A_x/\sigma_{x,inj} = 7.7$ and $A_y/\sigma_{y,inj} = 8.8$. For the injected electrons these radios are ten times higher. Hence the acceptance of the machine is large enough to capture the incoming particles.

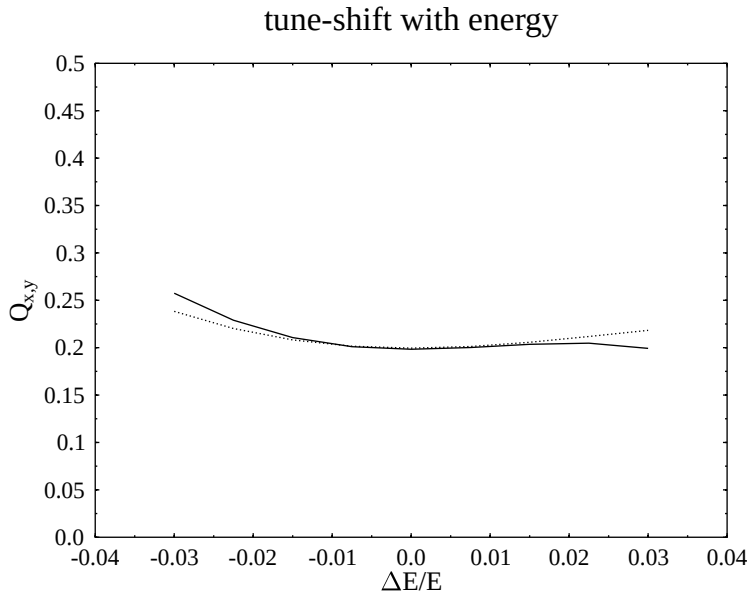

Figure 4.5.13: *Tune shift with energy of the SBLC damping ring.*

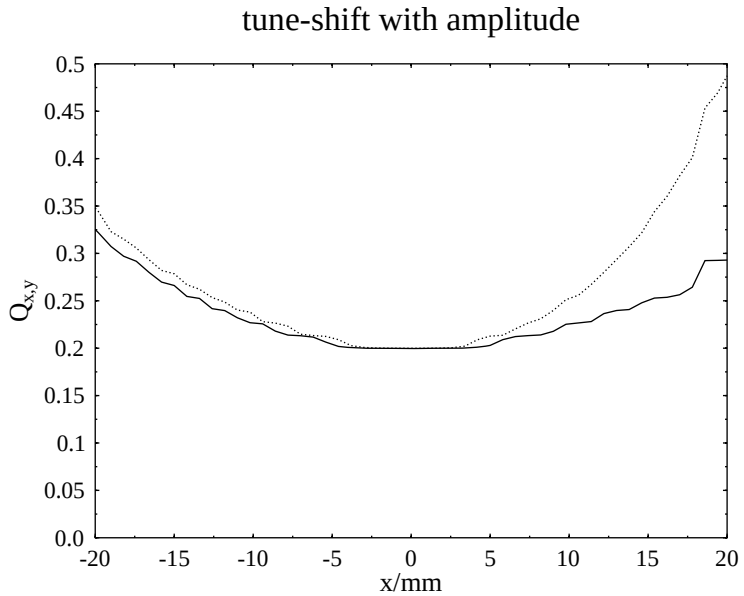

Figure 4.5.14: *Tune shift with amplitude of the SBLC damping ring at 75 % coupling, i.e* $a_y = 0.75 \cdot a_x$.

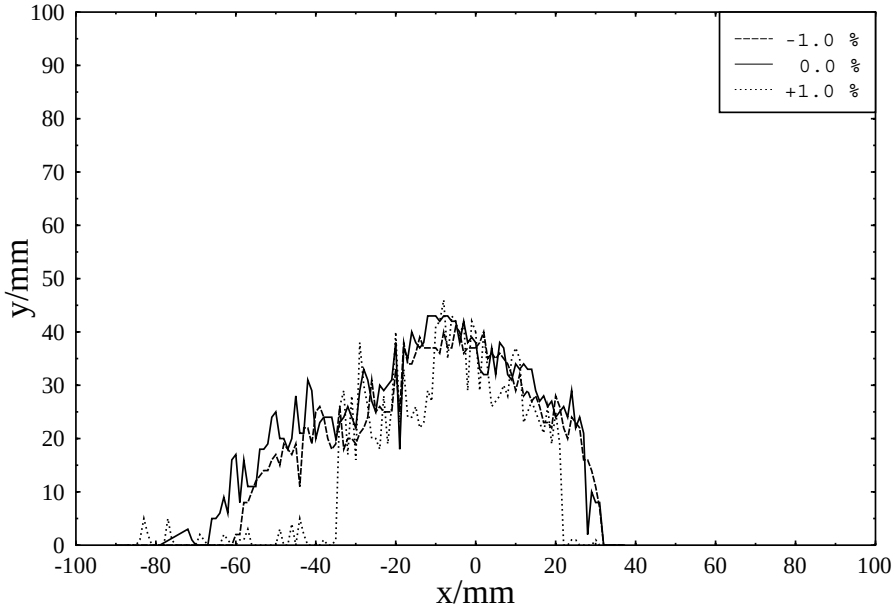

Figure 4.5.15: *The dynamic aperture of the SBLC damping ring with average alignment errors of all magnetic elements* $\Delta_x = \Delta_y = 75\mu m$.

4.5.8 Alignment Tolerances and the Vertical Emittance

The vertical equilibrium emittance is essentially determined by the magnet and beam position monitor (BPM) alignment tolerances and by the orbit correction procedures applied. We used the PETROS computer code to simulate alignment errors and orbit correction procedures. Assuming rms magnet and BPM position tolerances of $50\,\mu$m, the MICADO algorithm (a standard orbit correction method applied routinely at LEP, HERA and other storage rings) [32] is applied in several iterations until the quality of the orbit does not improve anymore. From 10 different random seeds of errors we obtain an average vertical normalized emittance of $(1.0 \pm 0.9)\cdot 10^{-7}$ m. So the required emittance could just be achieved with the assumed tolerances and standard correction techniques. Further improvements are possible by introducing dispersion correction orbit bumps and/or skew quadrupoles, and by better effective alignment of the BPM's w.r.t. to the magnets using beam-based methods.

4.5.9 Specifications of the Magnet Elements

The injected electron beam has a normalised emittance of $1 \cdot 10^{-4}$ m which leads to a maximum beam size of 0.5 mm (1 σ). In order to get a sufficient quantum lifetime the acceptance should be a factor six to ten larger. Including closed orbit deviations of 5 mm and a thickness of the vacuum chamber of 2 mm it was chosen to have a gap in

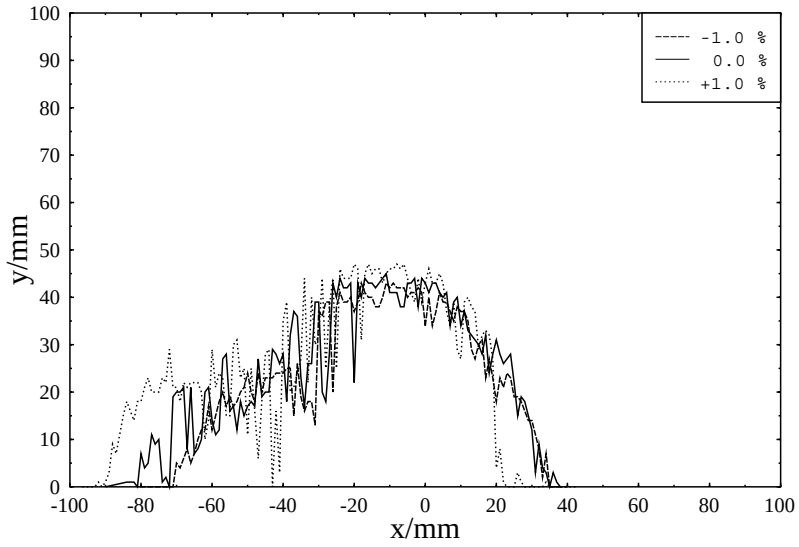

Figure 4.5.16: *Dynamic aperture of the SBLC damping ring with misaligned sextupoles* ($\Delta_x = \Delta_y = 75\mu m$).

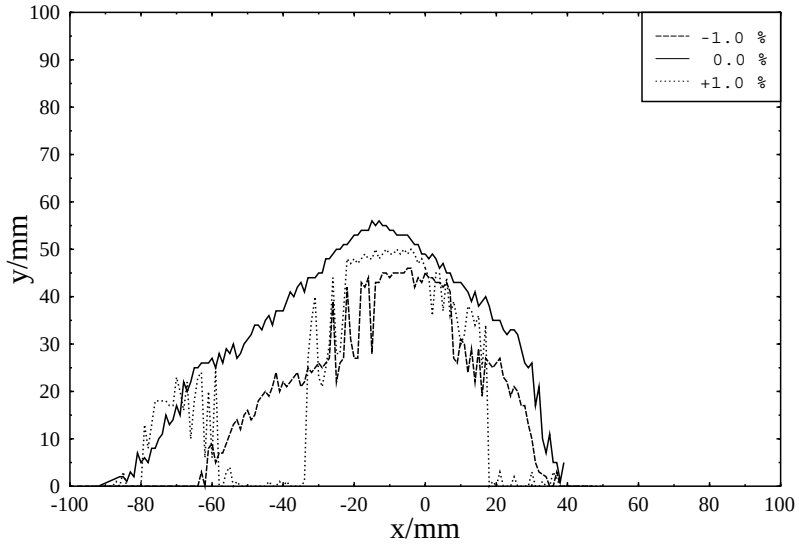

Figure 4.5.17: *Dynamic aperture of the SBLC-damping ring with field errors* $\Delta B/B = 5 \cdot 10^{-4}$ *for the bending and* $\Delta G/G = 5 \cdot 10^{-3}$ *for the quads.*

the bending magnet of ± 15 mm and a bore within the quadrupoles and sextupoles of $r_0 = 20$ mm. With a pole tip field for the quads and sextupoles of 0.6 T and 0.5 T, respectively, the maximum gradients are $g_{max} = 30$ T/m and $g'_{max} = 2500$ T/m^2. The specifications of the magnets for the electron damping ring are summarised in Table 4.5.5.

For the positrons the size (1 σ) of the injected beam will be 5 mm. A factor of 6 between the physical aperture and the cross section should be enough in order to get a sufficient lifetime, because the acceleration time is only 20 ms. The gap within the bendings was chosen to be $\pm$ 20 mm and the bores within the quadrupoles and sextupoles of $\pm$ 35 mm. Similar values have been used for 3rd generation light sources. With this diameters in the quads and sextupoles the maximum gradient decreases to:

$$g_{max} = 18\ T/m \text{ and } \mathrm{g'_{max}} = \ 816\mathrm{T/m^2} \tag{4.5.35}$$

The specifications of the magnets for the positron damping ring are summarised in Table 4.5.6.

Table 4.5.5: *Specification of the magnets for the electron damping ring.*

Bendings:

Energy	3 GeV
Number of magnets	72
Curvature	13.54 m
Magnetic flux	0.739 T
Gap	30 mm
Magnetic length	1.18 m
Ampere turns	23.6 kA
Number of coil windings	72
Nominal current	245

Quadrupoles:

Type	Q_A	Q_B	Q_C	Q_D	Q_E
Number	72	144	72	78	12
Magnetic length [m]	0.05	0.20	0.15	0.10	0.10
Aperture [mm]	40.0	40.0	40.0	40.0	40.0
Gradient [T/m]	1.0	25.5	28.0	28.0	13.0
Ampere turns [kA]	0.16	4.06	4.46	4.46	2.07
Number of coil windings	10	20	20	20	20
Current	16	203	223	223	103

Sextupoles:

Type	S_1	S_2	S_H	S_V
Number	72	72	36	72
Magnetic length	0.05	0.05	0.10	0.10
Aperture	40.0	40.0	40.0	40.0
Diff. gradient [T/m^2]	556	708	1810	1036
Ampere turns [kA]	0.59	0.751	1.921	1.099
Number of coil windings	20	20	30	30
Current [A]	30	37.6	64	36.6

Table 4.5.6: *Specification of the magnets for the positron damping ring.*

Bendings:

Energy	3 GeV
Number of magnets	72
Curvature	13.54 m
Magnetic flux	0.739 T
Gap	40 mm
Magnetic length	1.18 m
Ampere turns	17.5 kA
Number of coil windings	72
Nominal current	328

Quadrupoles:

Type	Q_A	Q_B	Q_C	Q_D	Q_E
Number	72	144	72	78	12
Magnetic length [m]	0.05	0.28	0.23	0.15	0.10
Aperture [mm]	70.0	70.0	70.0	70.0	70.0
Gradient [T/m]	1.0	18.0	18.0	18.0	13.0
Ampere turns [kA]	0.49	8.77	8.77	8.77	8.77
Number of coil windings	10	30	30	30	30
Current	49	292	292	292	211

Sextupole:

Type	S_1	S_2	S_H	S_V
Number	72	72	36	72
Magnetic length	0.05	0.05	0.25	0.15
Aperture	70.0	70.0	70.0	70.0
Diff. gradient [T/m^2]	556	708	724	691
Ampere turns [kA]	3.164	4.026	4.117	3.929
Number of coil windings	20	20	20	20
Current [A]	158	201	206	196

Bibliography

[1] R. Brinkmann, *A Study of Low - Emittance damping ring Lattices*, DESY M-90-09, July 1990

[2] ATF, Accelerator Test facility, Design and Study Report, Internal Report 95-4, June 1995

[3] NCL damping ring, Zeroth-Order Design Report for the next Linear Collider, SLAC, Stanford, 1996.

[4] A. von Steenberger, *Collider Damping Ring, Theoretical Minimum Emittance Structure*, Proceedings of the ICFA Workshop on Low Emittance $e^- - e^+$ Beams, BNL (1987), p.60.

[5] H.Z. Zyngier et. al., *VUV Radiation Source Super ACO*, IEEE Trans. on Nucl. NS-32, 3371 (1985).

[6] D. Einfeld and M. Plesko, *A modified QBA optics for low emittance storage rings*, NIM A335 (1993) 402-416.

[7] D.Einfeld, J.Schaper, M.Plesko, *Design of a Diffraction limited Light Source*, SPIE 2013 (1993) 201-212.

[8] D. Einfeld et al., *The synchrotron light source ROSY*, NIM B89 (1994) 74-78

[9] D. Einfeld et al., *Design of a SBLC-Damping ring with a TBA-optics*, to be published.

[10] 1-2 GeV synchrotron Radiation Sources, PUB-5172 Rev., July 86, LBL, California 94720.

[11] ESRF Foundation Phase Report, February 1987, European Synchrotron Radiation Facility, B.P.220-38043, Grenoble Cedex.

[12] 10th ICFA Beam Dynamics Panel Workshop, 4th Generation Light Sources, Grenoble 1996.

[13] J. Murphy, *Synchrotron Light Source DATA Book*, BNL/NSLS, BNL 42333, Version 4.

[14] A.Ropert, *High Brilliance Lattices and the Effect of Insertion Devices*, CAS: Synchrotron Radiation and Free Electron Laser, CERN 90-03, April 1990.

[15] R.P. Walker, *Wigglers*, Fifth Advanced Accelerator Physics Course, CERN 95-06, Vol.II, November 1995.

[16] D.Einfeld, J.Schaper, M.Plesko, *Design of a Diffraction limited Light Source*, WG3-53, see [7]

[17] A.Wrulich, *Overview of 3rd Generation Light Sources, Workshop on Forth Generation Light sources*, February 24-27, 1992, SSRL 92/02.

[18] ELETTRA, Conceptional Design Report, Sincrotrone Trieste, Padriciano 99, I-34012 Italy.

[19] H.Grote and F.C.Iselin, *The MAD Program,Version 8.16*, CERN/SL/90-13 (AP), 1995.

[20] F.Iazzourene,C.J.Bocchetta,R.Nagaoka,L.Tosi and A.Wrulich, RACETRACK USER'S GUIDE, Version 4.01, ST-IM-92/I ,July 1992.

[21] L.Farvaque,J.L.Laclare and A.Ropert, *BETA USER'S GUIDE*, ESRF-SR/LAT 88-08, 1988.

[22] R.Byrns, B. Dwersteg et al., *Status of the Superconducting Cavity Program for HERA*, Proceedings EPAC 90, Nice June 12-16, 1996.

[23] M.S.Zisman,S.Chattopadhyay and J.J.Bisognano, *ZAP USER'S MANUAL*, LBL-21230,December 1986.

[24] A.Wrulich,private communication.

[25] J.E.Karantzontis, *An Overview on Impedances and Impedance Measuring Methods for Accelerators*, ST/M-91/1, January 1991, Sincrotrone Trieste.

[26] J.E.Karantzontis, *The Coupling Impedance of the ELETTRA Storage Ring ST/M-TN-90/14*, August 1990, Sincrotrone Trieste.

[27] M.Svandrlik, A.Fabris, C.Pasoni, *Improved Methods of Measuring and Curing Multibunch Instabilities in ELETTRA*, Proceedings of the EPAC 96, Sitges, Spain.

[28] J.E.Karantzontis et.al., *Beam Lifetime Measurement in ELETTRA*, Proceedings of the EPAC 96, Sitges, Spain.

[29] M.Svandrlik et al., *The Cure of Multibunch instability in ELETTRA*, Proceedings of the PAC 95, Dallas, Texas, USA

[30] S.Belomestny et al, *Comparison of the Predicted and Measured Loss Factor of the Superconducting Cavity Assembly for the CESR Upgrade*, Proceedings of the PAC 95, Dallas, Texas, USA.

[31] S.Belomestnyk et al., *Wakefield and HOMs Studies of a Superconducting Cavity Mode with the CESR Beam*, Proceedings of the PAC 95, Dallas, Texas, USA

[32] B. Autin and Y. Marti, *Closed Orbit Correction in A.G. Machines Using a Small Number of Magnets*, CERN-ISR-MA-73-17, 1973.

4.6 Bunch Compressor

4.6.1 Introduction

In this section, a detailed design for a single stage beam bunch length compressor for the is presented. Compression is achieved by introducing an energy-position correlation along the bunch with an RF section at zero-crossing phase followed by a short bending section with energy dependent path length (momentum compaction). The motivation for a wiggler design is presented and many of the critical single bunch tolerances are evaluated. A solenoid based spin rotator is included in the design and transverse emittance tuning elements, diagnostics and tuning methods are described. Bunch length limitations due to second order momentum compaction and sinusoidal RF shape are discussed with options for compensation.

4.6.2 Bunch Compressor Design Issues

The bunch compressor design is influenced by several criteria:

- The compressor must reduce the bunch length extracted fom the damping ring to the appropriate size in the linac.
- The system must perform a 90 degree longitudinal phase space rotation so that damping ring extracted phase errors do not translate into linac phase errors which can produce large final beam energy deviations.
- The system must not significantly dilute the transverse emittances and should include tuning elements for correction.
- With its low energy and initially small energy spread, the bunch compressor is a convenient place to include solenoids for full control of the spin orientation.
- The compressor should be short, simple and as error tolerant as possible.

4.6.3 Bunch Compressor Parameters

The rms bunch length at the entrance to the linac (for uncorrelated Damping Ring energy spread σ_{δ_0}) is

$$\sigma_{zl} = \sqrt{(1+\alpha k)^2\sigma_{z_0}^2 + \alpha^2\sigma_{\delta_0}^2} \tag{4.6.1}$$

with $\alpha \equiv \int \frac{\eta(s)}{\rho(s)} ds$ and $k = \frac{2\pi e V_0}{\lambda E_0}$, where η and ρ are dispersion and bending radius along the beam line while V_0 and λ are amplitude and wavelength of the RF system. E_0 is the beam energy.

The minimum bunch length is achieved when $\alpha = -1/k$ which also decouples the linac phase from the DR phase. The momentum compaction is chosen to achieve the desired linac bunch length and the RF voltage is then given:

$$\alpha = -\frac{1}{k} = \frac{\sigma_{z_l}}{\sigma_{\delta_0}} \qquad eV_0 = -\frac{\lambda_{RF} E_0}{2\pi\,\alpha}. \tag{4.6.2}$$

parameter	symbol	unit	
Energy	E_0	GeV	3
rms horizontal emittance	ϵ_x	mm-mrad	4.0
rms vertical emittance	ϵ_x	mm-mrad	0.2
rms DR bunch length	σ_{z_0}	mm	4
rms DR energy spread	σ_{δ_0}	%	0.1
rms linac bunch length	σ_{z_l}	mm	0.3
rms linac energy spread	σ_{δ_l}	%	1.5
RF wavelength	λ_{RF}	m	0.1
RF voltage	V_0	MV	192
RF gradient	G_{RF}	MV/m	17
length of RF section	L_{RF}	m	11.3
momentum compaction	α	m	0.26

Table 4.6.1: *Bunch compressor parameters. Emittance values represent those immediately after DR extraction and are smaller than the design values at the IP in order to have a safety margin.*

The resulting energy spread at the linac entrance is approximately amplified by the inverse of the bunch compression factor.

$$\sigma_{\delta_l} = \sigma_{\delta_0}\sqrt{\frac{\sigma_{z_0}}{\sigma_{z_l}} + 1} \approx \sigma_{\delta_0}\frac{\sigma_{z_0}}{\sigma_{z_l}} \quad , \quad (\sigma_{z_l} \ll \sigma_{z_0}) \tag{4.6.3}$$

The damping ring (DR) and initial linac parameters relevant for bunch compressor design are listed in Table 4.6.1.

4.6.4 Bunch Compressor Optics

A simple way to produce the necessary momentum compaction is with a chicane made of four horizontal bending magnets. A chicane of total length 13 m for the SBLC design is possible, however, the peak dispersion required is large at 0.8 m. With 1.5 % rms energy spread the horizontal beam size becomes very large (σ_x=12 mm) and dipole field quality tolerances become tight. A more error tolerant design is achievable with a wiggler section [1] made up of N_p periods each with two bending magnets and two quadrupoles-one at each zero crossing of the dispersion function. If the bends are rectangular and each of length L_B with angle θ_B and separated by ΔL, and the quadrupoles alternately reverse sign to produce a phase advance per cell of $\Psi_x(=\Psi_y)$, the momentum compaction, α_w, and the horizontal emittance growth due to synchrotron radiation (SR), $\Delta\gamma\epsilon_x$, are given by [1]:

$$\alpha_w = \frac{1}{4}\theta_B^2[N_p(2\Delta L + L_B) - \frac{1}{6}(2N_p + 1)L_B] \tag{4.6.4}$$

$$\Delta\gamma\epsilon_x \approx (1.25 \cdot 10^{-8} m^2 \cdot GeV^{-6}) \cdot E_0^6 N_p \frac{|\theta_B|^5(\Delta L + L_B)}{L_B^2 |sin\Psi_x|} \tag{4.6.5}$$

parameter	symbol	unit	
momentum compaction	α_w	meters	0.26
dipole magnet length	L_B	meters	1.5
bend-to-bend separation	D_L	meters	2.5
bend angle / dipole	ϕ_B	degrees	12.0
total length	L_{tot}	meters	36
maximum x-dispersion	η_{max}	mm	170
SR x-emittance dilution	$\Delta\epsilon_x/\epsilon_{x0}$	%	0.7
dipole magnetic field	B_0	kG	14.67
number of periods	N_p	-	4
phase advance per period	q_x	degrees	90

Table 4.6.2: *Wiggler design parameters (NOTE: All non-correction quadrupoles in the entire beamline are of length 15 cm and pole-tip radius 1 cm).*

By setting the necessary momentum compaction [2] and choosing a horizontal SR emittance dilution of 1-2%, a dipole field strength of 15 kG, and roughly minimizing dipole magnet length and peak dispersion, the wiggler design parameters listed in Table 2 were developed. With $|\sin\Psi_x|^{-1}$ minimized at $\Psi_x = \pi/2$, the number of periods is chosen so that each dipole at peak dispersion has an opposing dipole separated by π in betatron phase advance: all orders of dispersion generated by equal multipole field components cancel. The peak horizontal beam size in the wiggler is 2.6 mm.

4.6.5 Peripheral Sections and the Full Beamline

In addition to the primary function of bunch compression, the beamline described here also includes sections for spin rotation, cross-plane coupling correction, and phase space diagnostics. This section describes these modules (for reference, the entire beamline is depicted in Fig. 4.6.1).

4.6.5.1 Spin Rotator

It can be shown [3] that for a chicane type "half serpent" $\pi/2$ spin rotator [4] constructed from horizontal and vertical bending magnets, and for $< 2\%$ SR vertical emittance dilution, the relationship between the length of the bending magnets and the beam energy is discouraging: $L[m] > 30 \cdot E[GeV]$. Even at 3 GeV the dipoles are about 100 m long. Therefore a spin rotator based on superconducting solenoids is proposed prior to bunch compression. Since the damped beam is flat ($\epsilon_y/\epsilon_x \ll 1$) the cross-plane coupling induced by the solenoids must be compensated. This is achieved by rotating the spin by $\pi/2$ around the longitudinal axis with a pair of $\pi/4$ solenoids separated by a 'reflector' beamline which causes the solenoid pair's coupling to cancel while their spin precession adds. In this way the solenoid coupling is always canceled regardless of the solenoid settings as long as the solenoid pairs have equal strength

parameter	symbol	unit	
momentum compaction	α_w	meters	0.600
effective solenoid length	L_{sol}	meters	2.275
maximum solenoid field	B_z	kG	38.0
total arc bend angle	ϕ	degrees	12.0
total length of rotator system	L_{tot}	meters	52
number of dipole magnets (12 degree arc)	N_{dipole}	-	4
dipole field	B_0	kG	6.1
SR x-emittance dilution	$\Delta\epsilon_x/\epsilon_{x0}$	%	$1 \cdot 10^{-3}$
momentum compaction of all arcs	α_a	m	0.02
chromatic ϵ_y dilution ($\sigma_{\delta 0}$) = 0.1%)	$\Delta\epsilon_y/\epsilon_{y0}$	%	0.7
chromatic ϵ_y dilution ($\sigma_{\delta 0}$) = 0.2%)	$\Delta\epsilon_y/\epsilon_{y0}$	%	4.6
chromatic ϵ_y dilution ($\sigma_{\delta 0}$) = 0.3%)	$\Delta\epsilon_y/\epsilon_{y0}$	%	10.9

Table 4.6.3: *Spin rotator parameters*

($\pm 2\%$). By separating two such solenoid pair systems with a $\pi/2$ spin rotation around the vertical axis (i.e. an arc of total bend angle $\theta = \pi/2\alpha\gamma$) full arbitrary control of the spin orientation is possible. The focusing effect of the solenoids is corrected with four matching quadrupoles per paired solenoid section. The matching quadrupoles are positioned between the paired solenoid sections and the central arc. At $\sim 0.1\%$ rms DR energy spread the emittance dilution due to chromatic coupling of the four solenoids together at maximum field is negligible at 0.7%. The parameters of the spin rotator system are given in Table 4.6.3.

4.6.5.2 Coupling Correction Section

In order to empirically correct anomalous cross-plane coupling due to either damping ring extraction errors or spin rotator errors, a skew correction section (SCS) is included immediately following the final rotator solenoid. The system is constructed from four small skew quadrupoles with zero nominal strength. The first and second skew quadrupoles are separated by betatron phases of $\Delta\Psi_x = \Delta\Psi_y = \pi/2$. This is also true for the third and fourth skew quadrupoles. The second and third are separated by $\Delta\Psi_x = \pi, \Delta\Psi_y = \pi/2$ such that the four skew quadrupoles orthogonally control the four coupling coefficients in the beam: $\langle x'y\rangle$, $\langle xy'\rangle$, $\langle xy\rangle$ and $\langle x'y'\rangle$, respectively. The four skew corrections are actually orthonormal in that the emittance sensitivity to each skew quadrupole is designed to be a constant (i.e. $\beta_x\beta_y$ is equal at each skew quadrupole). The relative emittance increase for one thin skew quadrupole of focal length f at beta functions of $\beta_x\beta_y$ is

$$\frac{\epsilon_y}{\epsilon_{y_0}} = \sqrt{1 + \frac{\epsilon_{x_0}}{\epsilon_{y_0}}\frac{\beta_x\beta_y}{f^2}}. \tag{4.6.6}$$

With skew quadrupoles of 10 cm length, 1 kG pole tip fields and 1 cm radii, a factor of about two in emittance increase can be corrected per skew quadrupole.

4.6.5.3 Diagnostic Section

It is important to provide measurement capability after the bunch compressor so that the beam emittance and matching can be monitored and corrected before entrance into the main linac. Following the wiggler section is a simple set of three FODO cells with phase advance per cell of $\Delta\Psi_x = \Delta\Psi_y = \pi/4$. By placing four wire scanners [5] near the vertical focusing quadrupoles the ideal four-wire scanner phase sampling is available to make high precision emittance and beta function measurements in each plane. The nominal rms beam size at the scanners is chosen as 19 μm vertically and 65 μm horizontally. A matched beam is easily identified since in this case the beam sizes per plane are identical at each of the four wire scanners. The cross-plane coupling in the beam is not fully measurable with this section. However, by simply minimizing the vertical emittance (flat beam) with the four SCS skew quadrupoles all coupling can be corrected (with some iteration necessary in extreme cases). A direct measurement capability is achievable, if desired, by using six wire scanners with phase advances similar to the SCS described above [6].

4.6.5.4 Compressor RF Section

The energy-position correlation is introduced with 12 meter S-Band structures with gradient of 17 MV/m in order to produce the necessary 192 MV for full bunch compression.

4.6.5.5 The Combined Beamline

The four sections described thus far (spin rotator, coupling correction, bunch compressor and diagnostics) are combined using various appropriate matching quadrupoles to preserve the periodic beta functions in the various FODO cells. The combined system floorplan is laid out in Fig. 4.6.1. The system, including the 3.1 meter spin rotator bump, should fit inside a 5 meter diameter tunnel. The angle of the first arc may be reduced and the angle of the third arc equally increased if it is necessary to horizontally displace the outgoing beamline relative to the incoming one. It is only necessary that the middle arc remains fixed so that the electron or positron spin orientation is fully controllable over a sphere.

4.6.6 Tolerances

4.6.6.1 Single Bunch Tolerances

The large energy spread and strong bending of the wiggler present some challenges for transverse emittance preservation, especially in the vertical plane. Several important tolerances are examined below. Table 4 evaluates these tolerances:

- A rolled dipole magnet introduces vertical dispersion which, if not corrected, will chromatically filament in the main linac and dilute the vertical emittance.

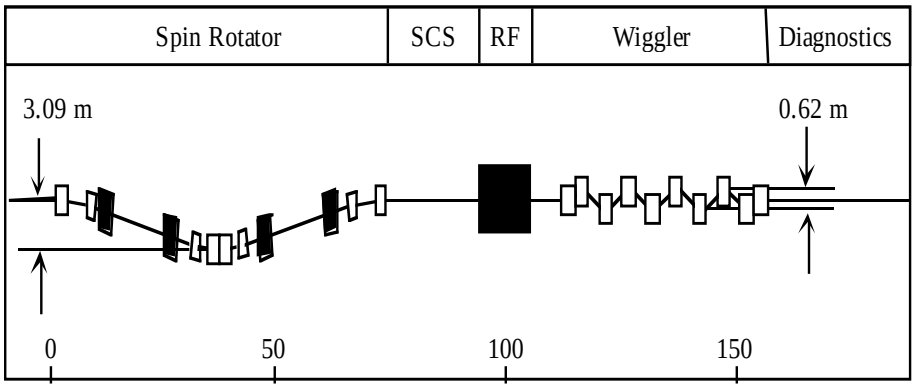

Figure 4.6.1: *Schematic layout of complete beamline floorplan. Solenoids and the RF-module are in black, dipole magnets are in white (quadrupole magnets not shown).*

- A quadrupole (sextupole) field component in a dipole with horizontal dispersion will dilute the horizontal emittance through the generation of first (second) order horizontal dispersion. The symmetry of the wiggler optics introduces a strong cancellation of these two effects if the dipole field errors are similar for all magnets. This tolerance, when applied to the wiggler dipoles, can therefore be considered as a constraint on the field uniformity over the eight inner wiggler dipoles (the first and tenth have near zero dispersion).

- A misaligned quadrupole will generate vertical and/or horizontal dispersion.

- A rolled quadrupole in a non-dispersive section will couple the beams while a rolled quadrupole in a dominantly dispersive section will generate vertical dispersion. Table 4 lists a range of roll tolerances with the tightest tolerance on one of the matching quadrupoles just after the RF section and also on the quadrupole in the center of the 12 degree arc. The loosest tolerances are on the wiggler quadrupoles which are weak.

- There are also tolerances on the difference of the field strengths between the paired solenoids and also on the absolute gradient of the eight quadrupoles which make up the reflector beamline between the paired solenoids. These tolerances have been evaluated with tracking and are included in Table 4.6.4. These tolerances assume no correction. The reflector beamline quadrupole gradient tolerances are evaluated at the maximum solenoid field and vary over the eight quadrupoles. The tightest of the eight are for the two quadrupoles which are most centered between the paired solenoids.

- If the phase, ψ_{RF}, of the compression RF were to deviate from the zero crossing this energy offset will advance or delay the phase of the bunch as it enters the linac and upset the collision timing at the interaction point (IP).

tolerance	symbol	unit	
wiggler dipole magnet roll tolerance	$\|\phi\|$	μrad	80
quad. field in wiggler dipole (r0=20 mm)	$\|b1/b0\|$	-	$4.0 \cdot 10^{-5}$
sext. field in wiggler dipole (r0=20 mm)	$\|b2/b0\|$	-	$1.4 \cdot 10^{-4}$
F-quad. x-misalignment tolerance	$\|\Delta_x\|$	μm	460
D-quad. y-misalignment tolerance	$\|\Delta_y\|$	μm	70
Quadrupole roll tolerance range	$\|\phi\|$	mrad	3.5 - 14
Paired solenoid field difference tolerance	$\|\Delta b_z/B_{z-max}\|$	%	2
reflector quad. grad. tol. range (max. sol.)	$\|\Delta G/G_0\|$	%	0.4 - 1.7
compression RF phase stability tolerance	$\|\psi_{RF}\|$	degrees	0.33

Table 4.6.4: *Single element tolerances for wigglers and spin rotators for $< 2\,\%$ emittance dilution or $|\langle z_l\rangle| < \sigma_{z_l}/3$ longitudinal stability at the IP (no correction assumed).*

The roll tolerances are quite tight and probably difficult to achieve. However, these tolerances can be relaxed by an order of magnitude by including small normal and skew quadrupoles of zero nominal field to be used for dispersion correction.

4.6.6.2 Damping Ring Extraction Phase Tolerances and Limits for Bunch Compression

The compression arguments presented thus far are limited to linear effects. In fact the bunch is not infinitely compressible and at some point second order momentum compaction limits the achievable bunch length. the second order momentum compaction, α_2, the linac bunch position of a particle has a quadratic dependence on its DR bunch position.

$$z_l = [\alpha + \alpha_2\delta_0]\delta_0 + (1 + k[\alpha + \alpha_2\delta_0])z_0 + \alpha_2 k^2 z_0^2 \approx \alpha\delta_0 + \alpha_2 k^2 z_0^2 \tag{4.6.7}$$

The approximation made in eq. 4.6.7 is possible since $\alpha_2\delta_0 \ll \alpha$ and $k = -1/\alpha$. For a wiggler, the approximate relationship between the second and first order momentum compaction is

$$\alpha_2 \approx -\frac{3}{2}\alpha. \tag{4.6.8}$$

For a DR bunch length distribution which is Gaussian (i.e. $\langle z_0^4\rangle = 3\langle z_0^2\rangle^2$) and 'full compression' ($k = -1/\alpha$), the linac rms bunch length is

$$\sigma_{z_l}^2 \approx \langle z_l^2\rangle - \langle z_l\rangle^2 = \alpha^2\sigma_{\delta_0}^2 + \frac{9}{2}\cdot\frac{\sigma_{z_0}^4}{\alpha^2} \tag{4.6.9}$$

If α is reduced in order to compress the bunch toward zero, the second term on the r.h.s. of eq. 4.6.9 begins to dominate the final bunch length. The minimum achievable bunch length is given by:

$$\sigma_{z_l-min} = \sqrt{3\sqrt{2}\sigma_{\delta_0}\sigma_{z_0}} \tag{4.6.10}$$

In addition to limiting the achievable bunch length, the second order momentum compaction also gives rise to a quadratic linac "phase" dependence on DR "phase". Thus, DR extraction "phase" errors, $\langle z_0 \rangle$, will transform into final beam energy deviations roughly depending on the mean accelerating RF phase in the main linac, $\langle \psi \rangle$ (=0 at RF crest). For small "phase" errors, $z_l \ll \lambda$, and including only the RF curvature in the main linac, final beam energy deviations, $\langle \delta_E \rangle$, can be approximated by

$$\langle \delta_E \rangle \approx -\frac{2\pi \tan\langle \psi \rangle}{\lambda} \cdot \langle z_l \rangle. \tag{4.6.11}$$

The DR extraction "phase" jitter tolerance is then:

$$|\langle z_0 \rangle| < \sqrt{\frac{|\langle \delta_E \rangle| \lambda \alpha}{3\pi |\tan\langle \psi \rangle|}}. \tag{4.6.12}$$

The necessary stability of the longitudinal beam position at the interaction point (IP) also sets a tolerance on DR "phase" jitter. The DR "phase" jitter tolerance for fraction bunch position IP stability of $|\langle z_l \rangle| < \sigma_{z_l}/n$ (e.g. n =3) is

$$|\langle z_0 \rangle|_{tol} < \sqrt{\frac{2\alpha\sigma_{z_l}}{3n}} \tag{4.6.13}$$

The bunch length is also limited by the sinusoidal character of the compressor RF. Including the 3rd order term of the $\sin(z_0)$ expansion and not including the second order momentum compaction, the bunch position of a particle in the linac, for full compression where $k = -1/\alpha$, is

$$z_l \approx \alpha\delta_0 + \frac{1}{6}\left(\frac{2\pi}{\lambda}\right)^2 \cdot z_0^3, \tag{4.6.14}$$

and for a DR bunch length distribution which is initially gaussian, the rms bunch length is

$$\sigma_{z_l}^2 \approx \alpha^2\sigma_{\delta_0}^2 + \frac{5}{12} \cdot \left(\frac{2\pi}{\lambda}\right)^4 \cdot \sigma_{z_0}^6 \tag{4.6.15}$$

In this case the minimum achievable bunch length is in the direction $\alpha \to 0$. The DR extraction "phase" jitter tolerance due to the sinusoidal RF is given by

$$|\langle z_0 \rangle|_{tol} < \frac{\lambda}{2\pi}\left(\frac{6|\delta_E|}{|\tan\langle \psi \rangle|}\right)^{\frac{1}{3}} \tag{4.6.16}$$

Required IP longitudinal stability sets a DR "phase" jitter tolerance of

$$|\langle z_0 \rangle|_{tol} < \left(\frac{6\sigma_{z_l}}{n}[\frac{\lambda}{2\pi}]^2\right)^{\frac{1}{3}} \tag{4.6.17}$$

Bunch length limitations and DR phase jitter tolerances for both second order momentum compaction and sinusoidal RF effects are summarized below in Table V.

parameter	symbol	unit	
linac linear bunch length	σ_{zl}	mm	0.3
linac frequency	f_{RF}	GHz	3.0
linac mean acc. phase	$\langle\psi\rangle$	degrees	2.0
The following include the effect of second order momentum compaction only.			
linac rms 2nd order bunch length	σ_{zl}	mm	0.33
min. 2nd order linac bunch length	σ_{zl-min}	mm	0.28
DR "phase" tol. for $\langle\delta_E\rangle < 0.01\%$	$\lvert\langle z_0\rangle\rvert_{tol}$	mm (deg)	9 (32)
DR "phase" tol. for $\lvert z_l\rvert/\sigma_{z_l} < 1/3$	$\lvert\langle z_0\rangle\rvert_{tol}$	mm (deg)	4 (15)
The following include the effect of the sinusoidal RF only.			
linac rms sinusoidal bunch length	σ_{z_l}	mm	0.34
min. rms sinusoidal linac b.l.	σ_{z_l-min}	mm	0.16
DR "phase" tol. for $\langle\delta_E\rangle < 0.01\%$	$\lvert\langle z_0\rangle\rvert_{tol}$	mm (deg)	9 (32)
DR "phase" tol. for $\lvert z_l\rvert/\sigma_{z_l} < 1/3$	$\lvert\langle z_0\rangle\rvert_{tol}$	mm (deg)	5 (19)
The following includes both non-linear bunch length limitations.			
linac rms bunch length	σ_{z_l}	mm	0.36

Table 4.6.5: *Bunch length limits and DR phase jitter tolerances, due to second order momentum compaction and sinusoidal compressor RF each taken in isolation. The DR extracted bunch length distribution is taken as a Gaussian for these calculations. The phase tolerances specified in deg. are w.r.t. the compressor-RF. They are smaller by a factor of three for the damping ring RF-system.*

It can be shown that the two non-linear bunch length limitations discussed above approximately add in quadrature. The net rms bunch length, including both effects, is listed at the end of the table. Note, with these non-linear effects the rms bunch length results are somewhat dependent on the initial DR extracted bunch distribution-taken as a Gaussian here.

Bibliography

[1] T. O. Raubenheimer, P. Emma, S. Kheifets, *Chicane and Wiggler Based Bunch Compressors for Future Linear Colliders*, Proc. of the 1993 Particle Accelerator Conference, Washington, D.C., 1993.

[2] The momentum compaction has been chosen slightly smaller than the linear design would require in order to somewhat compensate for RF non-linearities.

[3] P. Emma, *A Spin Rotator System for the NLC*, NLC-NOTE 7, December 1994.

[4] T. Fieguth, *Snakes, Serpents, Rotators and the Octahedral Group*, SLAC-PUB-4195, January, 1987.

[5] The term "wire scanner" may refer to a laser wire rather than a metallic filament, depending on survivability details. However, it will be prudent to include simple, well tested metallic filament type wire scanners for single bunch measurement to initially commission the beamline.

[6] P. Emma, *A Skew Correction and Diagnostic Section for Linear Colliders*, NLC-NOTE in preparation.

4.7 Beam Delivery System

4.7.1 Introduction

The Beam Delivery System (BDS) is the transfer line which transports the beam from the linac exit to the interaction point (IP) of the collider. Its main function is to demagnify the beams and to bring them to collisions with spot sizes down to 335 nm $\times$ 15 nm at the center of the detector. The overall $\approx 100 \times 200$ demagnification from linac to IP is mostly produced by a strongly focusing quadrupole doublet 2.2 m distant from the IP. Together with a weaker upstream doublet, it comprises a final transformer (FT), or telescope, with 16×46 demagnification.

The chromaticity of the final doublet, together with the expected 3.5×10^{-3} incoming beam relative energy spread, leads to large aberrations which blow up the spot size if uncorrected. The FT is therefore preceded by a Chromatic Correction Section (CCS) where sextupoles, located in dispersive regions, create the necessary quadrupole correction for the off-energy particles. The energy bandwidth of this correction determines the energy acceptance of the whole system.

The optics of the Final Focus System (FFS), namely the combination of the Chromatic Correction Section and the Final Transformer, derives from the one of the SLAC Linear Collider FFS [1] with one essential difference consisting in separate, rather than interleaved, horizontal and vertical chromaticity correction sections. The non-interleaved CCS optics which requires more space but in return reduces considerably the amount of non-linear aberrations, has been adopted and operated successfully by the Final Focus Test Beam (FFTB) facility [2] at SLAC In addition to the two non-interleaved pairs of sextupoles, additional sextupoles are placed at strategic positions to improve the bandwidth of the system.

The transverse beam tails passing through the doublet quadrupoles produce synchrotron radiation which in turn can be a source of background in the detector. The photon energies and angles are maximum in the last doublet where masking is difficult. As seen in Fig.4.7.16, the collimation requirement for a complete clearance of the interaction region is about $10.7\,\sigma_x \times 27\,\sigma_y$. The beam halo, possibly generated in the linac, is therefore scraped off in the collimation section (CS) by an arrangement of spoilers and absorbers described in Section 4.7.8.

A short Linac Matching Section (LMS) matches the beam from the linac exit to the entrance of the collimation section.

The essential ability to measure the beam emittances after the linac and before final focus system and to correct the incoming transverse coupling is provided by the Tuning and Diagnostic Section (TDS) (see Section 4.7.5), following the Collimation Section.

Finally, changing the beam sizes and angular divergences at the IP in order to optimize the collision parameters without modifying the FT and CCS sensitive optics can be done in the Beta Matching Section (BMS), located between the TDS and the CCS.

4.7.2 Magnet Lattice and Optics

The magnet lattice and beam optical functions along the beam delivery system are shown in Fig.4.7.1. The geometry is arranged such that the system fits into a straight tunnel (see Fig. 4.7.2) and matches the required crossing angle at the IP of 6 mrad. The BDS is composed of the 6 sections whose function has been described above.

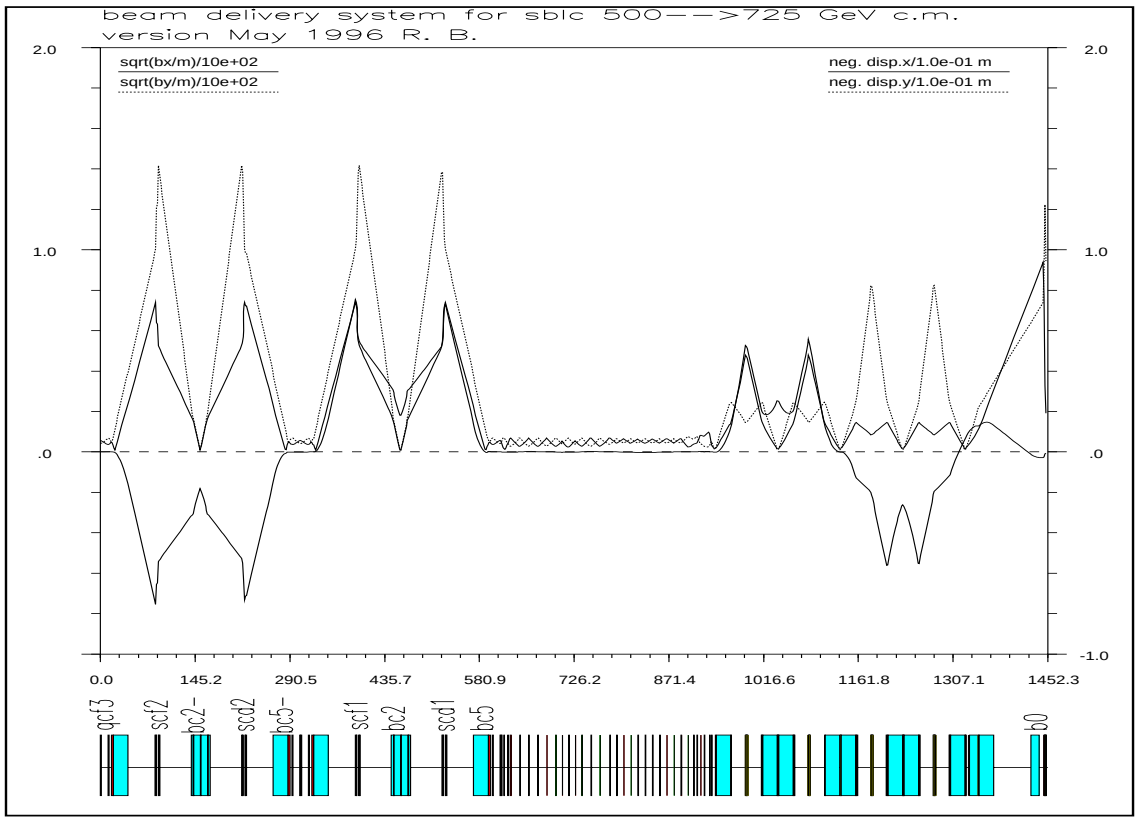

Figure 4.7.1: *Beam optics of the SBLC delivery system.*

• The **Linac Matching Section** (LMS) is composed of six quadrupoles, including the last focusing linac quadrupoles, which provide enough free parameters to match the beam to the entrance of the collimation section and therefore to tune the beam sizes at the collimator locations.

• The **Collimation Section** (CS) provides 4 regions of combined high horizontal and vertical betas as well as large horizontal dispersion. Each region hosts a pair of Titanium collimators to intercept off-momentum and large (x and y) amplitude particles. In normal operation, their aperture is set to $7\,\sigma_x$ and $18\,\sigma_y$ and they collimate particles with more than 2.2% momentum offset. The last two collimator pairs are in phase with the last doublet: they intercept the sine-like trajectories (with respect to the IP) which have the largest amplitudes in this doublet and therefore produce the most

harmful part of the synchrotron radiation in the last quadrupoles. The two upstream collimator pairs are in phase with the IP and thus intercept the cosine-like trajectories. This second phase collimation is necessary to protect the detector from phase mixing, of chromatic or non-linear origin, occurring between the collimation section and the last doublet. To minimize the chromatic phase mixing in the CS itself, the chromaticity created by the CS high-beta regions is corrected locally by embedded sextupoles pairs, in a way similar to the one described below for the CCS.

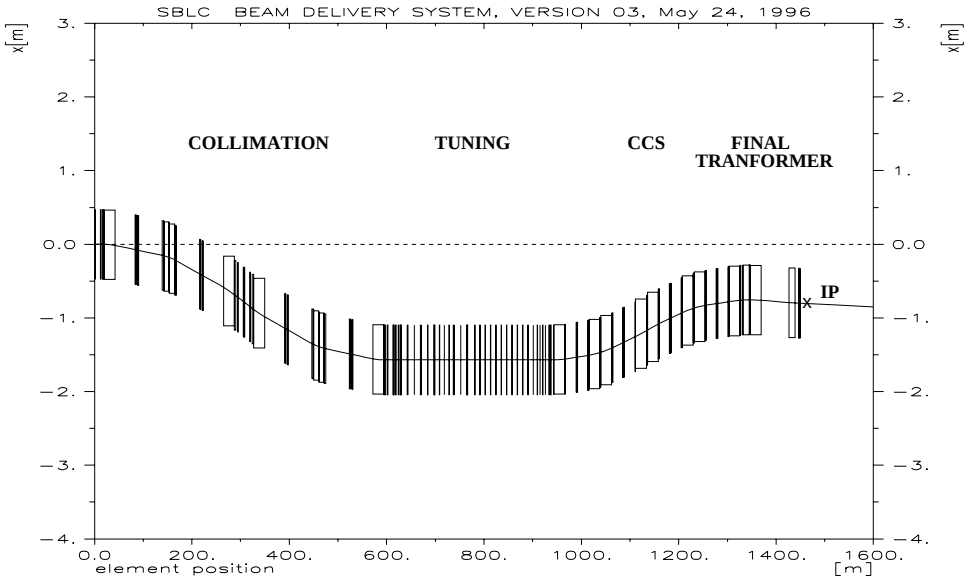

Figure 4.7.2: *Horizontal survey of the beam delivery system.*

• the **Tuning and Diagnostic Section** (TDS) is a section devoted to measuring and correcting the sensitive transverse coupling, inherited from the Linac transport and/or created in the Collimation Section. The coupling correction is performed in the Skew Quadrupole Correction Section (SQSC) which hosts four skew quadrupoles located at the proper relative phase advances to cancel the four coupling coefficients of the transverse beam matrix. Tuning is done by minimizing the vertical emittance which is measured, together with the horizontal one, in the Emittance Measurement Section (EMS). The EMS is a simple FODO lattice with three and a half 45° cells along which four wire scanners are regularly disposed every 45° in phase space. Each wire scanner measures the horizontal and vertical spot sizes, expected to be about equal to $14\,\mu$m and $4.6\,\mu$m. This is therefore in the range of solid carbon wires as the ones currently and reliably operated in the SLC. The regularity of the beam phase advances and spot sizes at the wire locations optimizes the reconstruction of the transverse emittances from the spot size measurements.

• the **Beta Matching Section** (BMS) contains 7 quadrupoles which allow to

match the beam matrix at the entrance of the final focus system over a wide range of parameters. Since the final focus system is a pure demagnifying telescopic system, the BMS can therefore be used to fine tune the beam at the IP as well as the phase advance from the collimators to the last doublet. It can also be used, for the start-up operation, to blow up the beam as much as a factor 10 with a relative variation of the quadrupole gradients limited to about $\pm 20\%$. The BMS magnets need therefore to be tunable over this range.

• the **Chromatic Correction Section** (CCS) is a one to one transformer composed of two FODO sections with four 90° cells each. Both sections contain four bending magnets symmetrically disposed to generate a closed horizontal dispersion bump, and a pair of strong sextupoles to tune the chromaticity. Since the two sections have opposite quadrupole polarities, the first one corrects the horizontal chromaticity and the second one the vertical chromaticity. Each of the four sextupoles is located next the central quadrupole where the phase advance is a multiple of $\pi/2$ and the relevant beta-function is maximum. In this way the sextupoles do not generate geometric or chromatic aberrations other than the ones needed to cancel the chromatic aberrations from the last doublet. With these two pairs of sextupoles alone, the resulting bandwidth amounts to $\pm 0.5\%$, sufficient to accomodate most of the energy spread of the beam (σ_E/E=0.35%, peak-to-peak spread $\pm 0.7\%$). In order to avoid spot size dilution from the tails in the beam energy distribution and to create a comfortable safety margin, a further optimisation of the bandwidth is applied by adding sextupoles at strategic positions in the lattice. The applied optimisation procedure is described in detail in ref. [3]. The resulting bandwidth is $\pm 1.1\%$, as shown in Fig. 4.7.5. The additional sextupoles are weaker than the four main ones and introduce only negligible geometric aberrations.

With opposite dipole polarities, the two sections of the CCS create an S-shaped orbit with two opposing deflection angles of about 4 mrad generated by four 22.2 m long dipoles with a field of 39 mT at a beam energy of 250 GeV. The beam relative energy spread due to synchrotron radiation along these 8 dipoles and the relative energy loss between sextupoles of the same pair are both very small, about 2×10^{-5}.

• the **Final Transformer** (FT) is a telescopic system which achieves the final demagnification of the beam spot sizes by a factor of 16 horizontally and 46 vertically. It is composed of a weak and a strong doublet separated by 120 m. The strong final doublet, located inside of the detector, is composed of two quadrupoles of 350 T/m and 210 T/m gradient, respectively. The stronger, vertically focussing one has an aperture radius of 3 mm and a length of 1.6 m, the corresponding parameters for the weaker, horizontally focussing quadrupole are a_Q=5 mm and l_Q=2 m. A superconducting solenoid has to be foreseen around the quadrupoles in order to shield the iron from the strong field of the detector. Superconducting coils are used in the strong vertically focussing quadrupole (superferric design). A detailed technical design for the final doublet still needs to be worked out, but field calculations based on the cross section shown in Fig. 4.7.3 indicate that the required field quality can be achieved and that the gradient can be increased to accomodate an upgrade of the beam energy to about 375 GeV.

Besides the two quadrupole doublets, the Final Transformer contains three dipole

magnets which create a dispersion bump at the position of the weak doublet. This allows compensation of the vertical chromaticity locally and contributes to the large momentum bandwidth of the system. The synchrotron light from the dipoles is collimated such that the remaining radiation fan can pass freely through the interaction region.

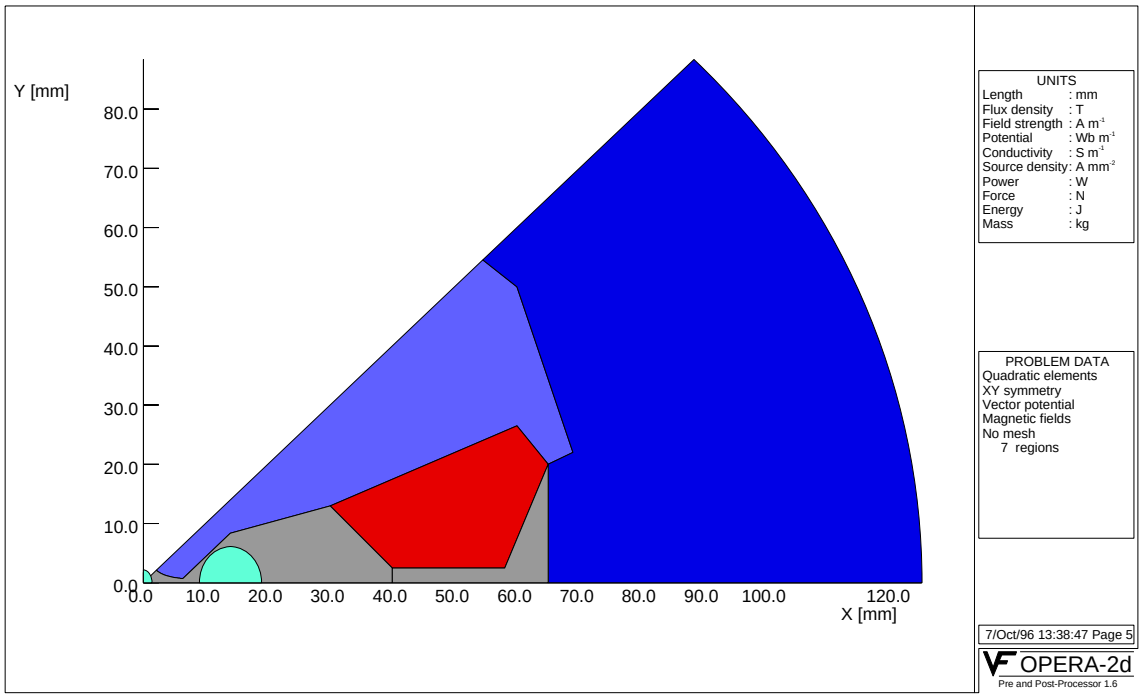

Figure 4.7.3: *Final quadrupole cross-section.*

• **Crossing angle**

Because of the 6 ns (about 2 m) bunch separation, the beams have to collide at an angle to avoid parasitic interactions. With a total crossing angle of 6 mrad, the outgoing beams are sufficiently offset to safely avoid the so-called multibunch kink instability. Furthermore, this separation is large enough for providing enough aperture for the outgoing synchrotron light. The disadvantage of the crossing angle scheme is a reduction of the luminosity due to the effective increase of the horizontal spot size at the IP. This effect can be avoided by rotating the bunches of both beams in the horizontal plane by half the crossing angle so that the beams collide quasi head-on ("crab-crossing"). In this design, the rotation is provided by a combination of the correlated energy spread in the bunches with a finite horizontal dispersion at the IP. The dispersion is easily generated by a slight detuning of two quadrupoles in the CCS. Simulations of the beam-beam interaction show that the correlated energy spread from the wakefield in the linac is sufficiently linear for this dispersive crab-crossing scheme

to keep the luminosity reduction at a crossing angle of 6 mrad within about 8 % (see Fig. 4.7.4).

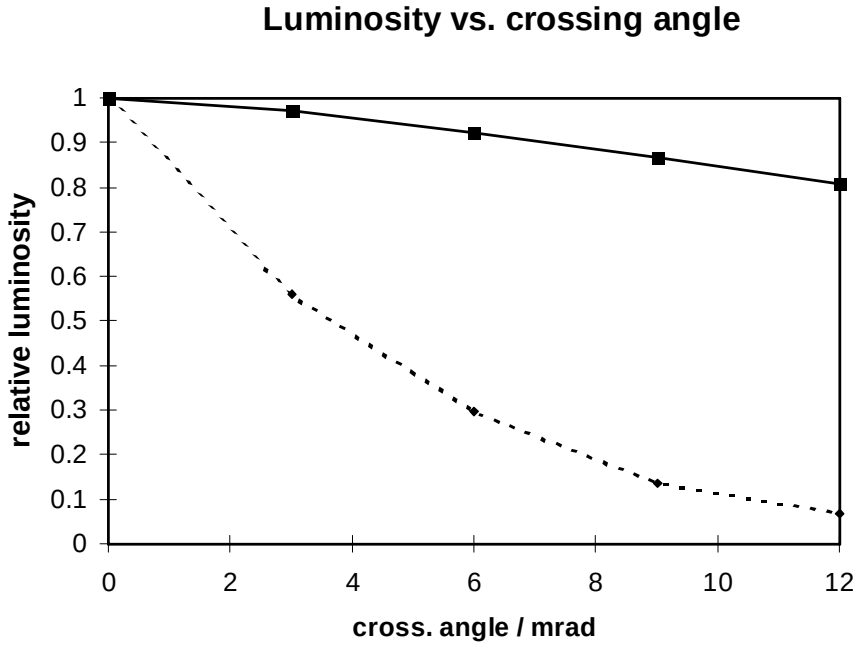

Figure 4.7.4: *Luminosity reduction vs. crossing angle with (solid line) and without (dashed line) the dispersive crab crossing scheme.*

• **Tracking Results**

Results of tracking simulations through the entire BDS are shown in Fig.4.7.5. They have been performed with an ensemble of 2,000 particles representing the longitudinal and transverse distribution in the bunch at the end of the linac and they include the effect of synchrotron radiation in the magnets. At a beam energy of 250 GeV the dilution of the spot size at the IP amounts to only 2 %. Results at higher and lower energies were obtained by assuming that the normalised emittances and the beta-functions at the IP remain unchanged. Over the entire energy range foreseen, including the 1st stage upgrade to E_{cm}=750 GeV, the increase of the spot size remains below 10 %.

• **Magnets and Beam Pipe Apertures**

The required strengths of the BDS quadrupoles (final doublet excepted) and sextupoles correspond to maximum pole tip fields of about 0.9 T at a beam energy of 250 GeV, assuming an aperture radius of 5 mm. A 1 cm diameter stainless steel beam pipe is acceptable from the impedance point of view since the relative energy spread and energy loss induced by the resistive wakefields along 1.4 km of beam pipe are about 3×10^{-5}.

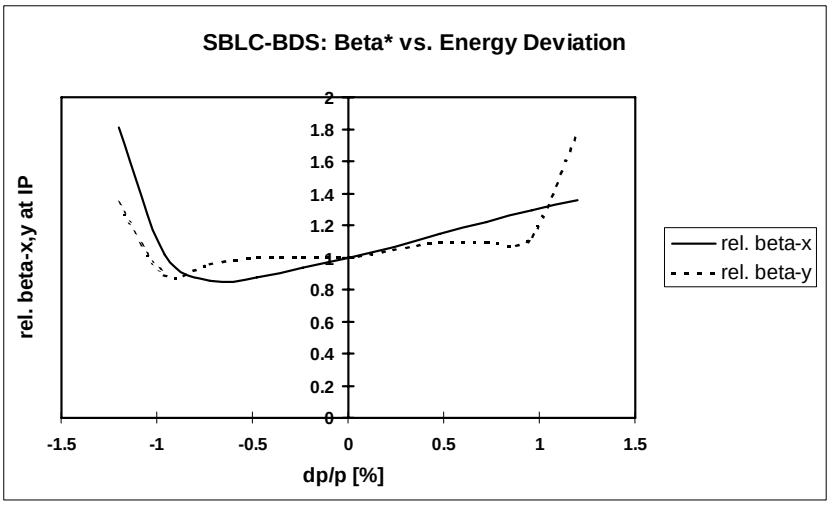

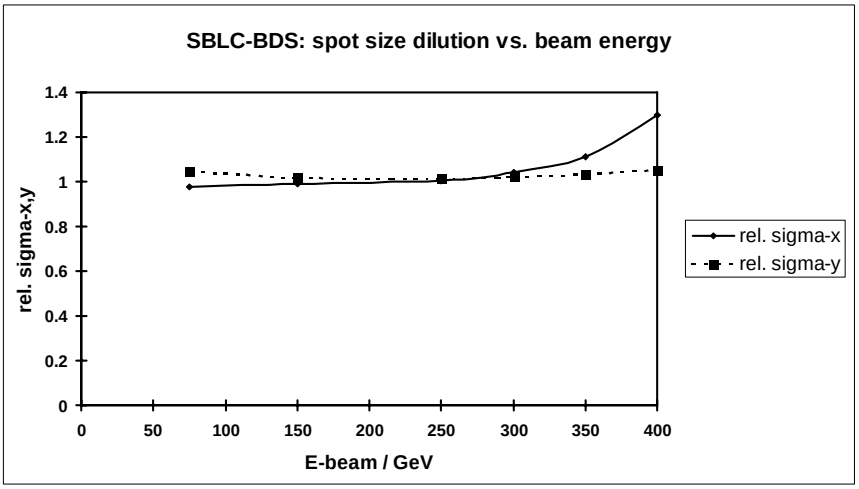

Figure 4.7.5: *Energy bandwidth of the beam delivery system calculated from the energy dependence of the beta-functions at the IP (top) and relative spot size dilution vs. beam energy (bottom).*

4.7.3 Sensitivity to Errors

Displacement and magnet errors occuring upstream of the beta matching section (BMS) will be accurately detected in the diagnostic section and corrected. Downstream errors will be more difficult to measure with the fewer and less precise beam size monitors equiping the IP and its image point at the exit of the CCS. This section is thus devoted to the study of the sensitivity to errors of the BMS and FFS final sections.

This error sensitivity is calculated from the first and second order derivatives of the IP orbit and transfer matrix with respect to magnet errors as well as from the first order derivatives of the T-matrix of the transfer map. This information, stored in large arrays, allows one to calculate the sensitivity of the optical system to any kind

of misalignments, vibrations or magnet field instabilities.

Once translated in terms of luminosity loss and spot size growth, this information can also be used to calculate tolerances of the final focus system to misalignment or field errors. To do so, one has to specify a model that describes the source of these errors, their spectrum and correlations over time and distance. In this section, the following two simple situations are considered: first, fixed (or static) errors affecting only one magnet, assuming all other elements are perfectly aligned and tuned, and second, uncorrelated random transverse vibrations affecting all magnets of both final focus beam lines. More realistic models taking into account ground motion are studied in Sect.4.7.4.

• Static Tolerances

The static tolerances are shown in Figs. 4.7.6, 4.7.7, assuming a beam energy spread of 0.35 %. They are derived from a 2% reduction of the luminosity calculated by assuming that one beam is perfectly matched while the other beam is affected by the error considered. In all pictures, the inverse tolerances are plotted in such a way that the highest bars correspond to the tightest tolerances. Black bars give the tolerances with no steering corrections, while the white bars give tolerances with IP offset corrections included. Besides the last doublet quadrupoles which, as expected, set the tightest tolerances, the CCS bending magnets show also a high sensitivity to skew rotations and field errors. Dispersion errors, especially vertical ones, are mainly due to last CCS quadrupoles and the first FT doublet.

• Uncorrelated Vibration Tolerances

For the model of mechanical vibrations where magnet transverse motions are uncorrelated and have the same horizontal and vertical RMS, $\sigma_x^{(mag)}$ and $\sigma_y^{(mag)}$, the RMS of the resulting relative beam offset, crossing-angle and the single beam dispersions at the IP are then given by:

$$\begin{array}{ccc} \sigma_{\delta x^*} = 0.71 \times \sigma_x^{(mag)} & , & \sigma_{\delta y^*} = 0.25 \times \sigma_y^{(mag)} \\ \sigma_{\theta_x^*} = 5.65\,\mathrm{rd}/m \times \sigma_x^{(mag)} & , & \sigma_{\theta_y^*} = 15.4\,\mathrm{rd}/m \times \sigma_y^{(mag)} \\ \sigma_{D_x^*} = 82.6 \times \sigma_x^{(mag)} & , & \sigma_{D_y^*} = 9.2 \times \sigma_y^{(mag)} \end{array}$$

Actually the offset RMS $\sigma_{\delta x^*}$ and $\sigma_{\delta y^*}$ do not include the dominant contribution from both the opposing last doublets which can be directly read from Figs. 4.7.6 and 4.7.7.

In this model, small luminosity losses can be parametrized as

$$\delta\mathcal{L}/\mathcal{L}_0 = -2\% \times \{(\sigma_x^{(mag)}/159\,\mathrm{nm})^2 + (\sigma_y^{(mag)}/25.6\,\mathrm{nm})^2\} \quad \text{(no offset correction)}$$

for the fast jitter with no steering correction done (again excluding the contribution from the last doublets), and

$$\delta\mathcal{L}/\mathcal{L}_0 = -2\% \times \{(\sigma_x^{(mag)}/295\,\mathrm{nm})^2 + (\sigma_y^{(mag)}/139\,\mathrm{nm})^2\} \quad \text{(with offset correction)}$$

for the case where steering correction is done. In the first case, the luminosity loss is dominated by the beam relative offsets. In the second case, this contribution is

removed and the luminosity loss is mainly coming from spot-size growth with a small contribution from the vertical crossing angle. Since a fast IP orbit steering feedback is foreseen, the latter case is the relevant one here. The 2 % luminosity loss tolerances can be read immediately from the above expressions. With the 0.35 % energy spread considered, the horizontal spot-size growth induced by horizontal misalignments comes 2 % from waist-shift and 98 % from horizontal dispersion while the vertical spot-size growth induced by vertical misalignments comes 5 % from yx'-coupling and 95 % from vertical dispersion. The vertical spot-size growth induced by horizontal misaligments comes totally from waist-shift, and the horizontal spot-size growth induced by vertical misalignments comes totally from xy'-coupling.

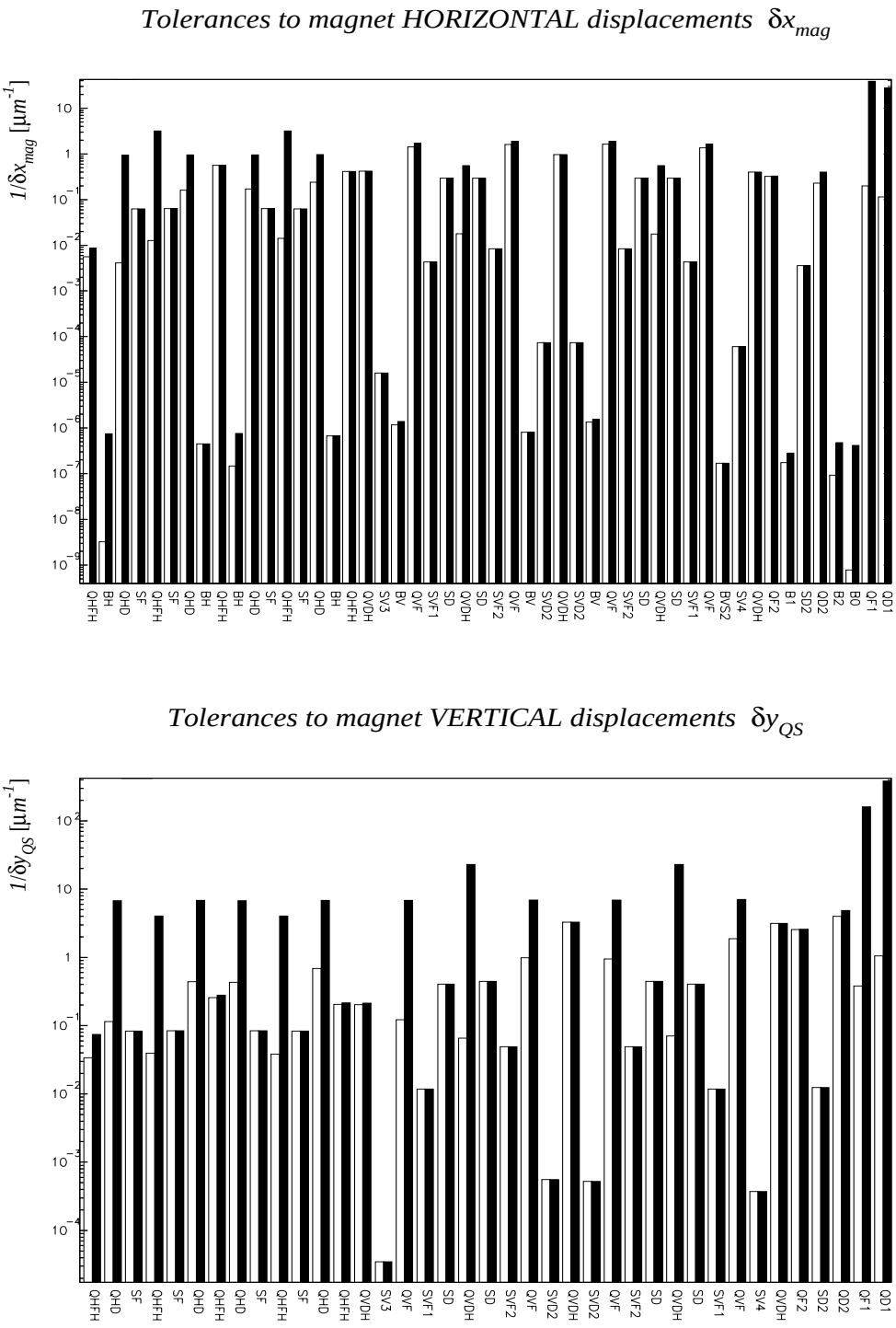

Figure 4.7.6: *FFS Sensitivity to transverse displacements (black bars: with IP offset ; white bars: IP offset corrected).*

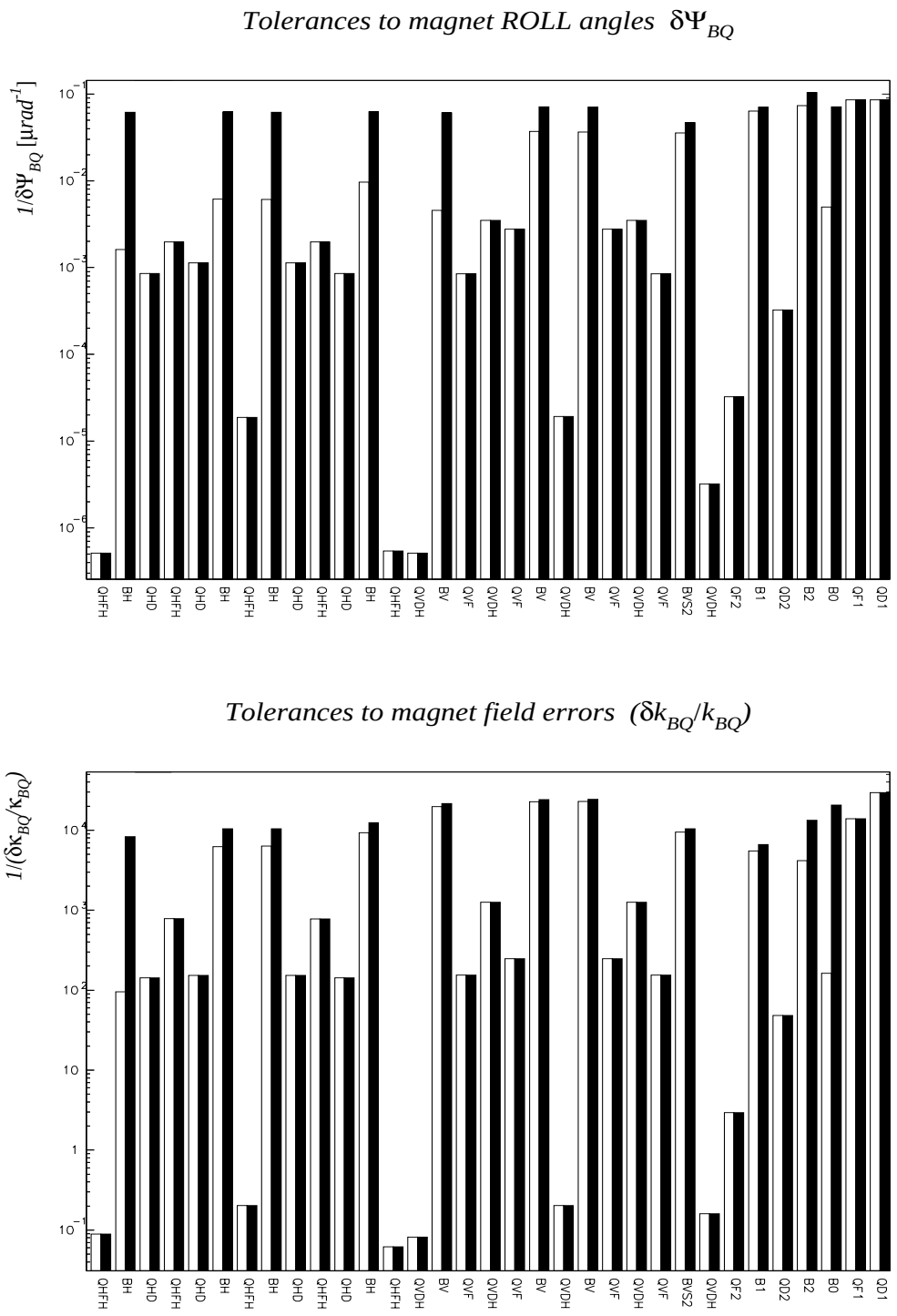

Figure 4.7.7: *FFS Sensitivity to skew rotations and field errors (black bars: with IP offset ; white bars: IP offset corrected).*

4.7.4 Ground Motion

Ground motion is an important issue for the linear collider, because it may result in misalignment of focusing and accelerating elements and thus in trajectory offset and emittance dilution. Ground motion influence is more severe in the beam delivery system, where tolerances are the tightest. It is therefore natural to discuss it in detail in this chapter. Some relevant considerations appear in the chapter describing beam dynamics in the main linac as well.

• **Mathematical description of ground motion** consists in spectral representation, because the relevant quantity $y(t,s)$, the vertical position of the ground surface, can be considered to move in a "random" fashion and should be characterized therefore by the corresponding power spectrum $P(\omega,k)$ [11]. Other characteristics (such as the measurable temporal power spectrum of absolute motion taken in a single point $p(\omega)$, the spectrum of relative motion of two separated points $\rho(\omega,L)$, the correlation $C(\omega,L)$ and the power spectrum $P(t,k)$ of the misalignment $y(t,s)-y(0,s)$ etc...) are all related to $P(\omega,k)$.

While spectral properties of the ground motion are described by the power spectrum, spatial spectral properties of the considered focusing structure of the linear collider can be described by a spectral response function [11]. The errors induced by misalignments, such as the rms beam offset or the rms beam dispersion at IP, can be determined by the integral of the corresponding spectral response function with the power spectrum of the misalignment. For example the rms beam dispersion at the IP is

$$\langle \eta^2(t) \rangle = \int_{-\infty}^{\infty} P(t,k)\, G_\eta(k)\, \frac{dk}{2\pi}$$

The spectral response functions $G_{\rm off}(k)$ or $G_\eta(k)$ show, in terms of rms relative offset or beam dispersion, the spectral response of the considered focusing section to the misalignment having spatial period $2\pi/k$ (Fig.4.7.8).

The spectrum of misalignments, if produced by ground motion, exhibits the following evolution

$$P(t,k) = \int_{-\infty}^{\infty} P(\omega,k)\ \ 2\,[1-\cos(\omega t)]\, \frac{d\omega}{2\pi}$$

In most cases it is essential to have the orbit stabilization feedback taken into account. The equilibrium beam characteristics, for example the rms equilibrium beam offset at the IP, can then be estimated using the function $F(\omega)$, which characterizes the spectral performance of the feedback, integrated with the ground motion spectrum and the corresponding spectral response function.

However, orbit stabilization or tuning algorithms may be quite complex and their performance may depend on many factors such as BPM or mover resolution. In these cases analytical methods based on the spectral response function cannot be applied, thus direct simulations of ground motion [17] and particle tracking should be used to determine the beam degradation.

• **Measured information on ground motion** is known from studies performed in many laboratories all over the world [5]-[10].

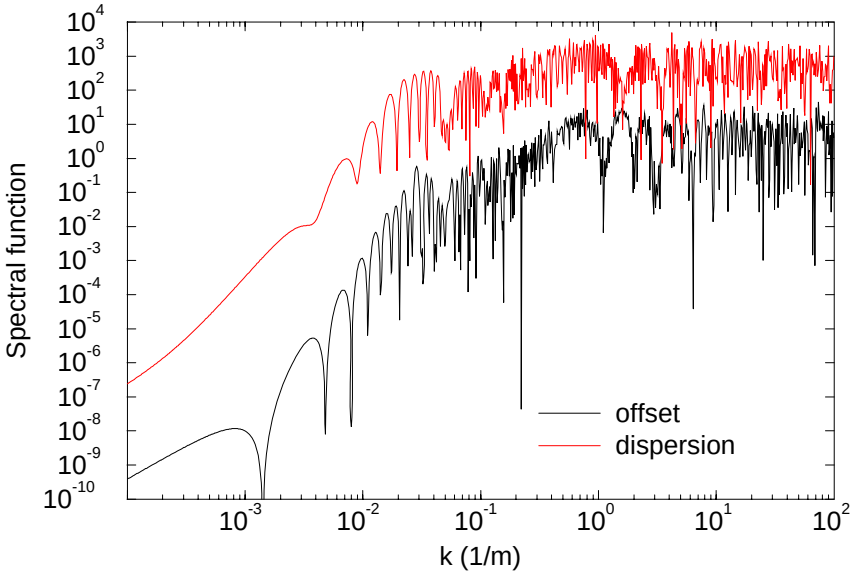

Figure 4.7.8: *Spectral response functions for the relative offset* $G_{\rm off}(k)$ *and for the beam dispersion* $G_\eta(k)$ *for the SBLC Beam Delivery system.*

It is known that the power spectrum $p(\omega)$ of absolute ground motion (which contains contribution of all k) grows very fast with decreasing frequency. In quiet conditions it behaves approximately as $p(\omega) \propto 1/\omega^4$ in a wide frequency band. The motion is unavoidable as it consists of seismic activity. At low frequency $f < 1$ Hz significant contributions to absolute ground motion come from remote sources like water motion in the oceans, atmospheric activity, temperature variations. A well-known example of the ocean influence is the peak in the band 0.1 – 0.2 Hz with a few micrometers amplitude (Fig.4.7.9).

On the other side, in the band $f > 1$ Hz the noise produced by human activity is usually dominating over the natural noise and the power spectrum depends very much on the local conditions (location of sources, depth of tunnel etc.). Locally generated noise can be much bigger than remotely generated. For example the spectrum measured at the tunnel of an operating circular accelerator (DESY HERA collider) presents high amplitudes at $f > 1$ Hz due to noise generated by different technical devices (Fig.4.7.9). This noise may have a big amplitude and poor spatial correlation. Technical devices of the future linear collider therefore should be properly designed in order to pass as low vibration as possible to the tunnel floor.

It is known from correlation measurements [6, 10] that in quiet conditions the motion in the band $f > 0.1$ Hz can be considered as wave-like, i.e. the frequency ω and wave number k are connected via phase velocity v. At $f \approx 0.1$ Hz the value of v was found to be close to the velocity of sound in the surrounding media: about 3000 m/s at LEP and about 2000 m/s at the SLC tunnel. For cultural noise this value decreases rapidly: the value of v determined from the SLAC data behave as $v \approx 450 + 1900\exp(-f/2\text{Hz})$ m/s (for $f > 0.1$ Hz) [10], HERA measurements gave $v \approx 400$ m/s [8]. The SLAC measurements have shown (at least at this place and these

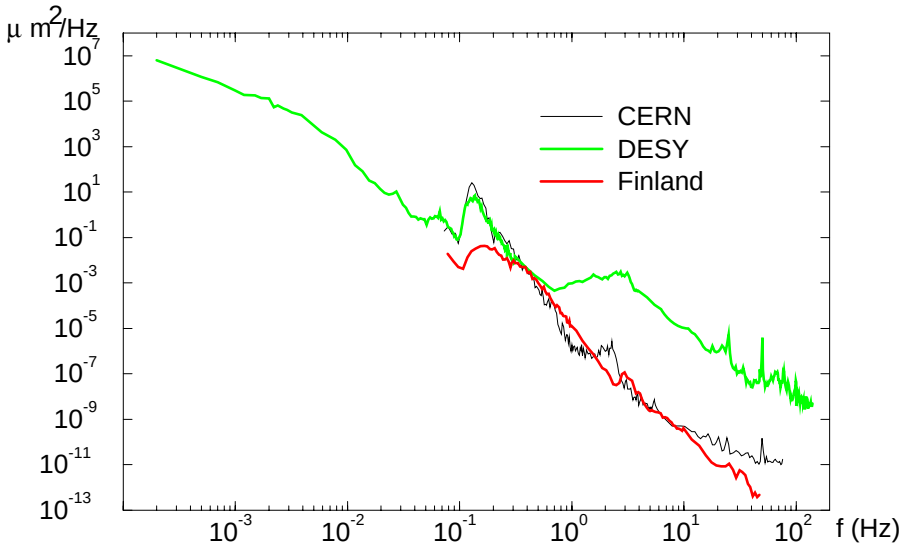

Figure 4.7.9: *Absolute power spectrum measured in quiet (CERN LEP tunnel, shutdown [6]; Finland, cave [7]) and noisy (DESY HERA tunnel, operational condition [8]) condition.*

conditions) that contribution of non-wave motion is negligible for $f > 0.1$ Hz.

The motion at $f < 0.1$ Hz is different. The elastic motion (produced by the moon, for example) is present here also, but of much bigger relevance is the inelastic diffusive motion, probably fed by the elastic motion and caused by its dissipation. The motion is believed to be described by the "ATL law" [5], which states that the relative rms displacement after a time T of the two points separated by a distance L is

$$\langle \Delta Y^2 \rangle = A\,T\,L$$

The parameter A was found to be $A \approx 10^{-6\pm1}$ μm^{2}s^{-1}m^{-1} at different places. One can see that this displacement is proportional to the square root of the time and separation: this stresses the random, non wavelike, diffusive character of the slow relative motion.

The parameter A was observed to be smaller in tunnels built in solid rock. It also depends on the method of tunnel construction: in the tunnel bored in granite $A \approx 10^{-6}$ μm^{2}s^{-1}m^{-1} was observed, while in a similar tunnel built by use of explosions, the parameter A is found to be 5 times larger probably because of the rock fragmentation, artificially increased during construction [9]. The high frequency correlation in the second case is also poor. The parameter A tends also to be smaller in deeper tunnels [13].

The ranges of T and L where the "ATL law" is valid are very wide. In [13] it was shown that "ATL law" is confirmed by measurements of ground motion in different accelerator tunnels in the range from minutes to tens of years and from a few meters to tens of kilometers. The measured relative power spectra, presented in [9] and in [12], exhibit the "ATL" behavior for $f < 0.1$ Hz (for $L \approx 30$ m). These measurements indicate that the transition region from wave to diffusion motion is placed at rather

short times (a few seconds). Measurements of the closed orbit motion in the HERA circular collider have shown that the power spectrum of this motion corresponds to the "ATL law" in a wide frequency range, from $f \approx 0.1$ Hz down to $f \approx 10^{-6}$ Hz and the parameter is $A \approx 10^{-5}$ μm^{2}s^{-1}m^{-1} [12].

The very slow motion can be systematic (not described by power spectrum) as well. Such motion has been observed at LEP Point 1 and PEP [14] where some quadrupoles move unidirectionally during several years with rate about 0.1 – 1 mm/year. Points spaced by a few tens of meters can move in opposite directions. The amplitude of the motion can be larger than the one of diffusive motion. The motion is probably due to geological peculiarities of the place or due to relaxation if the tunnel was bored in solid rock.

The elements of the linac will be placed not on the floor, but on some girder, which could amplify some frequencies due to its own resonances. It is not only this amplification that is dangerous, more important is that the different girders can amplify or change the floor motion in different ways, and hence spoil correlation of the floor motion. It is therefore preferable to push the girder resonances to high frequencies where the correlation is poor anyway and floor amplitudes are smaller. This requires firm connections of the girder to the floor. The active systems [16], which can help to isolate the quadrupoles from high frequency floor motion, should be made insensitive to small frequencies (below 1 Hz), otherwise imperfections and noise in the active system may reduce the correlation present for slow long-wavelength motion.

• **A model of the ground motion spectrum** $P(\omega, k)$ can be built [11] with the assumption that the low frequency part of motion is described by the "ATL law" [5], and the high frequency part is produced mainly by waves. The waves are assumed to be elastic, transverse, propagating at the surface of the ground with uniform distribution over azimuthal angle. The "ATL law" is included to the model in a modified form, in order to prevent overestimation of fast motion, which is an intrinsic feature of the pure "ATL law". The spectrum, which include both the waves and the modified "ATL law", is the following

$$P(\omega,k) = \frac{A}{\omega^2 k^2}(1-\cos(kB/A/\omega^2)) + \sum_i \frac{a_i}{1+[d_i(\omega-\omega_i)/\omega_i]^4}\,\frac{2}{\sqrt{(\omega/v)^2-k^2}}$$

We consider two set of parameters to cover two extreme cases of seismic conditions. Parameters of the first model are the following: $A = 10^{-5}$ μm^{2}s^{-1}m^{-1}, $B = 10^{-6}$ μm^{2}s^{-3}. The single peak described by $\omega_1 = 2\pi \cdot 0.14$ Hz for the frequency of the peak, $a_1 = 10\mu$m^2/Hz for its amplitude, $d_1 = 5$ for its width, and $v_1 = 1000$ m/s for the velocity. This parameters represent quiet conditions.

The second model corresponds to seismic conditions with big contributions from cultural noises (as in the HERA tunnel in operating conditions). The parameters are the following: $A = 10^{-5}$ μm^{2}s^{-1}m^{-1}, $B = 10^{-3}$ μm^{2}s^{-3} and three peaks: $f_1 = 0.14$, $f_2 = 2.5$, $f_3 = 50$ Hz; $a_1 = 10$, $a_2 = 10^{-3}$, $a_3 = 10^{-7}\mu$m^2/Hz; $d_1 = 5$, $d_2 = 1.5$, $d_3 = 1.5$; $v_1 = 1000$, $v_2 = 400$, $v_3 = 400$ m/s. The corresponding spectrum of relative motion is shown on Fig.4.7.10.

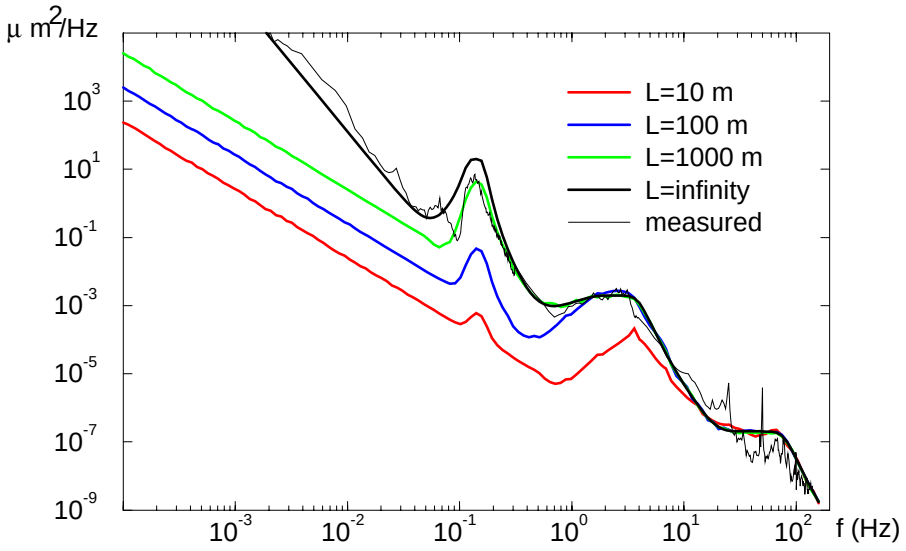

Figure 4.7.10: *Absolute power spectrum measured in a noisy conditions (HERA during operation [8]) compared to absolute and relative spectra for different spatial separation L calculated from the second model.*

• **Beam offset and spot size at the IP of SBLC** have been calculated analytically using the models of ground motion spectrum $P(\omega, k)$ and the corresponding spectral response functions, determined in linear approximation [11].

The most harmful effect of misalignments of focusing elements is the relative vertical offset of the opposite beams at the IP (Fig.4.7.11). The tolerance on the offset, corresponding to 2% luminosity loss, is around 4 nm for SBLC. It corresponds to critical times around 1 s for the quiet model and 1 ms for the noisy model. This means that the repetition rate based feedback (50 Hz) can provide luminosity stabilization if a low or medium level of cultural noise is present. Applying active stabilisation of magnet supports (see section 4.8.4) will help to reduce orbit jitter to amplitudes which can be handled by the repetition rate based feedback. The fast orbit feedback within a bunchtrain based on the pilot bunch measurements, described in section 4.8.3, can stabilize luminosity even for a high level of cultural noise.

Transverse displacements of focusing elements generate spot size growth at the IP induced by dispersion, longitudinal shift of the beam waists and xy-coupling generated by offset beams in quadrupoles and sextupoles. Corresponding spectral response functions have been calculated and the beam size growth due to all these effects has been determined (Fig.4.7.12). The main contribution to the vertical beam size growth comes from the vertical dispersion. One can see that the critical time scale for 2% luminosity loss is about 20 s that imposes quite relaxed requirements to the beam size stabilization feedback described in section 4.7.6.

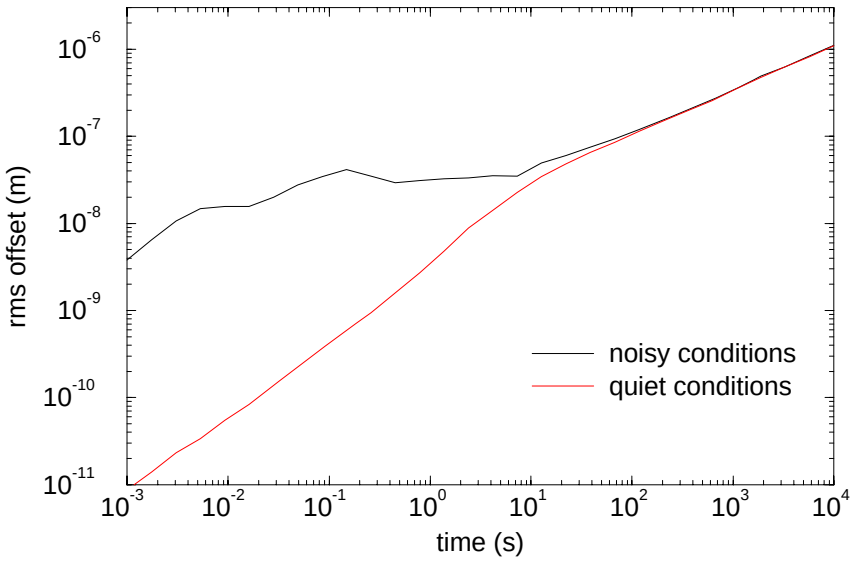

Figure 4.7.11: *Relative vertical rms offset of the beams at IP of the SBLC Beam Delivery system for the noisy and quiet models of the power spectrum of ground motion.*

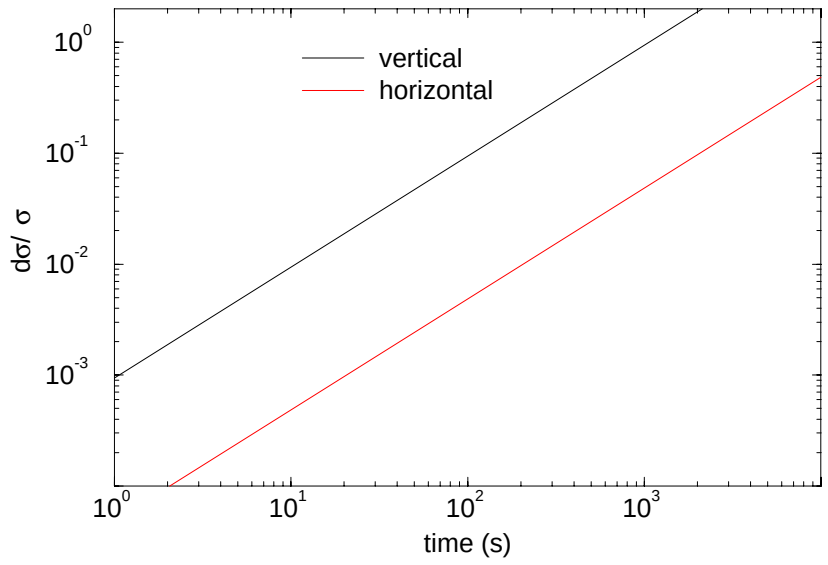

Figure 4.7.12: *Vertical and horizontal rms beam size growth $\delta\sigma^*/\sigma^*$ versus time for the "ATL" ground motion with $A = 10^{-5}\ \mu m^2 s^{-1} m^{-1}$. Rms energy spread of the beam is $\delta p/p = 3.5 \cdot 10^{-3}$.*

4.7.5 Phase Space Measurement and Tuning

4.7.5.1 Introduction

With the experience gained from two existing final focus systems (SLC and the final focus test beam, FFTB), the various tuning techniques which are required to produce the small beam sizes at the IP are already mature and well tested. For the next generation of linear colliders, the tuning used at the FFTB [18] is particularly relevant. In the following sections, we will discuss the application of these and other tuning techniques to the SBLC beam delivery system.

4.7.5.2 Energy Measurement and Correction

The beam delivery system offers several near optimum positions for the precise measurement of the relative energy (momentum) error of the bunches. Both the collimation sections and the chromatic correction sections have symmetric high dispersion points positioned -I apart in betatron phase, allowing any betatron component of the horizontal beam offset at these points to be effectively canceled out by taking the sum of the two measurements. The resolution of such a system is given by (a) the value of the dispersion function (b) the resolution (noise) of the BPM and (c) the accuracy of the cancelation of the betatron component. Table 4.7.1 gives the relevant parameters for the four sets of symmetric dispersion points available in the SBLC beam delivery system. The resolution is calculated assuming the given BPM precision (5 μm) and a (conservative) random beam jitter of $\sigma/4$.

section	D_x (mm)	β_x (m)	σ_x (μm)	σ_{BPM} (μm)	resolution
collimation	73	5448	348	5	3×10^{-4}
CCS X	53	2210	240	5	10^{-4}
CCS Y	21	74	78	5	3×10^{-4}

Table 4.7.1: *Key parameters for -I paired BPMs used as spectrometers in the beam delivery section. The collimation section refers to both the sine- and cosine-like sections which have identical parameters.*

Either of the two BPM pairs in the collimation sections can be used in an energy feedback system to compensate any variation in beam energy, using two back-phased correction cavities situated at the exit of the linac.

4.7.5.3 Beam Based Alignment

The most critical aspect of the initial final focus tuning is the alignment of the magnets. The strong quadrupoles and sextupoles within the system have tight tolerances that must be met in order to reduce optical aberrations below the acceptable values. Since

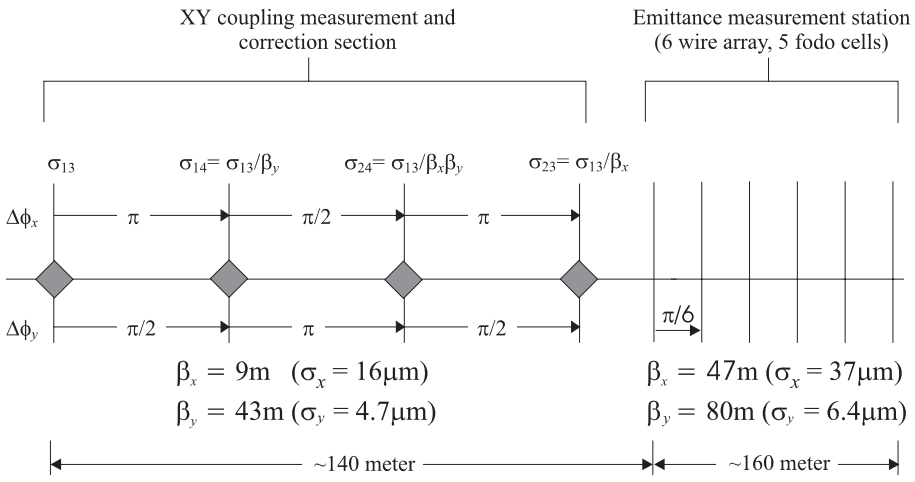

Figure 4.7.13: *Schematic of coupling measurement and correction section together with the downstream six wire array emittance measurement section. The fodo parameters for the emittance measurement station are chosen to give a 1% measurement resolution (assuming a 1 μm rms wire).*

the alignment tolerances are tighter than can probably be achieved using conventional survey techniques, the position of the magnets must be corrected using the beam based alignment techniques already successfully demonstrated at the FFTB [19]. The excitation of each magnet is changed and the resulting difference in downstream orbit is recorded, from which the relative offset of the magnet with respect to the beam can be estimated. Each magnet (excluding dipoles) is placed on a remotely translatable stage (magnet mover) which enables the precise (sub-micron) positioning of the magnet [20]. With high precision BPMs (approximately 1 μm), alignment precisions on the order of a micron or less should be feasible. The strong Sextupoles can be aligned using the waist shift techniques first demonstrated successfully at the SLC [21].

4.7.5.4 Coupling Correction

With emittance ratios of 25:1 it is important to reduce any cross plane (X-Y) correlations in the 4-dimensional beam phase space. The linear correlations ($\langle xy \rangle$, $\langle xy' \rangle$, $\langle x'y \rangle$ and $\langle x'y' \rangle$ can be completely removed with four skew-quadrupoles placed at non-degenerate phases. There are two possible correction schemes that can be applied:

1. measure the correlations and adjust the four skew-quadrupoles accordingly.

2. generate a set of four orthogonal coupling knobs, and minimise the vertical emittance as a function of each in turn [23],

In SBLC, both possibilities are supported in a single tuning section. The lattice shown in Fig. 4.7.13 is chosen to make each single skew-quadrupole correct an independent coupling term (i.e an orthogonal knob) [23]. Immediately downstream of the skew-quadrupoles is a 6-wire emittance measurement section as described in [22], which is

capable of a relative emittance measurement error of approximately 1%. The vertical emittance is minimised as a function of each skew-quadrupole strength in turn. It should be noted that the skew-quadrupoles are only orthogonal over a limited range around zero: should a large amount of correction be required, then the procedure must be iterated.

The orthogonal split-phase lattice utilised for the coupling correction also affords an elegant de-coupled measurement of the four individual X-Y correlations. Four wire scanners are placed at the same locations as the skew-quadrupole as discussed in [22]. Each wire scanner has an additional angle wire (the u-wire), which together with the horizontal and vertical wire measurements can be used to determine the $\langle xy \rangle$ correlation of the beam at that wire scanner. At each wire scanner location, the measured $\langle xy \rangle$ correlation relates directly to an individual correlation term of the beam as measured at the first wire scanner (as shown in Fig. 4.7.13). Together with the downstream emittance measurement station, the coupling measurement station allows the complete determination of the 4-dimensional phase volume, the results of which can be used to determine the settings of the matching quadrupoles (skew and normal) with the aid of some suitable optics program, preferably on-line.

4.7.5.5 Beta Matching

By design, a final focus system for a linear collider contains large chromatic elements which are so positioned in order to cancel the resulting aberrations. Given the delicate balance of this cancelation and the subsequent tolerances of the components, it is highly desirable to limit the amount of tuning which takes place within the final focus to a minimum: the IP tuning should be considered as a final fine tuning of the IP phase space (see section 4.7.5.6). To facilitate this, care must be taken to make sure that the incoming phase space is matched correctly to the final focus. The wire array system described in section 4.7.5.4 allows the determination of the full 4-dimensional phase volume, from which the setting of the a) skew-quadrupoles in the coupling correction section and b) the normal quadrupoles in the downstream β-matching section can be determined. As an additional cross check, a single wire scanner can be placed at the IP image point at the entrance of the horizontal chromatic correction section. If the final focus lattice is correctly adjusted, then a waist at this wire scanner corresponds directly to a waist at the IP. Waist scans can be made at the wire by driving six upstream quadrupoles in the correct (non-linear) fashion[26]. Assuming the coupling has already been corrected, the β-function at the image point can be obtained from the waist scan information, and a subsequent adjustment made to obtain the correct beam size. For the design vertical emittance the vertical beam size at the image point is 700 nm ($= 46 \times \sigma_y^*$), the measurement of which is well beyond the carbon fiber limit and will require laser technology or possibly a gradient undulator beam size monitor[24].

4.7.5.6 IP tuning

The final focus optics must first be checked and if necessary adjusted to given the correct box-structure lattice. Specifically the -I sections between sextupoles in the

chromatic correction sections must be measured using the corrector-BPM null method outlined in [18]. Additional wire scanners at the intermediate IP image points can be also used to check the consistency of the optics (since they should all measure the same beam size). Unfortunately the beam sizes at these downstream image points have a large contribution from the chromaticity generated by the CCS sextupoles, and so it will be necessary to turn the sextupoles off during the measurement.

Final (linear) tuning of the IP phase space requires in principle six orthogonal knobs:

1. X and Y waist IP shift,

2. X and Y IP dispersion,

3. $\langle xy \rangle$ and $\langle x'y \rangle$ coupling.

For the last case (coupling), only the $\langle x'y \rangle$ is important, since there is no generating term for the $\langle xy \rangle$ correlation due to the single phase nature of the lattice (this assumes that the incoming coupling has been corrected using the techniques described in section 4.7.5.4). The remaining coupling term can be tuned out using a single skew-qudrupole placed close to the final doublet, or using the sextupole mover technique discussed below.

All five required tuning knobs can be easily generated using transverse displacement of the sextupole pairs in the CCS. This technique is particularly appealing since errors in alignment of the sextupoles are expected to be a significant source of the aberrations we wish to use them to correct. For a given sextupole pair, the transverse offset (horizontal and vertical) can be driven symmetrically or anti-symmetrically. The two sets of sextupoles movers can be ganged together to produce orthogonal X and Y knobs (for the waist and dispersion correction). Table 4.7.2 shows the various knob combinations while Table 4.7.3 gives the numerical parameters. Exactly the same effect can be achieved by placing small normal and skew quadrupoles at the sextupoles and ganging the power supplies in pairs.

	symmetric	a-symmetric
horizontal	waist shifts	horizontal dispersion
vertical	$\langle x'y \rangle$ and $\langle xy' \rangle$	vertical dispersion

Table 4.7.2: *The four combinations of sextupole movers and their effect at the IP.*

The typical amount by which the sextupoles must be displaced depends on the size of the scan range and subsequent correction necessary. As a good guideline, we assume that a scan range is such that it increases the effective IP β-function by a factor of three (i.e. it increase the beam size by a factor of $\sqrt{3}$). Combining the above coefficients into orthogonal knobs, Table 4.7.4 gives the amount of transverse motion of each sextupole to complete a 3β scan (for the coupling, only the vertical beam size is scanned using

		X	Y
X CCS	waist	980	4.0
	dispersion	5.3	0.19
	coupling	31	
Y CCS	waist	95	344
	dispersion	1.0	2.0
	coupling	90	

Table 4.7.3: *Coefficients for the various mover combinations given in Table 4.7.2. The coefficients are per unit sextupole offset.*

the vertical CCS sextupoles). Mechanical movers of a similar design as those developed for the FFTB [20] should be adequate given the requirements in table 4.7.4.

	CCS X (μm)	CCS Y (μm)	motion
x-waist	16.	-0.18	horizontal
Y-waist	-0.18	1.9	horizontal
x-dispersion	25.		horizontal
y-dispersion		2.2	vertical
coupling		5.5	vertical

Table 4.7.4: *Expected motions of the sextupole pairs in the X and Y CCS to give orthogonal 3β scans at the IP.*

All the tuning described above requires some measurement of the beam size at the IP. While colliding beams are available, beam-beam scans can be used as a tuning signal, as can any fast luminosity monitor. It is considered essential that a single beam diagnostic be available at or near the IP for initial tuning and fault diagnostics. A laser interferometer beam size monitor[25] will be placed some 30 cm along the beam axis from the actual IP. The focal point of the beam must be moved to the location of the the laser monitor requiring an adjustment of the β-match (a waist shift). Such a waist shift is easily produced by the sextupole pairs as previously mentioned (a symmetric horizontal displacement of 222 μm for X and 870 μm for Y).

4.7.6 Luminosity Stabilisation

The alignment tolerances in the beam delivery system are some of the tightest in the machine. While it is expected that initial beam-based alignment can achieve these tolerances, the question still remains how stable the system is over time, given that ground motion will slowly displace all the components from their ideal positions. The effects of ground motion on the luminosity can be separated into three distinct time

scales:

1. displacement of the beams relative to each other at the IP
2. dilution of the IP beam sizes by linear optics aberrations
3. dilution of the IP beam sizes by non-linear optics aberrations.

The relative displacement of the beam at the IP has the shortest time constant: if the effects of ground motion are left uncorrected, the luminosity drops rapidly as the beams move out of collision. Assuming that this offset is corrected using the proposed fast feedback system (section 4.8.3), the next effect is that of linear optics aberrations increasing the beam size at the IP. As the ground motion displaces the magnets, the RMS of the beam trajectory through the system will increase rapidly, generating spurious dispersion, IP waist shifts and X-Y coupling (the latter two effects coming from the strong sextupoles in the chromatic correction sections). These effects can be dramatically reduced by routinely re-steering the beam delivery systems. In addition, the linear IP tuning knobs can be scanned during routine luminosity operation to remove any residual linear aberration not corrected by the steering. Once (1) and (2) are corrected, the only remaining effects are non-linear aberrations (most notably non-linear dispersion). When these effects become large enough to reduce the luminosity below an acceptable limit, then the beam delivery system will require invasive tuning, and most probably a re-alignment of the magnets (using beam-based alignment).

To study the effects of ground motion and how effective the various tuning and orbit correction strategies are, a purpose built simulation tool known as MERLIN has been developed at DESY. The MERLIN model of the SBAND beam delivery system has the following key points:

1. both electron and positron systems are simulated, and the luminosity is calculated from the results of particle tracking though both (independent) models
2. ground motion (ATL) is applied to both electron and positron models in a consistent way to obtain the correct correlations between the two
3. components can be placed on girders (supports), and will then move together under the influence of ground motion
4. each magnet has an associated BPM, both of which are placed on magnet movers (which in turn are placed on a support).

Figure 4.7.14 shows recent result of the MERLIN SBAND BDS model. The four graphs shown are the averaged results of running twenty random seeds for the ground motion, with $A = 10^{-5}\mu m^2/m/s$. The logarithmic time scale represents thirty days of running. The first graph (a) shows the effect of ground motion alone with no tuning, from which it is clear that the luminosity drops below an acceptable level within seconds. The second graph (b) shows how the effect of the IP steering feedback stabilises

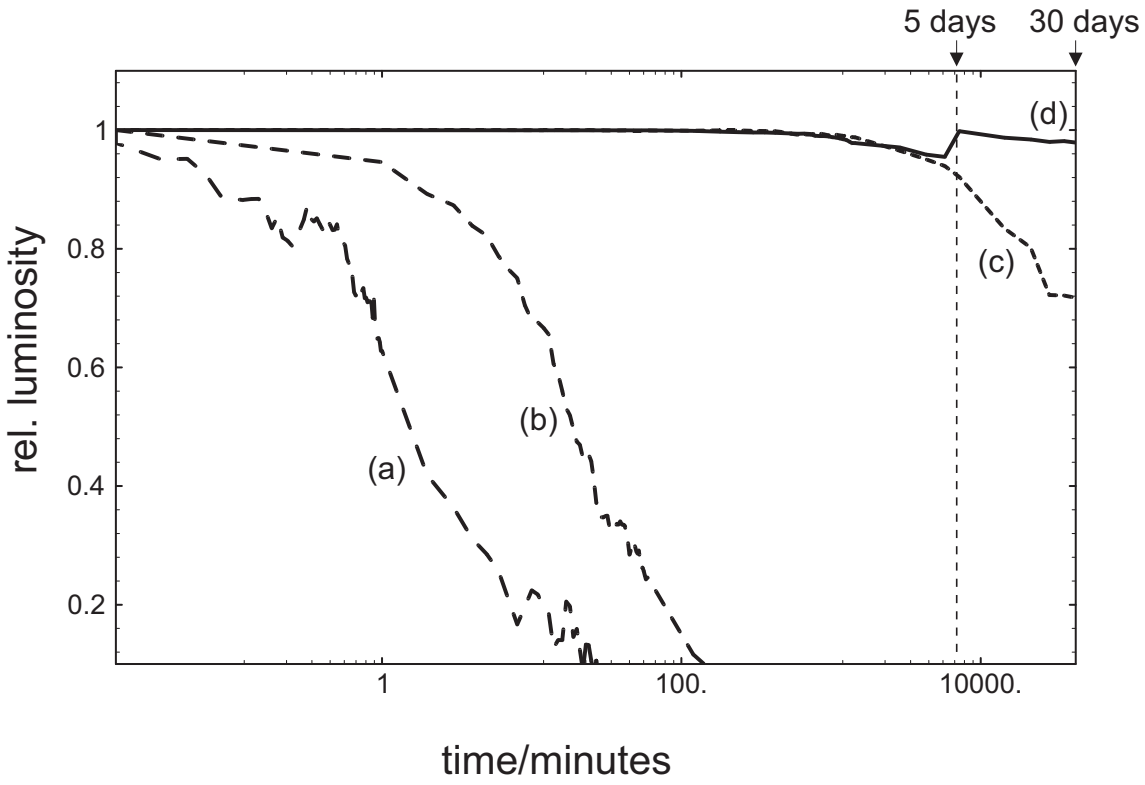

Figure 4.7.14: *Simulations of luminosity (relative to the design value) as a function of time. Four separate simulation runs are shown depicting (a) no correction, (b) IP beam offset correction (IP steering feedback), (c) full 1-to-1 orbit correction of both electron and positron beams and finally (d) application of linear knob tuning every five days (see text for additional details).*

the luminosity by keeping the beams in collision. The critical time for luminosity loss is now of the order of a minute. Graph (c) shows the effects of so-called one-to-one orbit correction: the beams are steered to zero the beam offset in all the BPMs (and consequently the centres of the their associated magnets). Particular care is taken to steer to the centre of all sextupole magnets and the final doublet (in the latter, a single BPM placed between the two doublet magnets is used). The result indicates that a 5% drop in the luminosity after approximately 4 days can be expected. Finally, application of linear tuning knob scans (here applied every 5 days) can recover the luminosity almost back to its original value. The tuning cycle scans the following "knobs":

1. IP angular dispersion (x and y)
2. IP waists (x and y)
3. IP dispersion (x and y)
4. IP coupling (ym IP waists (x and y)

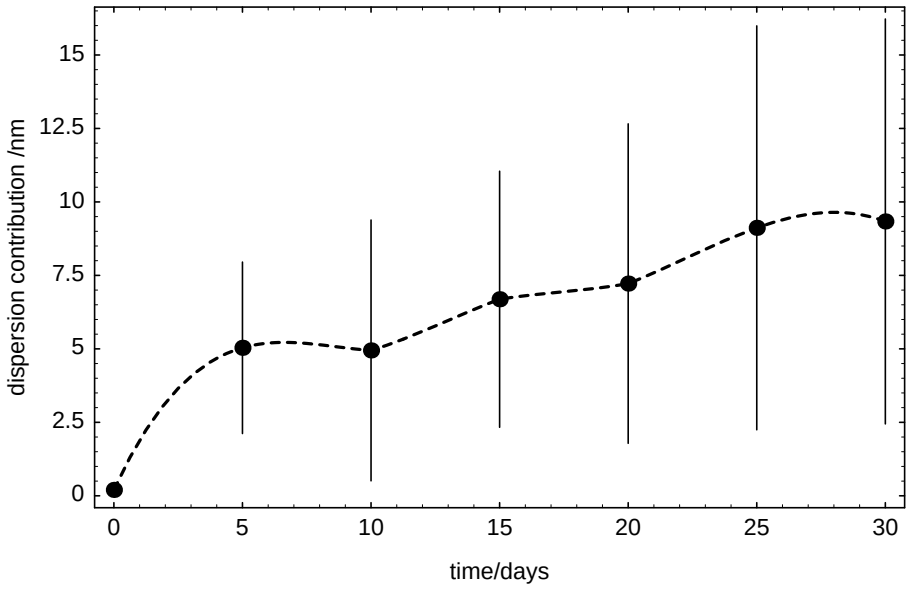

Figure 4.7.15: *IP dispersion tuning history from a MERLIN simulation. The graph shows the average over 20 random seeds of the vertical IP dispersion knob, represented as an rms contribution (in nm) to the vertical IP beam height ($\delta_{rms} = 3.5 \times 10^{-3}$). The error bars represent* ± 1 *standard deviations of the 20 random seeds.*

5. IP dispersion (x and y)

6. IP coupling (y only)

Angular dispersion is corrected via the use of sets of pairs of quadrupoles and skew-quadrupoles placed in the sine-like collimation system. The tuning signal is a beam size monitor placed just in front of the final doublet, where IP angular dispersion becomes dispersion. Although the presence of angular dispersion does not influence the directly the beam size at the IP (to first order), it does cause the waist and dispersion scans to be coupled, requiring iteration of the tuning procedure. By first zeroing the $\langle y'\delta \rangle$ correlation at the IP, the waist and dispersion scans are effectively de-coupled, and iteration is no longer required. The four remaining tuning knobs (waist, dispersion and coupling) are corrected by remotely displacing the sextupoles in the CCS: by ganging the $-I$ sextupole pairs together in symmetric and anti-symmetric combinations, pure dispersion, coupling and waist shift knobs can be obtained. These knobs are assumned to be scanned against a fast luminosity monitor, and the signal maximised. Since the only source of waist motion and coupling are the sextupoles, it was expected (and observed in the simulation) that the 1-to-1 steering would effectively eliminate these aberrations by centering the beams in the sextupoles. The main term causing lumoinosity loss is the residual dispersion which remains after application of the 1-to-1 steering. Figure 4.7.15 shows the history of the IP dispersion correction for a typical seed of ground motion.

4.7.7 Beam-Beam Effects

The two colliding bunches focus each other at the interaction point, reducing the effective beam cross section compared to the nominal one. The actual luminosity is thus larger than the geometrical one by the pinch enhancement factor H_D. Due to the bending of their trajectories the particles emit a radiation called beamstrahlung. The resulting energy loss smears the luminosity spectrum and has thus to be limited, which in turn limits the achievable luminosity. The resulting spectrum is especially important for studies of the top quark at threshold and is discussed the appropraite section in more detail.

The strong bending of the trajectories requires a numerical simulation to estimate the actual luminosity and the beamstrahlung. The numbers in the following are obtained using the computer code GUINEA-PIG [27]. For the standard beam parameters of SBLC the simulations yields a luminosity of $5.3 \cdot 10^{33}\,\mathrm{cm}^{-2}\mathrm{s}^{-1}$ ($H_D = 1.7$) and an average relative energy loss of the beam particles of $\delta = 2.8\%$. The total power of the beamstrahlung of one beam is about 200 kW.

The beamstrahlung is emitted into a small cone in the forward direction of the beams. Its angular spread is dominated by the angular spread of particles in the bunches during the interaction and the core is well below 400 μrad. The photons pass the final quadrupoles safely. They have to be collimated outside the detector to protect the magnets of the line for the spent beam. The possibility for this collimation was investigated for TESLA and found to be feasible—this should also apply for SBLC.

The beamstrahlung increases the background produced in the interaction point. An important contribution to the background are the three processes creating e^+e^--pairs: $ee \to ee(e^+e^-)$, $\gamma e \to e(e^+e^-)$ and $\gamma\gamma \to e^+e^-$, where the real photons are due to beamstrahlung. The pair particles are produced mainly at small angles with respect to the beam axis but since their energy is small their trajectories are strongly bent by the fields of the beams. If a particle moves in opposite direction of the bunch with the same sign of charge, it is deflected by the fields to a relatively large, energy dependent angle.

Simulation with GUINEA-PIG predicts the production of about $24 \cdot 10^3$ particles with a total energy of $53 \cdot 10^3$ GeV per bunch crossing in SBLC. Most of these particles hit the final quadrupoles where they produce secondary photons and neutrons. The detector is shielded from the photons by a tungsten mask. In Table 4.7.5 the number of particles with a transverse momentum of more than 20 MeV and an angle of more than 150 mrad is given. This number is about 7 per bunch crossing. The numbers for other parameter sets can also be found in Table 4.7.5.

The rate of hadronic two photon events is 0.04 per bunch crossing with a photon-photon centre of mass energy in excess of 5 GeV. The visible energy of each of these events is about 10 GeV.

SBLC				
E_{cm}	[GeV]	500	750	1000
L	$[10^{33}\,\mathrm{cm}^{-2}\mathrm{s}^{-1}]$	5.3	5.4	10.5
δ	[%]	2.8	4.9	7.6
N_P	$[10^3]$	24	73	157
E_P	$[10^3\,\mathrm{GeV}]$	53	297	1125
$N_\perp$		7.1	18	34
N_{Hadr}		0.04	0.17	0.5
N_{MJ}	$[10^{-2}]$	0.1	0.62	2.7

Table 4.7.5: *Luminosity L average energy loss δ and background for different SBLC parameter sets. N_P pair particles with a total energy of E_P is produced per bunch crossing $N_\perp$ of which have transverse momentum in excess of* 20 MeV *and an angle with respect to the beam axis of more than* 150 mrad. *The number of hadronic events is N_{Hadr} including N_{MJ} minijet pairs with a transverse momentum of more than* 3.2 GeV.

4.7.8 Beam Collimation

In order to avoid that the detector can be blinded by background produced from large amplitude halo particles in the interaction region, the trajectory amplitudes have to be restricted such that (a): the entire beam remains within the aperture of the final quadrupoles in front of the IP and (b): the synchrotron light produced by particles with large offsets in the final doublet (FD for short) can pass freely through the aperture of the doublet downstream from the IP. The second condition is more stringent than the first and we lay out the collimation system according to this boundary condition. With a crossing angle of 6 mrad and a layout of the final quadrupole as sketched in fig. 4.7.16, the free aperture for the outgoing synchrotron light corresponds to 10.7 horizontal and 27 vertical standard deviations. It is difficult to estimate the amount of halo particles outside this acceptance. Provided that the beam at the entrance of the linac is properly collimated, the re-population of tails in the linac from gas-scattering and from wakefields is small, likely below 10^{-6}. Since field emission at the design gradient of 17 MV/m is almost negligible, dark currents are also expected to be very low . Including an efficient collimation system in the beam delivery design will thus generate a considerable amount of safety concerning protection of the interaction region from unwanted background.

4.7.8.1 Layout of the System

In principle, only large amplitude trajectories at the FD-phase are harmful, since the acceptance for IP-phase trajectories is orders of magnitude (in units σ's) larger. FD-phase collimation can easily be provided at the high-β positions in the final focus system (FFS). However, being relatively close to the IP, muons originating from the FFS-collimators can reach the detector with high probability and the tolerable amount of beam halo scraped off in the FFS would be small. We therefore include a first

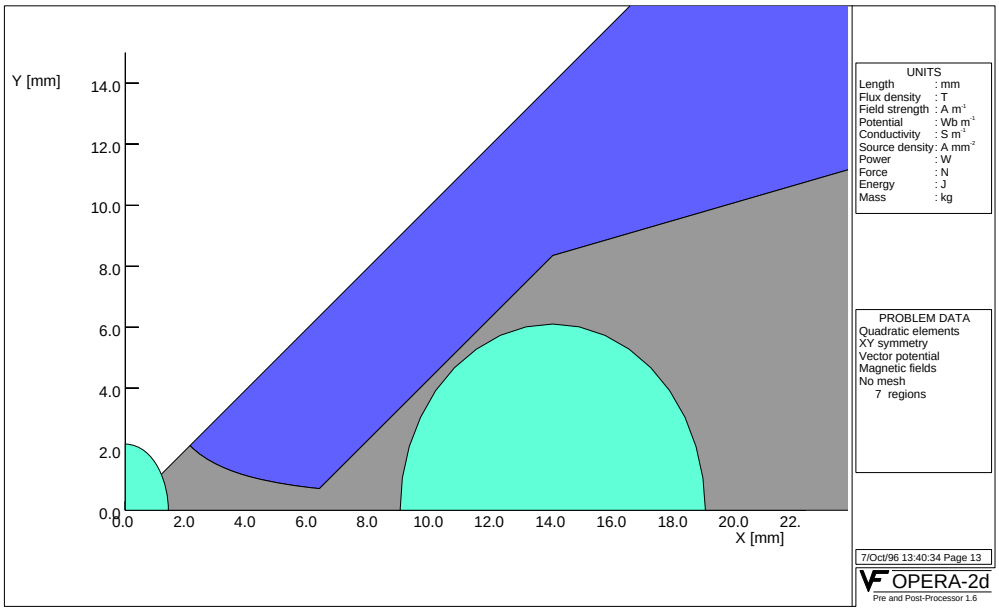

Figure 4.7.16: *Cross section of half of one quadrant of the final quadrupole, showing the* $10.7\sigma_x \times 27\sigma_y$ *ellipses of the incoming beam and the outgoing synchrotron light.*

collimation stage farther away from the IP, inserted between the end of the linac and the tuning and diagnostic section. Only a small fraction of halo particles escaping from the primary system will then hit the secondary collimators in the FFS.

In this scheme, one must take into account the possibility of trajectories changing amplitude and phase due to aberrations in the beam optical system between the 1st stage collimators and the FD. This leads to the requirement that collimation at both the FD and the IP phase is necessary and that the collimator aperture must be smaller by about a factor of 1.5 compared to the FD acceptance defined above. The resulting layout of the 1st stage system is sketched in fig. 4.7.17. Two pairs of spoilers, placed at high β and high dispersion points in the lattice, provide simultaneous collimation in x, y and $\Delta p/p$. The first pair collimates at the IP-phase, the second one at the FD-phase. We follow here a concept of mechanical collimation originally developed at SLAC [28]. The spoilers are thin (1.3 R.L. graphite, see below) and act to increase the angular and momentum spread of the part of the beam outside the acceptance while 20 R.L. Cu-absorbers downstream catch the halo emerging from the spoilers. An overview of the spoiler and absorber parameters is given in table 4.7.6. The secondary collimators in the FFS are set to apertures corresponding to $10\sigma_x$ and $26\sigma_y$ and are safely in the shadow of the primary system.

The overall efficiency of the system is tested by particle tracking calculations using the STRUCT code [29]. The beam halo is simulated by a $|x|^{-1} \cdot |y|^{-1}$ particle distribution outside the collimator aperture. The efficiency of the primary stage is shown in

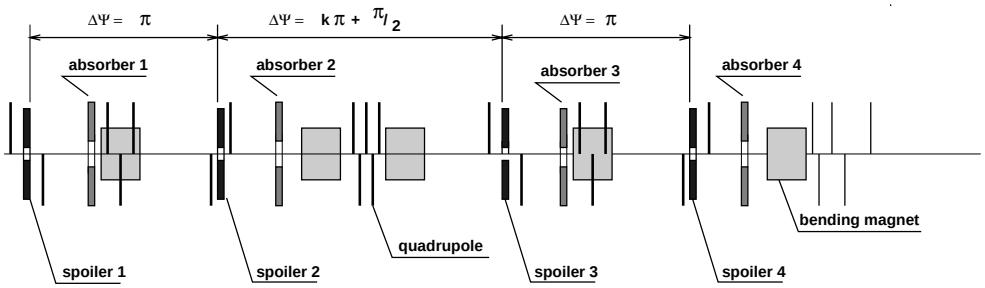

Figure 4.7.17: *Sketch of the 1st stage (main) collimation system.*

element	SPOILERS				ABSORBERS			
number	1	2	3	4	1	2	3	4
half gap g_x [mm]	1.4	1.4	1.4	1.4	1.8	2.3	1.8	2.3
half gap g_y [mm]	1.5	1.5	1.5	1.5	1.2	1.7	1.2	1.7
# of σ_x	7	7	7	7	30	30	30	30
# of σ_y	18	18	18	18	60	60	60	60
acceptance $\Delta p/p$ [%]	2.2	2.2	2.2	2.2				

Table 4.7.6: *Apertures of the main collimation system spoilers and absorbers.*

fig. 4.7.18 as a function of spoiler length. For 2 R.L. Titanium, a fraction of 3×10^{-4} of the simulated beam halo escapes from the system. The amount of particles escaping from the system can be further reduced by installing additional absorbers in the last section of the lattice. With 4 additional absorber blocks it goes down to 8×10^{-5}. In the simulation, all of these particles are stopped in the 2nd stage collimators. From the tracking results we estimate that less than 10^{-7} of beam halo particles have a chance to produce a hit in the interaction region quadrupoles if we conservatively assume an efficiency of the 2nd stage collimators of 10^{-3}. For one hit per bunch crossing, a beam loss of up to about 0.1% in the collimators would be tolerable, far in excess of a conceivable halo population of the beam.

4.7.8.2 Spoiler Protection

Though the beam is enlarged at the spoiler position by optical magnification it still exhibits an enormous power density of $P_{tot}/2\pi\sigma_x\sigma_y \approx 100$ MW/mm^2. Of course there is no material which could withstand such a power density for a longer time. On the other hand the spoilers are close to the beam and one has to take into account the possibility that a mis-steered beam hits the spoiler head on. Pyrolytic graphite appears to be the best choice of spoiler material under these conditions.

	$(dE/dx)_{min}$ [MeV/cm]	ρ [g/cm^3]	$c(T = 298\text{K})$ [J/gK]	λ [W/cmK]	X_0 [cm]
C	4.0	2.20	0.71	2...3	19.3

Table 4.7.7: *Some properties of pyrolytic graphite.*

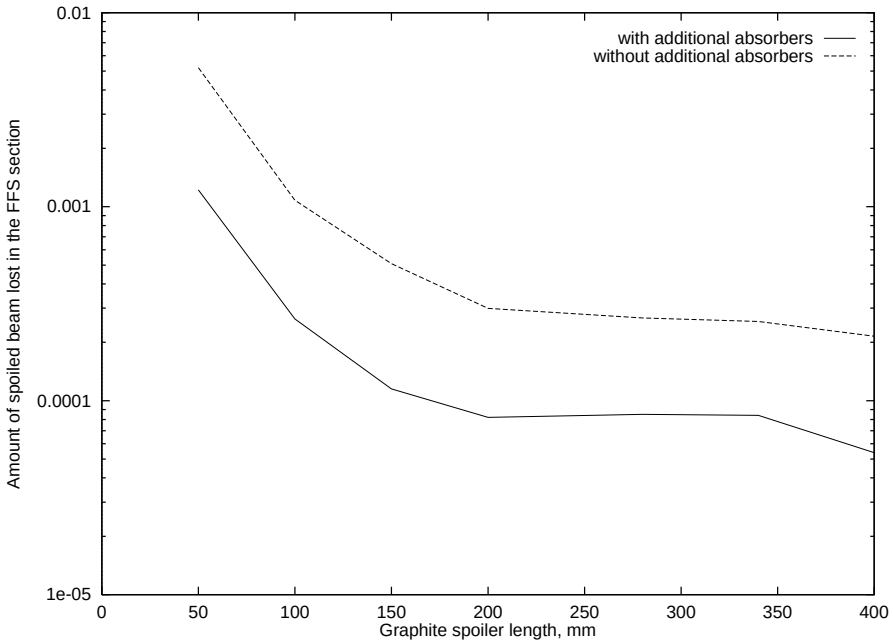

Figure 4.7.18: *Fraction of beam halo escaping from the primary collimation system as a function of spoiler thickness. The upper curve is the result for 4 absorbers, the lower curve for the case of 4 additional absorbers installed in the last section of the lattice. For graphite 1.3 R.L. correspond to 25 cm.*

Due to the large radiation length the graphite spoiler is relatively long. This leads to a larger transverse spread of the induced shower and results in a lower maximum energy deposition. In order to determine the instantaneous temperature jump due to the deposited energy one has to take into account the temperature dependence of the heat capacity:

$$\frac{dE}{dm} = \int_{T=T_0}^{T_0+\Delta T_{inst}} c(T)dT. \tag{4.7.1}$$

The instantaneous temperature jump ΔT_{inst} can be calculated by solving (4.7.1) numerically. Parameterizations for $c(T)$ can be found in [30].

The heating induces thermal stresses in the material which, if too high, will lead to cracks and damage the spoiler. The temperature limit can be estimated from the induced stresses:

$$\sigma_{UTS} > \frac{1}{2}\alpha E \Delta T_{inst}. \tag{4.7.2}$$

Here one should take into account that the material dependent parameters σ_{UTS} ultimate tensile strength, α linear expansion coefficient and E elastic modulus are also functions of temperature. From (4.7.2) we estimate limits of 2650 ^{o}C for pyrolytic graphite. It is found that a 1.3 R.L. thick spoiler could accept up to 400 bunches before the limit is reached. This means that a full bunch train (333 bunches) can hit

the spoiler without destroying it. The safety factor does not appear to be large, but one also should note that it is unlikely that a bunchtrain being many σ's off-axis will have the design emittances.

4.7.8.3 Emittance Dilution by Wakefields

Ultrarelativistic particles moving in a perfectly conducting pipe experience no transverse kick since the forces caused by the electric and magnetic field cancel exactly. However, at discontinuities as the entrance or the exit of a beam spoiler this cancelation is distorted and particles in a off-axis bunch will experience an effective kick due to the induced fields. The so called geometric wake field kick varies along the longitudinal direction of the bunch and can be estimated for rectangular spoilers by [31]:

$$\Delta y'(z) = \theta_1 \exp\left(-\frac{z^2}{2\sigma_z^2}\right); \quad \theta_1 = \frac{\pi^2 r_e N_B}{2\sqrt{2\pi}\gamma\sigma_z}\frac{\langle\Delta y\rangle}{g}, \tag{4.7.3}$$

where $r_e = 2.8 \cdot 10^{-15}$ m the classical electron radius, $\sigma_z = 0.3$ mm the rms bunch length, $N_B = 1.1 \cdot 10^{10}$ the bunch population, $\langle\Delta y\rangle$ the transverse bunch offset and g the half gap between the spoilers.

Since the strength of the kick varies along the bunch it dilutes the beam emittance. We assume that the mean kick can be corrected with steering elements and demand a luminosity reduction of less than 2 % for one σ_y offset at the spoiler:

$$\frac{\Delta L}{L} = \frac{1}{2}\frac{\Delta\varepsilon}{\varepsilon} = \frac{1}{2}\frac{\Delta y'^2_{rms}}{\sigma'^2} \leq 0.02, \text{ or } \quad \Delta y'_{rms} \leq \frac{1}{5}\sigma'.$$

The rms-wakefield kick $\Delta y'_{rms}$ is obtained by averaging of $\Delta y'$ and $\Delta y'^2$ over the longitudinal charge distribution (which is assumed here to be Gaussian):

$$\Delta y'_{rms} = \left(\langle\Delta y'^2\rangle - \langle\Delta y'\rangle^2\right)^{\frac{1}{2}} = \left(\frac{2-\sqrt{3}}{2\sqrt{3}}\right)^{\frac{1}{2}}\theta_1 = 0.278 \cdot \theta_1.$$

In order to reduce the geometric wakefield the spoiler can be tapered as shown in fig. 4.7.19. For taper angles $\theta_{tap} \ll 1$ the reduction factor is a linear function of θ_{tap} [32]:

$$k_1 = \frac{6\theta_{tap}}{\pi} \approx \frac{12(R-g)}{\pi(L_{tot}-L_{sp})}. \tag{4.7.4}$$

Of course the beam spoilers are not perfect conductors and for narrow gaps the resistive losses act back on the bunch. The so called resistive wall wakefield kick can be estimated by [33]:

$$\Delta y'(z) = \theta_2 \frac{1}{\sqrt{2\pi}}\int_{s=0}^{\infty}\frac{ds}{\sqrt{s}}\exp\left(-\frac{(z-s)^2}{2}\right); \quad \theta_2 = \frac{\pi^2 r_e N_B L_{sp}}{2\gamma}\sqrt{\frac{\lambda_{sp}}{\pi\sigma_z}}\frac{\langle\Delta y\rangle}{g^3}, \tag{4.7.5}$$

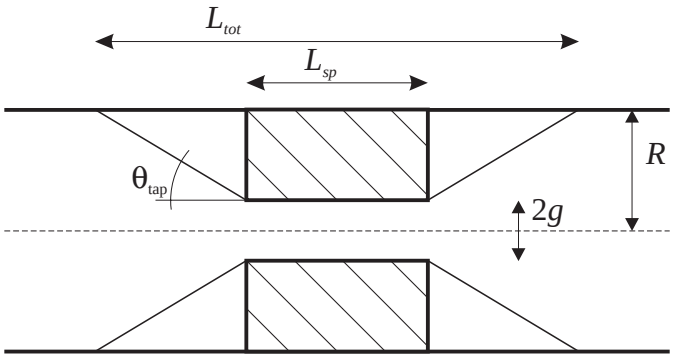

Figure 4.7.19: *Sketch of the tapered spoiler.*

where L_{sp} is the length of the spoiler and λ_{sp} is a characteristic length calculated from the conductivity σ_{sp} of the spoiler material:

$$\lambda = \frac{1}{c\mu_0\sigma_{sp}}.$$

Here the rms-kick is given by [28]

$$\Delta y'_{rms} = \left(\frac{K(\sqrt{3}/2)}{2\sqrt{\pi}} - \frac{\Gamma^2(1/4)}{8\pi} \right)^{\frac{1}{2}} \cdot \theta_2 = 0.292 \cdot \theta_2.$$

Tapering increases the length of the spoiler and therefore the resistive wall kick. The increase can be estimated by replacing the factor $\sqrt{\lambda_{sp}} L_{sp}/g^3$ in (4.7.5) by an integral over the total length:

$$\frac{\sqrt{\lambda_{sp}} L_{sp}}{g^3} \approx \int_{l=0}^{L_{tot}} \frac{\sqrt{\lambda(l)}}{g^3(l)}\, dl.$$

Thereby we obtain an enlargement factor for the rms-resistive wall wakefield kick of the tapered spoiler of (see geometry in fig. 4.7.19)

$$k_2 = 1 + \frac{1}{2}\sqrt{\frac{\lambda_{tap}}{\lambda_{sp}}} \left(\frac{L_{tot}}{L_{sp}} - 1 \right) \left(1 + \frac{g}{R} \right) \frac{g}{R}. \tag{4.7.6}$$

Here λ_{tap} is the characteristic length of the taper material which could be a thin copper foil for instance. Note that the heating of the taper material is not critical since the beam spot is enlarged by $1/\theta_{tap}$.

As long as the resistive wall wakefield kick is smaller than the geometric wakefield kick, tapering of the spoiler is helpful. The optimum total length of the tapered spoiler L_{tot} is achieved when both kicks have equal strength:

$$0.278 \cdot k_1(L_{tot}) \cdot \theta_1 = 0.292 \cdot k_2(L_{tot}) \cdot \theta_2.$$

Now we can apply these formulas to the SBLC parameters. For the spoiler we assume a thickness of 1.3 radiation lengths and a radius of the beam-pipe of $R = 10$ mm.

	$\gamma\varepsilon$ [mm mrad]	β [m]	σ [μm]	σ' [nrad]	g [mm]	g/σ
X:	5	4000	200	50	1.4	7
Y:	0.25	15000	87	5.8	1.5	18

Table 4.7.8: *Some beam related parameters at the spoiler locations.*

	$C_\perp$	$C_\parallel$
λ [m]	$2.65 \cdot 10^{-6}$	$1.06 \cdot 10^{-8}$

Table 4.7.9: *Characteristic length of pyrolytic graphite. Note the anisotropic properties. We assume that the material is aligned along the beam in the direction of the higher conductivity.*

The taper is suppose to be made of copper.Beam parameters relevant for the beam spoilers are given in Table 4.7.8, material parameters in Table 4.7.9 and results in Table 4.7.10. It turns out that the graphite spoiler slghtly misses the goal of $\Delta y'_{rms} \leq \sigma'/5$ due to the resistive wall effect (see Table 4.7.10). The emittance dilution for an offset of one σ_y amounts to about 9%. If coating of the inner surface of the graphite spoiler with a thin layer of copper or another material with high electrical conductivity is possible, this effect can be significantly reduced.

The conclusion from these considerations is that mechanical collimation of the SBLC beam at amplitudes of $7\sigma_x$ and $18\sigma_y$ can be realized with a tapered graphite spoiler. Emittance growth from wakefields is not negligible in that case and requires orbit offsets at the spoilers to remain somewhat below one σ. If coating of the graphite with Cu or other good conducting material is feasible, this effect can be significantly reduced.

4.7.9 Beam Extraction and Dump

4.7.9.1 Extraction Beamline

After the interaction, the spent beams pass through the exit aperture in the final doublet after which they are guided either directly to the beam dump (positron beam)

	geometric		resistive wall		opt. tapered		opt. len. [m]	
	$\frac{\sigma'_x}{\Delta x'_{rms}}$	$\frac{\sigma'_y}{\Delta y'_{rms}}$	$\frac{\sigma'_x}{\Delta x'_{rms}}$	$\frac{\sigma'_y}{\Delta y'_{rms}}$	$\frac{\sigma'_x}{\Delta x'_{rms}}$	$\frac{\sigma'_y}{\Delta y'_{rms}}$	L^x_{tot}	L^y_{tot}
C	3.0	0.9	9.4	3.5	9.0	3.3	1	1

Table 4.7.10: *Wakefield kicks for a beam offset of 1 σ. The Table contains the geometric and resistive wall kicks for the untapered spoiler and the geometric kicks for an optimal tapered spoiler. Given is always the value of $\sigma'/\Delta y'_{rms}$ which should be larger than 5 for a luminosity reduction of less than 2%. Furthermore the total length for an optimal tapered spoiler is given.*

or into a large-bandwidth capture optics (electron beam) for the positron source (see section 4.4.2). The beamline to the dump does not require any focussing elements. The beam is deflected horizontally to increase the separation from the incoming beamline and downwards to enter the absorber block under an angle of about -20 mrad, which suppresses muon radiation at the surface. The emittance dilution from synchrotron radiation is sufficient to fulfill the boundary condition of a minimum spotsize at the absorber block (see next section) even for a beam which has not experienced the beam-beam interaction.

4.7.9.2 Beam Dump

This section focusses on the question how to dispose of both the electron- as well as the positron beam after the collision. Based on shower, heat transfer and mechanical stress calculations a beam dump design capable of handling the $250\,GeV$ beams in SBLC is presented. After introducing the requirements on such a beam dump simple estimations on energy deposition and heat transfer answer the question of adequate absorber materials. Using shower simulation codes a beam absorber is calculated in more detail with respect to absorption efficiency and local energy densities the latter one giving a lower limit for the effective beam size when entering the absorber. The problem of induced radioactivity (production and handling of long lived isotopes) is mentioned very briefly, since the whole complex of radiation safety is discussed separately in section 4.11.

Requirements

The energy E_t carried in one bunchtrain, i.e. macropulse, is $0.15\,MJ$ for the SBLC scheme. Although being rather high, solutions exist to handle macropulse energies of that amount, e.g. at the proton machine of HERA, where the beam dump is capable of absorbing a complete fill, i.e. $820\,GeV$ protons with a total energy of $2.6\,MJ$ in a train of $20\,\mu s$, but this repeats typically less than one time in 8 hours only. Contrary to that the linear collider operates with high repetition rate, leading to an enormous average beam power of about $7\,MW$. This represents not only a huge heat load, but is also a source of high radiation and isotope production. In addition to the thermal capabilities the integral radiation leakage should not exceed 1 % of the incident beam power, which is still $70\,kW$. Of course the shielding around the dump will take some fraction of it and the contribution from the leaking particles to the total activation is less than 1 % because of their low energy.

The decision on the location of the beam dump depends strongly on its size. From the point of view of civil engineering costs and simplicity a solution of putting the absorber inside the tunnel is preferred instead of building an extra hall for it. On the other hand, additional shielding around the tunnel would be required to avoid activation of ground water. The final layout for the dump region still needs to be worked out.

Assuming the absorber would fit into the tunnel, Fig. 4.7.20 illustrates a very schematic top view of the area between interaction point (IP) and beam dump. From

the point of view of radiation and induced radioactivity there is no strong argument to put the beam dump outside if it would fit inside, since there will be already an area of higher dose rate level in the vicinity of the IP due to the presence of a collimation system, that can not be avoided there. Getting different deflection in the separation region the low energy tail of the disrupted beam can not be transported through the beamline towards the dump. Distributed collimators have to scrape this fraction of the beam (see also section 4.4.2), which is between 10 % and 20 % of the total intensity corresponding to a power in the order of 1 MW.

Besides the absorber for the spent beam there need to be a possibility to dispose of the beam when not passing through the IP but being extracted after the main linac during its commissioning. If it is designed symmetrically the same absorber could be used for both purposes being hit either by the spent beam or the commissioning beam from opposite sides, but excluding simultaneous operation because of power reasons. Since this would not allow independent commissioning of one main linac while the other beam passes through the IP, two beam dumps with identical specification have to be put behind each other as indicated in Fig. 4.7.20 on either side of the IP.

Apart from these main dumps there have to be additional beam absorbers in the whole complex of the linear collider facility, e.g. at the FEL laboratory. Nevertheless the requirements on the main dump are the most severe ones. Having found a feasible concept for the main dump will automatically give a solution for the other dumps. From the previous discussion the requirements on such a main dump can be summarized as follows:

1. Withstand absorption of 0.15 MJ energy pulses in combination with 7 MW average power
2. Energy absorption efficiency $\geq 99\,\%$
3. Compact as possible to be put inside the tunnel
4. Production rate of dangerous and long lived isotopes as small as possible

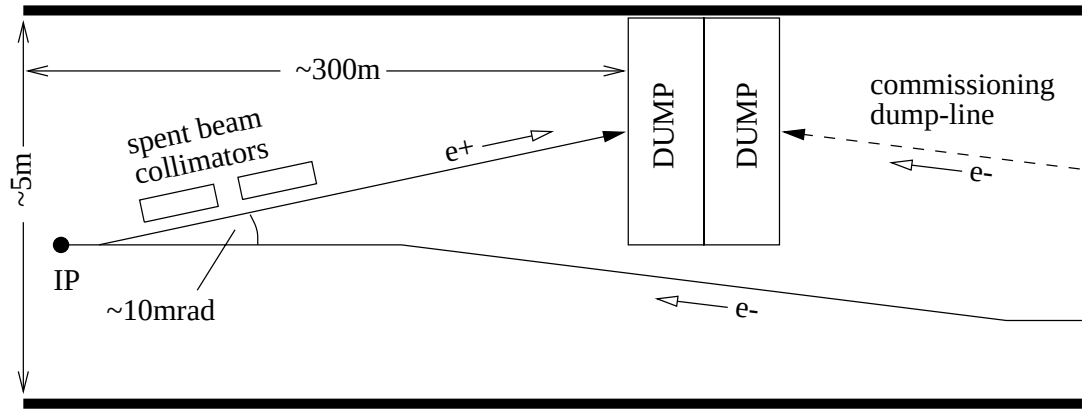

Figure 4.7.20: *Schematic topview of the area between IP and dump assuming the absorber fits inside the tunnel.*

5. Sufficient shielding to prevent groundwater and soil from being activated

Electromagnetic Showers

When hitting the absorber a high energy electron or positron beam initiates an electromagnetic shower (EMS), consisting of electrons, positrons and photons. In addition high energy photons can produce hadrons by means of photonuclear reactions. This is of major interest for the estimation of induced radioactivity, but less important for considerations on energy deposition since this is dominated by ionisation and exitation of atoms due to charged EMS components.

With respect to a cylindrical coordinate system an electron of energy E_0 enters a homogeneous material at $r = z = 0$ in positive z-direction. At first the combination of bremsstrahlung and pair production happening in average once in every radiation length for every electron, positron or photon leads to an exponential growth of the number of particles with z. Since the energy of the secondaries reduces similarly, this process stops when particles have reached the critical energy E_c, where ionisation reactions become dominant. The corresponding longitudinal position $z = t_{max}$ is called the shower maximum. That is where the longitudinal energy density defined as:

$$dE/dz = \int_{r=0}^{\infty} \int_{\phi=0}^{2\pi} dE/dV \; r \, d\phi \, dz$$

has its maximum value. Since this integration depends on the radial shower distribution it is obvious, that for a given material the maximum local energy density $(dE/dV)_{max} = \rho \cdot (dE/dm)_{max}$ appears at a position that depends on the incoming beamsize, while t_{max} is independent of it. With the radiation length X_0 and the critical energy E_c of a given material the development of the shower can be parametrized. Therefore the position of the shower maximum t_{max} and the particle multiplicity $M(t_{max})$ at that point can be expressed as [34]:

$$\begin{aligned} t_{max}(E_0) &= 1.01 \cdot \left(ln(\tfrac{E_0}{E_c}) - 1 \right) \cdot X_0 \\ M(t_{max}, E_0) &= 0.31 \cdot \tfrac{E_0}{E_c} \cdot \left(ln(\tfrac{E_0}{E_c}) - 0.37 \right)^{-\frac{1}{2}} \end{aligned} \tag{4.7.7}$$

where E_0 is the energy of the primary electron resp. positron. Assuming that at the shower maximum all the particles are still minimum ionising a rough estimate on the longitudinal energy density $(dE/dz)_{max}$ at the shower maximum created by one primary particle can be given as:

$$(dE/dz)_{max} \approx M(t_{max}, E_0) \cdot (dE/dz)_{min} \tag{4.7.8}$$

where $(dE/dz)_{min}$ is the energy deposited by one minimum ionising particle. The radial size of the shower is characterized by the Molière radius $R_M = 21.2MeV \cdot X_0/E_c$. In order to contain 98 % (1 % energy leakage radially and longitudinally) of the primary energy a cylindrical absorber has to have a radius $R_{99\%}$ and a length $L_{99\%}$ given by [35]:

$$L_{99\%} = \left[1.52 \cdot ln(\tfrac{E_0}{MeV}) - 4.1 \cdot ln(\tfrac{E_c}{MeV}) + 17.6 \right] \cdot X_0 \quad \text{and} \quad R_{99\%} \approx 5 \cdot R_M$$

		C	Al	Fe	Cu	Pb	H_2O
$X_0\ [cm]$		25.1	8.89	1.76	1.44	0.56	36.1
$R_M\ [cm]$		7.01	4.71	1.78	1.62	1.56	9.53
$E_c\ [MeV]$		75.9	40.0	21.0	18.8	7.6	80.3
$(dE/dz)_{min}\ [MeV/cm]$		3.03	4.37	11.6	12.9	11.7	2.03
$L_{99\%}\ [cm]$		470	190	42	35	16	670
$R_{99\%}\ [cm]$		35	24	8.9	8.1	7.8	48
$\rho\ [g/cm^3]$		1.7	2.7	7.87	8.96	11.35	1.0
$m\ [kg]$		3080	930	82	65	35	4850
$t_{max}\ [cm]$	from eq. 4.7.7	180	69	15	12	5.3	257
	MARS	200	80		14		260
$(\frac{dE}{dz})_{max}\ [\frac{GeV}{cm}\ per\ e]$	from eq. 4.7.7	1.11	2.93	14.3	17.6	37.7	0.707
	MARS	1.1	2.8		16.8		0.8

Table 4.7.11: *Basic properties of an electromagnetic shower initiated by a primary particle of energy $E_0 = 250\,GeV$ in different materials.*

From the given expressions most of the basic properties of the shower can be estimated. They are listed in Table 4.7.11 for most likely absorber materials, where t_{max} and $(dE/dz)_{max}$ are compared with the result of the simulation code MARS, which has been developed over many years at IHEP (Protvino, Russia) and FNAL (Batavia, USA). As for calculating the maximum steady state temperature level, which is determined by $(dE/dz)_{max}$ a simulation code is not required since the calculated result agrees within 15 %. But when dealing with local energy densities dE/dm, designing a composite absorber or including hadronic effects the simulation can not be avoided. In addition to the shower size for 98 % energy containment the mass $m = \rho \cdot \pi \cdot R_{99\%}^2 \cdot L_{99\%}$ of a corresponding absorber is given as well. Absorbers of that size would take 98 % of the shower but whether they withstand heating due to local energy densities and average power is subject to the following section. It has to be mentioned, that the graphite parameters are valid for a material coming from a pyrolytic production process. Therefore the density is 75.9 % of the theoretical value only. As a consequence the radiation length is increased and the minimum ionisation loss is decreased by the same factor.

Basic Considerations on Heating and Choice of Material

The incident particle leads to a certain distribution of deposited energy with a maximum local energy density $(dE/dm)_{max}$ somewhere on the shower axis. During the short passage time $T_t = 2\,\mu s$ of a bunchtrain, heat conduction is negligible. Therefore the instantaneous temperature rise ΔT_{inst} is directly proportional to the density of the deposited energy. Its maximum value $(\Delta T_{inst})_{max}$ is given by:

$$N_t \cdot (dE/dm)_{max} = \int_{T_0}^{T_0+(\Delta T_{inst})_{max}} c(T)\,dT \qquad (4.7.9)$$

where T_0 is the temperature just before the passage of the bunchtrain. The integral form takes a temperature dependent specific heat $c(T)$ into account, which is quite important in the case of graphite, where it can be described using the following fit function:

$$c(T) = 1.48 \cdot \frac{J}{g \cdot K} \cdot (1.44 - e^{-\frac{T}{511\,^\circ C}}) \quad \text{with T in degree celcius}$$

After the passage of the bunchtrain this temperature on the shower axis decays until the next bunchtrain arrives. Therefore the temperature varies with time in a sawtooth-like manner. On the other hand for a continuous beam with the same average power as for the pulsed one an equilibrium temperature drop ΔT_{eq} is expected between the shower axis and the cooled edge.

Let us first deal with the equilibrium situation, i.e. how to get rid of the average beam power. For all solids besides their heat conductivity this problem is determined by the area and the thickness through which the heat has to flow. We assume that the beam is evenly distributed along a circle with radius r_1 on the face of a cylindrical dump. In order to contain the shower radially the outer radius r_2 has to be $r_2 = r_1 + R_{99\%}$. Assuming that all the deposited energy flows radially from r_1 to r_2 the temperature drop $(\Delta T_{eq})_{max}$ between both radii at the position of the shower maximum can be given as:

$$(\Delta T_{eq})_{max} = (\frac{dP}{dz})_{max} \cdot \frac{1}{2\pi\lambda} \cdot ln(r_2/r_1) \quad \text{with} \quad (\frac{dP}{dz})_{max} = \frac{I_{ave}}{e} \cdot (\frac{dE}{dz})_{max} \qquad (4.7.10)$$

For each material of interest we set a maximum allowed temperature difference ΔT_{max}, either given by its plasticity limit $\sigma_{0.2}$ or by 20 % of its melting temperature T_{melt}, depending which of both represents the lower limit, i.e.:

$$\Delta T_{max} \approx \text{Min}\,[\sigma_{0.2}/(E \cdot \alpha) \text{ or } 0.2 \cdot (T_{melt} - 20^\circ C)]$$

where E is the elastic modulus and α the coefficient of linear thermal expansion.

For an average beamcurrent $I_{ave} = 32\,\mu A$, the power density at the shower maximum $(dP/dz)_{max}$ was derived from the calculated values of $(dE/dz)_{max}$ according to equation 4.7.8 as listed in Table 4.7.11. They vary between $36\,kW/cm$ (C) and $1.2\,MW/cm$ (Pb). From these values the required radius $r_1 = r_2 - R_{99\%}$ and the resulting outer diameter of a dump $D = 2 \cdot (r_1 + R_{99\%})$ in order to keep $(\Delta T_{eq})_{max} \leq \Delta T_{max}$ can be calculated according to equation 4.7.10. The results are listed in Table 4.7.12. Except for graphite the diameter of all other materials exceeding several $10\,m$ excludes their installation inside the tunnel and is even far off from a reasonable limit to be built anyhow. On the one hand graphite has a high radiation length leading to moderate power densities. On the other hand its excellent thermomechanical properties allow a high working temperature around $800^\circ C$ not determined by the plasticity limit as it is for the other materials. In addition there is no safety problem in handling and machining graphite and its relatively low mass number limits the variety of produced isotopes. This all makes graphite the best candidate for a dump built from a solid material. When estimating the diameter of the solid cylindrical dump only cooling

	C	Al	Fe	Cu	Pb
$(dP/dz)_{max}\ [kW/cm]$	36	94	458	560	1200
$\lambda\ [W/(cm \cdot K)]$	1.6	2.0	0.8	3.8	0.35
$\Delta T_{max}\ [K]$	800	60	240	150	30
$r_1\ [m]$	1.4	30	34	13	1400
$D = 2 \cdot (r_1 + R_{99\,\%})\ [m]$	3.5	60	68	26	2800

Table 4.7.12: *Minimum required diameter D of a dump in order to keep the maximum equilibrium temperature drop $(\Delta T_{eq})_{max} \leq \Delta T_{max}$ for $E_0 = 250\,GeV$ and $I_{ave} = 32\,\mu A$.*

at the outer surface at $r_1 + R_{99\%}$ was assumed. Since r_1 is large enough additional cooling at an inner surface at $r_1 - R_{99\%}$ is possible. This will either reduce the equilibrium temperature or it allows to decrease the radial size. Nevertheless a graphite based absorber will have an outer diameter between $2\,m$ and $3\,m$ determined by heat conduction not shower containment and a length given by $L_{99\%}$ of about $5\,m$.

This is completely different for a liquid absorber such as water. Having even a little higher radiation length than graphite it is also a good candidate for a dump design. With $23\,kW/cm$ the maximum power density is not significantly less than in graphite, but instead of distributing the beam across the absorber in order to increase the area for heat conduction, one can introduce a sufficiently high water flow transversely to the shower axis, so that the water in the core of the shower is exchanged within the repetition time of bunchtrains. Under these circumstances the average power will be transported to an external heat exchanger and the size of the absorber is purely determined by the 99 % shower containment constraint. This will give a diameter of $2 \cdot R_{99\%} \approx 1\,m$ and a length of $L_{99\%} \approx 7\,m$ in the case of water. Being at least a factor of 2 more compact radially the length is only 40 % increased with respect to a graphite absorber. Although this is advantageous there are qualitative differences that will be discussed at the end of this section.

Now we have to consider the implications due to instantaneous heating during the passage of one bunchtrain. As described in equation 4.7.9 the maximum temperature rise $(\Delta T_{inst})_{max}$ depends on the number of particles N_t in a bunchtrain and the maximum local energy density in the shower $(dE/dm)_{max}$ deposited by one particle. For a given material only the size of the incident beam can be varied in order to reduce the local energy density and thus the instantaneous heating. Assuming a $250\,GeV$ gaussian beam with an aspect ratio of 1:1 the maximum local energy density $(dE/dm)_{max}$ and its longitudinal location on the shower axis was calculated for graphite and water as a function of the transverse beamsize $\sigma_x = \sigma_y$ by means of the shower simulation code MARS. From these results as listed in Table 4.7.13 a lower limit for the required beamsize at the dump entrance can be given. Due to steady state heating the temperature T_0 before the passage of a bunchtrain will be about $400°C$ in a graphite based dump (see next section). The remaining margin up to the working temperature limit of $800°C$ can be allowed for instantaneous heating. Taking into account the temperature dependent specific heat of graphite the corresponding difference in enthalpy per

Graphite								
$\sigma_x = \sigma_y\ [mm]$	0.1	0.5	1	2	3	5	7.5	10
$(dE/dm)_{max}\ [GeV/g\ per\ e]$	13	2.8	1.1	0.45	0.27	0.13	0.07	0.05
z-position of $(dE/dm)_{max}\ [cm]$	50	80	100	125	130	150	165	175

Water						
$\sigma_x = \sigma_y\ [mm]$	1	3	5	10	30	50
$(dE/dm)_{max}\ [GeV/g\ per\ e]$	1.05	0.25	0.12	0.05	0.009	0.004
z-position of $(dE/dm)_{max}\ [cm]$	145	190	205	220	230	250

Table 4.7.13: *Maximum local energy density normalized to one primary particle in a graphite or water absorber deposited by a* $250\,GeV$ *beam as a function of its transverse beamsize.*

mass unit is $660\,J/g$ for $T_0 = 400°C$ and $(\Delta T_{inst})_{max} = 400\,K$. For a bunchtrain with $N_t = 3.75 \cdot 10^{12}$ this requires a $(dE/dm)_{max}$ of less than $1.1\,GeV/g\ per\ e$ corresponding to a beam size with $\sigma_x = \sigma_y$ not less than about $1\,mm$.

In the case of water $T_0 = 40°C$ and $(\Delta T_{inst})_{max} = 40\,K$ are reasonable assumptions in order to prevent it from boiling. Therefore about $170\,J/g$ can be used for instantaneous heating. From the same considerations as above the relevant limits are $0.28\,GeV/g\ per\ e$ and $\sigma_x = \sigma_y \approx 3\,mm$. The estimates on the required beamsize have to be regarded as lower limits for an effective spotsize over which the particles of one bunchtrain have to be distributed at the dump entrance. In most cases being rather large this spotsize is not automatically achieved by the betafunction and the emittance of the beam at the position of the dump. Additional measures such as a defocussing quadrupole, a thin foil for spoiling the emittance, a fast sweeping system which distributes the beam within the time T_t of one bunchtrain passage or any combination of it have to be taken. From this point of view a water absorber requires more effort.

As proven in this section even for the high average power of $7\,MW$ an edge cooled solid dump made from graphite is possible. Water can be used as an alternative as proposed for the NLC [36]. On the one hand a water absorber is more compact and due to the main contribution from short lived isotopes the dose rate in $1\,m$ distance after $1\,year$ of $7\,MW$ operation decays rather rapidly within a waiting time of $3\,hours$ down to a level of $20 - 30\,mSv/h$ $(1\,Sv = 100\,rem)$, which can be reduced by a shielding factor of 10^2 with $5\,cm$ of lead [37]. The corresponding dose rate for a graphite absorber is around $70\,mSv/h$, i.e. only a factor of 2 higher. This would allow access or at least walking by at the dump region. The remaining dose rate is determined by $^7Be\,(t_{1/2} = 54\,days)$ but can be removed in a resin filter. On the other hand there are severe safety problems correlated with a water absorber. Having an annual production rate of $11.4\,Ci/MW$ the activity of tritium $(t_{1/2} = 12\,years)$ after 1 year of $7\,MW$ operation is $77\,Ci$ equivalent to $29\,cm^3$ of $^3H_2$ gas. Since distributed in the whole system of water cooling special care has to be taken to prevent leaking of it. There is no conclusive approach how to handle the tritium. Dilution of course is a bad idea. The presently allowed concentration of $800\,\mu Ci/m^3$ which can be put into waste

water would require $3.5\,l/s$ continous exchange of the absorberwater with fresh water. Another safety problem arises from the radiolysis of water. Due to a production rate of $0.3\,l/s$ per MW deposited beam power [38], $2.1\,l/s$ hydrogen is produced at $7\,MW$ operation, which can be recombined to H_2O catalytically. Again any leakage of the system has to be avoided because a concentration of $4\,\%$ H_2 in air is explosive. Being proportional to the directly deposited beam power all the water related problems are less by a factor of 100 for the cooling circuit of an edge cooled graphite dump. Although the amount of ^3H production will not be significantly different in graphite, it will like all other produced isotopes be bounded and localized inside the solid and not spread around in a fluid with the danger of getting lost by leakage. For this qualitative difference the graphite based solution is preferred. An optimized design using shower simulations is presented in the following section. The solution using water can be regarded as a backup.

Absorber Design Based on a Graphite Core

From considerations in the previous section we know that the graphite absorber has to look like a hollow cylinder with a radial thickness of Δr between an inner resp. outer radius of $r_1 \pm \Delta r/2$, while the beam is distributed along a circle with radius r_1 at the face of this dump. Putting a material of higher density and better thermal conductivity in the region of the transverse shower tails, where it can survive, will reduce both Δr and r_1. Longitudinally the dump is not sectioned. Several runs of MARS simulations were made to optimize this layout. The result is shown in Fig. 4.7.21. A graphite tube with $r_1 = 1\,m$ and a radial thickness of $10\,cm$ is embedded between an inner and outer radial layer of aluminium $10\,cm$ thick each. For its smaller radiation length (see Table 4.7.11) only $5\,cm$ of copper can be used alternatively. This compound has a total radial thickness of $\Delta r = 30\,cm$ with Al respectively $\Delta r = 20\,cm$ with Cu, an outer diameter D of $2.3\,m$ resp. $2.2\,m$, a total mass of $27\,tons$ resp. $40\,tons$ and will be cooled at the inner and outer surface at $r_1 \pm \Delta r/2$. A total length of $L = 6\,m$ guarantees $99\,\%$ absorption of the primary energy in both cases.

Distribution of the beam along a circle with radius $r_1 = 1\,m$ can be achieved by means of an orthogonal pair of dipoles harmonically excited at the same frequency but shifted in phase by 90°. If placed $100\,m$ upstream from the dump the maximum deflecting angle of each magnet has to be $10\,mrad$, which requires an integrated field-strength of about $9\,Tm$ for a $250\,GeV/c$ beam. To provide a homogeneous azimuthal heat source the oscillation period of this slow sweeping system has to be significantly faster than thermal diffusion processes. Since the thermal time constant for this dump scheme is around $200\,s$ the frequency of the slow sweepers should be $1/50\,Hz$ or more.

The resulting equilibrium temperature rise at the shower maximum ($t_{max}(\mathrm{C}) \approx 2\,m$) for a $250\,GeV$ beam with $I_{ave} = 32\,\mu A$ is listed in Table 4.7.14. The maximum heat flux at the water cooling boundary is roughly $27\,W/cm^2$. The temperature will rise by about $50\,K$ according to a typical heat transfer coefficient of $0.6\,\frac{W}{cm^2 \cdot K}$ for water at metallic walls. The graphite metal boundary is more crucial, because specific heat

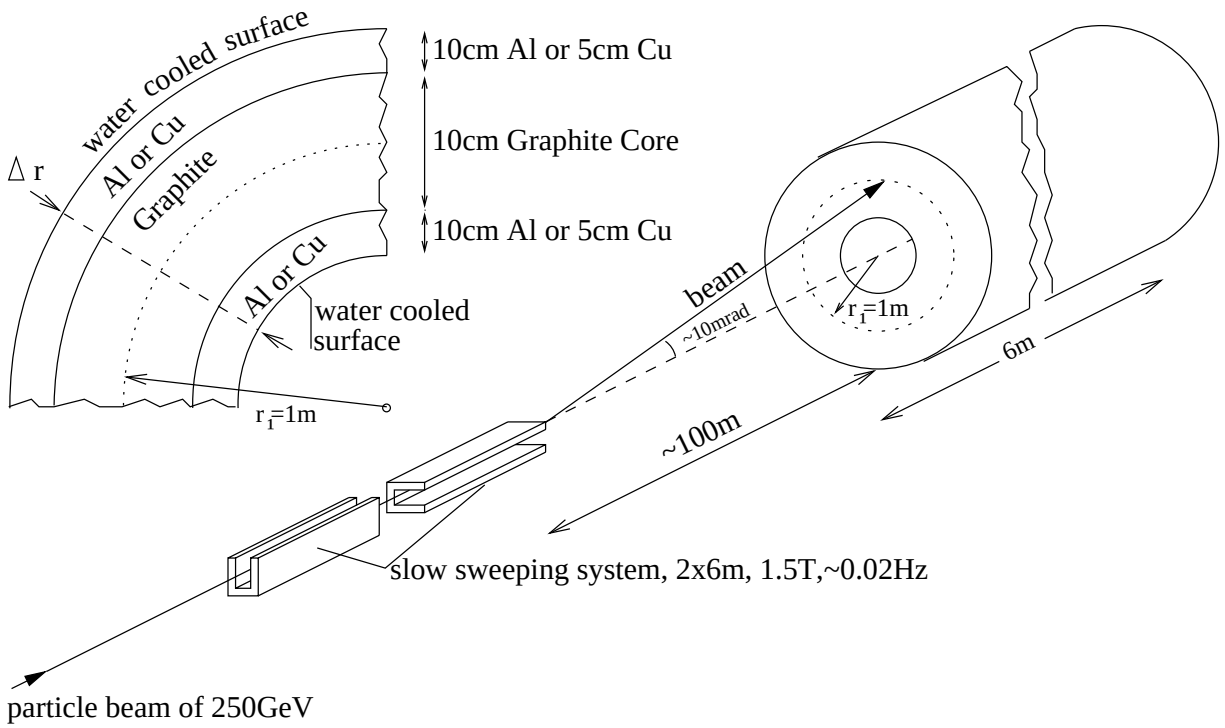

Figure 4.7.21: *Dump scheme based on a solid absorber with a graphite core.*

conduction in C between $100cm \leq r \leq 105cm$	transfer C → Al or Cu at $r = 105cm$	conduction in Al between $105cm \leq r \leq 115cm$	conduction in Cu between $105cm \leq r \leq 110cm$	transfer Cu or Al → H_2O at $r = 105$ or $110cm$
$190\,K$	$\approx 50\,K$	$135\,K$	$45\,K$	$\approx 50\,K$

Table 4.7.14: *Contributions to the equilibrium temperature rise due to heat conduction or heat transfer in the C-Al or C-Cu composite dump at the shower maximum for* $E_0 = 250\,GeV$ *and* $I_{ave} = 32\,\mu A$.

transfer is only about $0.2\,\frac{W}{cm^2 \cdot K}$ [39]. The effective surface has to be increased at least by a factor of 2, which was already taken into account when estimating a ΔT of $50\,K$ across this boundary. The technical design has to guarantee that the thermal contact of this boundary is not lost due to different expansion during warm up or cool down of the dump. Including the temperature drops from heat conduction and assuming a temperature of $50°C$ for the cooling water, the graphite core at $r = 1\,m$ rises up to a temperature of $475°C$ when neighboured by aluminium. For its better thermal conductivity this temperature can be reduced to $385°C$ when using copper.

The following considerations on instantaneous heating are based on a beamsize with $\sigma_x = 3\,mm$ and $\sigma_y = 0.5\,mm$ at the dump entrance for a beam having not interacted. From Table 4.7.13 we know already that a minimum effective spotsize of $\sigma_x \cdot \sigma_y = 1\,mm^2$ is required in order to keep $(\Delta T_{inst})_{max} \leq 400\,K$. Therefore the above given beamsize is large enough and a fast sweeping system during the passage of one bunchtrain is

not needed. The main parameters of the slow deflection system are summarized in Table 4.7.15. The instantaneous temperature rise in the Al or Cu material is only

	magnetic field in deflector	length of deflector	frequency $[Hz]$
slow deflection system	$1.5\,T$	$2 \times 6\,m$	$\geq 0.02\,Hz$

Table 4.7.15: *Main parameter of the sweeping system for a* $250\,GeV$ *beam.*

about $20\,K$.

With this scheme the maximum temperature in graphite is kept below a maximum reasonable working temperature of $800°C$. As a consequence of the slow deflection system a large beampipe and if not directly flanged onto the dump a huge exit window is required. The angle of $10\,mrad$ needs to be taken into account by shaping the dump conically rather than cylindrically.

Bibliography

[1] Murray J.J., K.L. Brown and T. Fieguth, *The Completed Design of the SLC Final Focus System*, Proc.of Part. Acc. Conf., Washington, D.C., March 1987 and SLAC-PUB–4219 (Feb.1987).

[2] D. Burke for the FFTB Collaboration, *Results from the Final Focus Test Beam*, Proc. of the IVth European Particle Accelerator Conf., London 1994, Vol. I, p. 23.

[3] R. Brinkmann, *Optimization of a Final Focus System for Large Monentum Bandwidth*, DESY-M-90-14, 1990.

[4] Grote H. and F.C. Iselin, *The MAD Program*, CERN/SL/90-13 (AP) Rev.3 (Jan.1993).

[5] B. Baklakov, P. Lebedev, V. Parkhomchuk, A. Sery, A. Sleptsov, V. Shiltsev, INP 91-15; Tech. Ph. **38**, 894, (1993).

[6] V. Juravlev, A. Sery, A. Sleptsov, W. Coosemans, G. Ramseier, I. Wilson, CERN SL/93-53, CLIC-Note 217, 1993.

[7] V. Juravlev, P. Lunev, A. Sery, A. Sleptsov, K. Honkavaara, R. Orava, E. Pietarinen, *Seismic Conditions in Finland and Stability Requirements for the Future Linear Collider*, HU-SEFT R 1995-01, Helsinki 1995.

[8] V. Shiltsev, B. Baklakov, P. Lebedev, J. Rossbach, C. Montag, *Measurement of Ground Vibrations and Orbit Motion at HERA*, DESY HERA 95-06, June 1995.

[9] Shigeru Takeda, K. Kudo, A. Akiyama, Y. Takeuchi, T. Katoh, Y. Kanazawa, S. Suzuki, *Slow Ground Motion and Large Future Accelerator*, Proc. EPAC 96, 1996.

[10] C. Adolphsen, G. Mazaheri, T. Slaton, in: Proc. of Workshop on Physics and Experiments with Linear Colliders, Tsukuba, 1995.

[11] A. Sery, O. Napoly, Phys. Rev. E. **53**, 5323, (1996).

[12] R. Brinkmann, J. Rossbach, *Observation of Closed Orbit Drift at HERA Covering 8 Decades in Frequency*, Nucl.Instr.Meth.A **350**, 8, (1994).

[13] V. Shiltsev, *Space-Time Ground Diffusion: the ATL Law for Accelerators*, Proc. of Workshop on Accelerator Alignment, Tsukuba, 1995.

[14] R. Pitthan, *Re-Alignment: It is the Tunnel Floor which Moves, Isn't it?*, SLAC-PUB 95-7043, 1995.

[15] A. Sery, A. Mosnier, DAPNIA/SEA/96-06, CEA Saclay, 1996.

[16] C. Montag,*Active Stabilisation of Quadrupole Vibrations for Linear Colliders*, DESY 96-053, 1996.

[17] A. Sery,*Ground Motion Studies with Respect to Linac Performance*, Proc. of the Linac 96 Conference, Geneve 1996.

[18] P. Tenenbaum, D. Burke, S. Hartman, R. Helm, J. Irwin, R. Iverson, P. Raimondi, W. Spence, V. Bharadwaj, M. Halling, J. Holt, J. Buon, J. Jeanjean, F. Le Diberder, V. Lepeltier, P. Puzo, K. Oide, T. Shintake, and N. Yamamoto, *Beam Based Optical Tuning of the Final Focus Test Beam*, SLAC-PUB-95-6770, May 1995. 3pp. Presented at 16th IEEE Particle Accelerator Conference (PAC 95) and International Conference on High Energy Accelerators, Dallas, Texas, 1-5 May 1995.

[19] P. Tenenbaum, D. Burke, R. Helm, J. Irwin, P. Raimondi, K. Oide, and K. Flöttmann, *Beam Based Magnetic Alignment of the Final Focus Test Beam*, SLAC-PUB-95-6769, May 1995. 3pp. Presented at 16th IEEE Particle Accelerator Conference (PAC 95) and International Conference on High Energy Accelerators, Dallas, Texas, 1-5 May 1995.)

[20] G. Bowden, P. Holik, S.R. Wagner, G. Heimlinger, and R. Settles, *Precision Magnet Movers for the Final Focus Test Beam*, Nucl. Instrum. Meth.A368:579-592,1996.

[21] P. Emma, J. Irwin, N. Phinney, P. Raimondi, N. Toge, N.J. Walker and V. Ziemann, *Beam Based Alignment of the SLC Final Focus Sextupoles*, SLAC-PUB-6209, May 1993. 3pp. Presented at 1993 Particle Accelerator Conference (PAC 93), Washington, DC, 17-20 May 1993.

[22] N. J. Walker, *Beam Phase Space and Energy Measurements in TESLA and SBLC*, to be published as a TESLA report.

[23] *Zeroth-Order Design Report for the Next Linear Collider*, SLAC Report 474, May 1996.

[24] E. G. Bessonov, J. Pflüger, G.-A. Voss and N. J. Walker, *Beam Size Measurements in a Linear Collider using an X-ray Gradient Undulator*, DESY internal report DESY M 96-18, September 1996.

[25] T. Shintake, K. Oide, N. Yamamoto, A. Hayakawa, Y. Ozaki, D. Burke, R.C. Field, S. Hartman, R. Iverson, P. Tenenbaum, and D. Walz, *Experiments of Nanometer Spot Size Monitor at FFTB using Laser Interferometry*, KEK-PREPRINT-95-46, May 1995. 3pp. Contributed paper at 1995 Particle Accelerator Conference and

International Conference on High-Energy Accelerators, May 1 - 5,1995, Dallas, Texas, U.S.A.

[26] N.J. Walker, J. Irwin, and M. Woodley, *Global Tuning Knobs for the SLC Final Focus*, SLAC-PUB-6207, Apr 1993. 3pp. Presented at 1993 Particle Accelerator Conference (PAC 93), Washington, DC, 17-20 May 1993.

[27] D. Schulte, *Study of Electromagnetic and Hadronic Background in the Interaction Region of TESLA.*, Ph.D. thesis, University of Hamburg 1996.

[28] N.Merminga, J.Irwin, R.Helm, R.D.Ruth, *Collimation Systems for a TEV Linear Collider*, SLAC Pub. 5165 Rev. (1994)

[29] I.Baishev, A.Drozhdin, N.Mokhov, *STRUCT Program User's Reference Manuel*, SSC-MAN-0034, February 1994.

[30] Handbook of Chemistry and Physics, Chemical Rubber Publishing Company (1976)

[31] K.L.F. Bane, P.L. Morton,*Deflection by the Image Current and Charges of a Beam Scraper*, SLAC Pub. 3983 (1986)

[32] Kaoru Yokoya, *Impedance of Slowly Tapered Structures*, CERN SL/90-88 (1988)

[33] A.Chao, *Physics of Collective Beam Instabilities in High Energy Accelerators*, J.Wiley & Sons, New York (1993)

[34] B. Rossi, *High-Energy Particles*, Prentice-Hall, New York, 1952.

[35] I.S. Baishev, M.A. Maslov, M. Seidel, *Design Study of a Beam Dump for the TESLA and S-Band Test Facilities at DESY*, DESY-TESLA-95-10, 1995.

[36] NLC-ZDR Design Group, *Zeroth Order Design Report for the Next Linear Collider*, SLAC, February 1996.

[37] K. Tesch, *A Note on Residual Radioactivity of Beam Absorbers for a Linear Collider*, DESY, March 1996.

[38] D.R. Walz, A. McFarlane, E. Lewandowski, *Beam Dumps, Stoppers and Faraday Cups at SLC*, SLAC-Pub. 4967, 1989.

[39] J. Kidd et al.,PAC IX, Washington, 1981.

4.8 Instrumentation and Controls

With the passage of time, the instrumentation and control systems have come to play a role of steadily increasing importance for the achievement of accelerator performance goals. They are no longer just the means for intermittent operator intervention; rather, they provide the complex of feedback loops necessary to performance. In this respect, the linear collider resembles the "fly-by-wire" characteristics of modern high performance aircraft. The lower frequency S-band approach ameliorates but does not avoid this situation.

The discussion to follow gives an overview of the beam instrumentation and feedback systems foreseen for the SBLC.

4.8.1 Beam Diagnostics

We begin with a summary of some of the basic ideas and numbers which lead to instrumentation needs, requirements, and device descriptions. Sections elsewhere in this report where detailed information can be found are referenced. This introduction concludes with a tabulation of issues and approaches.

The Linac

For the linac the main requirement which has been addressed is the preservation or control of the transverse emittance.

Transverse emittance (Section 4.3) is preserved by control of alignment of the quadrupoles, BPM's and cavities. In addition energy variation and energy spread must be controlled (i.e. longitudinal emittance).

RMS alignment tolerances of 100 μm for quads, BPMs, and accelerating structures have been chosen. These values are relative to the ideal beam line and are assumed to be valid over distances of up to 600 m. Beyond this distance, typical of a betatron wave length, sensitivities decrease rapidly.

Using the above alignment errors, single bunch vertical emittance growths is untolerable large for simple "one to one" beam steering (i.e., steering from the center of one detector to another). In the more time consuming beam-based alignment method, described later on together with the beam position monitor system, the center of the beam is found relative to the center of the quad and to the BPM. The total emittance budget is $20\pm10\,\%$ and can be achieved if the BPM resolution is 5 μm. (Section 4.3). A BPM resolution and stability of $\pm2\,\mu$m for the linac has been chosen in order to be able to further decrease emittance dilution which is desirable for an upgrade of the luminosity and the energy. In principle this accuracy has to be achieved only by averaging of entire bunch trains, but at least a small number of special monitors should be able to resolve individual bunch positions.

The above emittance growth is based on a bunch energy spread necessary for BNS damping of 3×10^{-3} which results from the longitudinal wake-field and operating on

the RF crest. Multibunch emittance growth with inter-bunch energy spread of 6×10^{-4} shows very little difference from the single bunch results (Section 4.3).

The effect of ground motion on orbit stability has been estimated. Beam resteering (1 to 1) should be performed every 25 minutes in order to limit vertical emittance dilution to less than 6% for ground motion frequencies $< 2.5\,\mathrm{Hz}$ (i.e., 50Hz/20 - the high cutoff frequency of the conventional beam steering feedback system).

The Beam Delivery System

The beam delivery system (BDS) reaches from the end of the linac to the IP and is 1400m long. The about 50 quads, sextupoles, and 16 bends per beam will each be provided with BPM's attached to the magnets and the assemblies placed on magnet movers for beam based alignment and tuning.

To make the following discussion easier to follow, functional sections are in order (see Section 4.7):

- (LMS) linac matching section,
- (CS) collimation section,
- (TDS) tuning and diagnostic section which is composed of the (SQSC) skew quad correction section and the (EMS) emittance measurement section,
- (BMS) beta matching section,
- (CCS) chromaticity correction section,
- (FT) final transformer.

The CS collimation section contains high beta and high dispersion regions with collimator pairs, energy measurement and correction, energy spread measurement, beam loss measurement for protection of the collimators.

The TDS tuning and diagnostic section provides for measurement and correction of transverse coupling in the SQSC and for measurement and minimization of emittance in the EMS. This is the major measurement and tuning area which sets, measures and adjusts the beam properties prior to the final transport to the IP. Six wire scanners are used for emittance measurement; four additional scanners are used at the skew quads are implemented with "u" angle wires as well as x, y wires. The emittance measurement station is capable of 1% measurement error. The carbon wires are $4\,\mu$m diameter.

The BMS provides for fine tune at the IP and adjustment of phase from the collimators to the final focus. Measurements made in the TDS give information for adjustment of these quads. Beam can be checked at the IP image points that occur at the begining of the CCS and within the CCS at the beginning of the FT. The vertical image of the 15 nm spot has a magnification of $46\times$ to give a spot of 700 nm. This will require laser wire or gradient undulator (see below) instruments. The sextupoles in the CCS have to be turned off for this measurement at the image point in the FT in order not to dilute the spot size by large chromatic aberrations. The CCS " -I" optics sections must be checked by a BPM-corrector null method to assure the proper optics.

Final tuning of the IP spot size requires movement of the sextupole pairs in a variety of combinations. The crucial vertical spot size measurement must be carried out with a

laser interferometer (Shintake monitor [1]). The required resolution is about a factor of five better than what has already been demonstrated at the FFTB [2]. The horizontal spot is better measured with a laser wire [3]. These monitor laser beams pass through the electron beam 30-80 cm from the IP point and the low-β^* point must be shifted in z to this location. This is accomplished by the sextupole adjusters in the CCS.

The Shintake monitor has limited dynamic range of spot size that it can accurately measure for any specific laser wavelength. At a laser wave length of 262 nm spot sizes from 10 to 45 nm can be measured with 10% accuracy. On the other hand the laser wire spot can not be made smaller than ≈ 380 nm diameter using the an ArF excimer laser. This comes close to the beam size of 335 nm horizontally.

The profile scans using laser beams must detect the scattered Comptons which come out straight ahead with an opening angle of $1/\gamma$. For systems within the IP detector, the Comptons must be detected dowmstream of the IP.

The Shintake monitor has the potential for bunch length measurement as well. But as both it and the horizontal laser wire are deeply embedded in the detector, other less invasive instruments or instruments at other locations may be more practical for measurements that do not have to be done at the IP.

Other monitors are planned for the IP region (see also Chapter 2):

- Beam-Beam deflection monitor
- Fast luminosity monitor
- Precision energy measurement
- Polarization measurement

These monitors are noninvasive and can be used during standard operation.

The steering from the beam-beam force is used to monitor the offset of the two colliding beams. A kick angle of 75 microradians per vertical sigma offset is expected. A BPM 2 m downstream of the IP would see typically 150 μm offset per beam sigma separation. Individual bunch measurements are possible. The signal can be used for beam steering feedback (see Section 4.8.3).

A fast luminosity monitor can be used to detect beam detuning at the IP to do noninvasive fine adjustments and beam scans. Radiative Bhabha pairs detected about 9 m from the collision point could provide the appropriate monitor information.

Precision absolute energy measurements will be made of the beams in the extraction lines after the IP. The measurement uses displacement synchrotron light fans from bend magnets to measure the bend angle of the beam in a spectrometer magnet. A resolution of 10^{-4} is expected. However beams must not be colliding if precise before collision beam energy is to be measured.

The polarimeter uses laser beam scattering and detects Compton scattering asymetry. It is likely to be located before or after the IP.

Beam Steering – Initial Setup and Drift

Static tolarances of BDS magnet alignment indicate that typically y alignment tolarances of 0.5 to 10 μm are needed for many of the magnets if less than 2% luminosity

decrease (with collision beam steering) is to result from an individual magnet. A model for uncorrelated rms motions of the magnets in x and y predicts that rms motions of 139 nm in y and 295 nm in x will yield 2% luminosity reduction (again with collision beam steering) (Section 4.7.3).

The simulation program Merlin has been used to check possible noninvasive tuning proceedures to correct the deterioration of the beam size by linear optics aberrations (Section 4.7.6). It was found that simple one-to-one steering of the BDS elements using the BPM's and magnet movers every minute was sufficient to restore the luminosity to almost its full value. A drop in peak (after retuning) lumimosity of 5% occured after about 5 days indicating that an invasive retune would be necessary on this time scale.

	where	typical beam size [μm]	resolution required [μm]	freq. of adjustment	bunch structure	invasive y,n
POSITION x, y						
bpm	linac	120-14 x,27-3 y	2 y	25 min.	pulse avg.	n
	BDS	360-13 x,75-0.9 y	2 y	1 min.	pulse avg.	n
(disp. tuning)				5 days	pulse avg.	y
slow feedback	IP	0.335 x,0.016 y	10 y	0.4 sec.	pulse avg.	n
fast feedback	IP		10 y	0.1μs	pulse avg.	n
BEAM SIZE						
carbon wire	TDS	20 x, 6 y	1 x, y, u	5 days	one bunch	y
laser wire	IP image	13 x,0.9 y	0.3 y	demand	bunch by b.	y
	IP$\pm$0.8m	0.335 x	0.3 x	5 days	pulse	y
Shintake mon.	IP$\pm$0.8m	0.016 y	0.01	5 days	average	y
BEAM ENERGY						
bpm	CS or CCS	180 x	3 x	0.4 sec.	bunch-by-b.	n
synch. light	extr. line			exp. demand	bunch-by-b.	n
ENERGY SPREAD						
wire	CS or CCS	40 x	5 x		one bunch	y
BUNCH LENGTH						
streak camera,	before	300 z	100 z	demand	one bunch	n
interferometer	linac			demand	or avg.	n
BUNCH CHARGE						
toroid/wall current	linac, BDS		1%	observe	bunch-by-b.	n

Table 4.8.1: *Overview of beam diagnostic requirements and tools. Additional instrumentation for luminosity and beam polarization measurement (not shown in the table) is foreseen in the IR.*

4.8.1.1 The Beam Position Monitor System

Introduction As described in section 4.3, measurement of the beam position with respect to the quadrupole plays an important role in the design of a linear collider. Single and multi bunch beam blow up generated by uncontrolled orbit distortions has to be minimized. To preserve the small emittance generated in the damping ring in the SBLC an accuracy of a few micrometer relative to the magnetic axis of the quadrupoles is necessary. At the same time any movement of the quadrupoles in the main linac of less than a few micrometer has to be controlled. For example the expected movements of the quadrupoles induced by temperature variations will be in the region of 10 - 20 μm per degree C°. The reach the equilibrium temperature in the linac tunnel will need a few days or weeks of continuous operation during which fast and accurate orbit correction is particularly important. Taking into account the different thermal time constants of the different components individual movements have to be expected.

Beam Properties and Design Criteria A number of design criteria are comparable with existing beam position measurement systems in the circular accelerators. Only a moderate dynamic range for the intensity is required and just a few millimeters of sensitive range where the specified accuracy has to be guaranteed are necessary (see table 4.8.2).

Particle per bunch	2×10^9 to 5×10^{10}
Number of bunches per burst	1 to 330 bunches
Bunch to bunch distance	6 nsec to single bunch
Burst length	2 μsec. max
Repetition rate	Single pulse to 50 Hz
Monitor resolution	$\pm 2\,\mu$m
Monitor alignment	$\pm 5\,\mu$m
Operation range	± 2 mm
Operation mode	single and multi bunch
Readout frequency	up to 50 Hz

Table 4.8.2: *Design specifications for the beam position monitor system for the SBLC*

The Type of Pick Up and the Signal Processing The pick-ups of existing beam position monitor systems can basically be divided into three different types: buttons, loops and cavities.

A button monitor is a pick-up which is usually (in storage rings) smaller than or comparable to compared to the bunch length, just a few mm diameter circular plate, embedded inside the vacuum chamber. This pick-up couples primarily capacitive to the beam and transmits the signal via one RF feed-through to the outside electronics. Combinations of two or more pick up signals result in a beam position measurement.

One of the first designs was made for PETRA, a 2.2 km long e^+e^- storage ring at DESY, in 1976 [4]. Most of the circular lepton accelerators with a short bunch length like PEP, TRISTAN, LEP, DORIS, ESRF and HERA-e ring etc. make use of the advantages of this kind of pick up, such as the simple mechanics and the high electronic stability.

Loops are pick ups which have different dimension in the longitudinal and transverse direction with respect to the beam, e.g. like a wire with two feed-throughs at the ends. A loop couples primarily inductive to the beam. If the impedance is matched to both ends we call this monitor a strip line or a directional coupler. Two operation modes are given depending on the length of the antenna. First, the antenna is long and second, the antenna is short relative to the bunch length in the beam. Due to the longitudinal dimension of the loops the coupling factor for longer bunches is higher in comparison to buttons. Therefore the loops are mostly under operation in proton machines like, for example, in the HERA P-ring. At the FFTB [1] loops are also in use for a high resolution beam position monitor.

More recently, a number of proposals and also first results using cavities as high resolution beam position monitors, have been presented [5]. The beam passes through a cavity with a dipole mode frequency of several GHz. Two pick-ups are located on opposite sites of the cavity. The beam position is detected using the difference signal of the two pick ups. One of the advantages of a cavity based monitor is the intrinsic frequency filter, and if used in a resonant mode, excited in resonance by a multi-bunch train, the amplified signal produced by the beam.

Processing the signals, the beam position detected with two opposite antennas to first order is simply given by:

$$X = C \cdot \frac{(\mathrm{P}_1 - \mathrm{P}_2)}{(\mathrm{P}_1 + \mathrm{P}_2)}$$

C is the so called monitor constant which is a geometric factor. This factor is usually related to the vacuum chamber cross section.

With the diameter of the SBLC vacuum chamber of ≈ 25 mm, C will be of the order of 10 to 15 mm for loop or button monitors. Therefore the stability of the pick up and the resolution of the signal processing has to be 10^{-4} to fulfill the required accuracy in beam position measurement of $\pm 2\,\mu$m .

The SBLC bunch timing from single bunch up to 330 bunches in one burst of two microseconds length is one of the critical issues in designing the pick up and the signal processing. Two principle schemes, either narrow or wide band signal processing are typically used in today's operating accelerators.

A narrow band layout with state-of-the-art filters, amplifiers, mixers or analog combiners delivers directly the difference and sum information of two pick up signals as described in the above formula. Schematically this is shown in the upper part of Figure 4.8.1. The resolution and the accuracy is limited by the non-linearities of the components, the signal-to-noise ratio and a number of other smaller errors.

For single bunch detection a broadband signal processing has some advantages like the higher power of the signals or the redundant information, because each individual pick up signal can be digitized independently. But the resolution and accuracy is

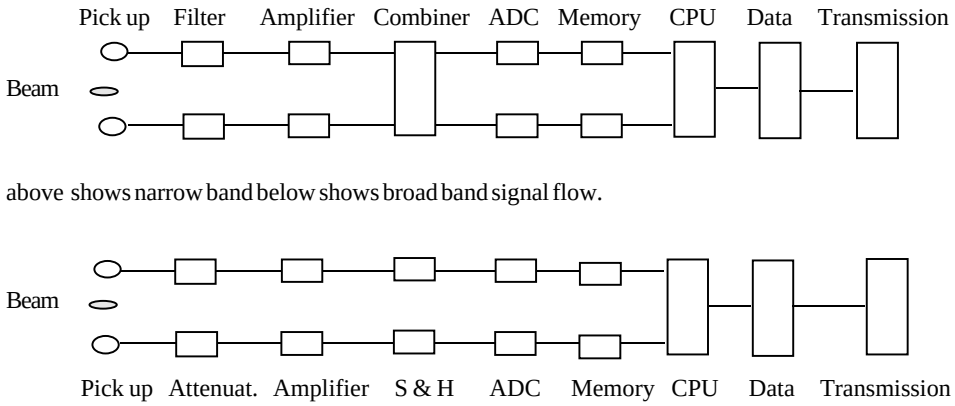

Figure 4.8.1: *Sketch of the two principal transmission schemes for either narrow band (upper part) or broadband (lower part) signal processing of BPM signals.*

limited by properties of the ADC (see lower part of Fig. 4.8.1). A Strip Line Monitor is designed and under operation at the S-Band Test Facility [6] and a sketch is presented in Fig. 4.8.2. Mechanical pre-alignment in principal is possible and has been done for these bpm's down to approximately 20 μm [8].

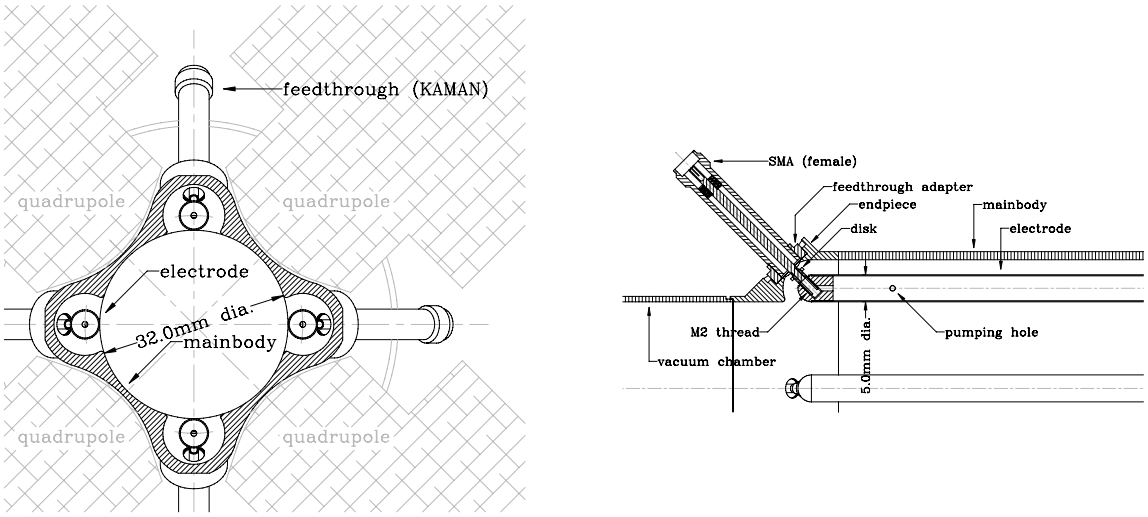

Figure 4.8.2: *SBLC stripline beam position pickup (cross- and longitudinal-section)*

With today's technology for high frequency electronic components both concepts, the narrow and the broad band signal processing, will fulfill the requirements of the S-Band Linac beam position monitor system. The choice for buttons or loops instead of cavities seems natural due to the wide operation range from single- bunch to multi-bunch with a bunch spacing of 6 ns and 330 bunches per burst.

Calibration The most important information to be extracted from the beam monitor system is the beam position relative to the magnetic quadrupole axis in the horizontal and vertical plane. With the necessary accuracy of less than $\pm 5\mu$m relative to the quadrupole axis a calibration of the monitors without the beam is extremely complicated, expensive, ineffective and not advisable.

The alternative, in-situ calibration of each beam position monitor to its associated quadrupole with the beam, offers all advantages we need. It is a well known procedure to change the current of a quadrupole and measure the change of the beam position with all the monitors downstream in the linac. This procedure is simple, repeatable at any time and can be done in a fast, proper and fully automated way.

With the use of the so called Beam Based Alignment - shown for example at SLAC with the FFTB [1] and at DESY with the HERA e-ring [7] - any other monitor calibration is not necessary. The accuracy is much higher as compared to standard alignment techniques, because the number of involved monitors is large and limited only by the resolution of the monitor being investigated without any other significant error contributing.

Controls With the foreseen orbit read out frequency up to 50 Hz this procedure can be fast compared to any thermal or diffusive ground motion time constant. Assuming, for example, 5 seconds for a one monitor calibration, with approximately 600 monitors in each linac in total only one hour will be required. Once the accelerator is set-up this procedure can be performed in parallel at different sections.

Each beam position monitor will be equipped with a local memory management where all pick up information can be stored in parallel. With the worst case of four pick up signals from each bunch in one burst of 330 bunches we get 4 * 330 Words (of two bytes each) per pulse. A local micro computer at each monitor will calculate from this the 330 horizontal and vertical positions in a few milliseconds.

The distributed beam position control system transmits the beam position averaged over one burst to the machine control system within the 20 msec given by the linac repetition rate.

Summary The typical demands from the SBLC beam position system are challenging but feasible with todays available electronics and control. With the expectable improvements of the industrial standard analog and digital electronics in the future the more extended features seem to be possible in a few years.

Finally with today's data transmission technology in controls - used for example at the new PETRA Control System - the entire orbit information from both linacs is transmittable at real time (50 Hz repetition rate) to the central machine control system.

From this point of view the beam operation should be possible on a controlled pulse-to-pulse basis with an accuracy of less than $\pm 5\,\mu$m for each beam position value along the 30 kilometer long accelerator.

4.8.1.2 Bunch Length Measurement

The rms bunch length for the SBLC design is 300 μm (1 ps). For the FEL operation, the rms bunch length is 0.025 mm (80 fs) (see chapter 5).

For bunch length measurements in this regime, different kinds of radiation emitted by the particle beam can be used. This can be transition radiation, synchrotron radiation or Čerenkov radiation. Transition radiation has the advantage that it can easily be produced by moving a thin metal target into the beam. However, at high current the target can be destroyed. This can be avoided either by doing measurements at low current only or by using diffraction radiation [9]. Alternatively, synchrotron radiation produced non-destructively by magnetic elements can be used [10].

Short radiation pulses can be measured in the time domain using streak cameras. A streak camera consists of a photocathode which converts light pulses into electron pulses. These are then deflected and displayed longitudinally on a phosphor screen (Fig. 4.8.3). These systems offer the unique possibility of single bunch observation in real time. The time resolution, widely assumed to be limited to 1 ps and longer, has been improved significantly by the manufacturers. Fast streak cameras are now commercially available with a resolution of down to 180 fs. This might be even improved in the future.

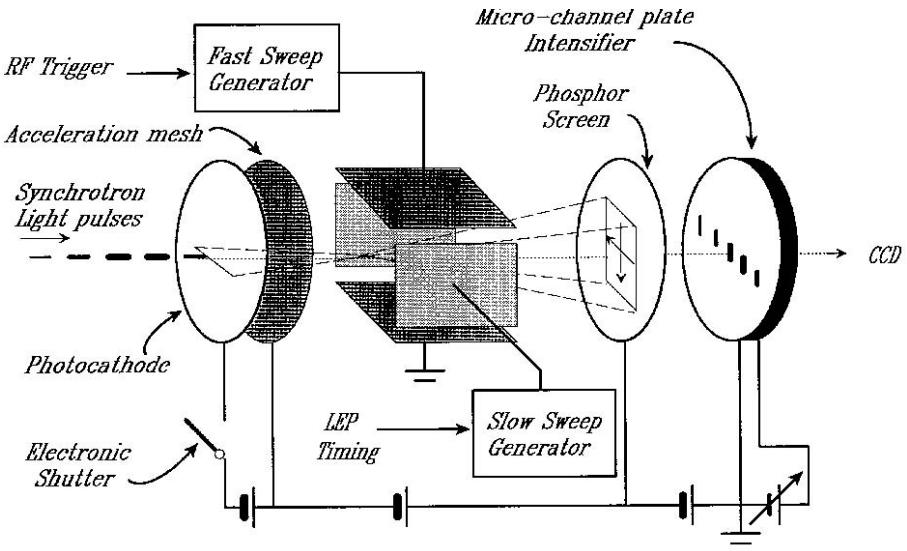

Figure 4.8.3: *Streak camera for measurements in the time domain as used at LEP.*

Alternatively, measurements in the frequency domain can yield information about the bunch length. This method works better the shorter the bunch length is. At wavelengths of the order of the bunch length and longer, coherent transition or synchrotron radiation is produced as the bunch acts as one single particle. The coherent part of the spectrum is much more intense than the incoherent part. It can be shown that the coherent radiation spectrum is just the Fourier transform of the longitudinal charge

distribution. Hence, measuring this part of the spectrum means measuring the bunch length.

From picosecond bunches, coherent radiation is produced in the millimeter wavelength range. For the observation of mm wavelength radiation, a photo-acoustic detector can be used. It works at room temperature and has a flat response from 0.1 mm wavelength up to 1 cm. For shorter bunch lengths, the onset of the coherence effect shifts to the far infrared where pyroelectric and bolometric detectors are available at low cost.

Two different types of spectrometers have been developed for use at the TESLA Test Facility and as prototypes for the linear collider. A series of high pass filters for mm waves serves, together with the broadband detector, as a simple spectrometer. This spectrometer has been successfully used for bunch length measurements at the CLIC test facility [11].

A polarizing Michelson interferometer (Martin-Puplett interferometer) can measure the autocorrelation function of the radiation pulses. The power spectrum can then be obtained as the Fourier transform of the autocorrelation function. The interferometer uses wire grids as beam splitter and roof mirror reflectors (Fig. 4.8.4). It has an intrinsic flat characteristic over the whole wavelength range of interest.

As a third option, the use of a new spectrometer based on superconductivity is being examined. A setup developed at the Forschungszentrum Jülich is being evaluated with respect to its possible application for bunch length measurements [12].

4.8.2 Beam Size Monitoring

An important class of diagnostics are the transverse beam size monitors which are required primarilly for the measurement of the beam emittance. Two modes of operation are expected:

1. problem diagnosis, commissioning and boot-strapping, i.e. non-luminosity operation possibly with single bunch per pulse, and

2. continuous or semi-continuous monitoring of the beam during nominal luminosity operation.

For the former case, either Optical Transition Radiation (OTR) screens or SLC-type wire scanners[13] using 4 μm or 7 μm carbon filaments are expected to be the standard diagnostic.

Carbon filament wire scanners are used to sample the beam at different positions within the beam profile, and the beam width is then determined by fitting a Gaussian distribution to the data. The technique requires several bunches to perform a single measurement, so the result is an effective beam size of all bunches measured including any position jitter between them. However, the jitter can be measured by high-precision ($\approx 1\mu$m) BPM's so that this contribution to the effective beam size can be unfolded. Two types of signal can be used: i) bremsstrahlung from the wire can be detected some distance directly downstream, or ii) secondarys which are eventually scattered out of

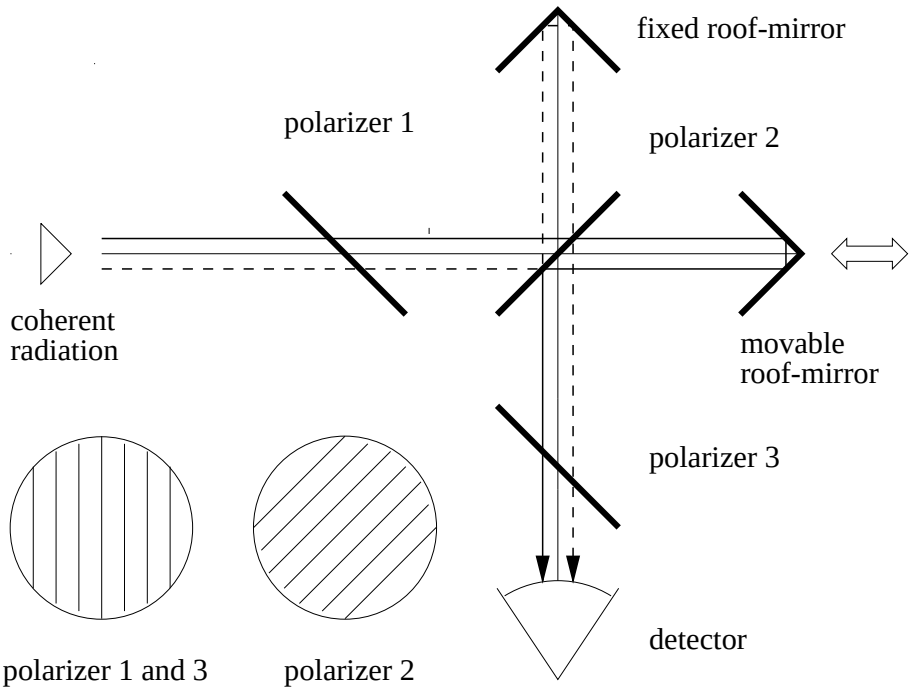

Figure 4.8.4: *Martin-Puplett interferometer for measurements in the frequency domain as to be used at TTFL.*

the beam pipe can be detected. The former requires a downstream dipole in order to position the bremstrahlung deletector on the downstream (photon) axis: such an approach is most applicable in the beam delivery system where bends occur naturally. In the linac and other straight sections, one must rely on the secondaries scattered out of the beampipe for detection. The wire scanners themselves are small compact devices which can easily be incorporated into the machine with the mimimum of impact to the lattice.

At the full SBLC bunch population of 1.1×10^{10}, the charge density of a single bunch should be sufficiently low that a 4 μm Carbon wire should survive single bunch operation at the nominal repetition rate of 5Hz. The temperature rise in the wire caused by a single bunch (with charge N_e) passage can be estimated from the energy loss $\mathrm{dE/dx} = 4\,\mathrm{MeV/cm}$, the heat capacity $c_p = 1.18\,\mathrm{J/(g\,K)}$ and the specific density $\rho = 2\mathrm{g/cm}^3$ of Carbon:

$$\Delta T \approx 0.44 \cdot 10^{-3}\mathrm{K} \times \frac{N_e[10^{10}]}{\sigma_x \sigma_y[\mathrm{cm}^2]} \tag{4.8.1}$$

In the TDS we have $\sigma_x\sigma_y \approx 120\,\mu\mathrm{m}^2$ and for $N_e = 1.1 \cdot 10^{10}$ we get $\Delta T = 400\,\mathrm{K}$, which seems tolerable. However, the wire will only survive a few bunches of the nominal bunch train in multi-bunch mode, and so Carbon wire devices cannot be used for monitoring

the beam size during luminosity production. Even in single-bunch operation, it is still possible that the wires will fail, and so it is prudent to have each scanner equipped with 5 to 10 separate wires.

The resolution of a beam size measurement with a wire is expected to be better than the wire diameter. The sytematic error for a 4μm wire and 6μm beam size is about 5%.

The OTR device In the measurement of transverse beam charge distribution, OTR present a number of advantages: it is fully linear with the beam charge, without any saturation effect, it is emitted by a surface crossing and thus does not show any depth effect. Its temporal emission in the subpicosecond range allows the selection of a single bunch. The main practical limits to OTR use at high energies, when the low emittance allows small beam dimensions, are the diffraction limit that, due to the angular distribution and the polarization properties, is larger than for standard point optical sources and for 500 nm wavelength is roughly $10\,\mu$m, and the fact that it is derived by an intercepting device, so that the screen can be destroied by the high energy density lost in the material by well collimated beams. For an aluminum foil, which is the preferred material for its high and uniform reflectivity over the whole optical spectrum, the temperature rise caused by a microbunch of $1.1{\cdot}10^{10}$ electrons is $.07\,^{\circ}\mathrm{C}/R^2$ in which R is the radius (in mm) of a flat circular beam distribution, and assuming a rather conservative value of $2\,\mathrm{MeV/cm}^2$ as the single particle energy deposition (energy independent). Limiting the temperature rise to 300 °C, we obtain a minimum beam radius of $6\,\mu$m (that corresponds to a rms value of about $3\,\mu$m). It will be important to study different materials to find the best compromise between emission efficency and thermal and mechanical properties.

For multi-bunch operation, there are three possibilities:

1. laser wire scanner
2. pulse snatching scheme (off-axis monitoring).
3. gradient undulator

In principle a laser wire acts in the same manner as a Carbon-wire scanner. A laser wire can be focused to a sub-micron spot, which is then scanned through the beam. The situation is also similar to the Carbon-wire approach with respect to signal detection: either the Compton scattered photons are detected directly downstream (again requiring a downstream dipole), or the back-scattered electrons (which are eventually sweeped out of the machine) are used. For SBLC, it is feasible that a long pulse-train laser can be used to sweep through the entire bunch train in a single shot, thus allowing a fast effective beam size measurement of a single bunch train. Such an approach is necessary for the laser monitors close to the interaction point, where it is neccessary to mitigate the effects of the final doublet vibratration on the (particle) beam. In a short-pulse mode, the laser wire can be used to sample single bunches in the bunch train, sampling on successive trains the same bunch location. This mode of operation is

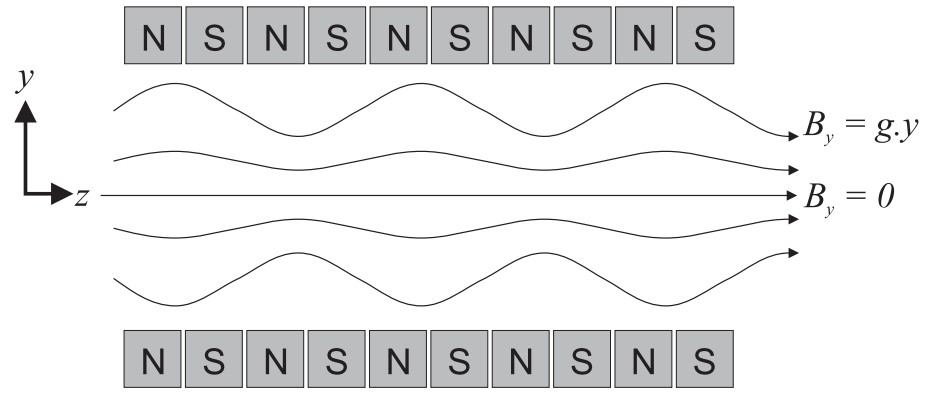

Figure 4.8.5: *Principle of the X-ray Gradient Undulator. The vertical undulator field is proportional to the vertical offset (y), being zero on the nominal axis (y = 0). Thus particles on-axis do no radiated, while particles off-axis do. The total power radiated by a centered beam is therefore proportional to* σ_y^2 *[14].*

directly analagous to the single-pulse Carbon-wire operation. As of writing, laser-wire technology is still in its infancy, although such a device now exists and operates at the SLC [3]. However, much work still remains to be done (especially for the back-scattered electron mode). It is advantageous (and prudent) to always place a carbon-wire device and a laser-wire device together, so that one can be used to calibrate and troubleshoot the other.

A more conservative approach (but slightly more invasive) is to use fast kickers to "steel" a single bunch from a bunch train and send it to an off-axis scanner. Here again Carbon-wire devices can be used (as well as any other fluorescent or OTR screen technique). The approach probably requires more tunnel space than the laser-wire option.

Of the three methods proposed, only the X-ray gradient undulator[14] offers a single-shot single bunch measurement of the beamsize. A gradient undulator is an undulator whose pole-pieces are displaced one-half period as shown in figure 4.8.5. The undulator field has now a linear gradient in the vertical direction. As a result, vertically off-axis particles radiate, while particles on-axis do not. The total power output from the undulator is directly proportional to the square of the beam height. Theoretical studies have shown that at the exit of the linac (250 GeV) in excess of 10^5 60 MeV photons can be expected for a 1 m device with a 1 cm undulator period, and a field gradient of 4.8 T/cm. The main disadvantage of the device is that it requires a dipole downstream in order to place the X-ray detector on the axis of the undulator (again making the device more suitable for the beam delivery section). If the device is to be used in the linac, then small chicanes will be required, and a length penalty will be incurred. It should be noted, however, that the gradient undulator is a conceptual device, and work is currently in progress to evaluate its performance and limitations.

4.8.3 The Interaction Region Feedback

Fast ground motion will cause independent orbit movements in the two linacs of a linear collider such, that the beams may miss each other at the interaction point (IP). But even at rather large vertical beam-beam separations at the IP, beams will deflect each other through their electro-magnetic fields. By measuring the position of a beam, which has just passed the IP and compare in it the position of a first pilot bunch -which does not have a partner in the opposing beam- with that of the following bunches in the same bunch train, the opposing beam can be steered with ultra fast kicker magnets for optimum collision at the IP. A feed-back system based on this principle will make the necessary steering corrections within a time short compared to the duration of the bunch train.

Fast beam steering at the interaction point, which relies on the beam-beam effect of colliding bunches, is a powerful tool to relax nanometer tolerances for final focus quadrupoles in linear colliders. Even betatron amplitude growth excited by vibrating quadrupoles further upstream in the linac, which is not filamented by the time the beam reaches the IP, can be corrected with fast beam steering. From Tracking calculations we expect only 30% filamentation over the entire length of the linac 4.3. One stringent requirement for a feedback, which corrects the bunch train offset in the IP is, that the beam pulse is long compared to the overall processing time of the detected signal from the beam position measurement (BPM) to the kicker magnet. Parameters which influence this delay are the distance of the beam position monitor to the IP, the processing time of the feedback loop and the required magnetic field strength compared to the available peak power of the amplifier (see Figure 4.8.6). The amplitude of pulse to pulse ground motion which can be expected from measurements done in the HERA tunnel, which is a tunnel under the city of Hamburg with an colliding beam facility [15, 16] is approximately 70 nm rms for Frequencies below 1 Hz which is roughly six times the design vertical beam size. In order to limit the Luminosity reduction to 5%, the jitter at the IP should be smaller than 30% of the beam size, which is 5 nm in our case. A list of the main interaction region parameters is extracted from the complete list and given in Table 4.8.3. One possibility to achieve this tolerance is to design a passive support system that keeps the final doublets at a given position over a time scale much larger than the repetition rate of the accelerator. This is certainly a challenging task for the technical design of the quadrupole supports which are part of the experiment of a linear collider. Vibrations from the linac quadrupoles are not correctable by this method with reasonable effort. For the S-Band Linear Collider study two feedback loops are foreseen to relax this tolerance well beyond the measured value of 100 nm which was mentioned before. One loop relies on a direct measurement of the quadrupole vibration in combination with a mechanical (or correction magnet) feedback. Such a loop has been tested already and a suppression of a factor of 4 in amplitude for the rms value at 2 Hz has been proven which is described in more detail in section 4.8.4. This feedback loops have mainly been developed to correct the linac quadrupole vibration.The second loop will be described in more detail in the following text.

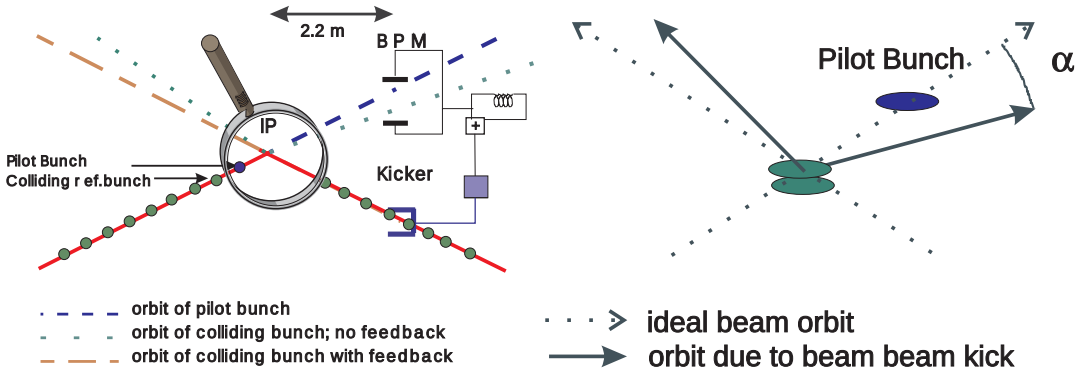

Figure 4.8.6: *Sketch of the interaction region layout and the location of the beam position monitor and the kicker magnet. The pilot bunch is the first electron bunch in the train with no interacting counter part.*

Ne per bunch		$1.1{*}10^{10}$
vert. beam size (no pinch)	nm	15
horiz. beam size (no pinch)	nm	335
Disruption (vertical)		7.1
Disruption (horizontal)		0.32
β_y at IP	mm	0.45
β_x at IP	mm	11.0
bunch length	mm	0.3
crossing angle	mrad	6
bunch train length	msec	2
bunch to bunch distance	nsec	6
distance: BPM to IP	m	≈ 2

Table 4.8.3: *Interaction region parameters for the 500 GeV S-band Linear Collider Study*

For a round beam the beam-beam force of two colliding bunches is proportional to the separation of the two bunches over approximately one σ. Operating with an aspect ratio($=\sigma_x/\sigma_y$) of 20 (or more), as it is foreseen in Linear Colliders to reduce the beamstrahlung, produces an almost linear beam - beam force over approximately $10\,\sigma_y$. According to the beam-beam simulations using the parameters from 4.8.3, the kick angle a per σ_y separation of the two colliding beams is given to within a good approximation by:

$$\alpha(\text{mrad}) = \frac{\Delta y}{\sigma_y} \cdot 0.057 \cdot (\text{mrad}) \qquad (4.8.2)$$

Let us assume that the BPM next to the IP is located at the position of the first quadrupole of the final doublet, which is 2 meters away. At this position the beam offset in the monitor according to formulae above be 120μm per σ_y separation at the IP, which is easy to measure as compared to the four micrometer resolution being required

for the rest of the linac BPM's. A method based on beam-beam deflections to measure precisely the offset of the two colliding beams has been used for single bunch operation in the SLC from pulse to pulse already [17]. On the other hand, a bunch to bunch measurement of the beam position, as being proposed for the TESLA Linear Collider study for both outgoing beams within one pulse can not be used, because of the delay time for signal processing as compared to the overall pulse length and bunch to bunch distance (compare 4.8.3). Therefore a combination of both methods is proposed which uses a pilot bunch in one of the two colliding beam pulses and only a single BPM in combination with a single kicker magnet.

In general, using such a scheme has the significant advantage, that almost no mechanical disturbance with an amplitude larger than a nanometer (vibration, girder resonance etc) can separate the colliding beams on the time scale of one bunch train length ($2\,\mu$sec $\rightarrow$ 500 kHz), once they are colliding.

The location of the beam position monitor and the kicker has to be as close as possible to the IP in order to reduce the processing time of the feedback loop. Because the quadrupole next to the IP will have an integrated BPM the shortest distance is 2.2 meters from the IP. If the delays on cables, the response time of the feedback amplifier and the finite rise time of the kicker are added up, an overall delay of 50 nsec is expected. If we assume in addition that one bunch train will have a pilot bunch, the delay will increase to about 60 nsec. Therefore 3% of the $2\,\mu$sec long beam pulse will not be corrected and, if far enough separated between pulses, will not contribute to Luminosity. In case of SLED operation with a 500 nsec long beam pulse, as foreseen for the energy upgrade to 800 GeV, the potential loss will increase to 12%. A continuous measurement of the beam-beam separation during the pulse will be done to correct even displacements which change along the bunch train.

aperture radius	mm	10
effective length	mm	500
magnetic field (max. possib.)	Tm	1.1x10−4
power amplifier		
pulse duration	msec	2
bandwidth of amplifier	MHz	50
peak power /amplifier	kW	2.5
pulse current	A	±10
rise time	nsec	20
repetition rate	Hz	50

Table 4.8.4: *Design values for the feedback kicker and the broad band amplifier.*

In order to allow orbit corrections at the IP for a value of 150 nm, the required kick is only $0.07\,\mu$mrad, if a distance from the kicker to the IP as close as the BPM position is assumed. For the 250 GeV beam a magnetic field of 6×10^{-5} T is sufficient. The kicker will be a strip line type kicker fed by two broad band amplifiers which can

excite a maximum magnetic field of 1.1×10^{-4}. The parameters are given in 4.8.4. The power amplifiers deliver a peak power of 2.5 kW each and have a bandwidth of more than 50 MHz to power each strip.

The Beam Position Monitor In order to measure the beam position of the pilot bunch with respect to the colliding bunches an analog delay will be used to subtract the two signals from the pilot bunch and the first colliding bunch directly. In addition the bunch intensity must be determined as well because the beam-beam kick is proportional to the bunch charge in the opposite beam. The resolution of the beam position measurement is 5 μm [18] which is 4% of the effect of a one σ_y separation and the bunch intensity measurement should be of the same order.

4.8.4 Active stabilization of mechanical quadrupole vibrations

To compensate ground motion induced quadrupole jitter at frequencies beyond approximately 2 Hz, an active mechanical stabilization system has been developed [19]. It consists of an inexpensive geophone measuring the motion of each single quadrupole and a piezo actuator to compensate the detected magnet motion. For simplicity reasons as well as cost limitation, the mechanical design is based on a single piezoelectric actuator tilting the quadrupole around its transverse horizontal axis thus keeping its center at rest, as schematically shown in Fig. 4.8.7. The opposite end of the magnet

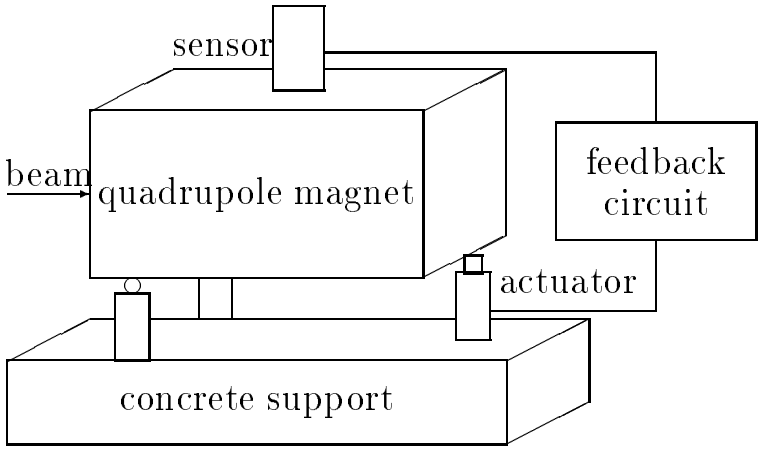

Figure 4.8.7: *Schematic view of the active stabilization system.*

is placed on two massive ball-ended feet to reduce dry friction. To fix the magnet's horizontal position, two horizontal "arms" with sufficient vertical compliance but high stiffness in the horizontal directions have been placed on one side of the quadrupole. The sensor is mounted on top of the magnet just above its center.
The internal noise of the geophones provided by KEBE [20] has been determined at 1.1 ± 0.3 nm in the frequency band beyond 2 Hz, which is well below the quadrupole jitter tolerance.
The whole system is placed on a very stiff concrete support with high internal damping

to avoid amplification of ground motion due to mechanical resonances. As experimentally confirmed, it has no mechanical eigenmodes in the frequency range up to 300 Hz. The triangular cross section ensures the transfer of horizontal ground motion without amplification.
The complete active quadrupole support is shown in Fig. 4.8.8.
For this first prototype of the active stabilization system, the feedback circuit has been

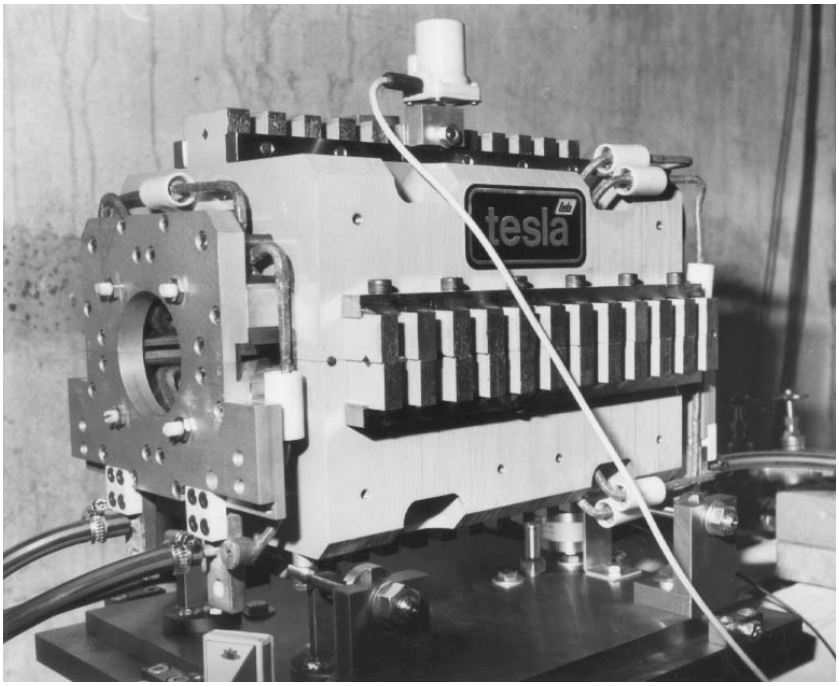

Figure 4.8.8: *Active stabilization system, consisting of a KEBE geophone on top of the magnet and a piezo actuator below it to tilt the quadrupole around its horizontal transverse axis. A match-box in the front indicates the size.*

realized on a PC with 16 bit A/D board. Compared to an analog system, this has several advantages. First of all, filters with extremely low time constants of many seconds can be realized, limited only by the numerical accuracy of the processor. Furthermore, the feedback algorithm can be easily changed, and even some built-in intelligence can be implemented.
The algorithm consists of a 100 sec highpass filter to cut offsets of the input signal, a 100 sec lowpass filter used as integrator to get the displacement from the velocity signal, and several digital filters, as schematically shown in fig. 4.8.9. An 8 Hz first order lowpass filter is used to suppress the 143 Hz resonance below 0 dB in order to achieve stability of the feedback system. To compensate the gain loss connected with this low cutoff frequency, a 7 Hz to 30 Hz first order bandpass filter is connected in parallel to the output of this lowpass filter, resulting in additional gain in this frequency band without any global but only some local phase shift. The gain factors G_1 and G_2 are

chosen as 2.9 and 1.5, respectively, which is close to the stability limit of the feedback system. Though this results in increased amplitudes at 0.8 Hz and between 30 and 70 Hz, this is experimentally confirmed to be the best compromise between a high attenuation factor in the frequency band from 2 Hz to 30 Hz and this amplification, resulting in the smallest rms value for frequencies higher than 2 Hz. Of course, this result depends on the ground motion spectrum and might therefore slightly change in the real linear collider environment.

As was observed during the tests, the feedback system tends to perform low frequency

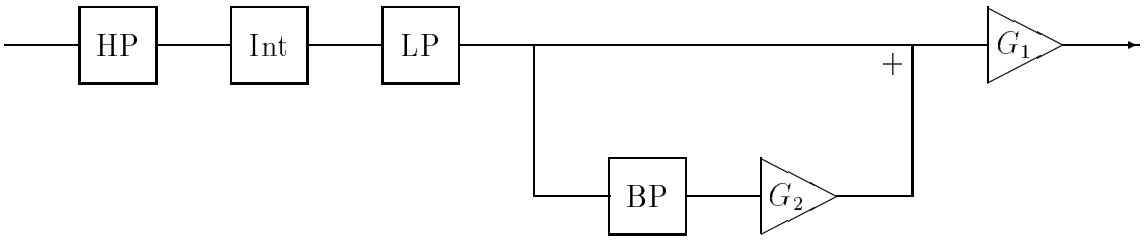

Figure 4.8.9: *Schematic view of the feedback algorithm, consisting of an integrator (Int) and several digital filters (lowpass LP, highpass HP, bandpass BP).*

oszillations over the total 16 bit range of the DAC after having accidentally reached its range limit due to some unusually high ground motion amplitudes. To stabilize the system again, it is necessary to decrease the gain. Therefore, the gain factor G_2 is reduced by 20 % each time the output value of the DAC reaches ± 15 bit and then increased again by an increment of $2 \cdot 10^{-4}$ in each cycle, resulting in a high reliability of the system even under extreme conditions.

The complete system has been set up in DESY hall 2, an experimental hall close to the DESY synchrotrons which has been chosen for the installation of the S-band test linac. Since there are two accelerators, several transformers and some other technical equipment operated nearby, it may be considered as an example of an operating Linear Collider environment. Therefore, the results obtained in this place should be comparable to those to be expected in the future accelerator.

To determine the performance of the system, a second KEBE sensor was placed on the floor just below the magnet. The signals of the feedback sensor as well as this second one were simultaneously sampled at 400 Hz to exclude artefacts in the results due to the statistical behaviour of ground motion. Sets of 1024 data points each were integrated to obtain the displacement from the velocity signal, multiplied by a Hanning window and Fourier-transformed in order to determine the power spectra Φ_{xx} and Φ_{yy} of the two signals. Here, the subscript x denotes the motion signal obtained on the ground, while y corresponds to the signal measured on top of the magnet. From these power spectra, the rms values σ_x and σ_y of the displacement in the frequency band f_0

to infinity can be calculated as

$$\sigma(f > f_0) = \sqrt{\int_{\omega_0=2\pi f_0}^{\infty} \Phi(\omega) d\omega}. \tag{4.8.3}$$

To ensure the reliability of this method, signals of both sensors were processed with the feedback system switched off. In this case, the transfer function is expected to be unity. Because the internal noise level of the two identical sensors is negligible compared to typical ground motion amplitudes, the correlation function γ can be estimated to be identically unity. With this assumption, the transfer function H reduces to

$$H(f) = \frac{Y(f)}{X(f)}, \tag{4.8.4}$$

and therefore, its modulus can be calculated from the square root of the ratio of both power spectra:

$$|H(f)| = \sqrt{\frac{\Phi_{yy}}{\Phi_{xx}}}. \tag{4.8.5}$$

The measured feedback gain calculated as the square root of the ratio of these two power spectra is shown in Fig. 4.8.10, together with the theoretically expected curve. As this figure shows, both curves are in nearly perfect agreement.

Fig. 4.8.11 presents the rms value σ of simultaneously measured ground and magnet

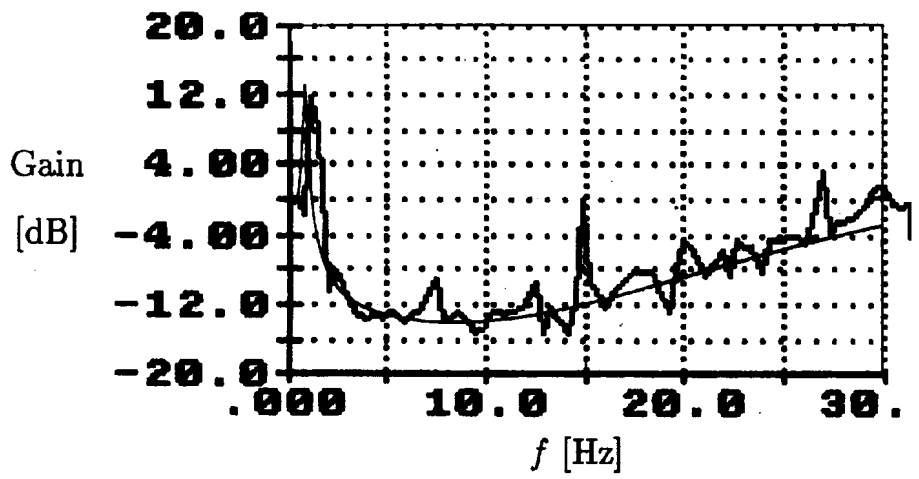

Figure 4.8.10: *Measured feedback gain (thick line) in the frequency band from 0 to* 30 *Hz, calculated from the square root of the ratio of the two power spectra simultaneously measured on the ground and on top of the magnet. The smooth thinner curve shows the theoretical transfer function.*

motion as a function of the lower cut-off frequency f_0, as has been calculated from the power spectra Φ_{xx} and Φ_{yy}. Although a vertical ground motion rms value of 100 nm at

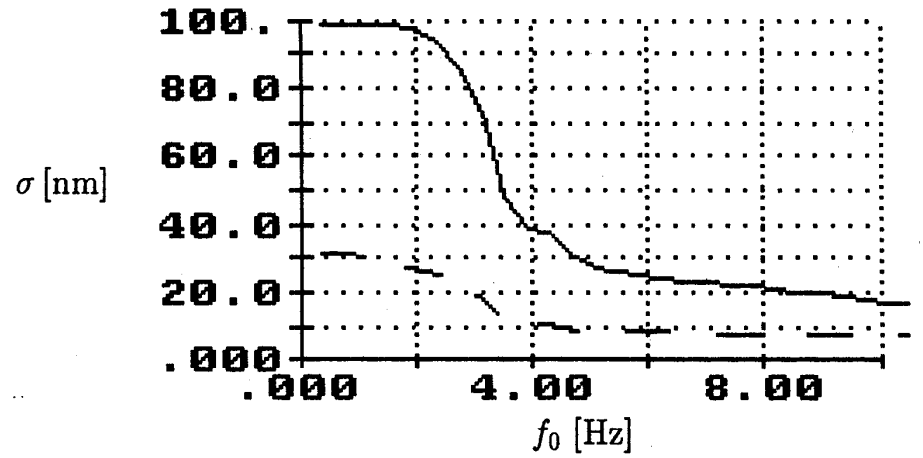

Figure 4.8.11: *rms value of ground (solid) and magnet motion (dashed) with the feedback system switched on in the frequency band f_0 to infinity as function of the lower frequency f_0, f_0 ranging from 0 to* 10 *Hz.*

$f_0 = 2\,\mathrm{Hz}$ is considered a noisy environment, the active stabilization system is capable to damp magnet motion to an rms value of about 26 nm in this frequency band. Taking into account the very low internal noise of the sensors, one can expect even lower values in less noisy environments. Therefore, this system might be even applicable in some parts of the final focus system where no klystrons and modulators operated at 50 Hz are present.

While the design water flow is 120 l/h, all data were taken at an increased flow of 220 l/h. It turned out that the influence of cooling water is almost negligible. The only difference in both power spectra is a small enhancement around 100 Hz which practically does not contribute to the magnet motion rms value.

To investigate the effect of ground motion on beam dynamics in the SBLC main linac, a simulation algorithm has been developed [21]. Adapting it to power spectra and coherence functions measured at DESY [22], the beam jitter at the end of the main linac was simulated. Here, a beam-based orbit correction system was assumed which applies a kicker signal measured at the nth bunch train to the $(n+1)$th bunch train in order to prevent slow beam motion.

Without active stabilization of mechanical quadrupole vibrations, the vertical rms beam jitter is about $\sigma_y = 1.3\,\mu\mathrm{m}$, while with active stabilization it is reduced to $0.45\,\mu\mathrm{m}$. Together with a vertical beam size being $\sigma_{\mathrm{beam}} = 9.1\,\mu\mathrm{m}$, the luminosity reduction due to beam jitter can be calculated as

$$\mathcal{L} = \mathcal{L}_0 \cdot \exp\left(-2\frac{\sigma_y^2}{4\sigma_{\mathrm{beam}}^2}\right). \tag{4.8.6}$$

Using equation (4.8.6), the obtained luminosity degradation is about 1 % without and 0.1 % with active stabilization of quadrupoles. Therefore, active stabilization of mechanical quadrupole vibrations might not be necessary in the SBLC main linac, but it may be considered as an option to increase the luminosity. Additionally, a similar system is planned to be used in the final focus system.

Bibliography

[1] T. Shintake, *Proposal of a Nanometer Beam Size Monitor for e+e- Colliders*, NIM A311, p. 453, 1992.

[2] T. Shintake et al., *First Beam Test of Nanometer Spot Size Monitor Using Laser Interferometry*, KEK-Preprint 94-129, Oct. 1994.

[3] M. Ross, *High Performance Spot Size Monitors*, LINAC96 Conf., Geneva Aug. 1996.

[4] F. Peters et al, *The PETRA control system*, IEEE Partic. accel. conf. 1977 Chicago.

[5] Results from the beam diagnostics working group, Linear Collider Workshop, LC'95, Tsukuba, Japan, 1995, KEK Proceeding 95-5, August 1995.

[6] W. Radloff, M. Wendt, *Beam Monitors for the S-Band Test Facility* DESY-M-95-08AG, Jun 1995. 3pp, presented at 16th IEEE Particle Accelerator Conference (PAC 95) and International Conference on High Energy Accelerators (IUPAP), Dallas, Texas, 1-5 May 1995.

[7] M. Boege, R. Brinkmann, *Optimization of Electron Spin Polarization by Application of a Beam Based Alignment Technique in the HERA Electron Ring* C95-11-14, 1996. Hamburg DESY - Int.Rep.MEA-95-02 (95/12,rec.Dec.) 1-8, In *Tsukuba 1995, Proceedings, Accelerator alignment* 412-420.

[8] F. Brinker et al. *Precision Alignment of BPM'swith Quadrupole Magnets*, DESY-M-96-24F, Dec.1996, 3pp.

[9] M. Castellano, private communication.

[10] C. Bovet, M. Placidi, *A dedicated synchrotron radiation source for LEP beam diagnostics*, CERN LEP note 532, 1985.

[11] K. Hanke, V. Schlott, K. Aulenbacher, H.H. Braun, F. Chautard, *Beam diagnostics using coherent transition radiation at the CLIC test facility*, CERN CLIC note 298, 1996.

[12] Y.Y. Divin, H. Schulz, U. Poppe, N. Klein, K. Urban, V.V. Pawlowskii, *Millimeter-wave Hilbert-transform spectroscopy with high-T_c Josephson junctions*, Appl.Phys.Lett. 68, p.11, 1996.

[13] M.C. Ross, E. Bong, L. Hendrickson, D. McCormick, M. Zolotorev, *Experience with Wire Scanners at SLC*, SLAC-PUB-6014, December 1992. Invited talk given at 1992 Accelerator Instrumentation Workshop, Berkeley, CA, Oct 27-30, 1992. Published in Berkeley Accel.Wkshp.1992:264-270 (QCD183:A22:1992)

[14] E. G. Bessonov, J. Pflüger, G.-A. Voss and N. J. Walker, *Beam Size Measurements in a Linear Collider using an X-ray Gradient Undulator*, DESY internal report DESY M 96-18, September 1996.

[15] V. Shiltsev, B. Baklakov, P. Lebedev (Novosibirsk, IYF), C. Montag, J. Rossbach (DESY), *Measurements Of Ground Vibrations And Orbit Motion At HERA*, DESY- HERA-95-06, Jun 1995, 64pp.

[16] R. Brinkmann, J. Rossbach (DESY), *Observation Of Closed Orbit Drift At Hera Covering Eight Decades Of Frequency*, DESY-HERA-94-04, Apr 1994. 10pp, published in Nucl.Instrum.Meth.A350:8-12,1994.

[17] P.Bambade, R.Erickson, *Beam-Beam Deflections as an Interaction Point Diagnostics for the SLC*, SLAC-PUB- 3979, May 1986.

[18] W. Radloff, M. Wendt (DESY), *Beam Monitors For The S Band Test Facility*, DESY-M-95-08AG, Jun 1995. 3pp. Presented at 16th IEEE Particle Accelerator Conference (PAC 95) and International Conference on High Energy Accelerators (IUPAP), Dallas, Texas, 1-5 May 1995.

[19] C. Montag, Active Stabilization of Mechanical Quadrupole Vibrations for Linear Colliders, Nucl. Instr. Meth. A 378 (1996), 369-375

[20] Dr. Kebe Scientific Instruments GmbH, Schwingungsmesser SMK-1, manual, Halstenbek 1994

[21] C. Montag, Active Stabilization of Mechanical Quadrupole Vibrations in a Linear Collider Test Facility, PhD thesis (in preparation)

[22] V. Shiltsev, B. Baklakov, P. Lebedev, C. Montag, J. Rossbach, Measurements of Ground Vibrations and Orbit Motion at HERA, DESY HERA 95-06

4.8 Survey and Alignment

4.8.1 Network on the Surface of the Earth

First, the coordinates of reference points along the linear collider have to be determined with respect to the existing coordinate system at the respective site (in case of DESY, this would be the HERA coordinate system). The reference points are the base to mark out the planned halls. The demanded global accuracy (standard deviation) of the reference points should be better than 5 mm over the whole area of the linear collider of about 30 km. Today the coordinates will be measured by the satellite system GPS (GPS = Global Position System). With points on the top of the halls the coordinates have to be transferred into the tunnel to control the tunnel boring machine and later on to mark out the supports of the components of the beam transport system. With a precision levelling a vertical network also has to be established.

4.8.2 Requirements for the Aligment of the Components

In the groundplan the tunnel axis is a straight line approximately. In the vertical plane the axis of the tunnel follows the earth curvature except for the first 6.5 km. Then the height of the tunnel in this area is constant everywhere. The heights are referenced to the geoid. Therefore it is possible that the earth radius for the tunnel axis is not constant. Depending on the gravity of earth small changes in the radius are possible.

In the tunnel there are 5 separate beam lines to be aligned. The components of each beam line have to be aligned with a high accuracy. The standard deviation of any point over a range of 400 m (this is the maximum betatron wave length) in the transverse direction should be better than 0.5 mm horizontally and 0.1 mm vertically.

Therefore it is too inefficient to align each beam line separately. It will be more efficient to have only one alignment (basic alignment). Then the components of each beam line have to be connected to the basic alignment.

4.8.3 Basic Alignment

The reference points for the basic alignment are fixed on the tunnel wall. They are only target points, not suitable to put geodetic instruments on. The distances between the points are between 25 m to 50 m. The geodetic instruments will be set on a moveable carriage (Fig. **??**). The carriage rolls on beams mounted on the tunnel wall above the causeway. The carriage can be fixed to the tunnel wall at any position with clamps.

The basic alignment can be carried out with Precision Total Stations (Tachymeters). A Tachymeter measures the horizontal angle, the vertical angle and the distance to the target point simultaneously. These measurements can be carried out either manually or automatically. The targets are Taylor–Hobson–Spheres for the manual and prisms in Taylor–Hobson–Spheres for the automatic methods. "Automatic" means that a computer controls the instrument, and the target recognition will be done automatically. The accuracy is for both instruments

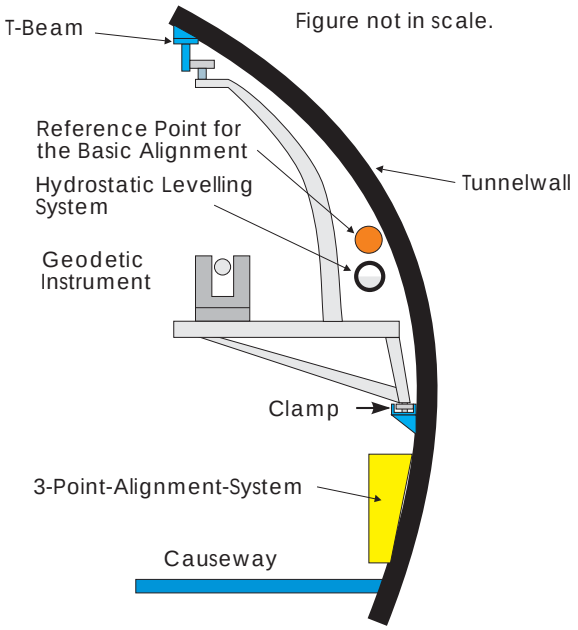

Figure 4.8.1: *Movable Carriage for the Geodetic Instruments and Locations of different Measuring Devices*

- horizontal direction 0.2 mgon (3 μrad),
- vertical angle 0.2 mgon (3 μrad) and
- distance 0.1 mm.

To coordinate the reference points on the tunnel wall the movable carriage with the Tachymeter can be set in front of each reference point. Now one can measure to several reference points, for example to two or three points back– and forward. How many points are to be measured is a question of the demanded accuracy. Fig. **??** shows the expected accuracy of a point in the middle of a 600 m long area in dependence on the number of measured target points and of the distances between the target points. The required accuracy can be achieved by using at least 3 reference points.

In the calculation only random errors are taken into account. What are the effects of systematic errors (for instance the refraction of air)?

4.8.4 Systematic Effects: Refraction of Air

Refraction of air means that if the density of the air is not constant then the line of sight to the target point is not a straight line exactly. The density depends mainly on the temperature of air. If there is a constant gradient in temperature for example of 0.1 degrees/m, a line of sight with a length of 600 m will follow a circular curve with an offset of 4.5 mm. These effects exceed the demanded accuracy by far and it is very difficult to determine their actual amounts. But there are some techniques available to reduce the effects of refraction of air:

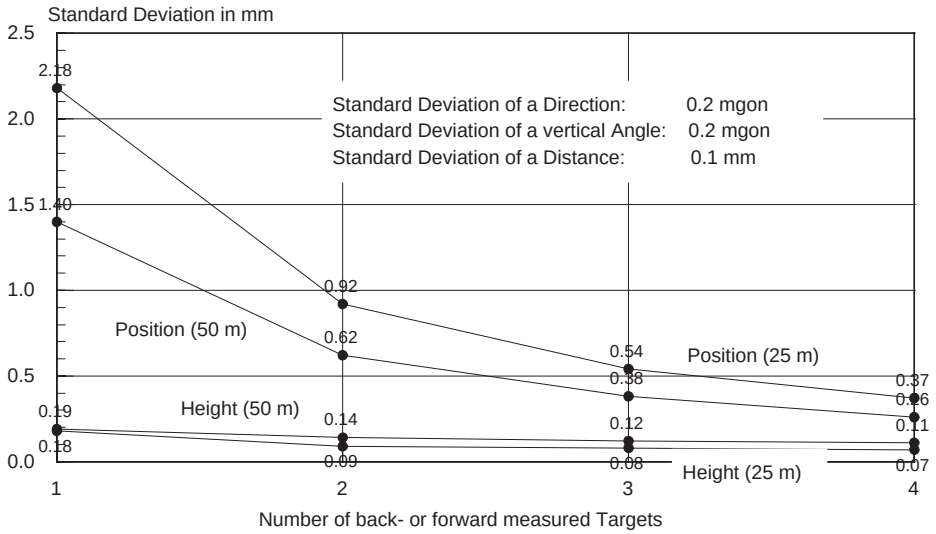

Figure 4.8.2: *Expected Accuracy in the Middle of a 600 m long section*

- hydrostatic levelling system for the vertical position,
- angle measurements without the effects of refraction (under development),
- Heelsche Alignment System (It does not work here, because the collider is not a straight line. In the vertical it follows the earth curvature.),
- stretched wires in an overlapping manner for the horizontal position,
- 3–point–alignment–technique for the horizontal position.

In the following the hydrostatic levelling system and the 3–point–alignment–technique will be described in detail.

4.8.5 Hydrostatic Levelling System

In the part of the tunnel which is horizontal, it is possible to install a pipe filled half with water. The pipe is mounted along the tunnel wall, so that the reference points are directly above the pipe (Fig. **??**). A movable device with a capacitive distance sensor can be set in the reference point to measure the height of the reference point in respect to the water level. The water level is horizontal but it is not a curve with a constant radius. The accuracy of the sensor is better than 5 μm und therefore it seems possible to measure the heights of the reference points over a length of about 600 m better than 0.1 mm. If the water level makes vibrations one can reduce this effekt by breakwaters which are mounted in the pipe.

4.8.6 3–Point–Alignment–System

A technique to reduce the effects of refraction of air will be given by the "3–point–technique". For example there are mounted reference plates on the tunnel wall in

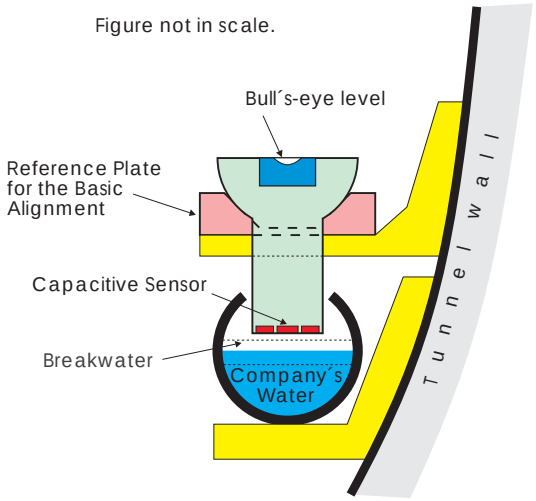

Figure 4.8.3: *Hydrostatic Levelling System*

regular distances (1 m oder 2 m). From a movable bar in each position the distances will be measured to the 3 opposite reference points (Fig. **??**) to better than 1 μm by capacitive sensors. The distances are very small, about 0.5 mm. The distances define the horizontal angle of the reference point in the middle to the both other neighbouring points. Therefore a traverse is measured and the displacements of each reference point in respect to a reference line can be calculated. The accuracy depends mainly on the stiffness of the bar. If the accuracy of the distance sensor is 0.1 μm, over an area

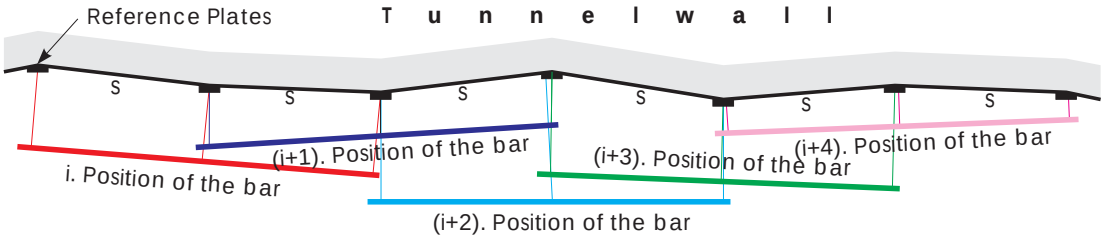

Figure 4.8.4: *Straightness measurements with the "3–Point–Technique"*

of 600 m the displacements of the straightness can be measured better than 0.5 mm (Fig. **??**). In this calculation the distances between the reference plates are 1 m and 2 m. Now it is possible to have bars with lenghts up to 10 m or 20 m. But in this case the bars are not stable enough by themselves. With a stretched wire and a differential diode mounted in the bar the stiffness of the bar can be controlled. A 26 m long test assembly with reference plates in 1 m distance has shown that the calculated accuracy will be achieved.

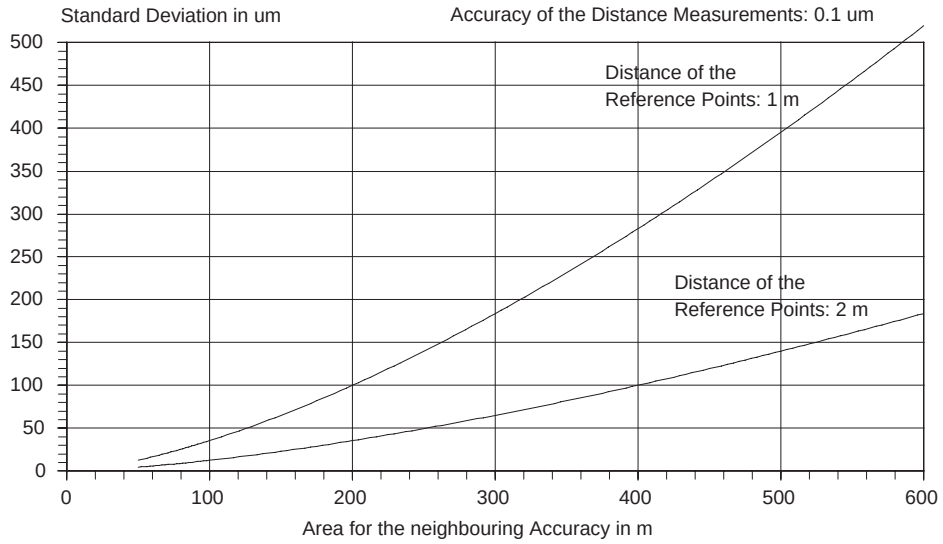

Figure 4.8.5: *Expected neighbouring accuracy for straightness measurements with the "3–Point–Technique"*

4.8.7 Transfering the Coordinates

After performing the measurements as discussed above, the coordinates of the reference points on the tunnel wall are available with the demanded accuracy. In the next step the coordinates of the reference points have to be transferred to the components of each beam line. For this each magnet should have two reference plates for targets and a support to measure the roll. The movable carriage is positioned at any place so that the neighbouring reference points and the points of the component which has to be aligned can be pointed out. The measurements to the reference points define the coordinates of the point on the movable carriage. Then the alignment of the component can start. For this one can use the following geodetic instruments

- Precision Total Stations (Tachymeters),
- Lasertracker and
- new instruments (under development).

The alignment will be carried out for each component individually. To control the adjustment it is advisable to make a control measurement in which the reference points and the magnet points are included simultaneously. To have a good redundancy each magnet point is measured twice from the neighbouring instrument station of the geodetic instrument.

4.9 Conventional Facilities and Site Considerations

4.9.1 Introduction

Different conventional facilities must be set up for the future Linear Collider. The detailed considerations in the following assume that the Linear Collider facility is built at DESY in Hamburg. Not all of them are valid at other locations without modifications. In any case coupling a new large accelerator complex to an existing laboratory site is advantageous from the point of view of investment cost, construction time and available know-how in accelerator technology, particle physics and synchrotron radiation research. Further boundary conditions we take into account here are the integration of the Free Electron Laser facility and the possibility to make use of existing accelerators and infrastructure at the DESY site.

These considerations lead us to a layout where the tunnel starts on the DESY site and runs northerly, along a straight section of HERA. By far the largest single construction is that of the tunnel for the accelerators, the beam line and for the various auxiliary components. This tunnel has a total length of approximately 33 km. The S-Band Linear Collider is housed in a double tunnel. The linear accelerator and beam lines are installed in a tunnel with an inner diameter of 2.5 m, while the service tunnel for the klystrons, modulators and auxiliary components has an inner diameter of 4 m. The accelerator tunnel is closed during beam operation but entry to the service tunnel is permitted so that repair and maintenance of components is possible during beam operation. An underground experimental hall for the Particle Physics detector is located in the center, surrounded by a tunnel for the damping rings. The central area layed out to also accomodate the X-ray Free Electron Laser laboratory. Administrative, social and technical buildings are placed on this common site, too. Additional underground halls and tunnels for the return arcs of the beam transfer lines are located at the two ends of the linac tunnel.

4.9.2 Overall Site Layout

The Linear Collider tunnel will be built underground at a depth of about 15 m. The main part of the tunnel is in sand and in ground water. With well-proven tunnel boring technology, buildings at the surface above the tunnel remain completely unaffected. As shown in the top view (see Fig. 4.10.1) the complete tunnel is straight (except for a short initial section, see below) and in a profile view (see Fig. 4.10.2) it is mainly horizontal (i.e. following the earth's curvature). HERA is rotated counterclockwise by an angle of 22.7^o out of the northerly orientation (approximately North-Northwest orientation). This orientation was chosen as the main direction of the Linear Collider. The beginning of the tunnel starts laterally shifted with respect to the HERA hall West and after 250 m bends with a radius of 500 m into the main direction. The main electron linac starts at the beginning of the straight tunnel. The initial section of the tunnel houses the pre-linac together with the beam preparation for the FEL operation. The injector linacs for the collider are located in the final focus section close to the

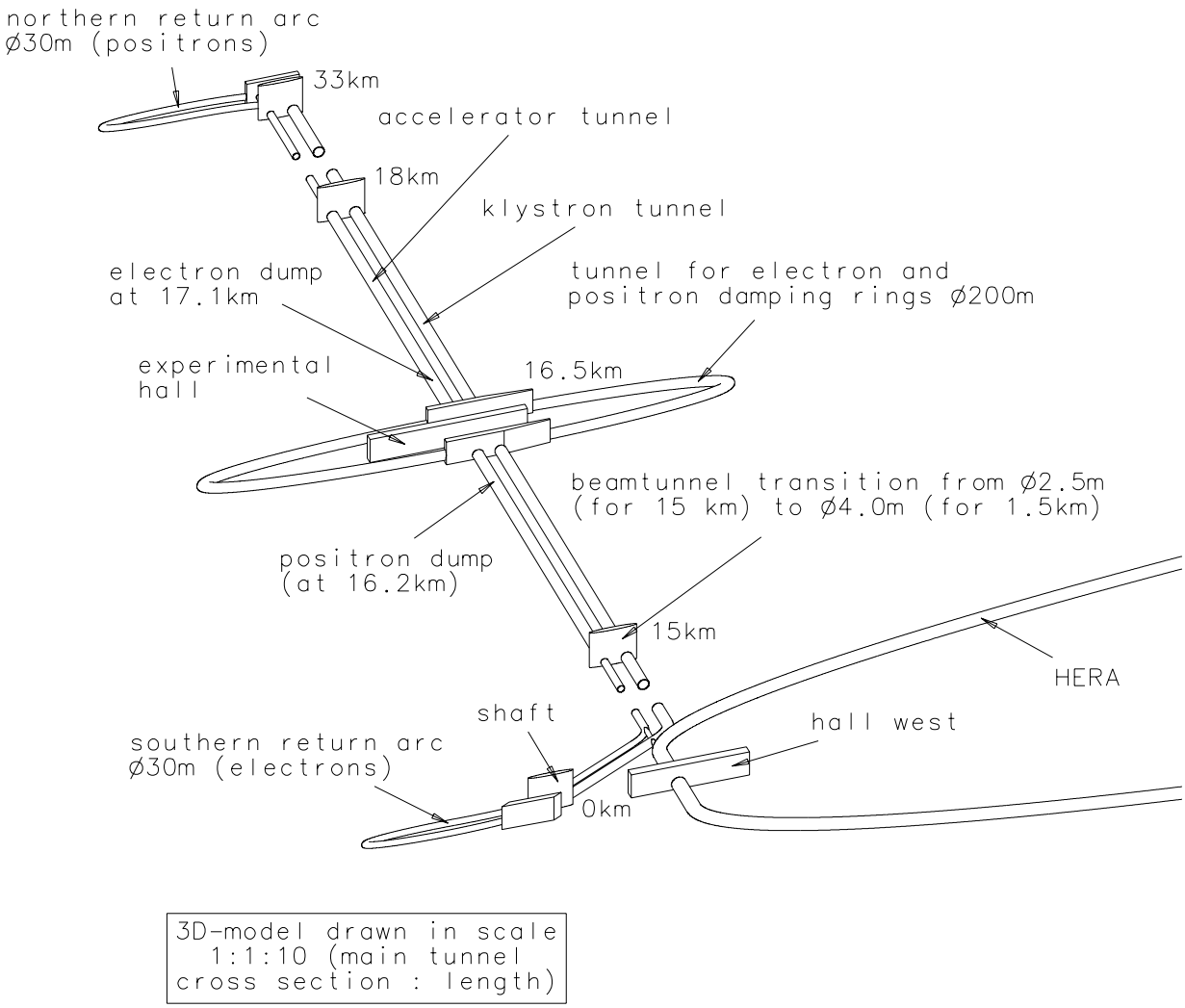

Figure 4.9.1: *Overall view of the S-Band Linear Collider at DESY.*

central area.

The interaction point HERA West is about 20 m above sea level. The axis of the main part of the linac tunnel lies about 10 m below sea level. The straight section HERA West has a slope of about 8 mrad out of the horizontal. Therefore there is a smooth transition from the initial slope into the horizontal direction with a bending radius of about 1000 km. Figure 4.10.2 shows an expanded profile of the linear collider area North-Northwest of DESY together with the collider tunnel. The depth of the tunnel below ground level of about 15 m is more than sufficient to guarantee shielding against radiation. The spacing between the linac tunnel and the service tunnel is 5 m (wall-to-wall). The tunnels are connected by 300 mm diameter pipes every 25 m. At 2 km intervals cross passages with a diameter of 2.5 m are foreseen. The tunnel is below

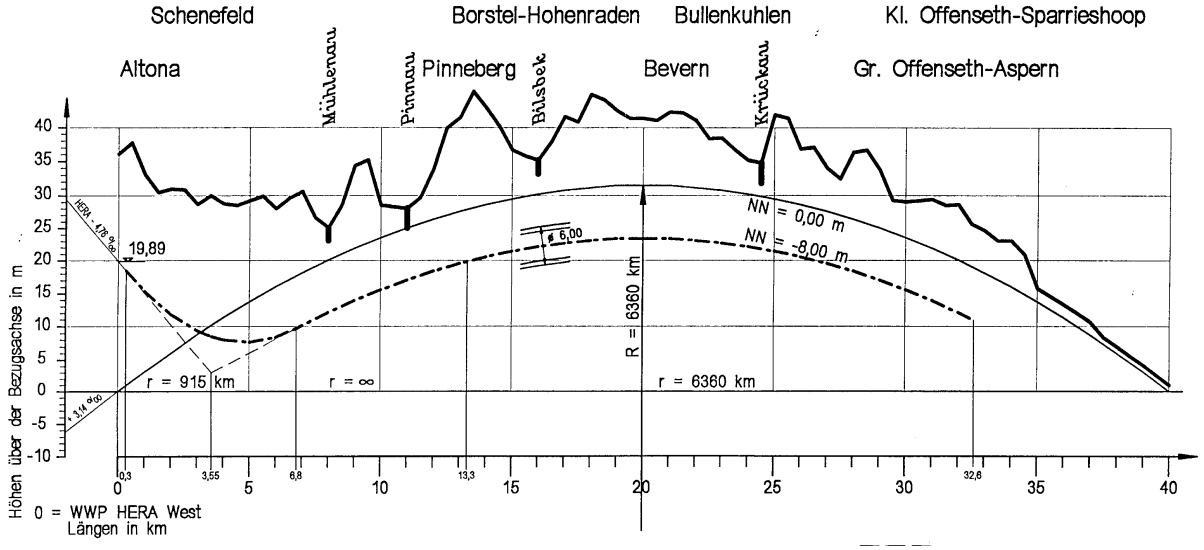

Figure 4.9.2: *Expanded profile of the Linear Collider area North-Northwest of DESY.*

the ground water level over nearly the entire length.

The service tunnel will be built by a tunnel boring machine similar to that used to construct the HERA tunnel. Identical concrete segments have been chosen for the lining of the auxiliary tunnel. The minimum inner diameter is 4 m, with the actual diameter increased to 4.2 m due to tolerances in the tunnel boring. A slightly different tunnel boring technology can be chosen for the accelerator tunnel, the return arcs and for the the damping ring tunnel. These tunnels will also be formed by a tunnel boring machine, but of a more simplified design. In this case complete concrete pipes are chosen for the lining of the accelerator tunnel. The tunnel boring machine and the complete piping will be moved by huge hydraulic cylinders. This tunnel boring technology is named "micro tunneling". An underground experimental hall is in the center of the Linear Collider complex, with additional underground halls at the two opposite ends. These three halls are built in open-cut excavations. The experimental hall and the end station are located on new areas. The start station together with the main return arc are located on the existing DESY area; no additional area is needed for the linac itself, though for the tunnel boring it could be an advantage to use intermediate temporary shafts. Two damping rings are used for the damping of the electron and positron beams before acceleration in the main linac. The damping rings are located in a common tunnel around the experimental hall. The diameter of the tunnel is 2.5 m and the arcs have a radius of 100 m. The total length reserved for the beam delivery system with the interaction point in the center is 3 km. In addition to the high energy beam lines the accelerator tunnel houses the positron source, the positron and electron pre-linacs and the beam extraction lines to the dumps. The inner diameter of the accelerator tunnel is extended in this region to 4 m, to accommodate all components.

4.9.3 DESY Site

The Linear Collider tunnel starts on the existing DESY area next to the HERA hall West. At the beginning there is an underground hall. The tunnel boring machines for the main tunnels and for the return arc start in this hall. The starting point for the main tunnel boring machines is laterally shifted from the HERA hall West. After a distance of about 250 m the machines bend with a radius of 500 m into the main direction. From that point the tunnel is straight in a top view up to the end station. The same point is the beginning of the main linac. The initial section houses the beam preparation for the FEL operation. The connection between the collider and the HERA tunnel can be made by a small tunnel.

4.9.4 Experimental Area

The experimental hall with the interaction point is located in the center of the Linear Collider, at a distance of 16.5 km from the interaction point HERA West. The underground hall has an area of 30 m $\times$ 82 m and a height of 20 m below the portal crane. Space for a second hall with the same dimensions and laterally shifted is available for a second detector. The X-ray Free Electron Laser Laboratory is located together on a common area with the administrative-, social- and technical buildings. The electron dump is located at a distance of 800 m from the interaction point; the positron dump at a distance of 300 m. Both dumps are downwards orientated with a minimum angle of 20 mrad. Small underground halls with access from the ground level are foreseen for the dumps. The total length of the final focus area is 3 km, the length of the new DESY site about 800 m. The positron dump is located outside below an external area.

4.9.5 End Station

The end station is a small underground hall. This hall is necessary as a starting point for the tunnel boring, for access to the tunnel during installation and operation and for one connection of the dog bone arc. An additional shaft is necessary for the other connection for the return arc.

4.9.6 Tunnel Layout

The main components installed in the collider tunnels are the S-band accelerating sections mounted on girders, the beam lines for the low emittance and low energy electron and positron beams and the beam lines for the FEL Laboratory and the ELFE@DESY (Nuclear Physics) operation. In addition there are numerous auxiliary components including klystrons and modulators. During beam operation access is necessary to these components. For example the klystrons and modulators have to be repaired quasi continuously due to the large number and their relatively short lifetime. Thus for the S-Band Linear Collider a double tunnel solution was chosen. A small tunnel with an inner diameter of 2.5 m houses the S-band linear accelerator and the beam lines. A

larger tunnel with an inner diameter of 4 m houses the auxiliary components. The tunnels are connected every 25 m by pipes of 300 mm inner diameter. In Figure 4.10.3 a tunnel cross section is shown, chosen at a position of the most complex situation. The cross section is vertically divided into two parts. One part is for the linear accelerator and the beam lines. The center of mass of an S-band section is just below the hook of the transport system. This allows an easier installation of most of the components. The transport system is a so-called monorail, utilizing an I-beam fixed at the top of the tunnel. The vehicle is used to transport equipment and persons. The other part is the main walk path, which is free at all times for emergency exit and for the lines-of-sight for optical survey. The auxiliary tunnel is divided horizontally and vertically into two parts. The lower part is reserved for cable connections and cooling pipes. The upper part is reserved for the horizontally oriented klystrons , modulators, electronics, power supplies and distribution, the transport system, similar to that in the other tunnel and for the emergency walk path. The two tunnels are connected by pipes housing the wave guides, which connect the klystrons and accelerating structures.

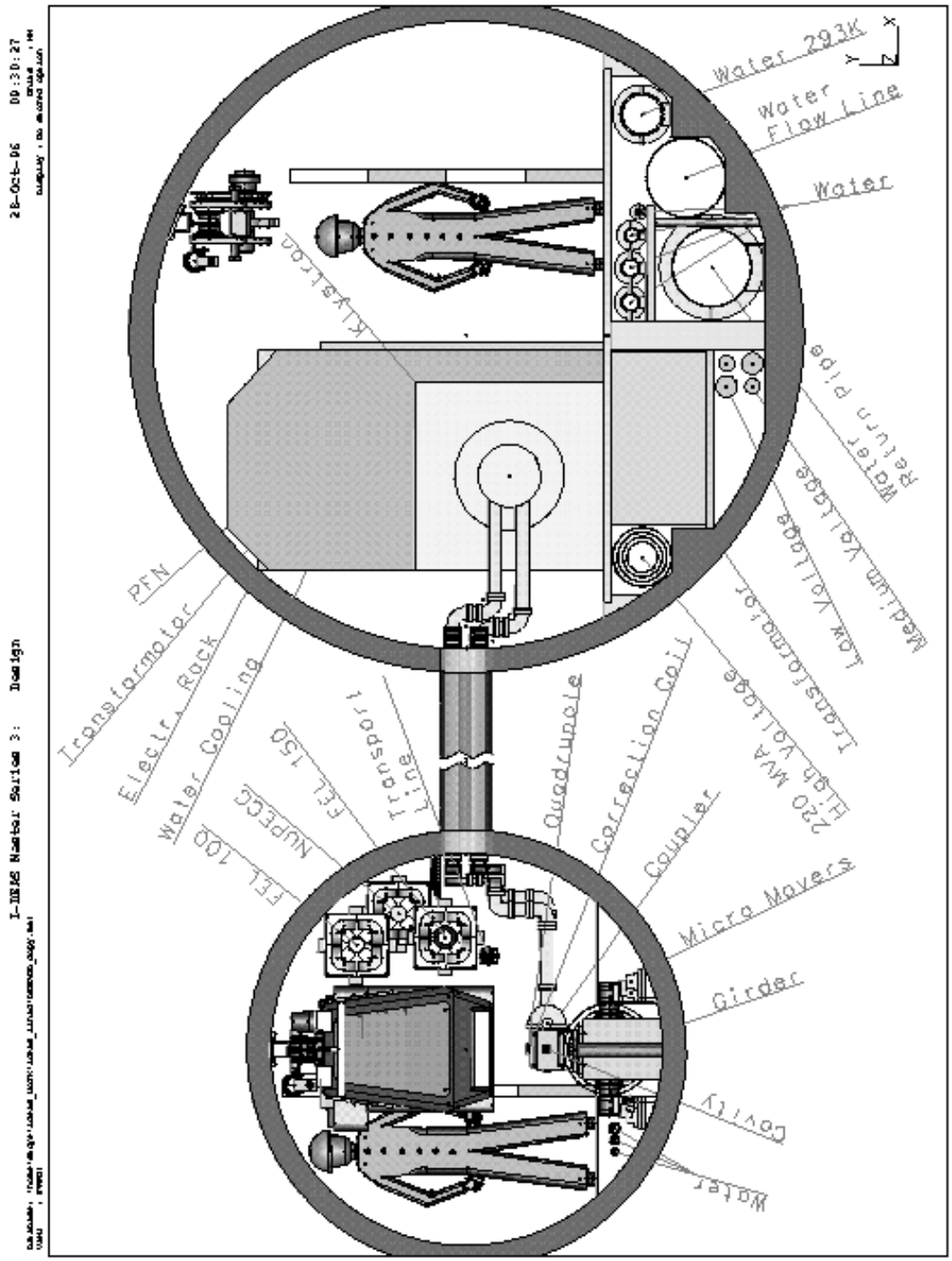

Figure 4.9.3: *Cross section of the S-Band Linear Collider tunnel.*

4.9.7 Power Distribution

The power distribution system is layed out for a total power of 225 MVA. This takes into account the reactive power, all subsystems and a safety margin for the linac power consumption (note that the nominal operating power is 140 MW). Three high voltage lines (110 kV) are foreseen at the two end stations and at the central area. After transformation to 36 kV, the power is distributed through the service tunnel (containing the klystrons and modulators) by 4 lines using 240 mm^2 Cu-cables. Each of these medium-high voltage networks supplies about 7.5 km of linac with 63 transformers, placed in the tunnel, which provide the low-voltage (690 V) network for the modulators and for the magnet power supplies. With this two-stage distribution system, power losses in the tunnel are reduced to 60 W/m in the medium-high voltage network and 30 W/m in the low-voltage network. The cable cross section can be successively reduced along the chain of 63 transformers. Heat losses in the transformers are removed from the tunnel by oil cooling and water heat exchangers. Installation of the transformers takes place in spaces available between modulators.

The cables are bundled in groups of three to minimize stray fields. In the linac tunnel, at a distance of about 6 m from the power line, the stray field amounts to less than 2 μT. In case machine operation demands lower stray fields, a solution with a co-axial power line is also conceivable.

In total some 1140 quadrupoles and 1720 correction magnets are installed in the linac (one vertical steerer for every quadrupole, one horizontal steerer for every 2nd quadrupole). All magnets have to be powered individually for optimum beam optics and beam-based alignment flexibility. In order to minimize cable costs and power losses, the power suppies are installed in the service tunnel. These devices are built in switched mode technology, which reduces the required volume and provides a high power conversion efficiency. For each linac, the total AC-power required for the magnets amounts to about 3 MW. Some additional power is needed for the beam transfer lines and for the beam delivery system.

4.9.8 Water Cooling System

The number of access points to the linear collider tunnel is minimized for cost reasons. We expect to have only three entrance points to the main tunnel where main supplies like water, air and electricity can be brought into the tunnel. This requires a carefully designed cooling system which is capable of transporting the power lost in the tunnel back to the surface. In order to reduce the amount of water, the beam pipe diameter and the velocity of water flow at the same time, maximum efficiency is required which leads to comparatively high operating temperatures of the components in the tunnel. We expect a water temperature of more than 70 C° in the return line. Such a high water temperature leads to an increase in efficiency of the heat exchangers and cooling towers as well, but also requires carefully heat shielded components in the tunnel to minimize the heat loss and keep the tunnel at reasonable temperatures. The layout for the cooling circuit of the S-Band linear accelerator is divided up into four separate

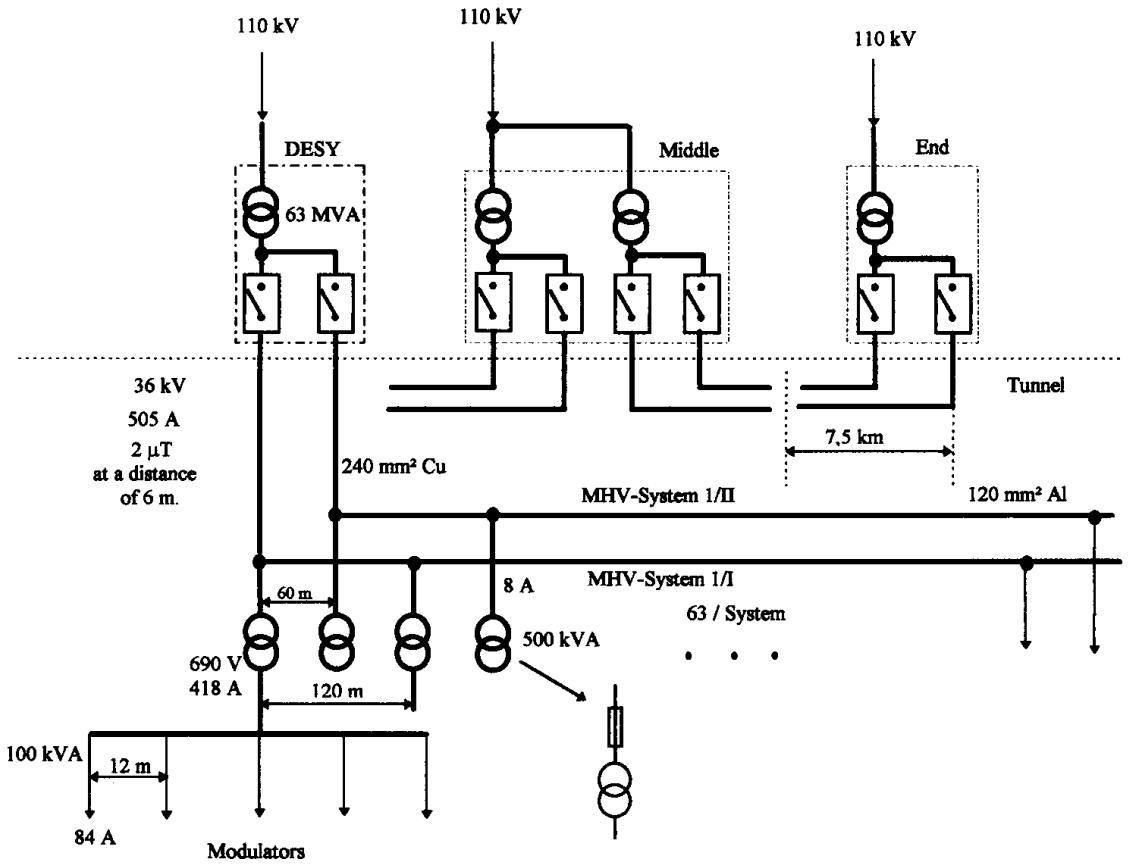

Figure 4.9.4: *Sketch of the power distribution system.*

cooling systems. Every cooling station has cooling towers, heat exchangers, pumps and control systems. In addition to the water system there will be a sub-cooling station for the air in the tunnel. This is important, because the air temperature in the tunnel increases with time due to residual power loss in the tunnel. The air cooling system heats up the cooling water from 15 C° to almost 30 C° and finally feeds the water into the main supply line. The diameter of the cold water tube is a function of the heat losses in the tunnel which we assume to be 300 W/m at maximum. This requires that this part of the supply water is cooled down by a refrigerator system which itself is connected to the cooling tower water.

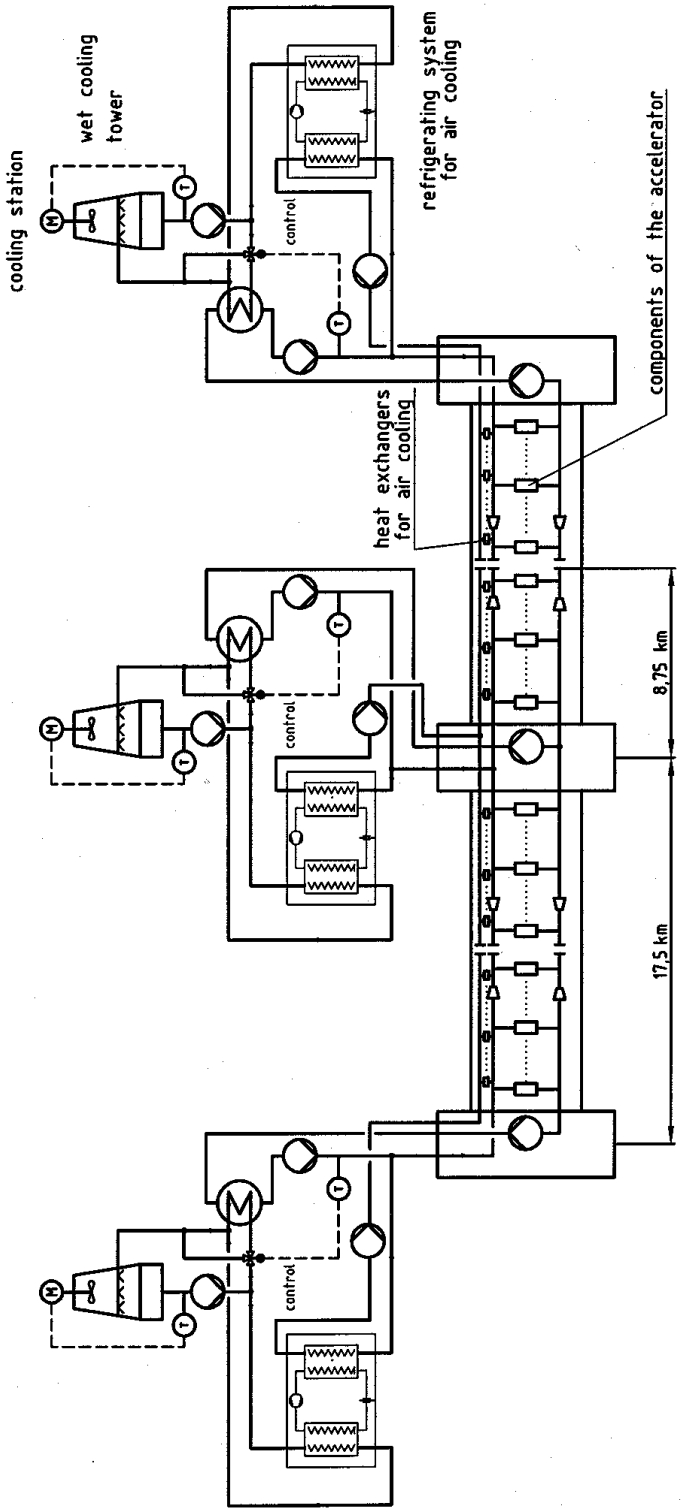

Figure 4.9.5: *Layout of the cooling plant for the linac. The middle station actually is twice as big as the end stations and consists of two stations.*

The cooling tower is a so called wet cooling tower which operates by evaporation of part of the water. An important number for such a cooling tower is the maximum humidity in the air which can be tolerated. A number derived from this is the wet bulb temperature. For this linac a value of 19.5 C° to 20.0 C° is preferable. Almost 25 towers for every station are required similar in size to those installed at DESY for the HERA ring. The fan velocity of the cooling towers will be controlled to maintain a constant temperature at the heat exchangers. The heat exchangers themselves will be controlled by a bypass system to provide a nearly constant temperature into the tunnel. The main tubes in the tunnel are distribution tubes. Because all elements are connected in parallel there will be a subdividing systems to avoid too many connections to the main tube which at the feed end have a diameter of almost 1 meter. The material of the main tubes is stainless steel and copper and copper for the distributing tubes. The length of the distribution system will be 14 to 28 meters, which is the distance between two or four sections. The next figure shows the elements of the distribution system in the tunnel.

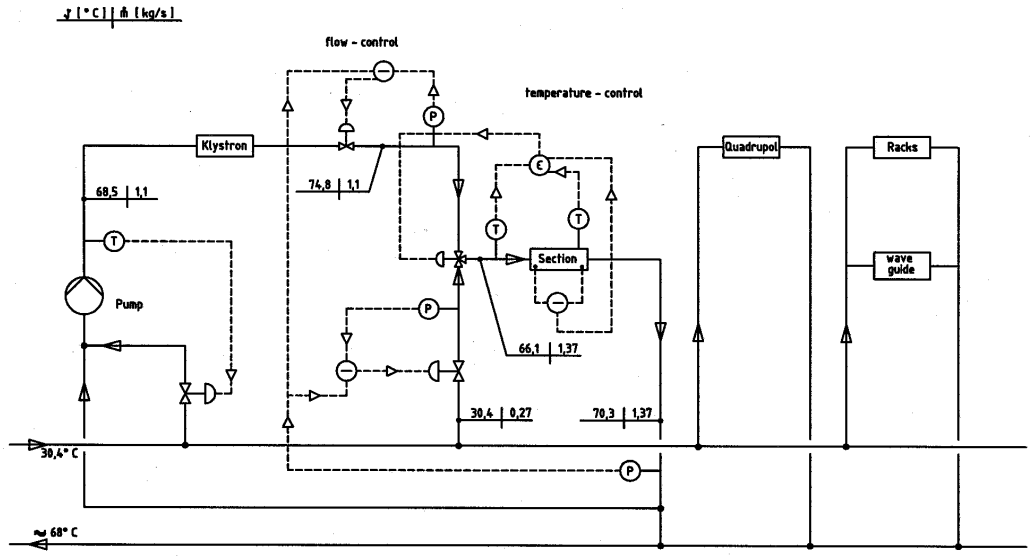

Figure 4.9.6: *The distribution system in the tunnel with the temperature control of the structures and the feedback/feed-forward controls.*

An important issue for the operation of a Linear Collider with heavy beam loading is the temperature stability of the accelerating structure. The phase and energy error is a function of the temperature distribution on the surface of the accelerating structure. Calculations prove, that keeping the temperature constant at a specific point on a constant gradient accelerating structure minimizes the energy error (see section 4.2.4). For control purposes the following values will be measured: the temperature at the

specific point, the temperature of the inlet water and the RF-power difference between the input and output. The last one will be used for a feedback system: with beam loading a definite input temperature is required and therefore it is possible to change the inlet water temperature before the surface temperature changes. The time available to do this depends on the water flow and the heat capacity of the structure and is about two seconds. This cannot be done by heating or cooling. Therefore a hot and a cold line is required and the required temperature is mixed by fast pneumatic mixing valves. For this circuit a simulation was made without the advantages of the feedback-system for the control. Fig. 4.10.7 shows the inlet water temperature into the structure and the structure temperature when the power into the structure and klystron is reduced to a third of the previous value.

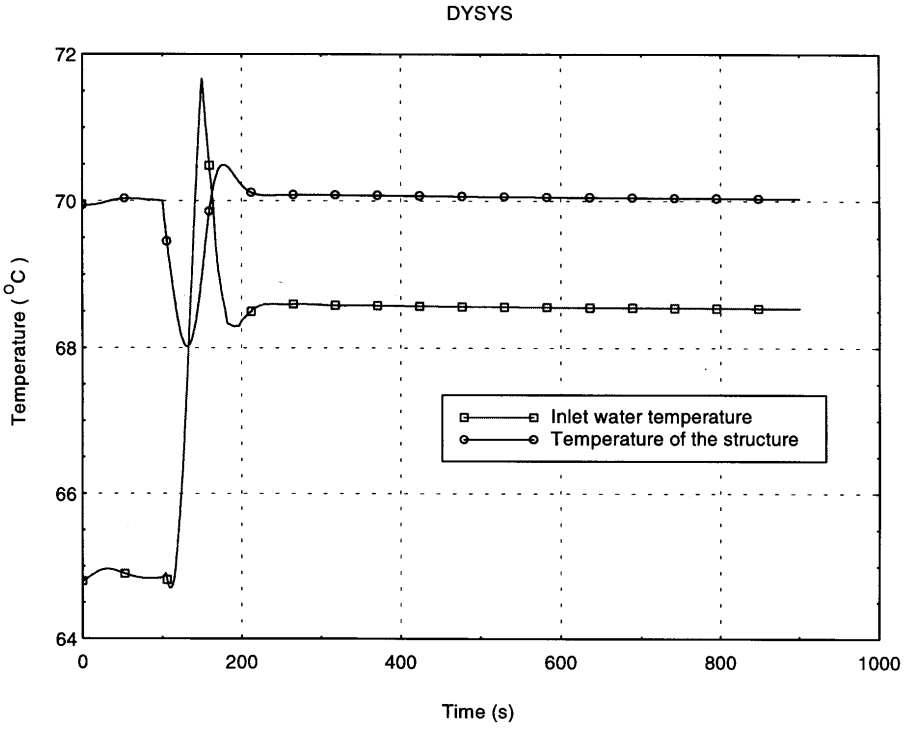

Figure 4.9.7: *Response of the cooling system to power change (3 times less) without any feed-forward and feedback.*

The water will be de-ionized with a conductivity of 1μS/cm. Therefore the only possible materials are: stainless steel, copper and bronze (gun-metal) . The maximum pressure in some of the RF-elements is very low. Therefore booster pumps in the return water line will be necessary to keep the pressure in the return line as low as possible. The diameter of the tubes varies over the length so that the pressure gradient will have a nearly linear characteristic. The first diameter will be 700 mm. The pressure losses

over the length will be 2.7 bar. The temperature of the return water will be 60 C° - 70 C°. Therefore the return water tube will be insulated with a thickness of 100 mm. The heat loss from the return water into the tunnel will be 50 W/m. To minimize the mechanical stress in the tubes by thermal expansion there will be compensators in the tubes. Every six meters will be a slide support point for the tube and between two compensators a fixed support point. For the slide elements PP-sheets are preferred. These elements are already used as slide sheets in the other DESY accelerators. The last or direct connections to all elements (e.g. magnets, klystrons etc.) will be done by EPDM-rubber tubes. The advantage is resistance to radiation, high flexibility for the connections, good and quick installation, direct connection between elements at a high electrical potential and ground shorted copper tubes.

4.9.9 Air Conditioning and Ventilation

The tunnels have a length of about 15 km without intermediate access. There are connections foreseen between the linac tunnel and the service tunnel every two km. During machine operation the latter tunnel is accessible for maintenance and repair work. The tunnel is an underground building and therefore forced ventilation is required. The regular velocity of air motion is 0.6 m/s, which will be enhanced to >0.8 m/s in case of an emergency for smoke removal. The pressure drop along the 15 km tunnel will be 1500 Pa. Special precautions are necessary in order to be able to open emergency doors at the tunnel end under this relatively high pressure. In case of a fire during machine operation, smoke detectors will shut down the machine and persons will leave the service tunnel through the nearest connection to the linac tunnel. The connections have fire-proof doors so that the linac tunnel serves as a safe and smoke-free escape exit. Both the fire load (transformer oil, cables, etc.) and the number of potential ignition sources (high voltage equipment, power supplies, etc.) are high so that such a safety concept is particularly important.

The power consumption in the service tunnel amounts to max. 7.5 kW/m. Most of the heat is removed by the water cooling system. Air ventilation does not contribute significantly to cooling, which is dominated by the tunnel walls. We allow for no more than 100 W/m of losses to the tunnel air, which requires to shield the hot water return pipe. For acceptable working conditions, the temperature in the service tunnel should not exceed 25°C.

The layout of the ventilation system is sketched in Fig. 4.10.8. A recirculation of the tunnel air is not possible. At the beginning of the linac tunnel fresh air is blown into the tunnel. If necessary, the air will be heated and dryed to ensure a relative humidity below 50 % in the tunnel. At the endstation hall the air from the tunnel is extracted.

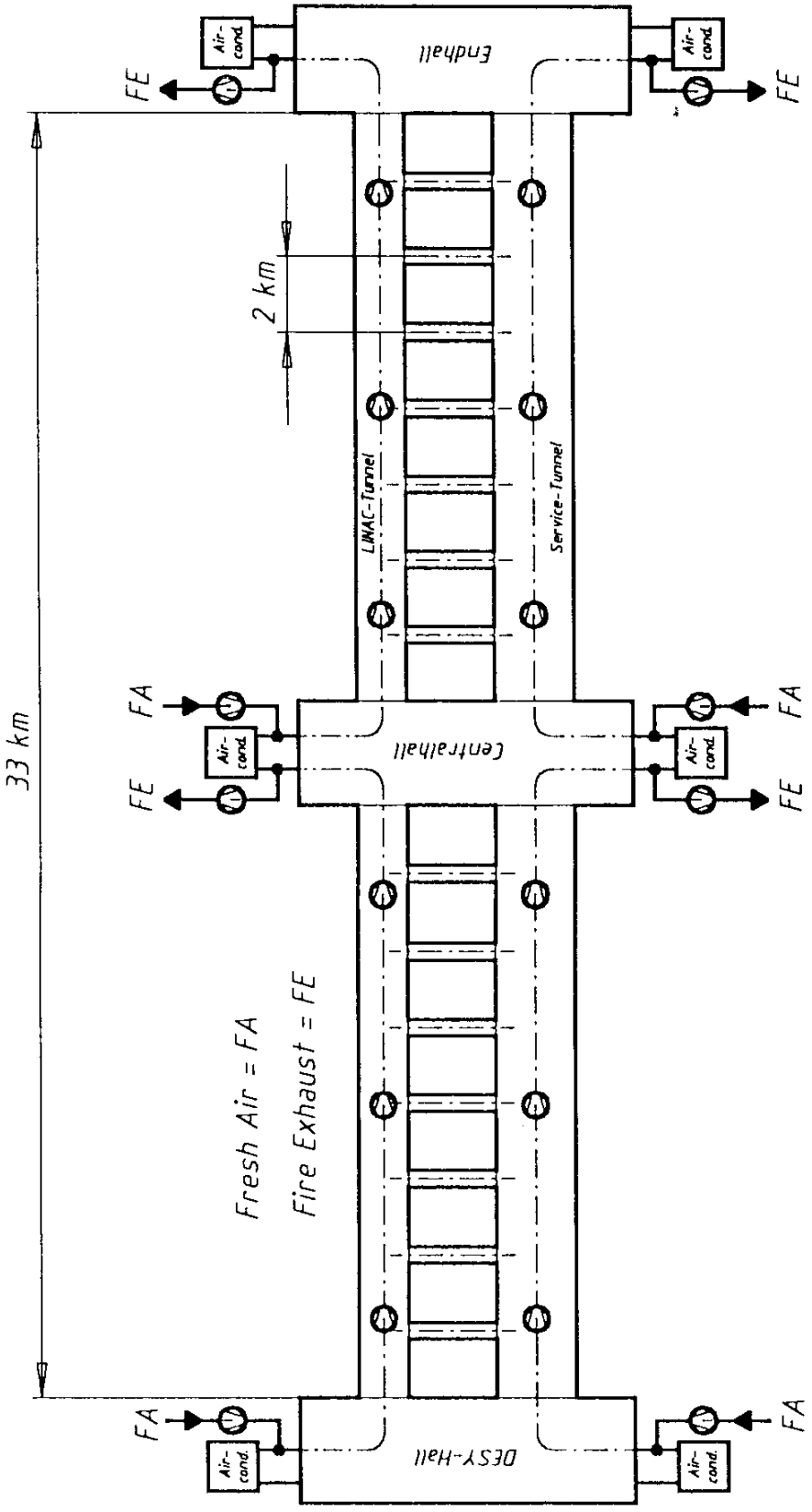

Figure 4.9.8: *Sketch of the ventilation system for the linac tunnel.*

4.10 Radiation Safety

This section describes the shielding requirements to guarantee radiation safety at the SBLC collider. The most important considerations here are, of course, the impact of the collider operation on the environment, i.e. conceivable radiation levels outside of the accelerator housing in areas accessible to the public and possible activation of soil and ground water. Other aspects are the safe working conditions for the operations personnel charged with repair and maintenance of the installations in the service tunnel.

The beam power in each of the two colliding beams (7 MW) is such that great care must be taken to avoid an uncontrolled loss of the beams. Such loss could immediately lead to a local destruction of the accelerator components and with this to an automatic cessation of operation. For equipment safety alone the monitoring of beam current along the machine is an absolute necessity, such that in case of unexpected significant loss ($> 1\,\%$) pulsing of the accelerator is interrupted instantly. Moreover, radiation monitoring in the accelerator housing will detect losses of much smaller magnitude such that corrective action can be taken in time.

The worst conceivable scenario is the failure of the beam loss interrupt system and the local deposition of a large amount of beam power, but just not large enough to significantly damage the accelerator and thereby terminate operation. Shielding of the produced radiation in such a case must be sufficient to avoid any significant radiation in the outside world.

The case of total beam loss in a small area will lead to immediate destruction of part of the accelerator and is harmless in comparison, as far as the maximum radiation dose is concerned. Particular attemtion must be paid to the beam dumps and the collimators for the spent beam close to the interaction point, because here all the beam power will be deposited during routine operation.

4.10.1 Radiation Levels on the Earth Surface Above the Tunnel

The most penetrating particles above the position of beam loss are high energy neutrons. For a point loss or a loss which occurs over only a few meters along the accelerator, the dose equivalent on the earth surface can be calculated with a simple formula given in [1], a report which also summarizes experimental and theoretical results. The thickness of the earth cover on top of the accelerator tunnel has an average value of 14 m. The smallest coverage will be 8 m. If a local beam loss would be as large as 0.1 % and would remain undetected and uncorrected, the radiation level at the surface would be $5{\cdot}10^{-8}$ Sv/h (0.005 mrem/h or 40 % of the natural background). With 5000 hours of operation per year, such radiation could, if left uncorrected, lead to an annual dose of 250 μSv (17 % of the legally permitted local radiation level). But such a continuous loss as assumed here would be produced by a continuous loss of 8 kW of high energy radiation in the tunnel, a huge signal for the above mentioned radiation monitors. Such a situation would be immediately corrected!

The beam dumps will be positioned below DESY ground and have an earth coverage

of at least 11 m (each additional thickness of 1.3 m reduces the rate from high energy neutrons by a factor of 10). With such shielding thickness the dose rate at the the surface can be made smaller than the natural background.

Another dose component at the earth surface is due to muons produced by beam losses along the accelerator. Muons are only created within a small cone in the beam direction, but they have a very large range. The doses were estimated by means of data given in [2]. First calculations of the conceivable dose rates show them to be small compared to the natural background. Muons from the beam dumps can be avoided at the surface by bending the beams downwards before they enter the dumps.

4.10.2 Radiation Levels in the Service Tunnel

Parallel to the accelerator tunnel (inside diameter 2.5 m) there is a service tunnel (inside diameter 4 m) which houses the klystron transmitters, power supplies, water cooling systems and all sensitive control and monitoring electronics. Continuous and unrestricted access also during times of collider operation must be available for the personnel charged with maintenance and repair work. It is therefore imperative that radiation levels in this service tunnel be low enough for radiation workers even under conditions of faulty accelerator operation.

The axis' of both tunnels are 9.5 m apart, such that more than 6 m of earth and concrete will separate both tunnels. Considering the numbers given above, it is evident that neutron doses in the service tunnel are just by a factor of 34 larger than those on the earth surface under comparable machine conditions:

- An undetected continuous beam loss of 0.1 % will lead to a maximum dose rate of 1.7 μSv/h (less than 15 times the natural background).

- Even for a local beam loss of 10 %, which might temporarily occur at collimator positions, the radiation level in the service tunnel would be only 0.17 mSv, still safely allowing access for a radiation worker.

- The beam dump will be located far enough away from the service tunnel such that radiation levels from that source can be neglected.

Other radiators in the service tunnel are the 150 MW klystrons, which need lead shielding around the collectors.

4.10.3 Activation of the Main Beam Dump

It was shown in section 4.7.9 that a dump made essentially of graphite and backed by aluminium is capable of handling a 7 MW beam. Such a dump has the additional advantage that the number of produced neutrons and its residual radioactivity are smaller than with any other material. In the following the activity of a pure carbon dump is estimated together with the dose rate near it after a long period of operation.

Nuclide	Saturation Activity [Bq]
^{11}C	$5 \cdot 10^{15}$
^{7}Be	$7 \cdot 10^{13}$
^{3}H	$7 \cdot 10^{12}$

Table 4.10.1: *Saturation activities in the Carbon beam dump.*

We assume an electromagnetic cascade completely developed in carbon, then the yield Y of a nuclide per incoming primary electron (energy E_0) is

$$Y(E_0) = \frac{L\rho}{A} \int_0^{E_0} \sigma(k) l\prime(k) dk \tag{4.10.1}$$

Here $\sigma(k)$ is the cross section of the nuclear reaction as a function of photon energy, $l\prime(k)$ the differential track length, and L, ρ, and Δ are Avogadro's number, density and atomic weight of the material. Approximation of cascade theory is especially valid at high energies, therefore we can write

$$l\prime(k) \approx 0.572 \frac{X_0 E_0}{k^2} \tag{4.10.2}$$

where X_0 is the radiation length.

For carbon only three nuclides have to be considered: ^{11}C (Half life 20 min), ^{7}Be (54 d), and ^{3}H (12.3 a). Their saturation activity in Bq is calculated which equals the number of produced nuclei per second. A full power operation of 7 MW is assumed to produce a saturation activity of ^{11}C, a mean power of 2 MW for the production of ^{7}Be and a mean power of 0.5 MW averaged over 25 years for calculating this magnitude for ^{3}H. The photon cross sections are mainly taken from [3, 4, 5] ; a small tail is added to the cross section curves to cover the photon energy range up to 200 MeV. The resulting saturation activities are given in Table 4.11.1.

A tritium activity of $7 \cdot 10^{12}$ Bq or 0.02 g produced in 25 years of operation is easily absorbed by the graphite (together with 1 g of stable hydrogen produced by nuclear processes), its absorption capacity is about $0.3 Ncm^3/g$ at room temperature. If part of it is exhaled due to elevated temperatures during operation it will be removed by the tunnel ventilation and presents no radiological hazard. The dose rate due to the residual activities of Table 4.11.1 is calculated taking roughly into account the extension of the source and the shielding effect of the surrounding aluminium. Immediately after stopping operation the ^{11}C gives a very high dose rate of 25 Sv/h at a distance of 1 m. After a cooling period of 3 h the dose rate is determined by the ^{7}Be which amounts to 10 mSv/h and decreases with the half life of 54 d. After a very long cooling period the dose rate is determined at a much lower level by the ^{22}Na activity produced in the backing aluminium (half life 2 a). The dose rate can be reduced by lead shields if necessary, depending on the position of the dump.

4.10.4 Activations Outside the Tunnel

The carbon/aluminium dumps described in this report are designed to absorb the total beam power of the two beams. In actual collider operation a significant amount

(about 10 %) has to be absorbed by collimators in the spent beam capture system for the positron source. These locations will be under DESY land and will have special shielding added. But except for these deliberate scraping losses at these collimators all beam power is dissipated in the dumps. Energetic neutrons produced in these dumps might penetrate the dump, lead shields and the concrete walls of the structures which house the dumps. These neutrons can then in turn activate soil and ground water. The resulting saturation activations under the assumption of no additional shielding have been calulated (see [6]. The results can be summarized as follows.

Saturation activity is essentially given by the product of neutron fluence and cross section, integrated over the neutron spectrum. The neutron fluence spectrum generated in a thick target is well known by measurements and calculations for primary protons. For high energy primary electrons no experimental results are available. Therefore we studied the shape of the neutron spectrum by preliminary calculations using the MC code FLUKA 92 for a thick target and as a function of concrete side shieldings. It turned out that the spectrum shape is independent of the shield for concrete thickness larger than 60 cm and that it is very similar to the neutron spectrum produced by primary protons. This can be expected. Neutrons in the relevant range up to 200 MeV are produced by intranuclear cascades (initiated by particles below 0.5 - 1 GeV) and by low energy nuclear reactions in the thick target and in the concrete or sand shield, rather independent of the high energy process. The spectrum was normalized in such a way that its total dose equivalent equals the dose of electron- produced neutrons given in [1] (which in turn is based on measurements and calculations).

When one considers nuclear reactions in the soil and ground water initiated by fast neutrons from an *unshielded* beam dump, radioactive nuclides with very short life time are of less interest, because of the time necessary to come in possible contact with people. Nuclides with very long life times are also of less interest, because of the low dose rates associated with long life times. The cross sections for the producing reactions of the interesting nuclides are not all accurately known. But since neutron induced reactions are known to be similar to proton induced reactions, the cross sections of the latter can be reasonably substituted.

The resulting saturation activity, assuming an unrealistic continuous 7 MW operation throughout the year, in the soil near the beam dump is, ^{7}Be: 6400 Bq/g, ^{22}Na: 12000 Bq/g, ^{55}Fe: 3000 Bq/g, ^{45}Ca: 300 Bq/g and ^{54}Mn: 150 Bq/g. Apparently these numbers present no radiological problem: The nuclides are permanently attached to solid soil and are neither accessible nor movable. With a half life for all of them smaller than 3 years, 40 years after final shutdown of the accelerator all remaining activities will be smaller than the natural activity of sand.

Accelerator-produced nuclides could also be expected in the ground water due to spallation of oxygen and leaching of nuclides produced in the soil. The somewhat complex situation is described and analyzed in [6]. As a result, only ^{22}Na and ^{3}H might be found in ground water. This has been confirmed by experiment [7]. If we assume that the slowly moving ground water will be close the beam dump for 100 days, the calculated activity concentration will be 320 Bq/g and 1400 Bq/g, respectively. These numbers would be of concern only, if the drinking water for people is taken without

dilution from a well in the immediate vicinity of the beam dump (they would be 5000 times as large as legally permitted for general consumption). This is an extremely unlikely scenario, since the beam dumps are under DESY land and there will be no wells in their immediate vicinity. A large dilution factor could therefore be reasonably assumed in practice. But it would also be very simple to add concrete shielding around the beam dump and reduce the water activity concentration there by a factor of 5000: One meter of heavy concrete gives a reduction factor of 30 for fast neutrons. Therefore 2.5 m of added shielding would already suffice.

Bibliography

[1] K. Tesch, Rad. Prot. Dosimetry 22 (1988) 27.

[2] E. Bräuer, K. Tesch, Internal Report DESY D3-62 (1987) (derived from W. R. Nelson, Nucl. Instr. Meth. 66 (1968) 293).

[3] B. C. Cook et al., Phys. Rev. 143 (1966) 724.

[4] H. Artus, Zeitschrift f. Physik 189 (1966) 355 V. di Napoli et al., Notas de Fisicas XIII (1967) No. 3 (Centro Brasil. Pesquisas Fisicas, Rio de Janeiro).

[5] V. V. Balashov et al., Nucl. Phys. 27 (1061) 337.

[6] K. Tesch, Internal Report DESY D3-86 (1997).

[7] S. Baker et al., SSC Dallas, SSCL-Preprint 538, 1994.